Thermal Management of the Permanent Magnets in a Totally Enclosed Axial Flux Permanent Magnet Synchronous Machine

By Adam Malloy

A thesis submitted in part fulfilment of the requirements for the degree of Doctor of Philosophy and the Diploma of Imperial College London

Department of Mechanical Engineering
Imperial College London

September 18th 2014

The work contained in this thesis is that of the author, and to the best of his knowledge is original. Reference has been made when the work of others has been used. Reference has also been made to publications where parts of this work have been presented.

Abstract

Elevated magnet temperature in Axial Flux Permanent Magnet Synchronous Machines (AF PMSM) adversely affects torque production, material cost, and the risk of demagnetisation. These machines show promise in applications requiring high power density, however the factors which affect magnet temperature have rarely been investigated. This is therefore the focus of the thesis.

A multiphysics numerical model was formulated which predicted the loss, flow, and temperature fields within an AF PMSM. A criterion for estimating the relative importance of the fluctuating component of a periodic heat source on the temperature response of a device was proposed and validated. In this work it was used to justify a steady state, rather than transient, thermal analysis.

Thermometric and electrical measurements were taken from an instrumented AF PMSM to validate the numerical predictions. A novel magnet loss measurement technique was implemented; losses were determined by measuring the initial temperature rise rate of the magnets. This was achieved via a calibration relating temperature rise to voltage constant.

It was found that 99% of the heat generated in the magnets was convected to the inner cavity of the machine, due to the inner cavity's recirculating flow structure this heat was dissipated to the casing and core. As a proportion of all heat entering the inner cavity 56-62% left to the casing while 28-41% left to the core. Magnet hot spots were found to be up to 13% greater than the mean temperature rise. Their location was influenced by the distribution of losses and the direction of shaft rotation. Temperature gradients within the inner cavity caused the magnet's trailing edge to incur a 10% greater temperature rise than the leading edge. As increasing temperature decreases the coercivity of magnet materials these findings are a crucial contribution to the understanding of devices where local demagnetisation is of concern.

Acknowledgements

First of all I would like to thank my supervisor Professor Ricardo Martinez-Botas for not only his guidance and support but for his uncanny knack for motivating me when I felt lost. Thanks to him for providing the opportunity to carry out this project, I'd go as far as to say 'I enjoyed it'.

I would also like to thank Dr Michael Lampérth and Dr Malte Jaensch for setting up the project and providing technical guidance throughout. Special thanks for arranging the use of Evo Electric Ltd.'s test facility for the experimental phase of this work.

To everybody at Evo Electric Ltd, past and present, thank you for your patience and support. For his trouble shooting expertise during the experimental work I am grateful to Dr Tim Allen. The prototype electrical machine could not have been built without the help and experience of Philip Mitchell, you stayed late when no one asked you to – I owe you one.

To everybody in the turbocharger research group at Imperial College 'thanks for having me'. Special thanks to Dr Peter Newton, Dr Clemens Lorf, and Dr Jonathan Hey for their friendship.

To my friends away from Imperial: I don't think you realise how important you've been over the last years; especially you Laura, Tom, Bob, Gareth, Annabelle, Paul and Ian. Thanks to Helen, Denis and Mark for 'over committing' with me and entering triathlons, half marathons, cycle races and the like. Not to mention all the climbing. Without those distractions the last years would have been very one dimensional; I'm a better person for it.

A big thank you to all my family, especially my parents and brother. You have been patient, encouraging and supportive: I'm 'back online' now. My biggest thanks go to Janine, you always knew I would get there in the end, even when I wasn't sure.

Grandad, I think you would have approved of all this, but you'd definitely have said:

'By 'eck, you're a queer lad'

It takes all sorts I guess…

Contents

List of Figures

List of Tables

Nomenclature

Abbreviations

AF	Axial Flux
BEMF	Back Electromotive Force
CHT	Conjugate Heat Transfer
EM	Electromagnetic
FEA	Finite Element Analysis
FVM	Finite Volume Method
PM	Permanent Magnet
PMSM	Permanent Magnet Synchronous Machine
RMS	Root Mean Square
SST	Shear Stress Transport
THD	Total Harmonic Distortion

Greek

α	Temperature coefficient of resistivity	1/K
α^*	Non-dimensional angular position	
Γ_t	Turbulent diffusivity	m^2/s
δ	Skin depth	m
	Phasor angular offset	rad
ε	Permittivity	F/m
	Emissivity	
θ	Angular position	rad
	Temperature difference	K
θ_m^*	Non-dimensional temperature rise in magnet	
μ	Viscosity	Pa.s
μ_t	Eddy viscosity	Pa.s
μ_0	Permeability of free space	H/m

μ_r	Relative permeability	
ν	Kinematic viscosity	m^2/s
	Periodic heat source criterion	
ρ	Density	kg/m^3
	Charge density	C/m^3
	Resistivity	Ohm.m
σ	Conductivity	S/m
	Stefan-Boltzmann Constant	$W/m^2.K^4$
τ	Thermal time constant	s
τ_w	Shear stress at the wall	Pa
τ'_{ij}	Viscous stresses	Pa
Φ	Flux	Wb
	Viscous diffusion	Pa
ω	Angular velocity	rad/s
ω^*	Non-dimensional angular velocity	
Ω	Magnetic scalar potential	A/m

Roman

A	Area	m^2
	'On' time during duty cycle	s
B	Systematic uncertainty	%
$\vec{B}$	Magnetic flux density	T
$(BH)_{MAX}$	Maximum energy product	J/m^3
Bi	Biot number	
B_m	Peak flux density	T
C_m	Drag torque coefficient	
C_p	Heat capacity	J/kg.K
C_{th}	Thermal capacitance	J/K
D	Duty cycle	
$\vec{D}$	Electric displacement	C/m^2
D_h	Hydraulic diameter	m
D_i	Inner diameter	m

D_o	Outer diameter	m
$\vec{E}$	Electric field strength	V/m
e	Back electromotive force	V
	Surface roughness	m
F	View factor	
Fo	Fourier number	
f	Frequency	Hz
	Fill factor	
G	Non-dimensional gap ratio	
g	Acceleration due to gravity	m/s^2
$\vec{H}$	Magnetic field strength	A/m
$\overrightarrow{H_c}$	Coercivity	A/m
H_m	Peak magnetic field strength	A/m
$\overrightarrow{H_s}$	Magnetic field strength from currents	A/m
h	Enthalpy	J
	Convective heat transfer coefficient	$W/m^2.K$
i_s	Short circuit current	A
i	Phase current	A
$\vec{J}$	Current density	A/m^2
K	Turbulence kinetic energy	J/kg
k	Thermal conductivity	W/m.K
k_h	Hysteresis loss coefficient	$W/m^3/Hz/T^2$
k_c	Eddy current loss coefficient	$W/m^3/Hz^2/T^2$
k_e	Excess loss coefficient	$W/m^3/Hz/T^{1.5}$
	Voltage constant	V.s/rad
k_{lam}	Stacking factor	
k_T	Torque constant	Nm/A
L_s	Synchronous Inductance	H
l	Length, length scale	m
Ma	Mach number	
$\vec{M}$	Magnetisation	A/m
m	Mass	kg

$\dot{m}$	Mass flow rate	kg/s
N	Number of turns	
N_L	Number of laminations	
Nu	Nusselt number	
P	Perimeter	m
	Random uncertainty	%
Pr	Prandtl number	
Pr_t	Turbulent Prandtl number	
p	Pressure	Pa
q	Heat Rate	W
q''	Heat flux	W/m^2
$\dot{q}$	Loss density	W/m^3
q^*	Non-dimensional heat source parameter	
R	Resistance	Ohm
	Relative roughness	
Re	Reynolds number	
R_o	Outer radius	m
R_{RMS}	Residual error between meshes	
R_{th}	Thermal resistance	K/W
r^*	Non-dimensional radial position	
S	Sutherland's constant	K
S_φ	Source term	
T	Torque	Nm
	Temperature	K
	Time period	s
T_{EM}	Electromagnetic torque	Nm
$\vec{T}$	Current vector potential	A/m
t	Time	s
t_L	Lamination thickness	m
U	Uncertainty	%
u	Velocity	m/s
u_*	Friction velocity	

$\overline{u_i' T'}$	Turbulent heat flux	W/m^2
$\rho \overline{u_i' u_j'}$	Turbulent stress	Pa
V	Volume	m^3
$\vec{V}$	Velocity	m/s
V_{DC}	DC bus voltage	Vdc
v	Phase to neutral voltage	V
v_i	Element volume	m^3
v^*	Ratio of phase-neutral voltage to DC bus voltage	
W	Stored magnetic energy	J
X	Reactance	Ohm
y^+	Non-dimensional distance of the first node to the wall	
Z	Phase impedance	Ohm
z^*	Non-dimensional axial position	

Subscript

c	Eddy current loss
cu	Winding
d	d-axis component
e	Excess loss
f	Fundamental component
fe	Core
h	Hysteresis Loss
i	Inlet
m	Magnet
MAX	Maximum value
$mech$	Mechanical
o	Outlet
q	q-axis component
rad	Radiative
rot	Rotating Domain
s	Wall surface
$stat$	Stationary Domain

w	Windage
∞	Free stream

Superscript

-	Mean component
‘	Fluctuating component

Chapter 1

Introduction

1.1 Perspective

Rotating electrical machines convert electrical energy into mechanical energy and vice versa. They are responsible for consuming 65% of electrical energy in industrialised countries [1]. The applications of electrical machines are numerous and familiar, ranging from industrial drives which power pumps and fans to automotive drives which provide traction and power ancillaries (like windscreen wipers or fuel pumps). They are a popular choice for power conversion as they are clean, cheap, and have low maintenance requirements due to the fact that they only have one moving part.

Today's society is dependent on electrical power, with global demand predicted to increase by 33% by 2035, and coal continuing to supply the majority of this energy [2]. When fossil fuels are combusted the gasses released as a by-product of the process have many harmful effects on our environment. These include reduced air quality, acid rain, and perhaps most ominously global warming. Consequently global targets have been set to reduce demand on power generation [2], see Table 1.1.

Another large contributor to air pollution and global warming is the transport sector, accounting for 23% of world energy related emissions [3]. As with energy demand, demand for vehicles has been growing in recent decades. Figure 1.1 shows global transport energy usage by year and mode from 1971 to 2006. The trend looks set to continue, especially in emerging economies such as China where it is projected that by 2030 more highway vehicles will be in use than are in the USA today [4].

Table 1.1 Global targets for energy demand reduction [2]

Country	Target reduction in energy demand [%]	Target date
China	16	2015
Japan	10	2030
European Union	20	2020

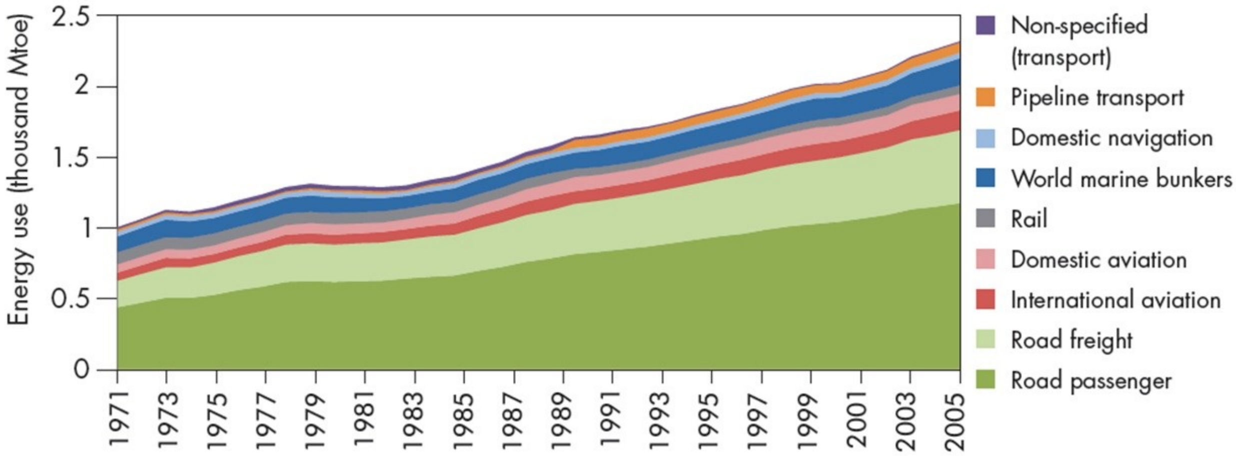

Figure 1.1 Global transport energy usage 1971-2006, Mtoe is megatonne of oil equivalent, [5]

Technology has the potential to play a large part in overcoming the problems of increasing energy and transport demand while meeting global targets for emissions reduction. As electrical machines generate and consume the majority of electrical energy produced, increasing their efficiency would help meet these targets. In terms of transport, electrification of the drive train is a potential solution for reducing emissions [6]. This depends of course on the method used to generate the electricity used for traction. When compared with industrial applications, automotive traction is a demanding application for an electrical machine. High efficiency over a wide range of speeds and torques is required in order to mitigate low battery capacity. High power density is desired to reduce vehicle weight. Low cost and high reliability are also typically requested from vehicle manufacturers.

The field of electrical machines has changed drastically in recent decades and many types are available. Induction machines are still the most common topology with the vector control methods developed in the 1970s allowing them to be controlled in the same way as D.C commutator machines. Since the discovery of rare earth permanent magnet (PM) materials in the 1980s PM machines have been increasing in popularity [7]. They exhibit higher efficiency, power factors, and power density than their counterparts [8].

The electrical machine is a multidisciplinary device with electromagnetic, thermal, and mechanical phenomena all playing a part in overall performance. Electromagnetic and mechanical analyses are advanced and well understood in general, with computational models able to produce accurate predictions of performance, and descriptions of the underlying physics involved. Thermal analysis is less common, though interest is growing, especially in power dense applications where maximum output power can be limited by the maximum operating temperature of certain components.

This thesis is focussed on increasing the understanding of the coupled electromagnetic-thermal phenomena occurring within an electrical machine. The axial flux permanent magnet synchronous machine (AF PMSM) topology is selected for study as in general radial flux machines are better understood. Axial flux machines have the main component of flux crossing their air gap axially while in a radial flux machine the flux crosses the air gap radially. Figure 1.2 shows the topological differences between radial and axial flux machines.

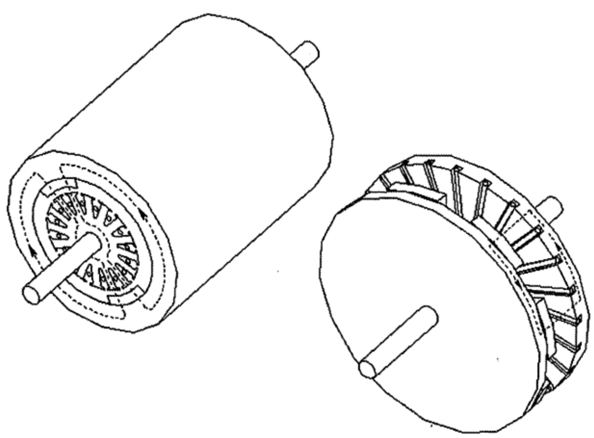

(a) Radial flux (b) Axial flux

Figure 1.2 Radial and axial flux topology, from [9]

1.2 The Surface Mounted Axial Flux Permanent Magnet Synchronous Machine

This section begins with a review of the applications which frequently make use of AF PMSMs. After this the electromagnetic and thermal aspects of the surface mounted AF PMSM are introduced in order to provide a background for, and introduce, the electromagnetic-thermal coupled problem. An introduction to permanent magnet materials is given where a basic understanding of electromagnetic field theory is assumed. The machine geometry which is the focus of this thesis is then introduced and used as a framework to describe some of the fundamental electromagnetic equations of the PMSM. Once the basic electromagnetic concepts have been presented the thermal aspects of these machines are introduced.

1.2.1 Applications

Radial flux machines are more common than axial flux machines due to their relative ease of manufacture. In recent years axial flux machines have received more attention as manufacturing methods have matured [10]. In order to identify suitable applications, Cavagnino et al. [11] performed a study comparing the torque density of a range of radial flux machines (all with one external stator and one internal rotor) to a range of axial flux machines (all with two external stators and one internal rotor). They kept the motor volume, rotational speed, air gap flux density and 'losses to thermal wasting surface' ratio constant while varying the aspect ratio and number of poles in the machine. The results are shown in Figure 1.3.

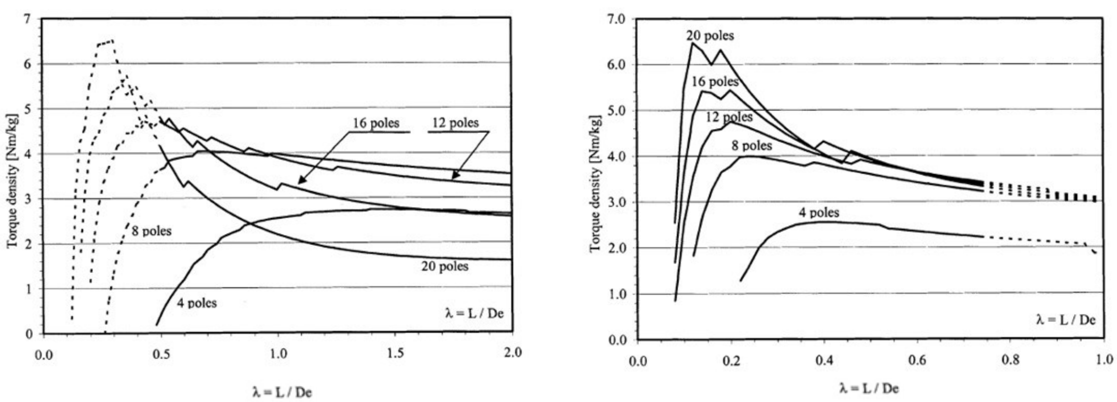

(a) Radial flux machine (b) Axial flux machine

Figure 1.3 Radial and axial flux permanent magnet machine torque density as a function of L/De where L is machine length and De is machine diameter, from [11]

As can be seen in the above figure, there is no significant difference in torque density between the two topologies at comparable aspect ratios. The dashed lines on the plots represent aspect ratios which are considered to be difficult to manufacture. This constitutes the biggest difference between the topologies with axial flux machines delivering more specific torque, but only at low aspect ratios, and radial flux machines delivering more at high aspect ratios.

Power Generation

Axial flux machines have been used in power generation applications such as wind turbines where relatively high torque at low speed is required. Bumby et al. [12] present the development of an air-cored generator for a wind turbine application, see Figure 1.4. They state that the wind turbine requirement for low starting (and cogging) torque favours their air cored design, which is also easy to assemble as there is no attraction force between the rotor and stator when the winding is not energised. The torque density of their generator allowed them to couple it directly to the turbine without a gear box.

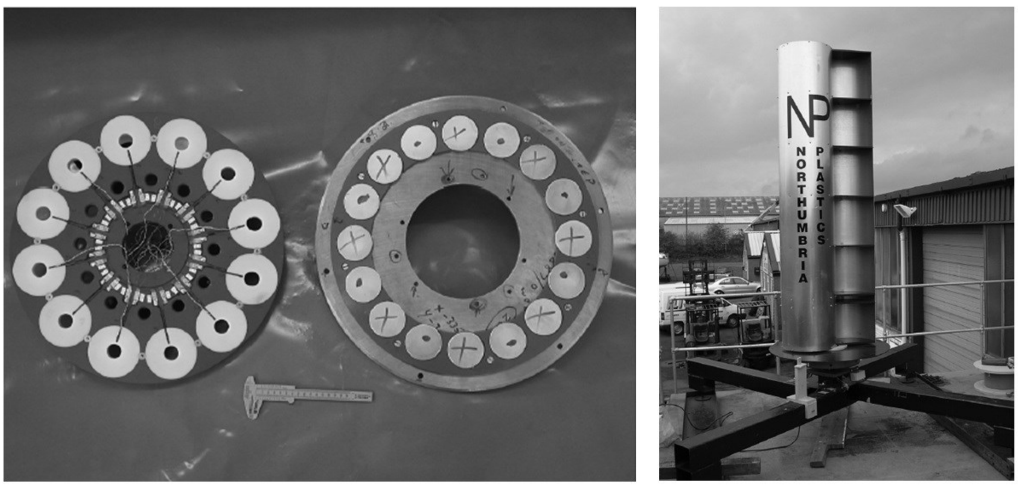

Figure 1.4 Axial flux generator (left), wind turbine application (right), from [12]

Axial flux machines were investigated for use in wind power generation systems by Park et al. [13]. Given a set of design requirements from a turbine manufacturer they employed a slotless stator which produced no cogging torque. The rated speed of their generator was 150rpm, while the power was 300W. The packaging space available fixed the stator diameter D to be 316mm and the active length L to be 56mm, this gave an aspect ratio L/D of 0.18. When referring back to Figure 1.3 this is an ideal aspect ratio for the axial flux topology. A similar generator concept was proposed by Wannakarn et al. [14], though the application was for a horizontal axis wind turbine.

Hwang et al. [15] present the design of a gearless wind power generation system. They found that an axial flux PMSM fulfilled their requirements for a generator with a rated speed of 300rpm and rated power of 10kVA.

Hybrid electric and pure electric vehicles

Having a high torque density and low aspect ratio axial flux PMSMs are particularly suited for use as traction drives for hybrid electric/pure electric vehicles [16]. In this application the torque density of the axial machine allows it to be integrated into the drive train without a gear box, simplifying the mechanical design. Their aspect ratio also allows them to be integrated into the wheel of a vehicle, or directly coupled to an internal combustion engine as a generator.

The latter implementation was investigated by Anpalahan et al. [17] who presented the development of a 165kW axial flux PMSM for a series hybrid drive system. The generator featured three 'double stator – single rotor' modules coupled together in series. The system was aimed at light rail vehicles and featured their generator directly coupled to the internal combustion engine without the need for a gear box.

Lamperth et al. [10] present experimental results from their axial flux PMSM tests. They give typical requirements for wheel motors and proceed to characterise their machine to show that it meets these requirements without the need for a gearbox.

Woolmer et al. [18] describe the design and present the analysis of a yokeless and segmented armature axial flux PMSM machine designed to provide traction for a fuel cell powered sports car, Figure 1.5. They increased the power density of their machine when compared with a conventional axial flux PMSM by redesign of the magnetic circuit, eliminating the need for a stator yoke. This enabled the stator to be segmented and therefore have each coil wound separately around each tooth, achieving a high fill of copper in the stator slots. They found that this combination of factors increased torque density by 20% when compared to 'other' axial flux PMSMs, making it ideal for their high performance sports car application.

Figure 1.5 Yokeless and segmented armature machine, from [18]

An axial flux PMSM is proposed by Takorabet et al. [19] as a traction drive for an electric vehicle. The stator of their machine is manufactured in the same way as a printed circuit board (PCB), see Figure 1.6. The axial flux topology is the most practical way to implement this kind of PCB based design, which offers reduced weight (due to its coreless design), cost, size (as there is no end winding), no cogging torque, and near sinusoidal winding flux density distribution due to the concentric nature of the winding.

(a) Stator winding (b) Rotor

Figure 1.6 PCB motor for automotive application, from [19]

Other Applications

Axial flux PMSMs have also been used in aircraft systems. De et al. [20] state that their popularity is due to their high power density, efficiency and reliability. The authors present the design and implementation of a drive system including an axial flux machine used to power aircraft applications such as hydraulic pumps, cabin air compressors and engine start systems.

Hill-Cottingham et al. [21] proposed an air-cored multi-stage axial flux machine to drive the propeller of an unmanned aircraft. They compare their machine to a radial flux machine aimed at the same application and find that the axial machine has a higher power density and efficiency.

An axial flux PMSM was proposed by Jussila et al. [22] for industrial use. They investigated a concentrated winding design with open slots, see Figure 1.7. In the axial flux topology this greatly simplifies manufacture because the coils can be prefabricated and subsequently inserted around the teeth of the stator. They acknowledged the increased magnet losses due to this choice of design and proposed segmentation of the magnets as a solution, negating some of the financial savings initially made by simplifying the manufacture of the stator.

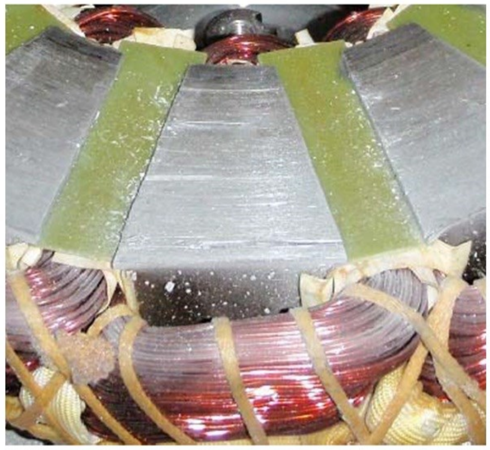

Figure 1.7 Prefabricated coil inserted into the open slot of an axial flux machine

Wu [23] presents the design and analysis of an axial flux PMSM suitable for use as a flywheel motor in nanosatellites. The author proposes a PCB stator (as was the case in Takorabet's [19] automotive traction drive) and cites that this, coupled with the increased power density of the axial flux topology, as being the main benefit for this application.

In summary, axial flux machines have been used in various applications; designers of wind turbines have taken advantage of the ability to manufacture an ironless core, eliminating cogging/starting torque; in package and weight restrictive applications like vehicles, aircraft, and satellites they are used for their increased torque and power density.

1.2.2 Electromagnetic Aspects

This section introduces some of the electromagnetic aspects of the axial flux PMSM, the goal is to introduce enough of the theory to put the thermal aspects of the device into context. For a more in-depth presentation of electromagnetic machine theory the reader is referred to [1,24,25,26]

1.2.2.1 Permanent Magnets

Below its Curie temperature a permanent magnet has a spontaneous magnetisation $\vec{M}$, where no external field is required for it to produce a magnetic field. The magnetisation $\vec{M}$ is a function of temperature, where it is a maximum at 0K and 0 at the Curie temperature. Figure 1.8 shows the magnetisation, and $\vec{B}\vec{H}$ characteristic for an ideal permanent magnet, where $\vec{B} = \mu_0\left(\vec{H} + \vec{M}\right)$.

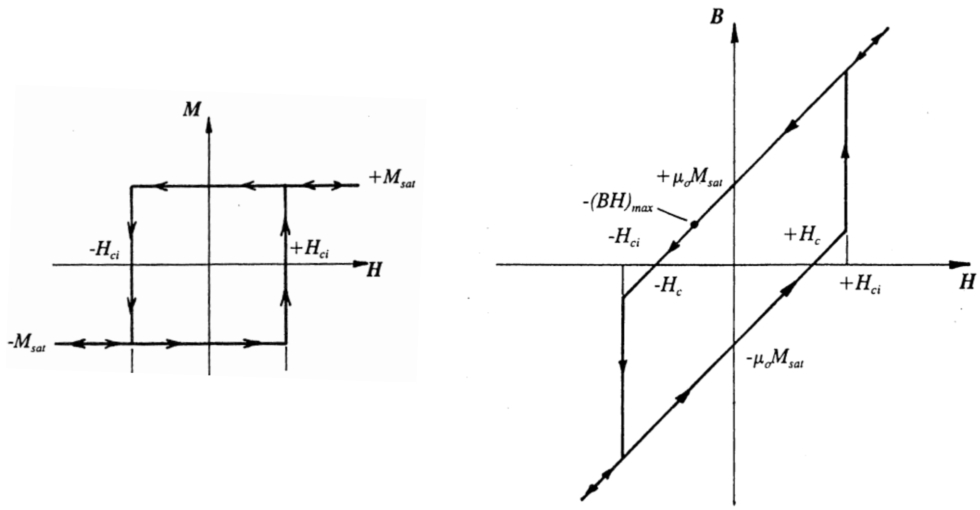

(a) Magnetisation characteristic

(b) $\vec{B}\vec{H}$ characteristic

Figure 1.8 Magnetisation & $\vec{B}\vec{H}$ characteristic of an ideal permanent magnet, from [26]

Figure 1.8 shows that a magnet has a constant value of $\pm\vec{M}$ apart from when the magnetising field $\vec{H}$ is equal to $\pm\vec{H}_{ci}$. At these points the magnetising field is strong enough to reverse $\vec{M}$. The second quadrant of the $\vec{B}\vec{H}$ curve in Figure 1.8 is known as the magnet's demagnetisation curve. When the magnet is operated in this region it is delivering a positive flux against a demagnetising force (e.g. an air gap). When the demagnetising force is 0 the flux delivered by the magnet is termed its remanent flux density. When the magnetising force is $-\vec{H}_c$ the flux delivered by the magnet is 0 and $\vec{H}_c$ is termed the magnet's coercivity. $\vec{B} \times \vec{H}$ at each point on the $\vec{B}\vec{H}$ curve represents the potential energy, in the second quadrant this can be seen to peak at $-\left(\vec{B}\vec{H}\right)_{MAX}$ which is the figure by which magnet materials are often compared.

1.2.2.2 Fundamental Equations of the PMSM

This thesis uses a 10-pole fractional slot machine with a single rotor sandwiched between two stators as a case study, the details of which are presented in Table 1.2. The major components of the machine are shown in Figure 1.9.

The magnets produce a flux density distribution throughout machine. In order to produce torque a stator flux density field must be generated which reacts against the rotor field. To produce the stator field current is pushed through the windings of the machine. The current produces a magnetising field $\vec{H}$ which in turn creates the stator flux density distribution. The rotor and stator fields interact in quadrature to produce torque, which can be calculated as the derivative of the stored magnetic energy W with respect to a small displacement θ, $T = dW/d\theta$, [24]. The distribution of the flux density is due to component geometries and material properties which are 'fixed' once a machine is produced. If nonlinearities in the magnetic circuit are ignored then machine torque is proportional to the phase current, where the constant of proportionality is the torque constant k_T which is a function of all of the machine geometries and material properties, [24].

Table 1.2 Axial flux PMSM details

Parameter	Value
Phases	3
Rotor Poles	10
Stator Slots	45
Magnet Material	Nd-Fe-B
Stator Material	M330-35A
Active Outer Diameter [mm]	245
Active Inner Diameter [mm]	140
Maximum Rotational Speed [rpm]	8000
Maximum Continuous Power [kW]	64
DC Bus Voltage [V]	360
Carrier Frequency [kHz]	12

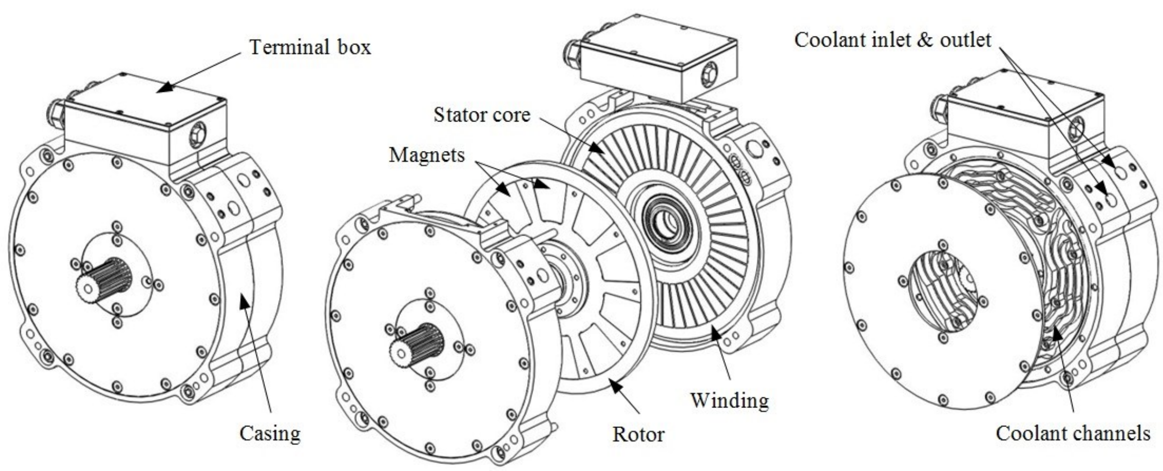

Figure 1.9 Major components of the axial flux PMSM

The voltage driving the current through the windings has a number of voltage drops to overcome. These include the ohmic resistance R and reactance $X = \omega L_s$ of the winding as well as the Back Electromotive Force (BEMF), e. The BEMF is induced by the rotor flux field passing through the coils in the stator as the rotor rotates. The voltage induced across the coils is described by Faraday's law, $e = N\, d\Phi/dt$. As with the torque constant, the material and geometric properties which define the rotor flux density distribution can be accounted for by the voltage constant k_e, which is the constant of proportionality between the machine speed and the induced BEMF, [24].

In this case, the machine studied is a three phase machine. If the phases are balanced its operation can be described by its equivalent circuit [24], shown in Figure 1.10.

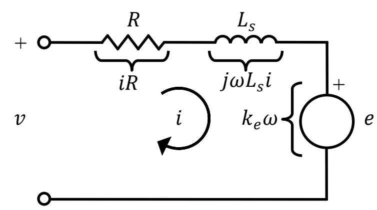

Figure 1.10 Equivalent circuit of a PMSM

As stated, the rotor flux Φ_r and stator flux Φ_s rotate in quadrature with each other, see Figure 1.11. It therefore follows that the BEMF and reactance are also in quadrature with each other. As the BEMF is proportional to $d\Phi/dt$ the phase current must be in phase with the BEMF. These relationships can be understood by considering all of the sinusoidal components as phasor quantities, see Figure 1.11. The angle between the voltage v and the current i is known as δ, where cos δ is the power factor.

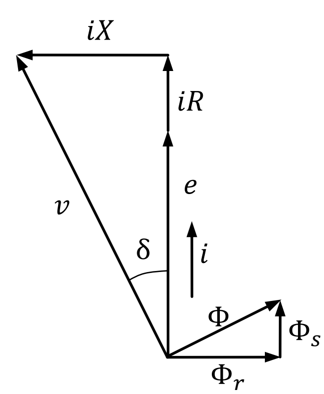

Figure 1.11 Phasor diagram of a PMSM

In cases where v exceeds the maximum available voltage from the source, i can be given an angular offset from e. Conceptually this creates two current components, i_q and i_d, where i_q is in phase with the BEMF and creates a stator flux density waveform which is in quadrature with the rotor flux waveform (this component creates torque). The direct component, i_d, is applied 90 degrees out of phase with the BEMF creating a stator flux density waveform which is in phase with, and directly opposing the rotor flux waveform. It can be thought of as demagnetising the rotor, or reducing the resultant flux passing through the coils, and therefore reducing the voltage v necessary to drive the current i. Figure 1.12 shows this relationship through another phasor diagram. For completeness the reactances have also been decomposed into d-q values, though the values can often be assumed to be the same in surface mounted PMSMs [24] as the relative permeability of the permanent magnet material is ~1.05.

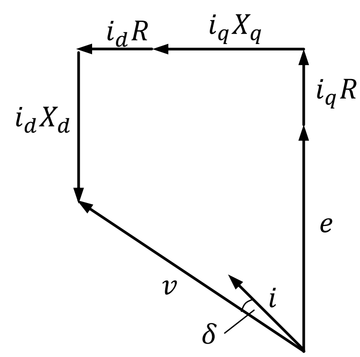

Figure 1.12 Phasor diagram of a PMSM decomposed into d-q components

1.2.3 Thermal Aspects

No electrical machine is 100% efficient. Device inefficiencies manifest themselves as heat sources throughout the machine, and the heat that is generated must be dissipated by its cooling system. During operation the heat sources cause temperature rises inside the machine limiting its maximum power output. Temperature limits are usually set by the insulation system employed in the stator and the maximum allowable operating temperature of the magnets. Losses within a PMSM include:

- Resistive losses in the windings due to armature current and eddy currents
- Eddy current losses in the stator core, rotor core and magnets caused by changing magnetic fields
- Hysteresis losses in the stator, rotor and magnets caused by changing magnetic fields
- Mechanical losses in the bearings caused by friction
- Windage losses in the air gap / internal cavity caused by fluid friction

The changing magnetic fields which induce eddy current and hysteresis losses can have a number of sources, in this thesis they are referred to as Reluctance, Winding MMF Harmonic, Magnet Harmonic, and Current Harmonic induced losses:

- Reluctance: As the magnets are rotated over a stator slot opening it effectively sees an air gap of varying length, changing the working point of the magnet and the magnetic field within it
- Winding MMF Harmonic: Losses induced due to the stator flux density field rotating with respect to the magnets or stator core
- Magnet Harmonic: Losses induced due to the rotor flux density field rotating with respect to the stator core
- Current Harmonic: Losses induced due to changing magnetic fields induced by the harmonic distortion of the current waveform

Figure 1.13 shows the distribution of losses throughout the machine, as well as some potential paths the heat may take before being dissipated by the coolant jacket (heat sink) of the machine.

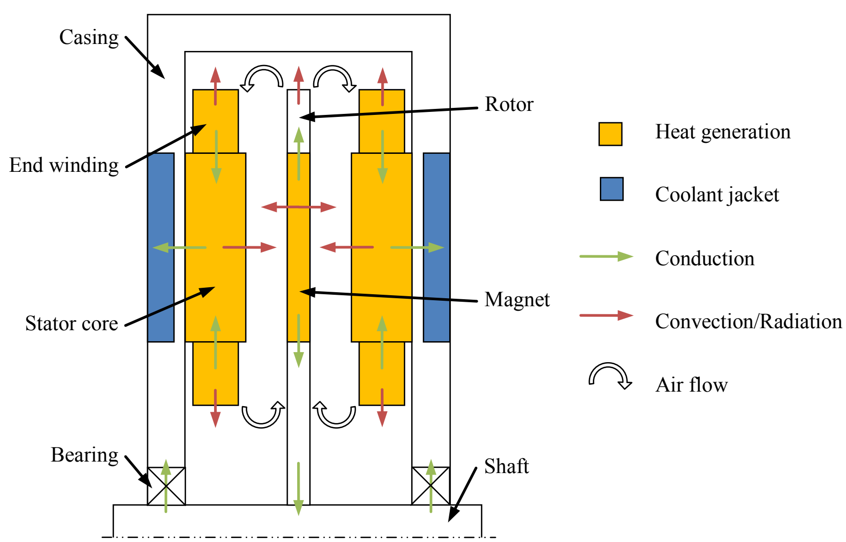

Figure 1.13 Distribution of losses and potential heat paths through the AF PMSM

Good design can limit the losses generated in a machine. Some techniques are straight forward: magnets and cores can be laminated to restrict eddy current flow, though lamination increases the complexity and therefore cost of manufacture. Other techniques are less straight forward and impinge on other aspects of the machine design: concentrated windings reduce end winding overhang and therefore reduce the resistance of the winding, leading to lower resistive losses. Conversely eddy current and hysteresis losses may increase due to the increased harmonic content of the winding magnetomotive forces. However good the electromagnetic design is, the losses will always increase with output power and ultimately the maximum output power will be limited by component temperatures.

Efficiency

It is not just maximum output power that is affected by component temperature. Efficiency decreases with increasing winding temperature. Resistive losses in the winding are equal to i^2R where the winding resistance R increases with winding temperature. Copper is by far the most popular material for PMSM windings; the resistivity of copper increases by ~40% for a temperature rise of 100K above ambient.

As magnet temperature increases the torque produced by the machine decreases as the remanent flux density and intrinsic coercivity of the magnet material both decrease with increasing temperature. This results in lower stored magnetic energy W in the air gap. This means that more current is required to achieve the same output torque, leading to higher resistive losses in the winding. These effects on performance and efficiency can again be understood by considering the phasor diagram in Figure 1.14, where e and R are now functions of winding temperature T_w and magnet temperature T_m respectively. In the figure the value of i_q has been increased in the hot machine to account for the reduction in torque constant due to the elevated temperature of the magnets (e is seen to decrease in the 'hot' machine). The larger value of i_q, along with the increased value of R has led to a larger reactive component.

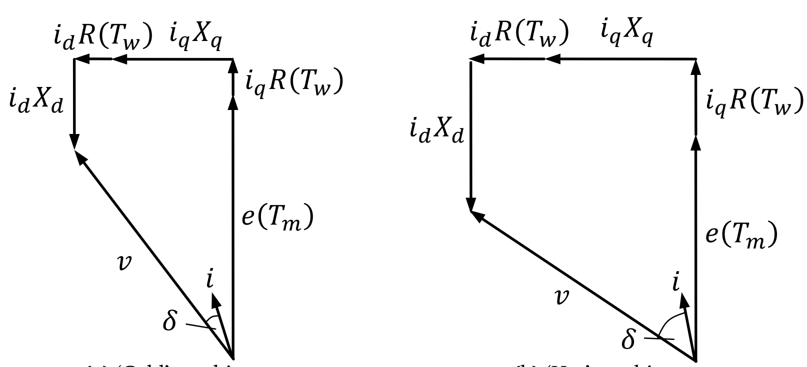

(a) 'Cold' machine (b) 'Hot' machine

Figure 1.14 Temperature dependant phasor diagram of a PMSM

Lifetime

The lifetime of PMSMs is highly dependent on their operating temperature. A common failure mode is insulation breakdown in the winding either between the winding and ground or between two phases. Figure 1.15 shows the reduction in lifetime of a machine against ‘excess temperature’ (temperature rise above maximum allowable). As a guideline, insulation lifetime halves for every 10K temperature rise above the maximum [27].

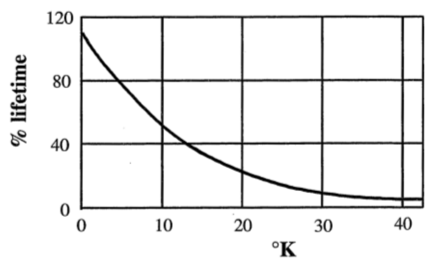

Figure 1.15 Winding insulation lifetime vs. excess temperature, from [27]

An additional failure mode may be demagnetisation of the permanent magnets. In an electrical machine the magnets are delivering flux against a demagnetising field induced by both the air gap and the phase currents. Care must be taken by the designer to ensure that the demagnetising field does not alter the magnetisation vector $\vec{M}$ in the magnets. Figure 1.16 shows the demagnetisation curve of a particular Nd-Fe-B grade at various operating temperatures. At low temperatures the demagnetisation curve of the permanent magnet is almost completely linear, and it can be operated on dynamically with no loss of magnetisation. However, between 100°C and 140°C the knee point of the demagnetisation curve enters the second quadrant of the $\vec{B}\vec{H}$ curve. This is undesirable as operation of the magnets at this temperature carries the risk of irreversible demagnetisation.

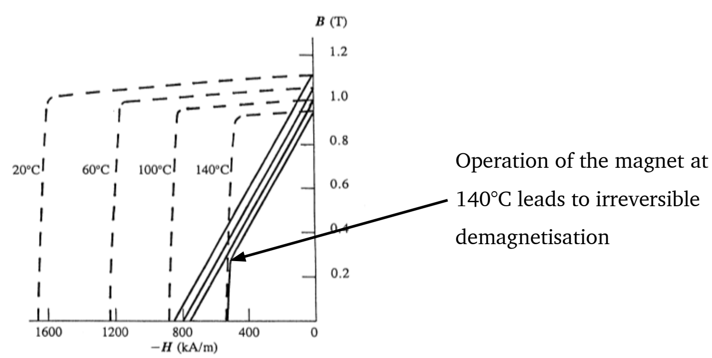

Figure 1.16 Demagnetisation curve for Nd-Fe-B at various temperatures, from [26]

Alternative materials

At room temperature Nd-Fe-B magnets have the highest energy product available, though at higher temperatures certain grades of Sm-Co outperform it, see Figure 1.17 where above 150°C the Sm-Co grade has a higher energy product. The data used to create Figure 1.17 was taken from manufacturer's data, available at [28]. To successfully use high energy product Nd-Fe-B it is clear that thermal management of the magnets is required. If the magnets cannot be kept cool alternative materials are more appropriate.

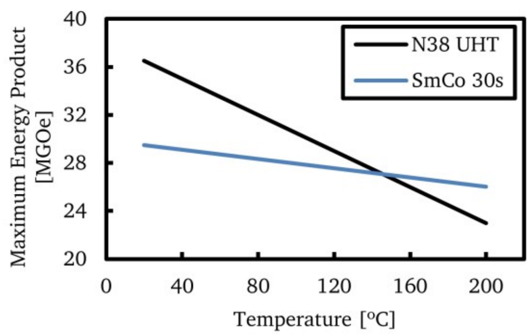

Figure 1.17 Maximum energy product vs. temperature of a Nd-Fe-B and a Sm-Co magnet grade

Cost

Table 1.3 presents the composition of the magnet grade used in the machine studied here. As can be seen, the largest cost is dysprosium, which is used to increase the maximum operating temperature of the material. Dysprosium is expensive and subject to price variation as shown in Figure 1.18.

Table 1.3 Composition and specific cost of a Nd-Fe-B magnet [27]

Material	Cost [$/kg]	Content [%]	Specific cost
Neodymium	102	22.8	0.24
Dysprosium	720	10	0.75
Iron	0.13	66	9e-4
Boron	4.6	1.2	6e-4

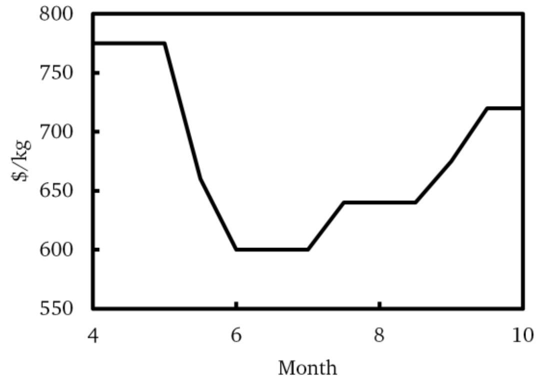

Figure 1.18 Price of Dysprosium, May-October 2013 [29]

1.3 Thesis Aim

It is clear from the previous sections and the literature review in Chapter 2 that the enclosed AF PMSM is a promising machine topology for applications requiring high torque density. It has been shown how permanent magnet temperature can affect the performance, efficiency, lifetime, and cost of an axial flux PMSM. It has also been shown that the thermal management of these machines has rarely been investigated, especially with regards to the magnets. It is proposed that by understanding the loss, temperature, and flow fields inside an AF PMSM insights can be made into how best to manage heat dissipation from the magnets of the machine. The objectives of the thesis are:

1. Describe and understand the thermal processes occurring within an enclosed AF PMSM by developing and analysing the results of a numerical model which predicts the loss, temperature, and flow fields within the device.
2. Describe and understand the thermal processes affecting permanent magnet temperature and discuss methods which may reduce it.
3. Develop an experimental procedure whose results improve the understanding of the numerical model's assumptions, and validate the numerical predictions.

1.4 Thesis Outline

Chapter 1: Introduction

This chapter made a case for the importance of the thermal design of PMSMs. The axial flux geometry was introduced with a discussion of suitable applications. The electromagnetic and thermal aspects of this machine were discussed, with permanent magnet temperature being identified as a key performance parameter.

Chapter 2: Literature Review

Here a review of previously published work by others relating to the thermal management of the permanent magnets in PMSMs is carried out. This includes work done to predict, measure, and reduce magnet losses as well as methods used for thermal analysis.

Chapter 3: Numerical Prediction of the Loss, Flow, and Temperature Fields within a Totally Enclosed Axial Flux Permanent Magnet Synchronous Machine

The numerical methods used to predict the loss, flow, and temperature fields in the AF PMSM are described in this chapter. Two coupled numerical components are presented, an electromagnetic finite element analysis is used to predict magnet and core loss fields while a conjugate heat transfer analysis uses the loss predictions as source terms to predict the flow and temperature fields. Arguments for all modelling decisions and mesh densities are given.

Chapter 4: Development of a Criterion for Assessing the Relative Importance of the Fluctuating Component of a Periodic Heat Source

This chapter presents the derivation and application of a criterion used to inform how best to couple the two numerical components of the model. It allows the user to assess whether fluctuations apparent in predicted loss fields are important when defining thermal analyses.

Chapter 5: Experimental Measurements in a Totally Enclosed Axial Flux Permanent Magnet Synchronous Machine

The experimental facility, prototype instrumentation, and experimental methods used to obtain boundary conditions and validation points for the numerical model are described in this chapter. A new method for measuring magnet losses is presented. An uncertainty analysis is carried out.

Chapter 6: Results and Discussion

The results of the numerical and experimental work are presented, discussed, and compared in this chapter. The main parameters affecting magnet temperature are identified and methods for reducing it are discussed.

Chapter 7: Conclusions and Further Work

A review of the work completed is presented. Areas suitable for future work are identified.

Chapter 2

Literature Review

The thermal management of permanent magnets traditionally consists of analytical and numerical predictions of magnet loss. Section 2.1 reviews the existing literature which deals with predicting the losses in permanent magnets and it is found that in terms of radial flux machines many studies have been carried out. Schemes for reducing losses are various and include segmenting the magnets, inclusion of eddy current shields, and rotor-stator design – be it slot/pole ratio or detailed design of the stator tooth tips. The same schemes are likely to be effective in axial flux machines, though existing work in the literature is less thorough. It is also noted that only one lengthy procedure for measuring magnet losses is published in the literature [30].

Section 2.2 reviews the existing literature which deals with the prediction of permanent magnet operating temperature through thermal analysis, it is found to be much less common than loss analysis with existing research mainly focussed on radial flux geometries. Axial flux machines have rarely been tackled and in cases where they have it is the through flow topology which has been selected for study.

The review carried out in this chapter highlights a number of gaps in the literature with regards to the thermal management of the permanent magnets within an enclosed axial flux PMSM. The subsequent chapters hope to fill these gaps by increasing the understanding of the thermal processes occurring in these machines. This is achieved via a coupled electromagnetic-conjugate heat transfer numerical analysis of the machine as well as the implementation of a novel experimental method used for measuring magnet losses in surface mounted PMSMs.

2.1 Prediction and Measurement of Permanent Magnet Losses

With regards to the thermal management of permanents magnets, loss prediction is inevitably focussed on assessing schemes for reducing losses. Methods are well documented in the literature; the area can be split up into three subdivisions:

- Reduction of losses via segmenting the permanent magnets
- Reduction of losses via eddy current shields
- Reduction of losses via rotor-stator design

In terms of measuring magnet losses, much less is published. The final part of this subsection is concerned with a review of the available literature in this area.

2.1.1 Segmentation

Division of a permanent magnet into electrically isolated segments reduces the eddy current loss generated within it by increasing its effective resistance. This effect was shown by Kawase et al. [31] who present the results of a computationally efficient scheme for representing magnet segmentation in a finite element code. They subsequently use it to show the relationship between the number of segments and permanent magnet losses in a radial flux interior permanent magnet machine. A similar trend between circumferential segmentation and permanent magnet losses in a surface mount radial flux machine was predicted by an analytical model presented by Atallah et al. [32]. Neither of these works presents any experimental validation of the results.

Sergeant et al. [33] used a 3D harmonic finite element analysis to investigate permanent magnet losses in a surface mount radial flux machine. They found that segmentation in both the circumferential and axial directions decreased losses greatly, but increased losses in the un-laminated rotor yoke (as before segmentation the magnets were acting as an eddy current shield). They therefore only recommend permanent magnet segmentation when the rotor yoke is laminated. The authors present an experimental estimate of magnet losses in order to validate the analyses. The estimate is based on subtracting i^2R losses as well as approximations of core loss derived from classical expressions from the total inefficiency of their machine.

Permanent magnet losses were predicted in an interior permanent magnet machine by Yamazaki et al. [34] using a time stepping 3D finite element analysis. Their predictions were validated against measurements of 'total iron loss', which they define as the sum of the magnet and iron losses. This was measured by subtracting i^2R and mechanical losses from the total inefficiency of their machine. Their numerical model incorporated all the contributors to eddy current losses including winding MMF, slot and current harmonics (generated by inverter commutation). They noted that while lower frequency components of the eddy current loss were always suppressed by segmentation, losses induced by current harmonics increased initially before reducing. The reason given by the authors was that the higher frequency eddy currents were limited by their skin depth, so segmentation actually reduced the effective resistivity of the permanent magnet at first until the segmentation width reduced to less than twice the skin depth (see Figure 2.1). This effect has also been noted by Wan-Ying et al. [35].

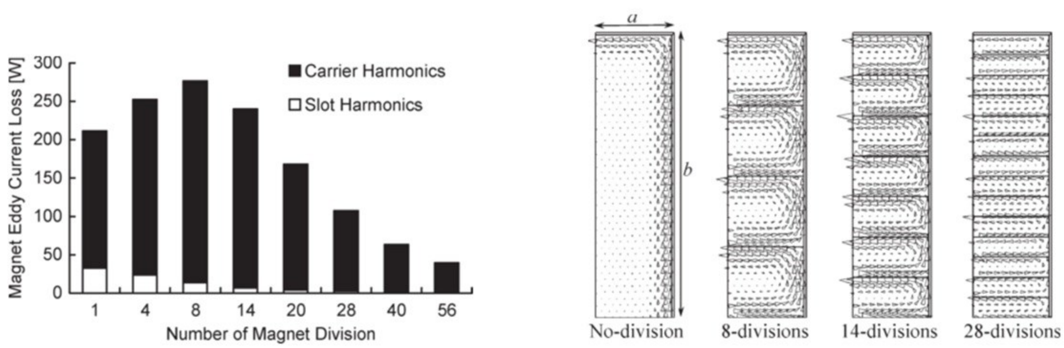

(a) Eddy current loss vs. segmentation (b) Eddy current visualisation

Figure 2.1 Eddy current loss and skin effect in a permanent magnet, from [34]

In a subsequent work by Yamazaki et al [36] the phenomenon of increasing losses with permanent magnet segmentation was investigated in different rotor configurations: Interior, inset and surface mount radial flux permanent magnet. Permanent magnet losses were again predicted using a 3D time-stepping finite element analysis which correctly accounted for winding MMF, slot and current harmonics, experimental measurements were also taken in the same way as before. Figure 2.2 shows the results of their analysis where for all machines losses induced by slot harmonics were always reduced by segmentation. However losses induced by the current harmonics initially increased for the interior and inset permanent magnet machines (as before in [34]) but were always reduced by segmentation in the surface mount permanent magnet machine. The reason given by the authors was that the eddy currents in the surface mount machine were resistance, rather than skin depth, limited. The skin effect was much more pronounced in the interior and inset configurations: The reaction field of the magnets had a lower reluctance path to follow when compared with the surface mount machine, whose magnets faced a relatively large air gap. The phenomenon is illustrated by the authors in Figure 2.2.

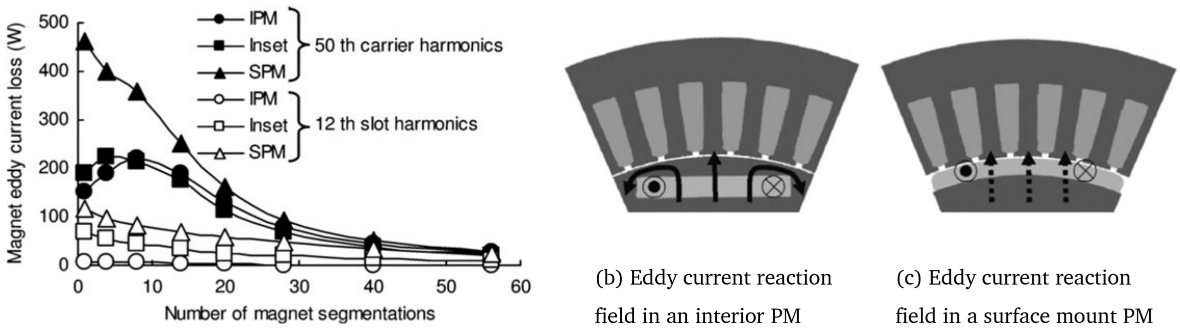

(a) Eddy current loss vs. segmentation

(b) Eddy current reaction field in an interior PM machine

(c) Eddy current reaction field in a surface mount PM machine

Figure 2.2 Effect of permanent magnet segmentation on magnet losses in various rotor configurations, from [36]

An interesting effect was noted by Madina et al. [37] when investigating segmenting permanent magnets in a radial flux surface mount machine. They developed an analytical method for calculating eddy currents (good agreement was found with their 2D finite element results) which was fast enough to investigate many different segmentation schemes, though it was not validated experimentally. They found that uneven segmentation, with the segments nearest the edge of the magnet being the thinnest, gave a 6% reduction in eddy current losses when compared with equally spaced segments. No explanation was given by the authors.

Literature specific to axial flux permanent magnet machines is less common, though examples have been found. Woolmer et al. [38] described the design and general performance of a yokeless and segmented armature axial flux machine and briefly mentioned that losses had been reduced in the permanent magnets by segmenting them into four pieces. A machine with a similar topology was studied by Vansompel et al. [39]. They used a series of 2D harmonic finite element analyses to represent the 3D nature of the machine, similar to Fu et al. [40], and found that in terms of torque, cogging torque and phase voltage the results matched their 3D finite element analysis well. They ultimately used their model to investigate magnet segmentation and found that this reduced eddy current losses greatly.

Permanent magnet losses in a 37kW axial flux permanent magnet machine with concentrated windings and open slots were investigated by Jussila et al. [41]. They compared the effect of segmented sintered magnets and plastic bonded magnets on general performance. They showed by a time stepping 2D finite element analysis that eddy current losses in the sintered magnets could be reduced by segmenting them, though no experimental validation was presented. Similar findings have been reported by Nguyen et al. [42] who used a 3D harmonic finite element analysis to investigate permanent magnet loss reduction by segmentation in an axial flux machine. They found that time harmonics in the current waveform induced by inverter current harmonics were the main contributor to losses and that segmentation in the radial and circumferential direction could dramatically reduce these. The authors validated their analysis via lumped measurements of iron loss and magnet loss, determined by subtracting measured winding and mechanical loss from measurements of machine inefficiency.

In general, the effect of permanent magnet segmentation in radial machines is well understood, although work on uneven segmentation may be an interesting avenue for further research. Although only a small proportion of the literature focuses on axial machines the underlying physical mechanisms are the same and it is has been shown that similar results are obtained when segmenting axial flux permanent magnets.

2.1.2 Eddy Current Shields

In radial flux surface mount permanent magnet machines a retaining sleeve is often used to hold the permanent magnets in place, see Figure 2.3.

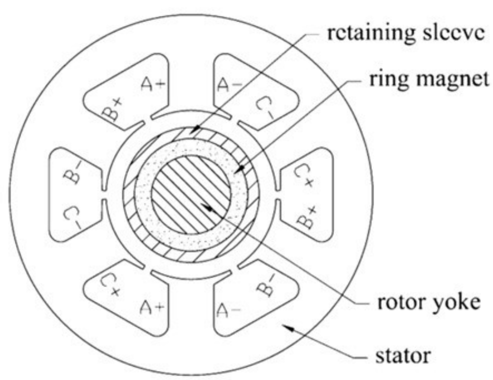

Figure 2.3 Radial flux machine rotor construction with retaining sleeve, from [43]

A number of authors have investigated different combinations of materials for use as the retaining sleeve. If an electrically conductive material is used then eddy currents are generated in the sleeve which damp the harmonic content of the stator flux waveform, reducing permanent magnet losses. This effect was reported by Al-Naemi et al. [44] who presented the calculation, via finite element analysis of permanent magnet and retaining sleeve losses in a radial flux surface mount permanent magnet machine when different sleeve materials were used. It was shown that including a conductive retaining sleeve reduced permanent magnet losses, though the combined losses for permanent magnet and sleeve were not presented so it is hard to conclude which material is best. No experimental validation of the predictions was presented.

A 2D finite element analysis was presented by Cho et al. [45] which compared rotor losses in two radial flux permanent magnet machines of identical rating (50kW, 70krpm) but with different rotor constructions. The two machines had carbon fiber and Inconel718 retaining sleeves respectively. The authors found that although the Inconel718 sleeve greatly reduced the losses in the permanent magnet, the losses in the sleeve itself were large. In terms of total rotor losses the carbon fiber configuration had 5.9 times lower losses than the Inconel718 one.

Rotor losses in a 3kW, 150krpm radial flux permanent magnet brushless DC machine were predicted using a 2D time stepping finite element analysis by Zhou et al. [43]. The predictions were not validated experimentally. Initially the effect of using carbon fiber or titanium for the retaining sleeve on rotor losses was compared. The authors found that due to the low electrical conductivity of the carbon fiber sleeve it had relatively low eddy current generation within it. As a result losses in the sleeve were low, but the winding MMF harmonics permeated through to the magnets and consequently eddy current losses there were high. Conversely, due to the relatively high electrical conductivity of the titanium sleeve high eddy current losses were incurred there. Due to the reaction field of the sleeve however the winding MMF harmonics did not permeate through to the magnets and consequently losses here were low. Overall the total rotor losses were similar between the two rotor constructions.

In the same work the authors investigated the effect of adding a thin copper sheet between the magnets and the retaining sleeve. They found that because the resistance of the copper was so low the eddy current reaction field was large and removed a great amount of the winding MMF harmonic content. The net effect was a reduction in overall rotor losses when compared with the carbon fiber or titanium sleeves alone. A similar result was reported by Kolondzovski et al. [46] when comparing carbon fiber retaining sleeves with aluminium eddy current shields to titanium retaining sleeves. The authors noted that even though the rotor losses were now reduced, the loss density in the copper sheet was high. As the copper sheet was located directly over the permanent magnets a thermal finite element analysis was carried out in order to check that the permanent magnets were not at risk of overheating and demagnetising. The thermal analysis was fairly rudimentary, though probably accurate enough to gauge the difference between each rotor construction. The authors note that the reduction in temperature due to the addition of the copper shield is so great that the higher energy product NdFeB magnets could replace the more temperature stable SmCo magnets used for this application.

No reference to eddy current shields being used in axial flux permanent magnet machines has been found. This could be an interesting avenue for further research, though it has not been pursued here.

2.1.3 Rotor-Stator Design

A number of authors have investigated the effect of different combinations of slots and poles on permanent magnet losses. Depending on the distribution of the winding coils and the number of slots in the machine the stator flux density waveform contains different levels of harmonic content, leading to different levels of permanent magnet losses.

An analytical analysis of permanent magnet losses in conventional and modular permanent magnet machines was presented by Toda et al. [7]. The analytical model took stator winding MMFs and magnet segementation into account to quantify the difference in losses between the two machines. Figure 2.4 shows the machines studied; both have concentrated windings but laid out in quite different arrangements. In the conventional machine the fundamental winding MMF has the same frequency as the rotor flux distribution, consequently torque is produced through interaction at the fundamental frequency. In the modular machine the fundamental winding MMF has fewer poles than the rotor, meaning torque is produced through the interaction of higher order winding MMFs with the rotor. In the case of the conventional machine permanent magnet losses are only incured at higher order winding MMFs, whereas in the modular machine both lower and higher winding MMFs cause losses.

The authors found that the permanent magnet losses in the modular machine were around double those in the conventional machine. They compared their analytical results with the results of a 2D time stepping finite element analysis and found good agreement with the predicted losses of the modular machine. Analytical predictions of rotor loss in the conventional machine did not have a good agreement with the finite element analysis results. The reason given by the authors was that their model did not take into account losses caused by stator slotting, and that this form of loss is relatively large in the conventional machine studied when compared with the modular machine.

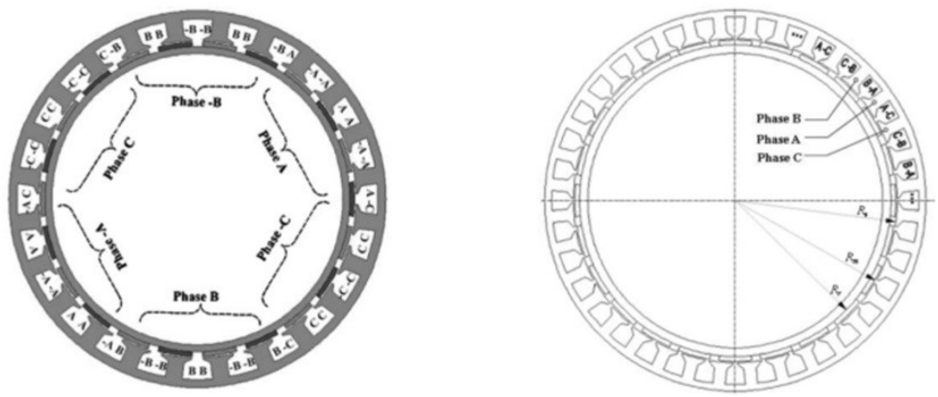

(a) Modular machine (b) Conventional machine

Figure 2.4 Modular and conventional permanent magnet machines, from [7]

A similar analysis was presented by Ishak et al. [47] where the permanent magnet losses in a number of different concentrated winding schemes were compared under brushless DC and brushless AC operation. The machines were all 10 pole/12 slot machines where the winding layout varied as shown in Figure 2.5.

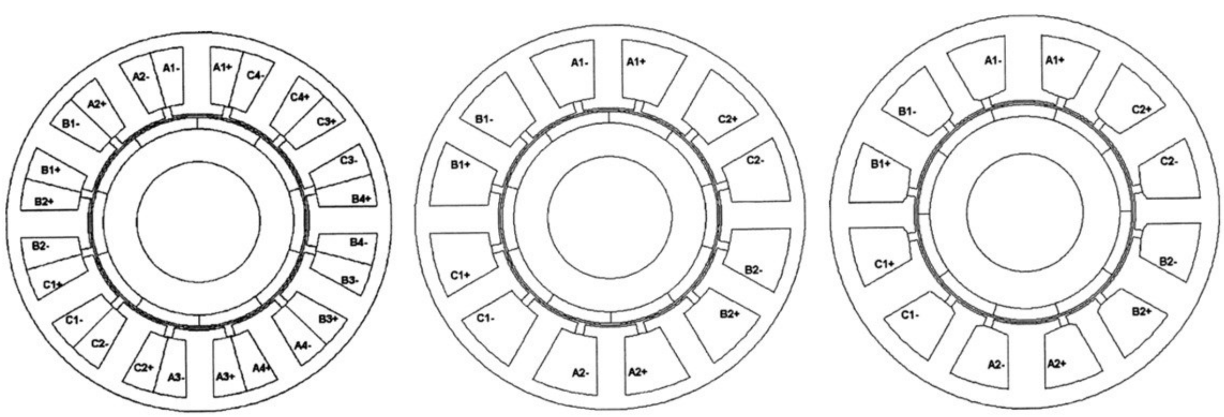

(a) Double layer winding (b) Single layer winding (c) Single layer winding with irregular teeth

Figure 2.5 Various concentrated winding configurations, from [47]

Their analytical model agreed well with their 2D time stepping finite element results as can be seen in Figure 2.6, though both models neglect end effects (they are both 2D), and neither was validated experimentally. They found that brushless DC operation caused higher permanent magnet losses than brushless AC, and that when every tooth was wound the losses were lowest.

Nakano et al. [48] used a 2D finite element analysis to predict the permanent magnet losses in five concentrated winding machines rated at 1.5kW, 3000rpm. The slot/pole combination was varied for each machine and permanent magnet losses were predicted under no load and rated load conditions. They found that the no load loss of all the machines was very small, but loss under load due to winding MMF harmonics varied greatly between machines with the 6 slot/8 pole machine generating 260W and 12 slot/8 pole machine generating 2.2W. The authors showed that this was due to different harmonic contents of the different slot/pole combinations; Figure 2.7 shows their results where a large low frequency component of the MMF in the 6 slot/8 pole machine can be seen rotating in the opposite direction to the synchronous component. They cite this as the largest contributor to eddy current generation in this particular machine. No experimental work was presented to validate the analyses.

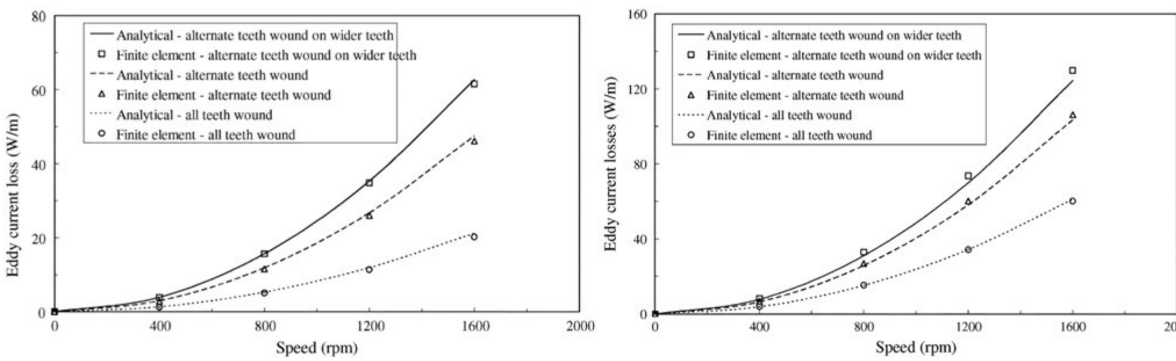

(a) Brushless AC operation (b) Brushless DC operation

Figure 2.6 Magnet losses in various concentrated winding configurations, from [47]

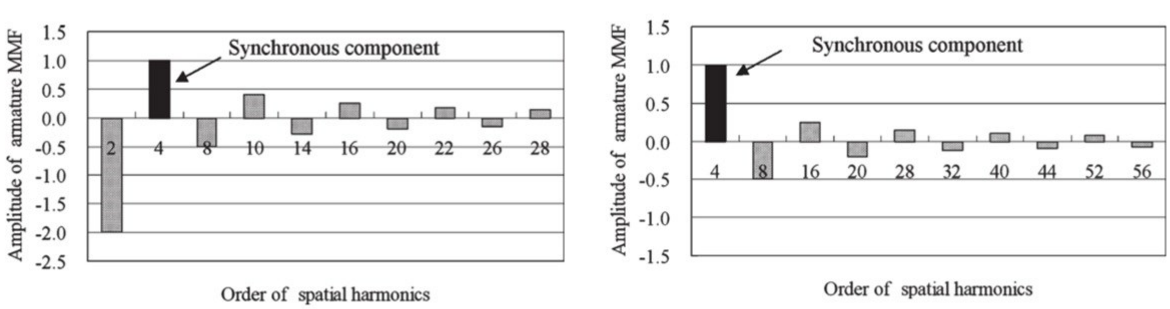

(a) 6 slot/8 pole (b) 12 slot/8 pole

Figure 2.7 MMF harmonics in 6 slot/8 pole and 12 slot/8 pole machines, from [48]

An analytical model which predicts permanent magnet losses in radial flux surface mount permanent magnet machines, based on winding MMF harmonics only, was used by Bianchi et al. [49] to compare machines of different slot/pole combinations. Although no experimental validation was presented, the authors claim good correlation of results between their model and more complex ones. The speed at which their model could be solved allowed them to build up an index of permanent magnet losses encompassing many slot/pole combinations. Their index clearly showed that the lowest losses occur when the ratio between slots and poles is 3, away from this ratio losses always increased although there were local minima at ratios of 2.5 and 1.5 for double layered windings and 1.5 and 1 for single layered windings. A similar study was carried out on concentrated winding fractional slot axial flux machines by Li et al. [50] where a 2D harmonic finite element analysis was used to compare permanent magnet losses caused by winding MMFs. They found that the largest losses occurred when a high pole number was combined with a low number of slots.

A time stepping 3D finite element analysis including the effect of current harmonics was used by Yamazaki et al. [36] to compare permanent magnet losses between two radial flux interior permanent magnet machines, one with a concentrated winding and one with a distributed winding. They validated their results by comparing predicted magnet and core loss with a lumped value obtained by experiment. The experimental value was determined by subtracting values of winding and mechanical loss from the total inefficiency of the machine. As shown in Figure 2.8 the permanent magnet losses in the concentrated winding configuration were much higher than in the distributed arrangement. The authors categorised losses with respect to their origins and found that both machines incurred the same loss from the current harmonics but vastly different amounts from winding MMF harmonics, which was the dominant cause of permanent magnet losses in the concentrated winding machine.

In the same work the authors compared permanent magnet losses in three different rotor constructions (interior, inset and surface mount permanent magnet), all paired with the concentrated winding previously studied. They found that losses due to the carrier frequency were highest in the surface mount machine, most likely due the lower inductance of this machine (because of the large air gap) and location of the magnets (they are not shielded by the rotor iron). Losses due to winding MMF harmonics dominated in all machines, the largest permanent magnet loss was found in the inset rotor and lowest in the interior rotor, though no reasons were stated for this.

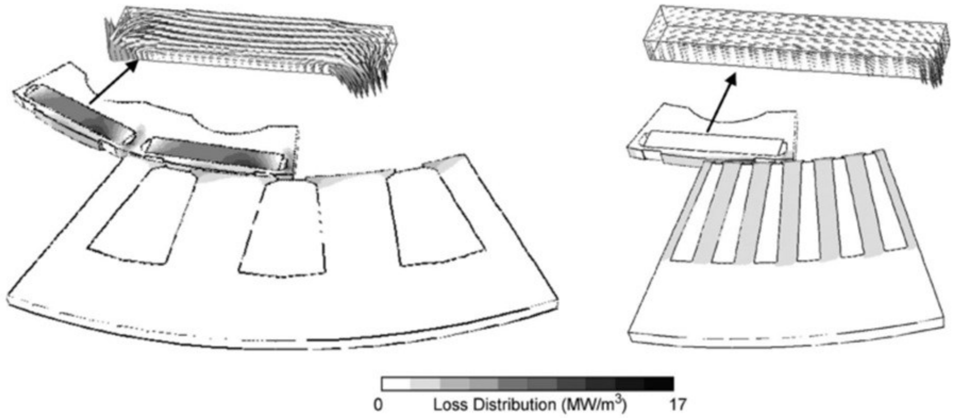

(a) Concentrated winding (b) Distributed winding

Figure 2.8 Magnet losses in concentrated and distributed winding machines, from [36]

In a pair of complimentary works by Yamazaki et al. [51], [52] stator tooth and rotor shape were optimised in radial flux interior and surface mount permanent magnet machines with concentrated windings in order to reduce permanent magnet losses. They used a time stepping 3D finite element analysis which included the effect of current harmonics to identify the main cause of permanent magnet loss in each machine. It was found that the biggest contributor in the interior machine was the changing path of the armature flux with rotation, while in the surface mount machine the effects of slotting were the greatest. The design of the stator teeth and rotor bridge were then optimised via a set of time stepped 2D finite element analyses. Figure 2.9 shows the optimised stator tooth shapes for each machine which both exhibited a reduction in permanent magnet losses of up to 50%, though incurred a reduction in torque of around 14%. The authors confirmed the predicted changes in performance through lumped measurements of magnet and core loss, obtained by subtracting winding and mechanical loss from total machine inefficiency.

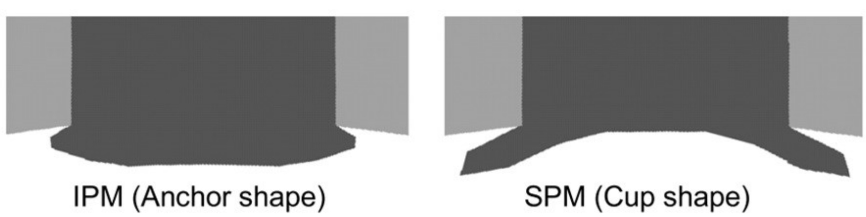

Figure 2.9 Optimised tooth designs which reduce magnet losses by 50%, from [51]

2.1.4 Measurement of Permanent Magnet Losses

Eddy current losses were estimated in a permanent magnet by [53] using a temperature rise rate technique. The results successfully validated their FEA results, though the technique could only be performed on a stationary magnet, removed from its motor. The authors used a number of temperature sensors to measure temperature rise and noted differences in each measurement due to the eddy current distribution. The average temperature rise rate was used to determine the final value of eddy current losses; this assumed that each point measurement represented an equal volume of magnet material.

Alberti et al. [30] present a method for measuring magnet losses in an axial flux PMSMs. They calculated losses from Equation (2.1), which defines the rotor losses as the difference between the total losses and all other losses.

$$q_{rl} = q_{tot} - q_{cu} - q_{fe} - q_{mech} \tag{2.1}$$

Where q_{rl} are the rotor losses, q_{tot} are the total machine losses, q_{cu} are the winding losses, q_{fe} are the core losses, and q_{mech} are the mechanical and windage losses.

The major conceptual uncertainty in this method is the measurement of the core losses, which were calculated from area averaged values of flux density measured by search coils around the teeth and yoke. These flux density values only give the correct value of losses when the flux density distribution across the area is uniform, this is especially unlikely in the yoke of an axial flux machine as (assuming the radial component of flux density is small, due to the lamination orientation of the stator) the face area of the magnets and coils reduce with radius, while the tangential area of the yoke remains constant. An additional problem is determining the core losses in parts of the stator not representative of the teeth or yoke, see Figure 2.10.

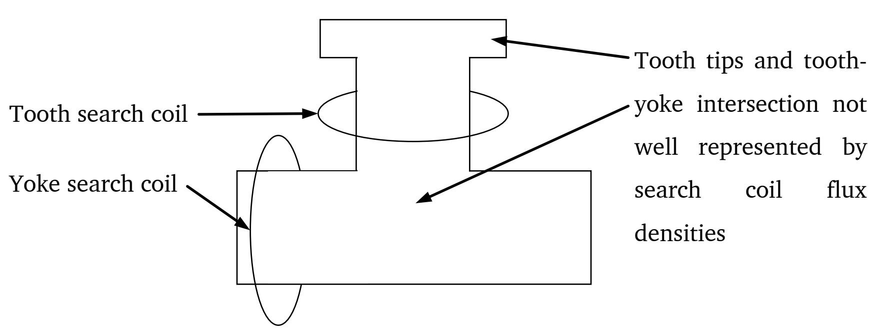

Figure 2.10 Conceptual uncertainty in determining core losses

In summary, the main causes of permanent magnet loss are well described and understood in the literature. Schemes for reducing this loss include segmentation of the permanent magnets and eddy current shields, while selection of an appropriate slot/pole combination and rotor and stator design can also reduce losses. Application of these schemes to axial flux machines has only been found in the case of slot/pole combinations. Predictions of magnet loss are largely unvalidated by experimental measurements. The most common technique is to lump predicted magnet and core losses together and compare them to experimental measurements of winding and mechanical loss subtracted from the total inefficiency of a machine. One example of measurements being taken within a PMSM was found, though this method has some unquantified conceptual uncertainty and, due to the number of experiments required to perform it, is quite lengthy.

2.2 Thermal Analysis of Electrical Machines

To complete the overall understanding of the thermal management of the permanent magnets in a PMSM thermal analysis is also required. Many examples of thermal models of electrical machines exist in the literature; the area can be split up into two subdivisions:

- Lumped Parameter Models
- Numerical Analysis

2.2.1 Lumped Parameter Models

In a lumped parameter model the electrical machine is divided into a number of components which can be assumed to have the same temperature. Each component is given a bulk thermal storage and heat generation rate and is connected to neighbouring components via thermal resistances. Thermal contact resistances and convective boundaries are usually dealt with empirically, with values taken from the literature. The resultant model, derived from dimensional data and material properties, can be solved easily and quickly using a computer. Indeed, Mellor et al. [54] presented the results of a lumped parameter model which was used to predict the temperature of various components in three induction machines (one 75kW and two 5.5kW) during varying load cycles. Their model was detailed enough to be useful at the design stage and could be solved in real time, also making it viable for on-line condition monitoring. The authors found good agreement between their model and measured values, despite uncertainties in contact resistances and coefficients of convective heat transfer. A sensitivity analysis showed that component temperatures were insensitive to the variation in any one of these values.

Lumped parameter models have also been applied to permanent magnet machines. Nerg et al. [55] applied their model to two high power density radial flux permanent magnet machines rated at 45kW and 1.56MW and found good agreement with experimental measurements of steady state temperatures. A 2D time stepping finite element analysis was used to calculate the core and magnet losses which were present in the thermal model, while the copper losses were calculated iteratively within the thermal model from the phase current and temperature dependent winding resistance. As in [54] a sensitivity analysis was presented; it showed that the solutions were most sensitive to the conductivity of the winding, thermal resistance of the slot insulation, and the core to frame contact resistance. Other more uncertain parameters like coefficients of convective heat transfer, which were calculated from correlations, had less of an effect on the solution.

A lumped parameter model was presented by Scowby et al. [56] of an axial flux machine rated at 300kW and 2300rpm. The machine had a radially finned hub to pump air through the air gap of the machine. The thermal resistance network was linked to a one-dimensional fluid flow model whose loss coefficients were either determined from the literature or experimentally from a scaled model of the machine. The resulting thermal model was used to investigate the effect of different gap ratios, material emissivity, air inlet temperatures, and the use of a heat pipe to cool the stator, on machine component temperatures. No comparison was made to experimentally measured temperatures in the machine.

Belicov et al. [57] predicted component temperatures in an axial flux machine using a lumped parameter model linked to an electrical model, which calculated copper losses based on current waveforms. A visualisation of their model is shown in Figure 2.11. Although the only loss mechanism taken into account in the model seems to have been copper loss, the model agrees well with the limited experimental data set presented.

Wang et al. [58] presented a lumped parameter model of an axial flux permanent magnet machine rated at 250kW and 1400rpm. The rotor had protruding permanent magnets which were used as a crude fan to drive air through the machine. They used a fluid flow model based on pipe flow correlations (see Figure 2.12) along with empirical correlations to determine coefficients of convective heat transfer linked to a network of thermal resistances. Measured temperatures were in reasonable agreement with predicted temperatures.

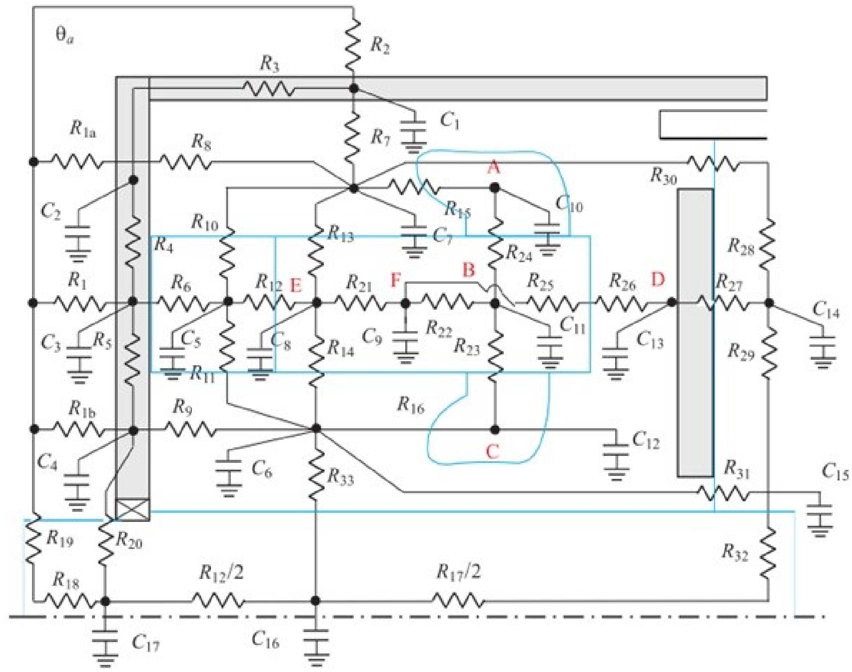

Figure 2.11 Lumped parameter thermal model of an axial flux PMSM, from [57]

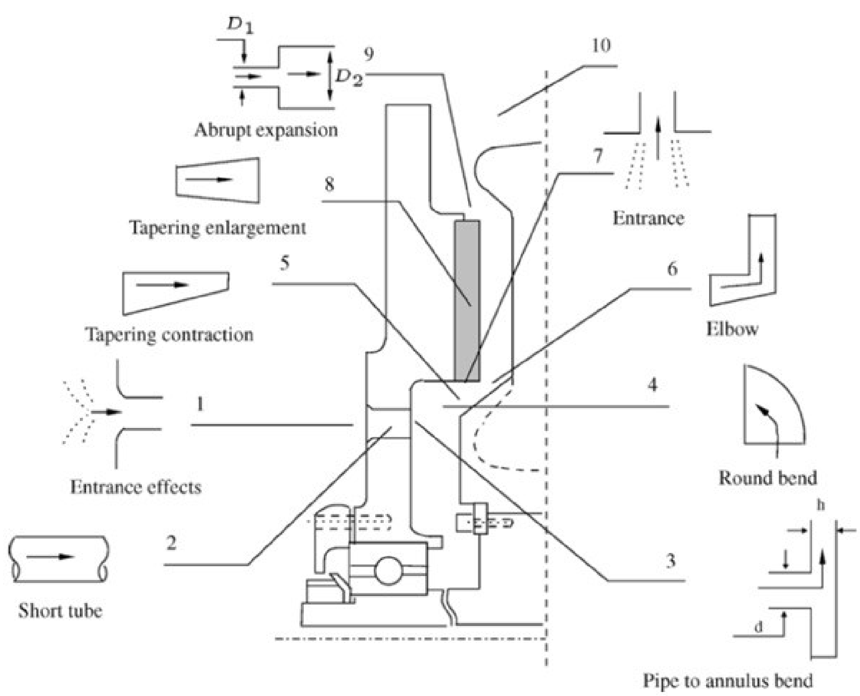

Figure 2.12 Pipe network representation of the fluid domain in an axial flux PMSM, from [58]

A lumped parameter model of an axial flux permanent magnet machine was presented by Lim et al. [59]. The work is similar to those presented previously, but gives an interesting study regarding the number of control volumes it was necessary to split the fluid domain up into to obtain an accurate solution. A comparison is made between the air temperature predicted by the lumped parameter model and by a computational fluid dynamics analysis, and good agreement is found.

The design and development of a totally enclosed axial flux permanent magnet machine rated at 30kW at 16krpm is described by Sahin et al. [60]. They present the results of a lumped parameter model of the machine, which shows only reasonable agreement with a limited experimental data set. Reasons for the discrepancy are not given, though convection correlations for use on cylindrical surfaces were applied to the plane surface of the disc.

In summary, many lumped parameter models have been presented in the literature which predict the average temperatures of the main components of electrical machines accurately – both in steady state and transient scenarios. They are fast to compute and as a result a popular choice for parametric design studies, and on-line condition monitoring. Empirical correlations are relied upon for modelling coefficients of convective heat transfer (see Howey et al. [61] for a comprehensive summary of this area), so they are limited in cases where these do not exist. Within the field of axial flux machines lumped parameter models have mainly been applied to through flow machines. Perhaps this is because the fluid domain is more easily represented as a network of pipes, and assumptions about flow structure are easier to make than in totally enclosed machines (the flow structures of which are discussed in Section 3.2.5.2). In terms of the application dealt with in the current work lumped parameter models could offer insights into reducing permanent magnet operating temperature through thermally optimising the solid domain, but they offer little insight into optimising the fluid domain as they cannot resolve the complex flow structures present in a totally enclosed machine.

2.2.2 Numerical Analysis

Finite element analyses (FEA), computational fluid dynamics (CFD) analyses and conjugate heat transfer (CHT) analyses have all been applied to the thermal modelling of electrical machines. Often analysis is performed on one component, or on part of the machine in isolation. This was the case for Borges et al. [62] who showed how CFD could be used to asses different design proposals for the coolant jacket of a radial flux induction machine. Heat transfer was not considered and they selected appropriate designs based on flow velocities and inlet to outlet pressure drops.

CFD has been used to investigate convection in the end winding region of radial flux electrical machines. Micallef et al. [63] used CFD to predict heat transfer between the end windings and casing of a strip wound totally enclosed fan cooled radial flux induction machine. They analysed a periodic section of the end region only, this allowed them to model each end turn of the winding explicitly. Their model contained 800,000 elements and used a $K\ \epsilon$ turbulence model with wall functions to model near wall fluid velocities. Results were used to inform design decisions and ultimately an improved design of the end region was proposed which showed a decrease in thermal resistance from the end windings to the case of 33%, while windage losses in the region were only increased by 19%. The improved design was prototyped and a reasonable agreement with predictions was shown. Only the thermal resistance between the end windings and the casing was presented in the work, and as this was not compared to thermal resistances between the end windings and other parts of the machine it is hard to quantify the improvement in terms of overall performance. Similar work has been presented by Hetteger et al [64] and Lampard et al. [65].

Convective heat transfer in the air gaps of electrical machines has also been investigated using CFD. Kuosa et al. [66] used a CFD analysis to model heat and fluid flow in a high speed radial flux electrical machine with a through flow of air being pumped through the air gap. The authors compared the use of three different turbulence models ($K\ \epsilon$, SST and $B\ L$) on local and average coefficients of convective heat transfer. They found that although there were local differences the average values were very similar. The agreement with their simulation results and experimental results was reasonable and the authors cite the use of turbulence models which assume isotropic turbulence in a rotating system as a cause of discrepancy. In a complimentary study by Kuosa et al. [67] CFD was used to investigate the effect of slotted geometries in both the rotor and the stator of a radial flux electrical machine on heat transfer from either component to a through flow of air in the air gap. Figure 2.13 shows the mesh in the air gap and geometry of the slotted features. The authors found that when compared with a smooth rotor-stator system slotting increased the coefficient of convective heat transfer to the air gap by 59% in the case of the stator, and 36% in the case of the rotor. Experimental measurements were presented though these were for a different through flow rate of cooling air so comparison with the numerical prediction was not possible.

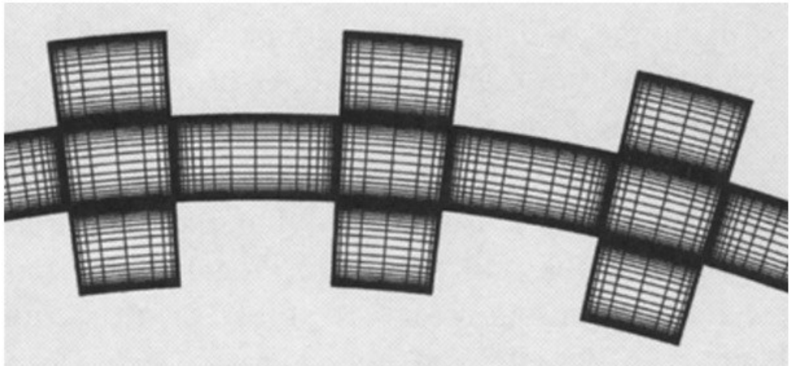

Figure 2.13 Air gap mesh in a slotted rotor-stator radial flux machine, from [67]

Li [68] presented a detailed study on the cooling of a radial flux permanent magnet machine using a conjugate heat transfer analysis. The machine used a centrifugal impellor to pump air through the air gap and the work focussed on the performance of this impellor in relation to machine component temperatures. A mesh independent solution was shown to be achieved with 3,200,000 elements: Good agreement was found between measured and predicted mass flow rate. The author suggests design improvements to the impellor and notes that increasing the mass flow rate through the machine further does not increase the coefficient of heat transfer between machine components and air as this is dominated by the rotation of the flow in this application.

A conjugate heat transfer analysis of a 27.5kW radial flux alternator, with a through flow of air pumped through the air gap, was presented by Maynes et al. [69]. A simplified version of the machine was built and tested both experimentally and numerically. Thermal contact resistances were used to tune the CHT model at one operating point, before being replicated for all the others. Agreement between measured and predicted temperatures was good. Turbulence was modelled by a 2-layer $K\ \epsilon$ model. The analysis was a useful tool for investigating heat transfer paths, for example it predicted that 30-40% of the heat generated in the stator diffused into the supporting members before being convected away by the cooling fluid, effectively increasing the area available for heat transfer.

Pickering et al. [70] used CFD to predict coefficients of convective heat transfer on the rotor of an air cooled radial flux synchronous machine with salient poles. Their model comprised of 1,300,000 elements and used the $K\ \epsilon$ turbulence model, with wall functions required to model flow velocity near to the wall. An experimental mock-up of the machine was built and equipped with heat flux sensors and heaters to simulate machine losses. The coefficient of convective heat transfer was always under-predicted by the numerical model when compared with experiment, sometimes by up to 30%. The reason given by the authors was that a reference frame model, rather than a sliding mesh model, was used.

A CHT study of a similar machine is presented by Shanel et al. [71]. In the fluid domain the $K\ \epsilon$ turbulence model is used, and the rotor and stator are connected by a reference frame model. The authors also model the solid domain of the rotor and state that the advantage of this is that the sensitivity of the solution to the predicted coefficient of convective heat transfer can be judged quantitively. A quarter of the whole machine is modelled using 2,000,000 elements. Copper losses were modelled in the rotor and the authors demonstrated that the copper coils could be represented as a homogeneous material with anisotropic conductivity by comparing 2D simulations with a model where strands were explicitly modelled. The model was used to investigate schemes for keeping the rotor cool; in the best case a reduction of 6°C was predicted. By investigating proposed designs numerically excessive prototyping was avoided. For example, one proposed cooling scheme actually increased the rotor coil temperature by 9.5°C.

Coefficients of convective heat transfer in a radial flux totally enclosed fan cooled induction machine were predicted by Trigeol et al. [72] via a CFD analysis. These were then used in a lumped parameter model to predict component temperatures. Experimental measurements of stator temperature were presented and the agreement was good. A comparison of predicted and measured rotor temperatures was not presented.

A radial flux synchronous generator with a built in fan used to pump air through the internals of the machine was modelled using CFD by Connor et al. [73]. The authors modelled the entire geometry as there was a lack of symmetry in the design, and this resulted in a model with 8,000,000 elements where a $K\ \epsilon$ turbulence model was used with wall functions to model near wall flow velocities. Experimental measurements of mass flow rate agreed well with predictions though measurement of windage losses were less conclusive. The authors cited uncertainty in the measurement of mechanical losses in the bearings as the main cause of discrepancy. The analysis focussed on the prediction of windage losses and it was found that viscous loss (due to rotation of the rotor for example) was small when compared with pressure losses associated with the fan design. The authors concluded that in terms of windage losses aerodynamic improvements should focus on the design of the fan.

Kolondzovski et al. [46] presented a 3D finite element model of the solid components of a high speed permanent magnet radial flux machine with coefficients of convective heat transfer determined from a 2D axisymmetric CFD analysis. Agreement between predicted and measured temperatures was within 10%. The model was used to compare three different rotor constructions. The first configuration had an aluminium eddy current shield and a carbon fibre retaining sleeve; the other two had no additional eddy current shield but had retaining sleeves made from differing grades of titanium alloy. The authors found that even though the carbon fibre configuration performed the worst thermally, the reduction in losses offered by the eddy current shield meant that this configuration incurred the lowest temperature rise.

In terms of axial flux electrical machines CFD was used by Airoldi et al. [74] to predict heat transfer from a stator facing a rotor with protruding magnets in a through flow permanent magnet machine. Air gap length and magnet groove depth were varied in order to gauge their impact on heat transfer, they found that the smallest air gap length gave the highest stator heat transfer rate. Their simulation was validated by experimental measurements made on a mock-up of an electrical machine. There was a good agreement between predicted mass flow rate and stator temperature. The authors state that heat flux from the stator was measured, but the data was not presented for comparison. Similar work was carried out by the same authors in [75] where a CFD analysis was used to predict coefficients of convective heat transfer on the rotor and stator surfaces of a through flow axial flux permanent magnet machine. Local Nusselt numbers are presented for the stator surface but no experimental validation was given.

Radially resolved CFD predictions of stator heat transfer in a through flow axial flux permanent magnet machine were presented by Howey et al. [76]. Experimental measurements of stator heat flux were made and these are in reasonable agreement with predictions. The authors note rather large discrepancies between experiment and simulation near outlet boundaries and in the transitional region of the flow. A rotor with protruding magnets is compared to the smooth case and enhanced heat transfer on the stator is found, though slotting of the stator is not investigated.

An axial flux through flow machine was thermally analysed using a 3D CHT model by Marignetti et al. [77]. The model was used to predict machine component temperatures and agreement with measured stator temperatures is good. There is poor agreement between predicted and measured rotor temperatures. The authors note that their model did not include any representation of rotor losses and cite this as the reason for the discrepancy. A similar work was presented by the same authors [78] and describes the thermal modelling of a similar machine. They again find discrepancies between measured and predicted rotor temperatures due to rotor losses being neglected by the model.

In summary, numerical methods have been used extensively to thermally analyse radial flux electrical machines with simulations ranging from determination of thermal resistances which are subsequently used in lumped parameter models to full conjugate heat transfer studies used to thermally optimise machine designs. Axial flux machines have received much less attention, with only through-flow machines being analysed in any detail. The use of numerical techniques to thermally analyse the design of totally enclosed axial flux machines remains an open topic for investigation.

2.3 Summary

Loss generation and reduction in the permanent magnets of radial flux electrical machines is well understood. Finite element analysis is commonly used to predict losses and show how these losses can be reduced via segmentation, eddy current shields, and various rotor-stator designs. Work specifically focussed on axial flux permanent magnet machines is less common, though many of the same techniques have been shown to be effective in this topology. Only one method of measuring magnet losses was identified in the literature, the method is fairly lengthy and relies on estimations of core loss.

Thermal modelling of radial flux machines via lumped parameter models and numerical methods is common, and in some cases they have been used to predict a reduction of permanent magnet operating temperature via alternative cooling schemes (especially rotor construction). In terms of axial flux machines it is mainly through-flow topologies which have been thermally modelled with only one example of a lumped parameter analysis of a totally enclosed machine being found.

There is an opportunity with the enclosed axial flux machine topology to improve the understanding of the thermal processes which affect permanent magnet temperature. There is also an opportunity to develop a more direct method for measuring permanent magnet losses which could be used to validate loss predictions.

Chapter 3

Numerical Prediction of the Loss, Flow, and Temperature Fields within a Totally Enclosed Axial Flux Permanent Magnet Synchronous Machine

Chapter 2 identified an opportunity with the totally enclosed axial flux PMSM to fill a gap in the literature by improving the understanding of the thermal management of their permanent magnets. This chapter presents the formulation of a numerical model of the axial flux machine presented in Figure 1.9, the purpose of the model being to give a detailed understanding of the physical processes occurring within the machine which affect magnet temperature.

The numerical model consisted of two coupled numerical components, the first of which was a transient electromagnetic FEA which determined the spatially discretised loss density in the machine's permanent magnets and core. Experimental measurements of current waveform were used as boundary conditions, meaning that losses caused by current harmonics, as well as winding MMFs and slotting were all accounted for. The second component was a CHT analysis which determined (from the predicted loss densities, and experimental measurements of the copper loss) the resultant flow and temperature fields. The method used to couple the two numerical model components is justified in Chapter 4 and has been presented separately as it is a novel approach which contains large amounts of validation work using the numerical methodologies presented in this Chapter, which may not be familiar to the reader.

In this Chapter, the two components of the model are presented sequentially with the same basic structure. First the governing equations are identified and the methods for discretising and solving them are given. After this the geometry of the electrical machine is presented with descriptions of any geometry simplifications, material properties and boundary conditions. Finally details of the mesh and the methods used to determine the mesh are given.

3.1 Prediction of the Loss Field in an Axial Flux Permanent Magnet Synchronous Machine

This section presents the numerical model which was used to predict the loss field in the permanent magnets and core of the electrical machine. Loss prediction in an electrical machine is an electromagnetic problem, and a solution to Maxwell's equations is required to solve it.

3.1.1 Maxwell's Equations

The governing laws of electromagnetics are a set of coupled partial differential equations along with a set of constitutive relations, known collectively as Maxwell's Equations. Direct analytical solutions are known in only a limited number of cases. In cases where analytical solutions are not known numerical techniques, such as the Finite Element Method (FEM), can be used to approximate a solution to the equations. The FEM is well suited to the analysis of electrical machines as the solution domain is composed of various materials, complex geometries and areas where differing element densities are required. The FEM uses the theory of the conservation of energy: An energy functional is derived from the governing equations which is then minimised, the premise being that, with the given boundary and initial conditions, the real system will always assume the lowest energy state possible. A commercially available FEM code 'Ansoft Maxwell 14.0.2' has been used in this work. A brief overview of the method is now given. First the governing equations are presented, followed by a description of the boundary conditions required to solve them. The model of the electrical machine is then presented. For a more detailed description of the FEM, the book by Silvester and Ferrari [79] presents the method through many practical examples and is highly recommended. Details of the finite element formulation are presented in Appendix A.

Maxwell's equations are shown in differential form in Equations (3.1), (3.2), (3.3) and (3.4). The accompanying constitutive relations which describe the relationship between the field quantities and material properties are shown in Equations (3.5), (3.6) and (3.7).

$$\nabla \times \vec{H} = \vec{J} + \frac{\partial \vec{D}}{\partial t} \tag{3.1}$$

$$\nabla \times \vec{E} = -\frac{\partial \vec{B}}{\partial t} \tag{3.2}$$

$$\nabla \cdot \vec{D} = \rho \tag{3.3}$$

$$\nabla \cdot \vec{B} = 0 \tag{3.4}$$

$$\vec{B} = \mu_0 \left(\vec{H} + \vec{M} \right) \tag{3.5}$$

$$\vec{D} = \varepsilon \vec{E} \tag{3.6}$$

$$\vec{J} = \sigma \vec{E} \tag{3.7}$$

Where $\vec{H}$ is the magnetic field strength, $\vec{J}$ is the current density, $\vec{D}$ is the electric displacement, $\vec{E}$ is the electric field strength, $\vec{B}$ is the magnetic flux density, ρ is the charge density, μ_0 is the permeability of free space, $\vec{M}$ is the magnetisation, ε is the permittivity, and σ is the conductivity.

As the highest excitation frequency of interest is the carrier frequency of the pulse width modulation waveform (12kHz) the displacement current $\partial\vec{D}/\partial t$ in Equation (3.1) can be neglected. It has been shown to be negligible in applications operating below 10-50MHz by Perry [80], making Equation (3.8) the applicable relationship between current density and magnetising force.

$$\nabla \times \vec{H} = \vec{J} \tag{3.8}$$

3.1.2 Boundary Conditions

Conditions must be prescribed at the boundaries of any finite element solution space in order to reduce the number of degrees of freedom to the same number as there are equations. Three kinds of boundary condition are used in this work, and these will be described now.

Dirichlet

The Dirichlet boundary condition sets the value of the normal component of the magnetic field at a point or surface. When $\mu\vec{H}.\vec{n} = 0$ at a surface, flux lines flow parallel to that surface. Real electromagnetic fields propagate infinitely into space so this constraint must be placed far away from the area of interest.

Neumann

The Neumann boundary condition sets the value of the normal derivative of the curl of the magnetic field at a surface. When $\partial\nabla \times \mu\vec{H}/\partial\vec{n} = 0$ at a surface, flux lines flow orthogonally to that surface. This boundary condition can be used to define symmetry with respect to a surface in a solution.

Interconnection

The Interconnection boundary condition defines the solution at one node or surface from the field solution at another. This boundary condition is commonly used to represent periodicity or translational symmetry in a solution.

3.1.3 Computational Domain

The machine studied produces torque at the fundamental frequency of the phase current excitation and the winding layout is seen the repeat itself every pole pair. Computationally then, only a single pole pair of the machine need be modelled, in addition to this a line of symmetry exists in the plane of rotation through the centre of the magnets (see Figure 3.1). Based on this information the computational domain was constructed as in Figure 3.2, which shows its development from the full geometry. In the actual electrical machine the stator is fixed along its back face to the machine casing with an array of screw fixings. Neither the holes nor the screws have been included in the computational domain, sacrificing accuracy for reduced computational time. For the same reasons other conducting media e.g. the shaft and casing, have been neglected.

Figure 3.3 shows the computational domain in isolation, with each domain and boundary condition labelled, and described in the following sections. Conductors of the same colour belong to the same phase.

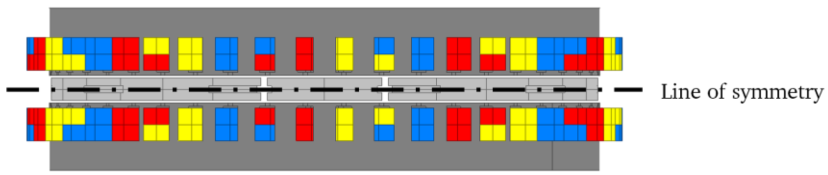

Figure 3.1 Symmetry in the AF PMSM geometry

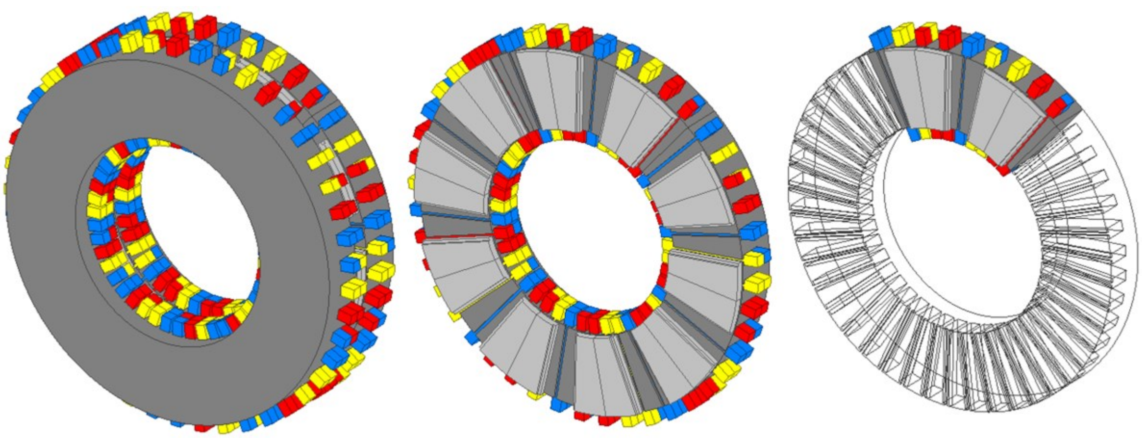

Figure 3.2 Periodicity in the AF PMSM geometry

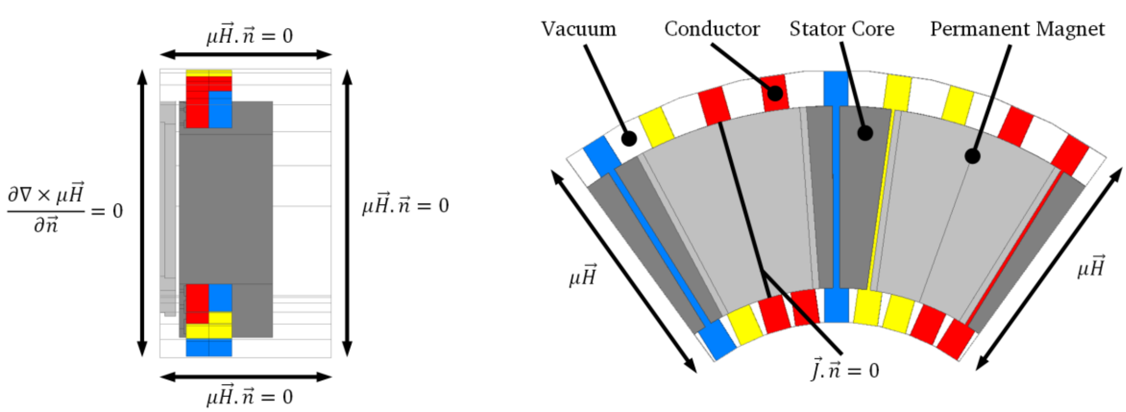

Figure 3.3 Electromagnetic computational domain of the AF PMSM

Permanent Magnet

These domains had temperature dependant material properties which are given in full by [81], for reference Table 3.1 shows the properties of the material at 20°C. The magnetisation vectors of each pole were set in opposite axial directions. The permanent magnets were contained within a 'moving mesh band', highlighted in green in Figure 3.4, which rotated every time step. An interface connects the moving and stationary meshes so that re-meshing is not necessary every time step. The induced electric vector potential was calculated as part of the field solution and subsequently eddy current densities were calculated from Equation (A.1) with the losses in each element calculated from Equation (3.9). Each magnet was segmented into two pieces which were electrically isolated from each other using boundary conditions.

Table 3.1 Permanent magnet material properties

Property	Value
Remnant Flux Density [T]	1.17
Coercivity [A m^{-1}]	850
Conductivity [S m^{-1}]	555,556

$$q_m = \frac{1}{\sigma}\int_V \vec{J}^2 dV \tag{3.9}$$

Where q_m is the loss in an element in the magnet domain.

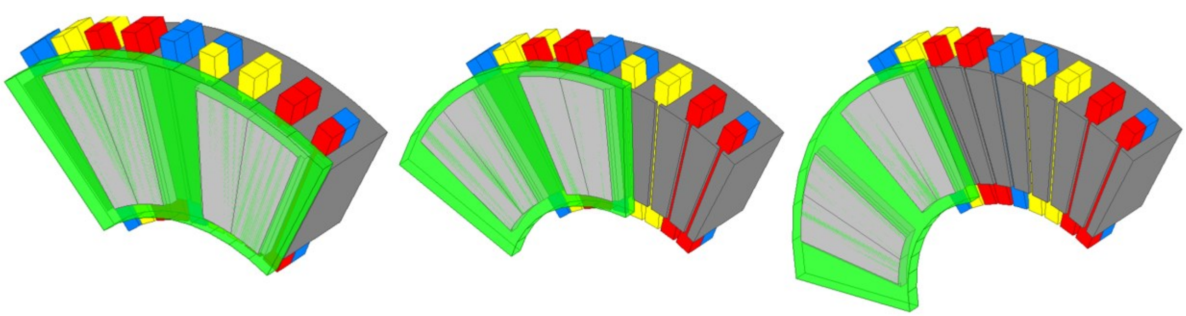

Figure 3.4 Moving mesh band

Stator Core

The stator core is manufactured from a continuous strip of stamped electrical steel, wound on a mandrel and spot welded at each end. This creates a stack which is laminated in order to reduce eddy current losses. Electromagnetically the laminations can be thought of as being separated by small air gaps, producing a component which at the macro level has an anisotropic permeability. Ansoft takes this into account by the user specifying a stacking factor, k_{lam}, and a direction rather than meshing each individual strip and air gap which would be computationally expensive, see Lin et al [82]. The stacking factor for this application is defined in Equation (3.10) and was found to be 0.99.

$$k_{lam} = \frac{N_L t_L}{r_o - r_i} \tag{3.10}$$

Where N_L is the number of laminations, t_L is the lamination thickness, r_o is the outer radius of the core, and r_i is the inner radius of the core.

The permeability in each direction is then given by Equations (3.11), (3.12) and (3.13) where r is the stacking direction. Figure 3.5 serves to orient the reader.

$$\mu_r = \frac{\mu_a \mu_{fe}}{(1 - k_{lam})\mu_{fe} + k_{lam}\mu_a} \tag{3.11}$$

$$\mu_\theta = (1 - k_{lam})\mu_a + k_{lam}\mu_{fe} \tag{3.12}$$

$$\mu_z = (1 - k_{lam})\mu_a + k_{lam}\mu_{fe} \tag{3.13}$$

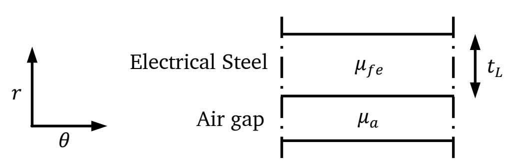

Figure 3.5 Lamination in the stator core

These permeabilities are then assembled into a tensor, Equation (3.14), which is used to calculate the flux density in each direction as shown in Equation (3.15).

$$[\mu] = \begin{bmatrix} \mu_r & 0 & 0 \\ 0 & \mu_\theta & 0 \\ 0 & 0 & \mu_z \end{bmatrix} \tag{3.14}$$

$$\vec{B} = [\mu]\vec{H} \tag{3.15}$$

Classically core losses can be calculated in the frequency domain for sinusoidally varying fields from the Steinmetz Equation (3.16).

$$\dot{q_{fe}} = k_h f B_m^2 + k_c (f B_m)^2 + k_e (f B_m)^{1.5} \tag{3.16}$$

Where $\dot{q_{fe}}$ is the loss density in the core, k_h is the hysteresis loss coefficient, f is the frequency, B_m is the peak flux density, k_c is the eddy current loss coefficient, and k_e is the excess loss coefficient. The core loss calculation performed by Ansoft differs from this, though it uses the same loss coefficients, k_h, k_c, and k_e. Detailed information about the method can be found in by Lin et al [83], a brief summary of the method is given in Appendix A.

The non-linear B-H curve, and loss densities obtained from an Epstein frame test, of the stator steel are shown in Figure 3.6. This information was kindly provided by the material manufacturer in tabular form and input directly into Ansoft to obtain the experimental loss coefficients k_h, k_c and k_e which were found to be 189W/m^3/Hz/T^2, 0.72W/m^3/Hz^2/T^2 and 0W/m^3/Hz/T$^{1.5}$ respectively. It should be noted that when the loss coefficients are determined in this way errors are expected as the Epstein frame test was carried out on an 'ideal' sample. In a real machine the stator core material has been stamped, formed, and welded before being fixed to a casing using screws. All of these processes introduce stress and strain in the material, potentially changing the loss coefficients.

Conductors

In order to focus computational resource in the areas of greatest importance (loss calculation in the magnets and stator core) the end windings of the coils were not explicitly modelled. Instead conductors were placed in each slot with their end faces coincident with the boundary of the computational domain. The end faces of the conductors were then attached to each other via boundary conditions rather than mesh intensive three dimensionally swept bodies to form a star connected three phase set. An experimental measurement of the current waveform was prescribed in each phase as shown in Figure 3.7. Losses in the conductors were measured via experiment, and were therefore not calculated by the numerical model.

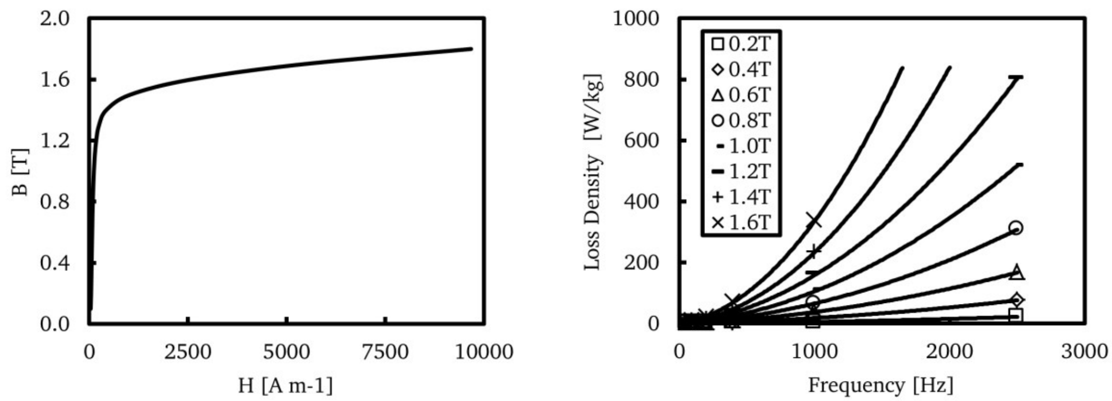

(a) $\vec{B}\vec{H}$ characteristic

(b) Losses

Figure 3.6 Material properties of M330-35A

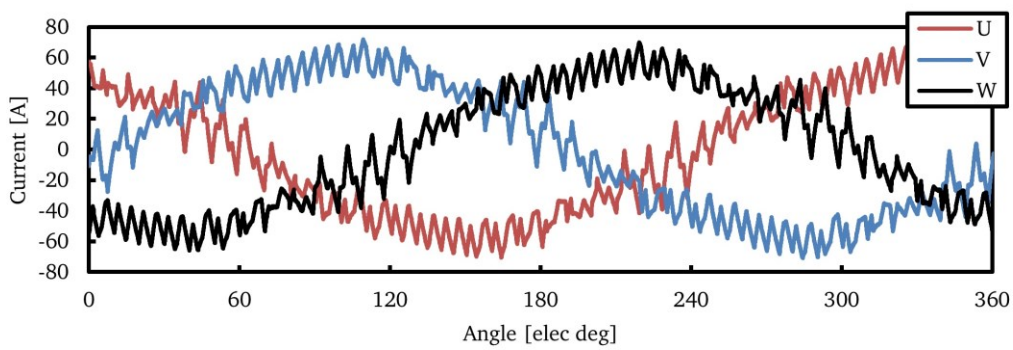

Figure 3.7 Current waveform taken from experimental work (4000rpm, 40Arms)

Vacuum

This domain was non-conducting and had a relative permeability of 1. Where Dirichlet boundaries were applied surfaces were moved away from the area of interest (the stator core and permanent magnets) to allow leakage flux to be correctly accounted for.

3.1.4 Mesh Study

A mesh study was conducted in order to gauge the accuracy of any solution the model produced. Due to the intense computational requirements of a transient analysis a study based on a series of magnetostatic analyses was used to determine the sensitivity of the solution to mesh resolution. In order to represent the largest gradients in solution which the mesh would have to resolve in the transient simulation, the current in each phase was set based on the nominal current of the machine with the stator and rotor flux being in quadrature. A direct, rather than iterative, solver was used for the study so that differences in solution between different grids could only be attributed to mesh resolution. Ansoft's adaptive meshing algorithm was used to progressively refine the mesh in areas where the gradient of the field solution changed rapidly over element edges. For each grid the resultant magnitude of the flux density was exported on to a set of independent coordinates and the solution was compared against the solution from the finest mesh. This was done by defining a residual which is presented in Equation (3.17) where v_i is the volume of each element, B_i is the magnitude of the flux density in v_i in the solution of the finest mesh, and B_j is the magnitude of the flux density in v_i in the solution of the comparison mesh. The residual then, is the average error between the solution computed on the finest mesh and solution computed on the comparison mesh.

$$R_{Stator\ Core} = \frac{1}{\sum_{i=0}^{n} v_i} \sum_{i=0}^{n} v_i \sqrt{\left(\frac{B_i - B_j}{B_i}\right)^2} \tag{3.17}$$

The simulations were also solved using different values of non-linear residual which differs from the residual described above. The non-linear residual is the amount that the field solution is allowed to change from solver iteration to iteration (due to the non-linear properties of the stator steel) before it is judged to have converged. Figure 3.8 shows the results of the mesh study where the 'Mesh Size' is the number of mesh elements normalised against the number in the finest mesh.

For the final mesh, element densities were selected which corresponded to an RMS residual error of 4% and 1% in the stator core and permanent magnet domains respectively. Though the solution of the simulation was not strictly mesh independent solving a finer mesh was not possible with the computational resources available. For reference the selected mesh densities corresponded to two weeks of computational time per simulation on a 6x3.33GHz core workstation with 16Gb of RAM. In addition to the mesh densities taken from the magnetostatic mesh study, the skin depth of the eddy currents flowing in the magnet domains was considered. Table 3.2 shows the skin depth calculated from Equation (3.18) for different frequencies present in the problem. As can be seen the skin depth of the eddy currents induced by the time harmonic content of the current waveform is the smallest length scale which needs to be resolved. The extra layers of elements added to the magnet domain can be seen in Figure 3.9, which along with Figure 3.10 presents the final mesh.

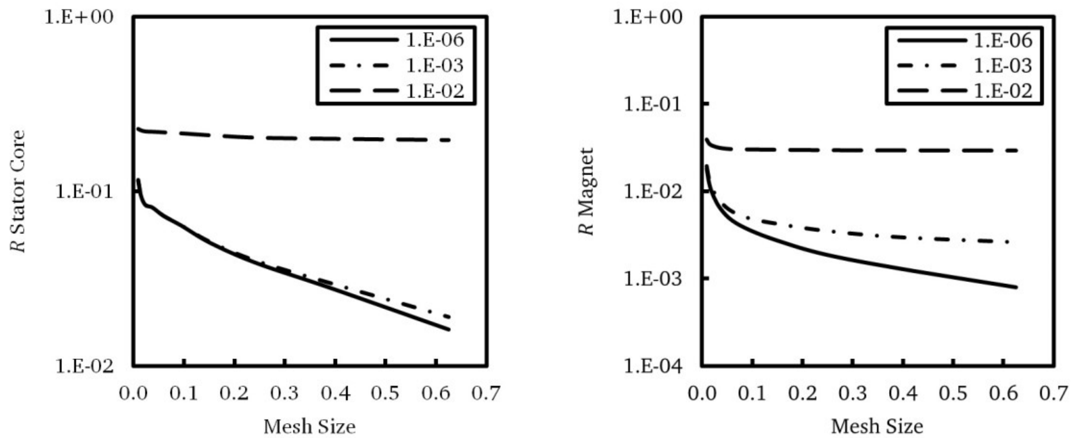

(a) Residual error in the stator core vs. mesh size

(b) Residual error in the magnet vs. mesh size

Figure 3.8 Results of EM FEA mesh study, each plot line represents a different value of non-linear residual

$$\delta = \sqrt{\frac{2}{\omega\sigma\mu_o\mu_r}} \tag{3.18}$$

Where δ is the skin depth, and ω is the angular frequency of excitation.

Table 3.2 Skin depth in the permanent magnet domain

Frequency Source	Value [Hz]	Skin Depth [mm]
Slotting @ 4000rpm	3000	12
Inverter Switching (fundamental)	12000	6
Inverter Switching (2nd Harmonic)	24000	4.3
Inverter Switching (3rd Harmonic)	36000	3.5

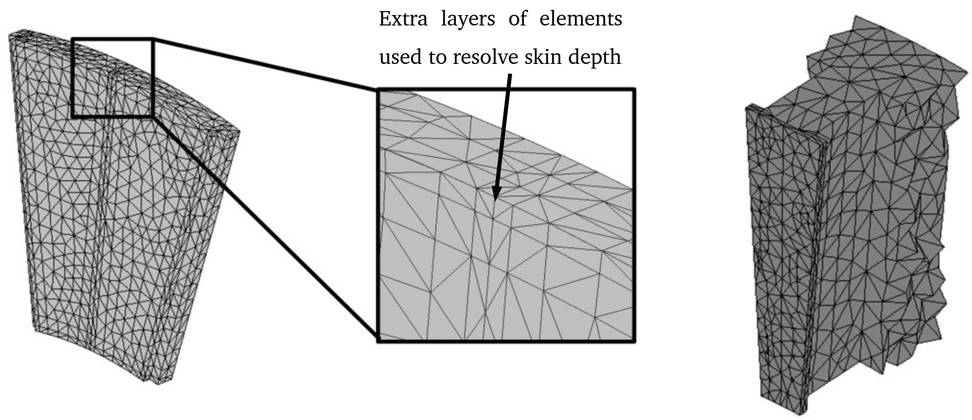

(a) Mesh in the magnet domain (b) Mesh in the stator core domain

Figure 3.9 Final computational mesh of magnet and core

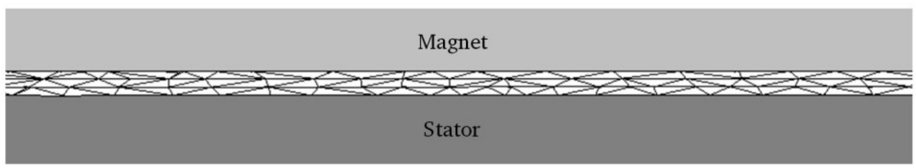

Figure 3.10 Final computational mesh of the air gap

3.1.5 Temporal Discretisation

Based on available computational resource it was decided that each simulation would be divided into 500 time steps per electrical period. This limitation set the harmonic content of the current waveform in the lowest rotational speed simulation to encompass the first two higher order harmonics of the switching frequency. In order to ensure a fair comparison between operating points this was maintained for the higher rotational speed simulations. Of course, the physical length of each time step was shorter in these simulations so therefore higher harmonics could have been included without a computational penalty. Defining the temporal discretisation in this way ensured that spatial and temporal harmonics were resolved to the same level in each simulation.

3.1.6 Post Processing

In order to process the resultant loss fields for use in the thermal model the solution was sampled using a fine coordinate grid to maintain the spatial discretisation, while the values at every grid point were averaged over time. The ‘sample grid’ size was determined by a study where the solutions obtained by different grid densities were compared to each other. As this study required the solution to the EM FEA to define it, it is presented alongside the numerical results in Section 6.2.2. In order to present the CHT method in this Chapter however it is necessary to describe the procedure used to transform the predicted loss profiles into source terms. Equation (3.19) describes the procedure and shows the values of losses at each grid point being assembled into a column vector, which was used as a source term in the CHT formulation.

$$\begin{Bmatrix} \dot{q}_i \\ \vdots \\ \dot{q}_n \end{Bmatrix} = \frac{1}{T}\sum_{k=0}^{T}\left(\frac{\dot{q}_{i_k} + \dot{q}_{i_{k-1}}}{2}\right).(t_k - t_{k-1}) \tag{3.19}$$

3.2 Prediction of the Flow and Temperature Fields in an Axial Flux Permanent Magnet Synchronous Machine

This section describes the second component of the numerical model, which used the results of the electromagnetic analysis (Equation (3.19)) as a source term in a CHT analysis to predict the flow and temperature fields within the electrical machine. Firstly, the concept of CHT analysis is summarised and the governing equations are presented with the method of numerical solution of them described. After this the computational domain is developed with appropriate material properties and boundary conditions prescribed and justified.

3.2.1 Conjugate Heat Transfer

The governing laws of fluid flow and heat transfer are a set of coupled, non-linear, partial differential equations. Direct analytical solutions are known in only a limited number of cases. In cases where analytical solutions are not known numerical techniques, such as the Finite Volume Method (FVM), can be used to approximate a solution to the equations. This is achieved by discretising the solution domain into a number of finite volumes and hence transforming the partial differential equations into many ordinary differential equations which can be solved easily using a computer. A commercially available FVM code, Ansys CFX V13.0, has been used in this work. A brief overview of the method is now given, for a more detailed description of the area the book by White [84] presents a clear derivation of the governing equations, whilst the FVM is described by Versteeg and Malalasekera [85].

3.2.2 Equations of Fluid Flow and Heat Transfer

The equations which govern heat and fluid flow are a set of coupled nonlinear partial differential equations which are based on three physical principles:

- Conservation of mass
- Conservation of momentum
- Conservation of energy

Conservation of mass can be expressed as in Equation (3.20) which reduces to Equation (3.21) for incompressible steady flow.

$$\frac{\partial \rho}{\partial t} + \nabla \cdot \left(\rho \vec{V}\right) = 0 \tag{3.20}$$

$$\nabla \cdot \vec{V} = 0 \tag{3.21}$$

Where ρ is the density and $\vec{V}$ is the velocity.

The Navier Stokes Equations express the conservation of momentum, as per Equation (3.22) where for a Newtonian fluid the viscous stresses are given by Equation (3.23). In order to present the equations in the most compact way suffix notation has been used. In this convention i or $j = 1$ corresponds to the x-direction, i or $j = 2$ corresponds to the y-direction, and i or $j = 3$ corresponds to the z-direction.

$$\rho \frac{D\vec{V}}{Dt} = \rho \vec{g} + \nabla \cdot \tau'_{ij} - \nabla p \tag{3.22}$$

$$\tau'_{ij} = \mu \left(\frac{\partial u_i}{\partial x_j} + \frac{\partial u_j}{\partial x_i} \right) + \delta_{ij} \lambda \nabla \cdot \vec{V} \tag{3.23}$$

Where $\vec{g}$ is the acceleration due to gravity, τ'_{ij} are the viscous stresses, p is the pressure, μ is the dynamic viscosity (which relates stresses to linear deformations), λ is the 'second' viscosity (which relates stresses to volumetric deformations), and u is the velocity.

The conservation of energy is described by the energy equation, shown in Equation (3.24) which reduces to Equation (3.25) for incompressible flow.

$$\rho \frac{Dh}{Dt} = \frac{Dp}{Dt} + \nabla \cdot (k \nabla T) + \tau'_{ij} \frac{\partial u_i}{\partial x_j} \tag{3.24}$$

$$\rho C_p \frac{DT}{Dt} = \nabla \cdot (k \nabla T) + \tau'_{ij} \frac{\partial u_i}{\partial x_j} \tag{3.25}$$

Where h is the enthalpy, k is the thermal conductivity, T is the temperature, and C_p is the heat capacity.

In a solid domain the energy equation reduces further to Equation (3.26).

$$\rho C_p \frac{DT}{Dt} = \nabla \cdot (k \nabla T) + \Phi \tag{3.26}$$

Where Φ is a heat source.

3.2.3 Turbulence

The Reynolds number Re of a flow gives the relative importance of inertial and viscous forces within it; it is given for a rotating disc system in Equation (3.27).

$$Re = \frac{\rho \omega r^2}{\mu} \tag{3.27}$$

Where r is the radius of the disc.

Below a certain threshold viscous forces dominate within the flow and act to stabilise it, the flow field can be thought of as a series of fluid sheets moving over the top of each other, with no movement of fluid from sheet to sheet. Above the threshold viscous forces can no longer stabilise the flow and inertial effects cause mixing between sheets. This mixing is known as turbulence and can be thought of as eddies within the flow induced by its vorticity, where the eddies vary greatly in length scale and are unsteady structures being created and destroyed continuously. Turbulent mixing is completely described by Equations (3.20)-(3.25) though as the equations are solved via a discretisation method very fine meshes are needed to resolve the smallest eddy length scales. When this is done the technique is known as Direct Numerical Simulation (DNS). With today's supercomputers only simple problems can be solved at modest Reynolds numbers, with simulations lasting weeks or months. A less computationally expensive technique is known as Large Eddy Simulation (LES). In this approach eddies at the length scale of the mesh are resolved, with turbulence models used for eddies at sub-mesh scales. A popular alternative to DNS or LES is to resolve only the largest flow structures with the computational mesh and use a turbulence model to include the effects of turbulence on the main flow. In order to use these models the governing equations are subjected to a decomposition, known as the Reynolds

Decomposition. It is a statistical approach where every variable is redefined as having a mean and a fluctuating component:

$$\vec{u} = \overline{\vec{u}} + \vec{u}' \tag{3.28}$$

When substituted into the governing equations and time averaged the Reynolds Averaged Navier Stokes equations result:

$$\nabla \cdot \left(\overline{\vec{V}} + \vec{V}'\right) = 0 \tag{3.29}$$

$$\rho \frac{D\overline{\vec{V}}}{Dt} = \rho \vec{g} + \nabla \cdot \tau_{ij} - \nabla \bar{p} \tag{3.30}$$

$$\rho C_p \frac{D\bar{T}}{Dt} = -\frac{\partial}{\partial x_i}(q_i) + \bar{\Phi} \tag{3.31}$$

Equation (3.32) expands τ_{ij} from Equation (3.30) and shows that it is comprised of the usual shear stress terms plus an additional 'turbulent stress' term $\rho\overline{u_i' u_j'}$, which represents the transport of momentum via turbulent interactions.

$$\tau_{ij} = \mu\left(\frac{\partial u_i}{\partial x_j} + \frac{\partial u_j}{\partial x_i}\right) - \rho\overline{u_i' u_j'} \tag{3.32}$$

Equation (3.33) expands the term q_i from Equation (3.31) and shows that it has gained a turbulent heat flux term $\overline{u_i' T'}$ whilst $\bar{\Phi}$ is expanded in Equation (3.34) to show how the decomposition has modified the viscous diffusion term.

$$q_i = -k\frac{\partial \bar{T}}{\partial x_i} + \rho C_p \overline{u_i' T'} \tag{3.33}$$

$$\bar{\Phi} = \frac{\mu}{2}\left(\frac{\partial \bar{u}_i}{x_j} + \frac{\partial u_i'}{\partial x_j} + \frac{\partial \bar{u}_j}{x_i} + \frac{\partial u_j'}{\partial x_i}\right)^2 \tag{3.34}$$

The decomposition results in fewer equations than unknowns. Turbulence models then, are the additional equations used to close the problem, many models exist, for a full overview see [86].

Two-equation turbulence models are a popular choice for closing the system of equations as they offer a good compromise between accuracy and computational time. They make use of the

Boussinesq assumption, which proposes an 'eddy viscosity' μ_t to model the effects of turbulence on the mean flow:

$$-\rho\overline{u_i' u_j'} = \mu_t\left(\frac{\partial \bar{u}_i}{\partial x_j} + \frac{\partial \bar{u}_j}{\partial x_i}\right) - \frac{2}{3}\left(\rho K + \mu_t \frac{\partial \bar{u}_k}{\partial x_k}\right) \tag{3.35}$$

$$\rho C_p \overline{u_i' T'} = \Gamma_t \frac{\partial \bar{T}}{\partial x_i} \tag{3.36}$$

Where Γ_t is the turbulent diffusivity and is related to the eddy viscosity by the turbulent Prandtl number, Pr_t: $\Gamma_t = \mu_t / Pr_t$. The turbulent Prandtl number is determined empirically, and is taken as 0.9 in the CFX code. The variable K is the turbulence kinetic energy, which is the RMS of the fluctuating velocity components, $K = 1/2\left(\overline{(u_1')^2} + \overline{(u_2')^2} + \overline{(u_3')^2}\right)$. Part of the Boussinesq assumption is, therefore, that the turbulence is isotropic, i.e. $u_1' = u_2' = u_3'$. By dimensional considerations the eddy viscosity can be defined as:

$$\mu_t = \rho C_\mu v l \tag{3.37}$$

Where v is a turbulent velocity scale, l is a characteristic length scale of the turbulent interactions and C_μ is an empirical constant. Two-equation turbulence models add two additional conservation equations which describe the production, dissipation, and transport of K and either a turbulent time scale t, a turbulent length scale l, rate of viscous dissipation ϵ, or turbulence frequency ω. K and the 'other quantity' are subsequently used to predict μ_t, the Reynolds stresses $-\rho\overline{u_i' u_j'}$, and the turbulent heat flux terms $\rho C_p \overline{u_i' T'}$, closing the system of equations. Two popular two-equation turbulence models are the $K\ \epsilon$ and $K\ \omega$ models. In the $K\ \epsilon$ model K and ϵ are used to define v and l on purely dimensional grounds as $v = \sqrt{K}$ and $l = K^{1.5}/\epsilon$, the eddy viscosity is therefore:

$$\mu_t = \rho C_\mu \frac{K^2}{\epsilon} \tag{3.38}$$

In the $K\ \omega$ model the turbulence frequency ω is used, and is defined as $\omega = \epsilon/K$. In this model the eddy viscosity is therefore:

$$\mu_t = \rho C_\mu \frac{K}{\omega} \tag{3.39}$$

In this work the Shear Stress Transport (SST) model is used to model turbulent behaviour in both of the computational domains presented in Sections 3.2.5 and 3.2.6. The SST model is a combination the $K\,\epsilon$ and $K\,\omega$ models. The $K\,\epsilon$ model has been shown to be a good general purpose turbulence model, though requires wall functions to be used to take velocity profiles near the wall into account. The $K\,\omega$ model has been shown to give good results within boundary layers. In the free stream however, as K and ω both tend to zero, μ_t becomes indeterminate. Small values of ω must be assumed and, unlike the $K\,\epsilon$ model, the solution seems to be very sensitive to these values. The SST model uses the best parts of both models by using a blending function to transition smoothly between the $K\,\omega$ formulation at the wall and the $K\,\epsilon$ formulation in the free stream. It also includes a redefinition of the eddy viscosity near the wall to take into account the transport of the Reynolds stresses. Detailed information about the formulations can be found in [85] and [86].

It has been shown empirically by Itoh et al. [87] that the Boussinesq assumption is not strictly correct for rotating flows, as the Reynolds stress components are not isotropic. In cases such as this Reynolds Stress Models (RSM) can be used to model each Reynolds stress term individually. This has the disadvantage that seven additional transport equations must be solved. In this work the SST model was found to be good enough to give reasonable predictions of component temperatures, and therefore the use of RSMs was not investigated, as the computational time was prohibitive within the time frame of the project.

3.2.4 Transition

A flow is said to 'transition' from a laminar to a turbulent regime. This happens once the Reynolds number of the flow exceeds a critical value, and the viscous forces between fluid elements can no longer overcome the inertial forces. It is shown in the presentation of both computational domains in Sections 3.2.5 and 3.2.6 that modelling the transition of the flow cannot be ignored. A transition model designed for use with the SST model is available within CFX. It requires the solution of two additional transport equations to model the effects of transition on the mean flow. Rather than attempt to model the 'physics' of transition the model is purely empirical, the result is a coefficient which modifies the production and destruction terms in the K equation of the SST model, see Langtry et al [88] for more details.

For details of how CFX discretises and solves the governing equations please refer to Appendix A.

3.2.5 Computational Domain I

This section describes the CHT model of the electrical machine. Due to computational constraints a number of simplifications had to be made within the domain which made it differ from the actual electrical machine geometry. Figure 3.11 and Figure 3.12 show the development of the domain, where it can be seen that certain geometries have been removed in order to make the domain periodic and symmetric. The simplifications mean that the stator domain can be represented by a 4/45th slice of the whole machine and the rotor domain by a 1/10th slice. Note that the stator could be represented by a 1/45th slice, the 4/45th slice was selected as this minimises the pitch change between the rotating and stationary domains. Symmetry down the centre of the rotor also reduces the size of the problem.

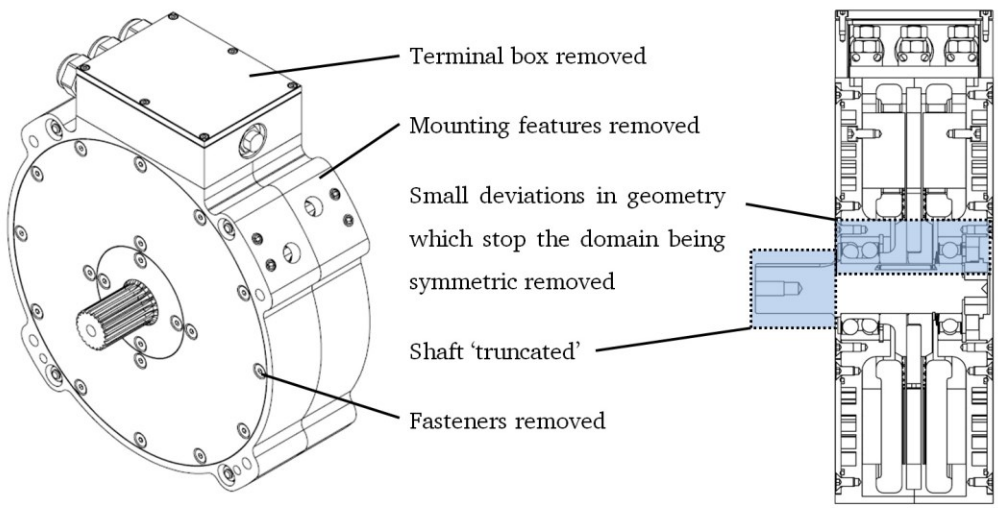

Figure 3.11 Geometric simplifications of the AF PMSM for CHT analysis

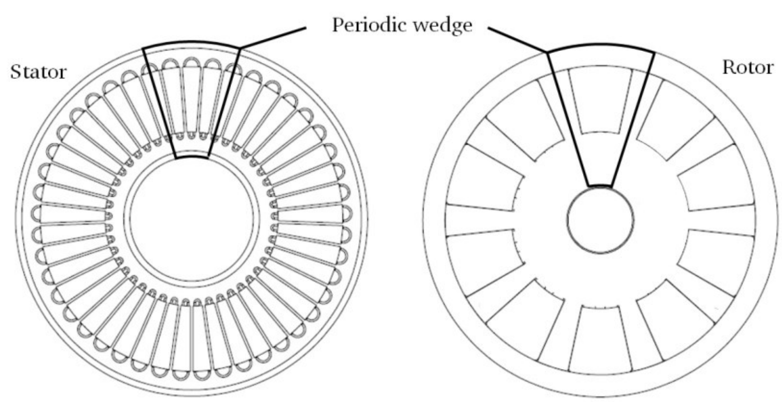

Figure 3.12 Periodicity in the AF PMSM geometry

A number of options exist within CFX which allow the motion of a rotor to be modelled,

- Sliding mesh interface: The rotor mesh moves every time step, this necessitates a transient simulation which is computationally expensive, but correctly models the 3D interaction between the rotor and the stator.
- Stage interface: The relative position of the rotor and stator are fixed during the simulation. A frame of reference change is applied across the interface which numerically models the rotation of the rotor. At the interface the fluxes are circumferentially averaged, scaled by the pitch change (if any), and 'passed upstream'.
- Frozen rotor interface: Similar to the stage interface but with no circumferential averaging of the fluxes.

To model the domain interface between the rotating and stationary fluid domains the 'Frozen Rotor' mixing model was selected. In this model the relative position of each domain remains constant throughout the entire calculation; rotation is modelled numerically in the fluid domain by setting the value of the velocity at the rotating wall to be ωr where ω is the rotational speed of the wall and r is the local radius. Values of flux across the interface are scaled by the pitch change. This creates a model which assumes a quasi-steady solution to be realistic at the interface.

Details of each domain are now given, Figure 3.13 summarises the geometry of the computational domain, while Figure 3.14 details the prescribed boundary conditions. Table B.1 in Appendix B summarises the material properties of each domain.

3.2.5.1 Solid Domains

Permanent Magnet

This domain was solid and located in the rotating domain, all material properties were taken from the manufacturer's data sheet [81]. A source term $\{\dot{q}\}$ was included in the formulation of the energy equation which was the result of Equation (3.19).

Banding

This domain was solid and located in the rotating domain. Its construction in the actual electrical machine is of a resin impregnated band of woven carbon fibre strands which is wrapped around the magnet-rotor assembly and subsequently cured. In order to represent this composite structure in the numerical model without explicitly modelling each individual strand the domain has been modelled as a homogeneous material with anisotropic thermal conductivity and volume fraction weighted density and specific heat capacity. In order to determine the values of the anisotropic thermal conductivities two methods were used. In the radial and axial directions a FVM model was used in order to correctly take into account the circular cross sectional shape of the strands, see 'Shape Factors' in [89] for a discussion on how the shape of the composite domains effect the equivalent thermal conductivity. The FVM model was set up as shown in Figure 3.15, the left hand figure shows how the carbon strands were assumed to arrange themselves in the component while the right hand figure shows the computational domain. A thermal potential was prescribed across the domain and the equivalent thermal conductivity was calculated from Equation (3.40).

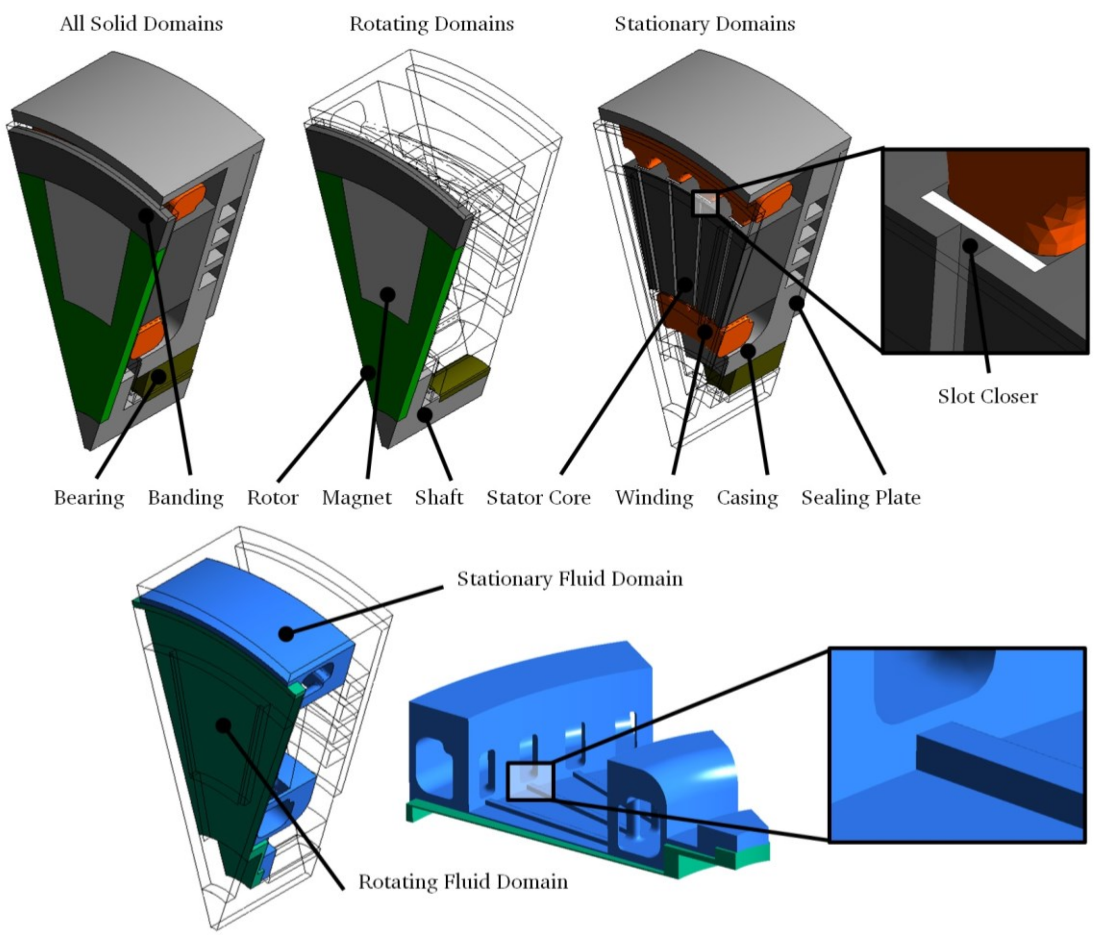

Figure 3.13 CHT computational domain of the AF PMSM

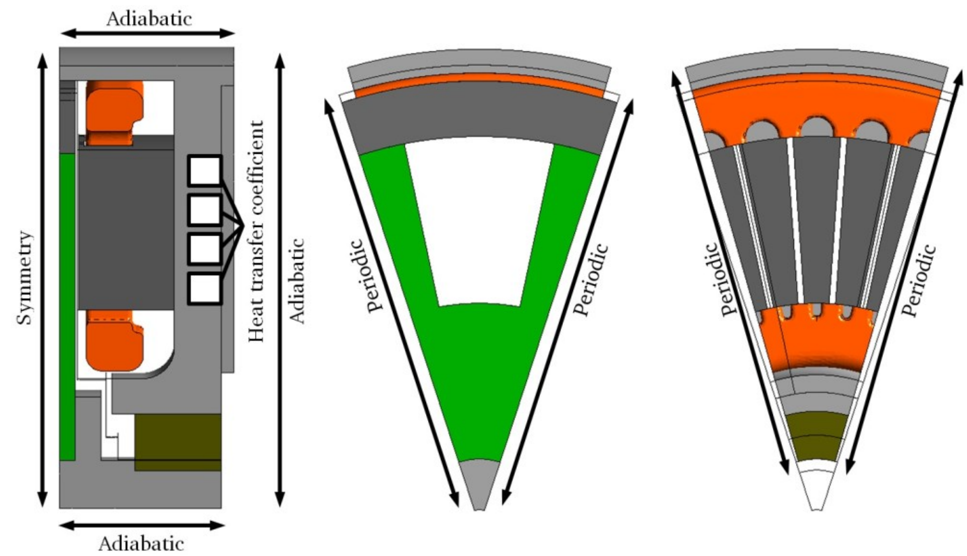

Figure 3.14 Boundary conditions of the CHT computational domain

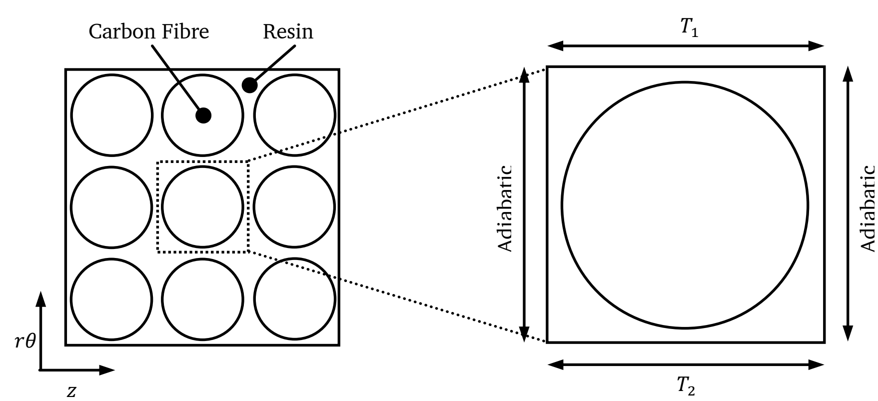

Figure 3.15 Computational domain used to determine the banding thermal conductivity

$$k_r = k_z = \frac{q''l}{T_1 - T_2} \tag{3.40}$$

Where q'' is the heat flux.

In the circumferential direction an analytical approach was used where the thermal conductivity was calculated using Equation (3.41) where f is the fill factor defined by Equation (3.42). This is acceptable in the circumferential direction as only the relative amount of each material, rather than the shape of each domain, affects the solution. The resulting material properties from this analysis are presented in Table 3.3.

$$k_\theta = f k_{carbon} + (1 - f) k_{resin} \tag{3.41}$$

$$f = \frac{V_{carbon}}{V_{composite}} \tag{3.42}$$

Table 3.3 Carbon fibre banding material properties

Material	Property	Value
Carbon Fibre	Density [kg m^{-3}]	1810
	Specific Heat Capacity [J kg^{-1} K^{-1}]	753.1
	Thermal Conductivity [W m^{-1} K^{-1}]	35.1
Resin	Density [kg m^{-3}]	1190
	Specific Heat Capacity [J kg^{-1} K^{-1}]	1175
	Thermal Conductivity [W m^{-1} K^{-1}]	0.175
Carbon Fibre-Resin Composite 62.5% Fill Factor	Density [kg m^{-3}]	1578
	Specific Heat Capacity [J kg^{-1} K^{-1}]	911.3
	Thermal Conductivity r [W m^{-1} K^{-1}]	0.82
	Thermal Conductivity θ [W m^{-1} K^{-1}]	22.0
	Thermal Conductivity z [W m^{-1} K^{-1}]	0.82

Rotor & Shaft

These domains were solid and located in the rotating domain, all material properties were taken from the manufacturer's data sheet, see Appendix B for a summary.

Inner & Outer bearing ring

These domains were solid and located in the rotating and stationary domains respectively. The equivalent thermal conductivity was calculated from the equivalent air gap thermal resistances presented by Staton et al. [90]. The geometry of the bearing was simplified and subsequently represented as a solid lump, friction losses generated in the bearing were calculated from the SKF bearing calculator [91].

Casing

This domain was solid and located in the stationary domain, all material properties were taken from the manufacturer's data sheet, see Appendix B for a summary. The development of this component is described in Section 3.2.6, along with the method used to determine the heat transfer coefficient boundary condition h shown in Figure 3.14.

Stator Core

This domain was solid and located in the stationary domain. A source term $\{\dot{q}\}$ was included in the formulation of the energy equation which was the result of Equation (3.19). The stator core's construction in the actual electrical machine is of a steel band coiled around a mandrel and spot welded at each end. As was described in Section 3.1.3 this produces an anisotropic component in terms of permeability, due to resin filled inter-lamination air gaps. By the same rationale the component also has an anisotropic thermal conductivity. In order to represent this composite structure in the numerical model without explicitly modelling each individual lamination the domain has been modelled as a homogeneous material with anisotropic thermal conductivity and volume fraction weighted density and specific heat capacity. To determine the values of the anisotropic thermal conductivities a composite wall approach was used (see [89] p.77 for an overview), see Figure 3.16, where Equations (3.43), (3.44) and (3.45) were used to calculate the radial, axial and circumferential thermal conductivities.

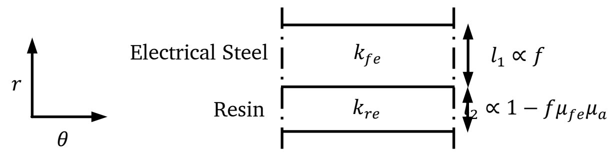

Figure 3.16 Composite wall representation of the core

$$\frac{1}{k_r} = \frac{f}{k_{fe}} + \frac{(1-f)}{k_{re}} \tag{3.43}$$

$$k_\theta = k_z = f k_{fe} + (1-f) k_{re} \tag{3.44}$$

$$f = \frac{V_{fe}}{V_{composite}} \tag{3.45}$$

The results are presented in Table 3.4, material properties for the electrical steel and resin were provided by the manufacturer, see Appendix B.

Winding

This domain was solid and located in the stationary domain. A source term $\{q\}$ was included in the formulation of the energy equation which was determined by experiment (see Section 5.3.4). Its construction in the actual electrical machine is of a resin impregnated bundle of copper wires inserted into each slot and subsequently cured. In order to represent this composite structure in the numerical model without explicitly modelling each individual strand the domain was modelled as a homogeneous material with anisotropic thermal conductivity and volume fraction weighted density and specific heat capacity. As with the stator core and banding components the thermal conductivity has been described with cylindrical components. This method of defining anisotropic thermal conductivities will incur an error at the inner and outer end winding regions where the copper wires are no longer aligned with the coordinate system, see Figure 3.17.

Table 3.4 Stator core material properties

Material	Property	Value
Electrical Steel	Density [kg m^{-3}]	7650
	Specific Heat Capacity [J kg^{-1} K^{-1}]	476.4
	Thermal Conductivity [W m^{-1} K^{-1}]	36
Resin	Density [kg m^{-3}]	1190
	Specific Heat Capacity [J kg^{-1} K^{-1}]	1175
	Thermal Conductivity [W m^{-1} K^{-1}]	0.325
Electrical Steel-Resin Composite 99.4% Fill Factor	Density [kg m^{-3}]	7611
	Specific Heat Capacity [J kg^{-1} K^{-1}]	480.6
	Thermal Conductivity r [W m^{-1} K^{-1}]	21.7
	Thermal Conductivity θ [W m^{-1} K^{-1}]	35.8
	Thermal Conductivity z [W m^{-1} K^{-1}]	35.8

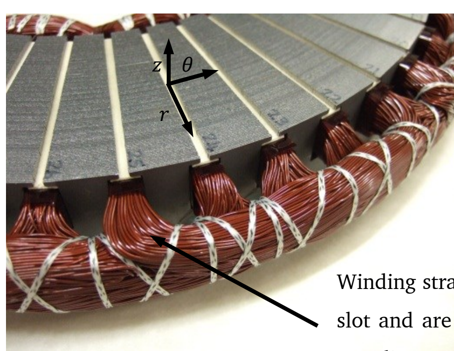

Figure 3.17 Coordinate system misaligned with end winding

Modelling each copper wire individually would correct this error, though is computationally prohibitive in the context of this model. The value of the thermal conductivity in the r direction was determined in the same way as that of the rotor banding in the tangential direction. The value of the thermal conductivity in the θ and z directions was determined via the DC heating experiments described in Appendix C. The resultant material properties are shown in Table 3.5.

Table 3.5 Stator winding material properties

Material	Property	Value
Copper	Density [kg m^{-3}]	8960
	Specific Heat Capacity [J kg^{-1} K^{-1}]	385
	Thermal Conductivity [W m^{-1} K^{-1}]	400
Resin	Density [kg m^{-3}]	1190
	Specific Heat Capacity [J kg^{-1} K^{-1}]	1175
	Thermal Conductivity [W m^{-1} K^{-1}]	0.325
Copper-Resin Composite 51.2% Fill Factor	Density [kg m^{-3}]	5168
	Specific Heat Capacity [J kg^{-1} K^{-1}]	771
	Thermal Conductivity x [W m^{-1} K^{-1}]	0.75
	Thermal Conductivity y [W m^{-1} K^{-1}]	205
	Thermal Conductivity z [W m^{-1} K^{-1}]	0.75

Slot Closer

This domain was solid and located in the stationary domain, all material properties were taken from the manufacturer's data sheet.

Solid Domain Interfaces

In thermal systems comprised of an assembly of different domains there may be a temperature drop across solid domain interfaces, this temperature drop is attributed to what is known as 'thermal contact resistance'. This additional resistance is caused by an imperfect contact between surfaces of neighbouring domains and is a complex function of surface roughness, surface hardness and interface pressure [89]. In the numerical model presented in this work, thermal contact resistances have either been taken from the literature or have been estimated based on knowledge of how the electrical machine is constructed. A summary of all the interfaces is given in Figure 3.18and Table 3.6.

In the actual electrical machine there is a thin sheet of soft thermally conductive material inserted in-between the back of the stator face and the casing. Rather than modelling this thin sheet explicitly (which would require many small elements) Interface 5 has been used to model it as a contact resistance. The value of this contact resistance was determined during the DC heating experiments which are presented in Appendix C.

Interfaces 6 and 7 have been modelled as if there were no contact resistance. In the case of interface 6 it has been assumed that the resin in the carbon fibre composite fills the interfacial gaps during the curing process. In the case of interface 7, during manufacture the magnets have a thin layer of epoxy applied in-between them and the rotor, its conductivity is similar to that of the rotor's (0.3 $Wm^{-1}K^{-1}$ compared with 0.25 $Wm^{-1}K^{-1}$). It is therefore assumed that the epoxy fills all the interfacial gaps during assembly and effectively no thermal contact resistance exists.

During stator manufacture there is a thin sheet of electrically insulating material inserted into each slot to provide an electrical resistance between the winding and the stator core. Rather than modelling this thin sheet explicitly (which would require many small elements) Interface 8 has been used to model it as a contact resistance. The equivalent air gap has been calculated from knowledge of the slot liner material properties and material thickness.

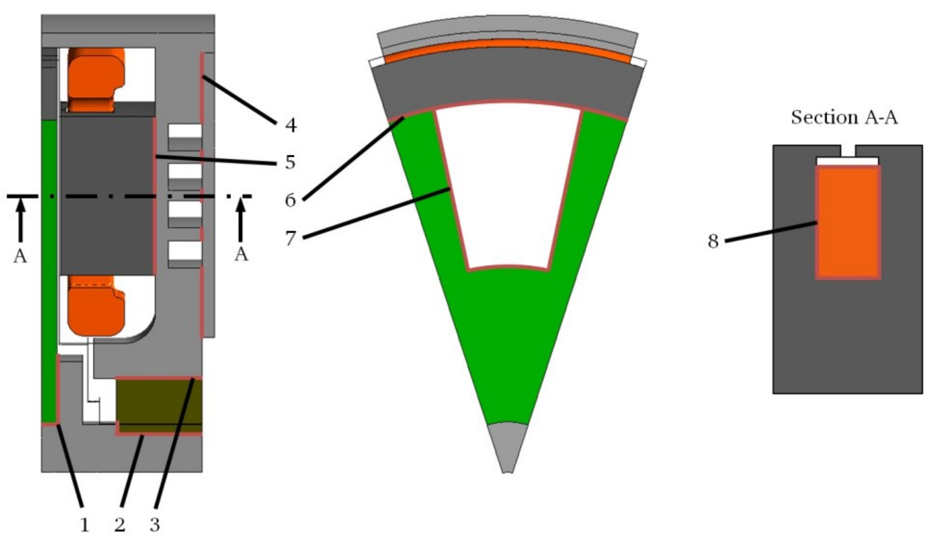

Figure 3.18 Thermal contact resistances in the AF PMSM

Table 3.6 Thermal contact resistances in the AF PMSM

Interface	Description	Equivalent Air Gap [mm]	Source
1	Glass Fibre-Steel	0.00725	[92]
2	Steel-Steel	0.01115	[92]
3	Steel-Aluminium	0.00725	[92]
4	Aluminium-Aluminium	0.0023	[92]
5	Thermal Interface Sheet	3.3e-6	N/A
6	Resin Joint	0	N/A
7	Epoxy Joint	0	N/A
8	Slot Liner	0.0208	N/A

3.2.5.2 Fluid Domain

The air gap of the electrical machine under study is similar to the often studied 'Rotor-Stator Cavity', or 'Annular Cavity' often referred to in the literature. As is it not the aim of this thesis to further this area of research (though it is an active area) only a short review is presented with the interested reader referred to [93] as an excellent starting point for further reading. Figure 3.19 shows the geometry of a typical rotor-stator cavity.

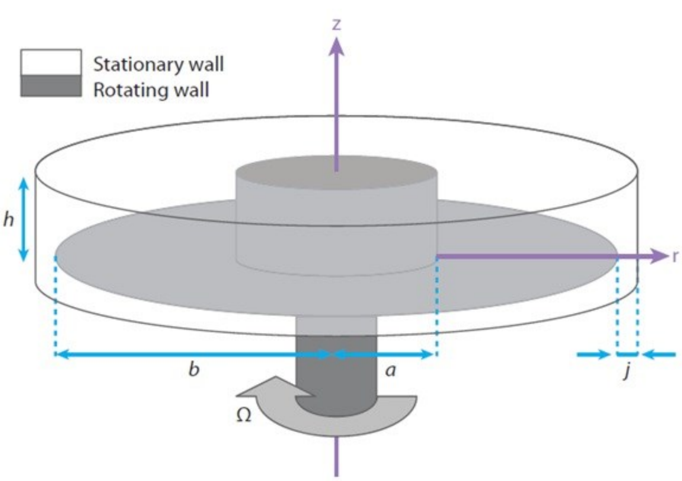

Figure 3.19 Rotor-stator cavity, from [93]

The geometry is often non-dimensionalised in order to generalise findings and present trends. The Reynolds number for the system has already been presented in Equation (3.27) while the non-dimensional gap ratio is defined in (3.46).

$$G = \frac{h}{b} \tag{3.46}$$

The flow structure in this system is characterised as follows. Due to the 'no slip' condition at the rotor surface a boundary layer of rotating fluid builds up in the vicinity of the rotor. As the inertial force of the rotating fluid overcomes the viscous forces fluid begins to flow out radially. To balance this enclosed system, fluid from the stator is entrained to replace the fluid flowing out along the rotor, while the rotor fluid replaces that from the stator. The primary flow is therefore in the circumferential direction while a secondary flow is set up in the meridional plane which recirculates fluid between the two boundary layers, see Figure 3.20.

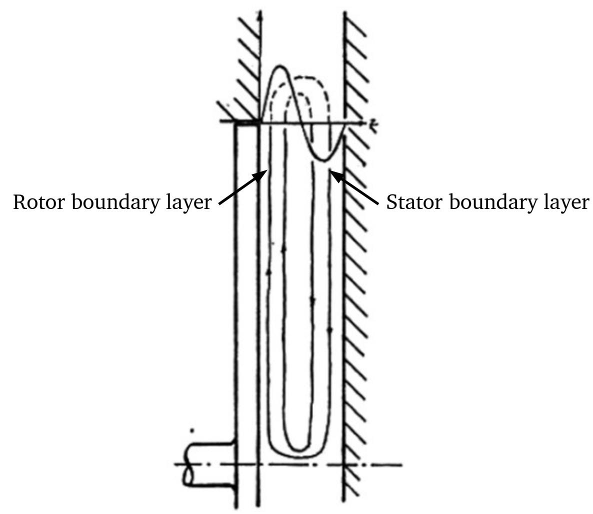

Figure 3.20 Secondary flow structure in an enclosed rotor stator cavity from [94]

Dailey and Nece [95] performed the first detailed experimental investigation into this geometry finding that for $G < 1$ four distinct flow regimes existed:

- I: Merged laminar boundary layers on rotor and stator
- II: Separate laminar boundary layers on rotor and stator
- III: Merged turbulent boundary layers on rotor and stator
- IV: Separate turbulent boundary layers on rotor and stator

Figure 3.21 presents the location of the regimes as functions of G and Re. Transition is observed between each regime which acts to blur the distinctions between them, indeed one may see transition from one regime to another within the same cavity as the value of the local Reynolds number increases with radius, see (3.47).

$$Re = \frac{\rho \omega r_{local}^2}{\mu} \tag{3.47}$$

The electrical machine's rotor radius r is 0.14m and the air gap h is 0.00115m giving a G of 0.0082. Between 2000 and 4000rpm the Reynolds number is calculated to be between 2.3e+5 and 4.6e+5 indicating that regime III is expected at all operating points. Though transition to regimes I and or II may occur at lower radii within the cavity.

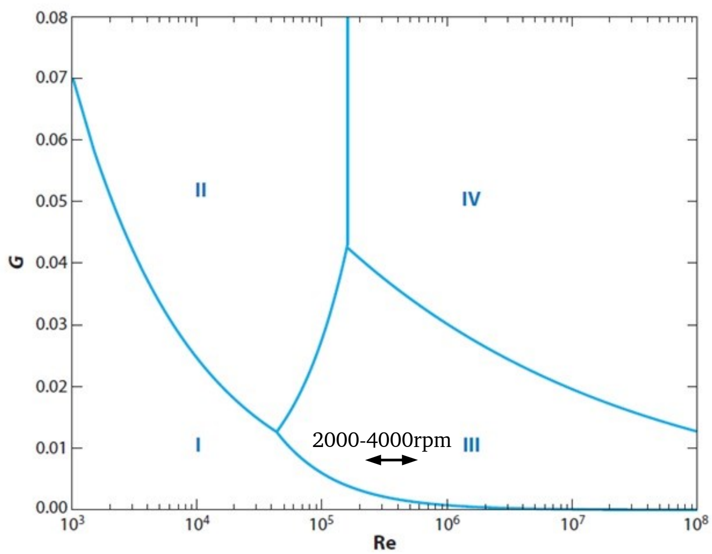

Figure 3.21 Flow regimes in an enclosed rotor-stator cavity, from [95]. The horizontal arrow indicates the expected operating region for the electrical machine

Boutarfa et al. [96] investigated heat transfer in a through flow rotor-stator system. They presented data describing when transition occurred in their system, and this has been used to estimate the radius on the electrical machine's rotor at which transition to turbulent flow will begin. The analysis can only be considered an estimate because their system was not totally enclosed. They found that for a system with comparable gap ratio transition began once Re>176,000, and flow was considered to be fully turbulent once Re>352,000. Based on the definition of Reynolds number a non-dimensional critical radius has been defined for the electrical machine, see (3.48).

$$r_{crit} = \sqrt{\frac{\mu Re_{crit}}{\rho\omega}} \Big/ R_o \tag{3.48}$$

Where r_{crit} is the non-dimensional radius where transition is predicted to begin, and R_o is the outer radius.

Using the Reynolds number limits given by Boutarfa et al. and the temperature dependant fluid properties from White [97] the non-dimensional radial position of transitional and fully turbulent flow have been calculated, the results are in Table 3.7. The two temperature limits were determined from the experimental work presented in Section 6.4. The lower limit is the coolant inlet temperature, while the upper limit is the highest temperature measured in the machine across all of the tests.

Table 3.7 Onset of transition and full turbulence in the air gap

Machine Speed [rpm]	Cold, T=323K r_{crit} for transition	Cold, T=323K r_{crit} fully turbulent	Hot, T=390K r_{crit} for transition	Hot, T=390K r_{crit} fully turbulent
2000	0.87	1.24	1.03	1.46
3000	0.71	1.01	0.84	1.19
4000	0.61	0.87	0.73	1.03

The results shown in Table 3.7 suggest that modelling transition cannot be ignored in the case of the 3000rpm and 4000rpm operating points, and this has been included as described in Section 3.2.4. In fact, only a small proportion of the domain can be considered fully turbulent, with the majority laminar and transitional.

Compressibility effects

The Mach number was calculated using the tip speed of the rotor to predict the maximum expected velocity in the domain:

$$Ma = \frac{\omega r}{v_{sound}} \tag{3.49}$$

It was found that at maximum rotor speed the Mach number was 0.16. It is usual to assume incompressibility for problems with a $Ma < 0.3$ [84], and therefore the fluid in the rotor-stator cavity was modelled as an incompressible ideal gas. Subsequently at the interfaces between the fluid and solid domains 'no slip' boundary conditions were prescribed along with conservative heat fluxes.

Fluid Properties

The properties of air were taken from White [97] and adjusted for temperature effects during the simulation using Sutherland's formula. Sutherland's formula for viscosity is shown below:

$$\mu = \mu_{ref}\left(\frac{T_{ref} + S}{T + S}\right)\left(\frac{T}{T_{ref}}\right)^{1.5} \tag{3.50}$$

Where S is Sutherland's constant.

3.2.5.3 Radiation

Radiative heat transfer has not been taken into account by the numerical model. An analytical approach has been used to substantiate this assumption, with radiative heat exchange between the magnets and stator, and between the end winding and casing, being estimated and shown to be small.

Radiative heat exchange between two surfaces depends on the temperature difference between the two surfaces, the view factor, and the material emissivities [89]:

$$q_{rad} = \frac{\sigma(T_1^4 - T_2^4)}{\frac{1-\epsilon_1}{\epsilon_1 A_1} + \frac{1}{F_{12}A_1} + \frac{1-\epsilon_2}{\epsilon_2 A_2}} \tag{3.51}$$

The temperatures of the magnets, stator, winding, and casing were all taken from the experimental results presented in Chapter 6. All emissivity values were taken from [98], and are presented in Table 3.8. The view factor calculated for the rotor-stator and end winding-case exchange were calculated to be 0.99 and 1 respectively using the methods described in [89] Ch. 13. The resultant heat transfer rates are presented in Table 3.9 as absolute values and as a percentage of the total magnet or winding loss at all operating points investigated. It can be seen that radiative heat exchange accounted for less than 1% of heat transfer during the experiment, therefore neglecting it in the numerical model only incurred a small error.

Table 3.8 AF PMSM material emissivities, from [97]

Component	Assumed material	Emissivity
Magnets	Nickel Plated	0.03
Stator Core	Steel, oxidised	0.79
End Winding	Copper, thick oxide layer	0.78
Casing	Aluminium 6061 'as received'	0.03

Table 3.9 Radiative heat transfer in the AF PMSM

Operating Point	Magnet-Core [W]	Proportion of total heat exchange from Magnets [%]	End Winding-Casing [W]	Proportion of total heat exchange from Winding [%]
2000rpm 40Arms	0.38	0.49	0.16	0.19
3000rpm 40Arms	0.53	0.42	0.23	0.28
4000rpm 40Arms	0.67	0.35	0.30	0.36

3.2.5.4 Mesh Study

A formal mesh study is difficult to define for such a complex domain. The approach taken here was to follow some basic meshing rules from the CFX documentation. For example, to resolve the boundary layer in the fluid near solid walls a growth rate of 1.2 was used to define element lengths, see Figure 3.22 for an example.

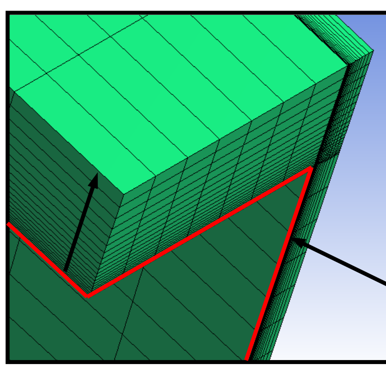

Figure 3.22 Element growth rate used to resolve the boundary layer near fluid-solid boundaries

The mesh was then solved successively, refining it until y^+ values were $\sim$1 for the turbulent simulation and predicted component temperatures stopped changing. The parameter y^+ is the non-dimensional distance of the first computational node from the wall and is defined in Equation (3.52).

$$y^+ = \frac{u_* y}{\nu} \tag{3.52}$$

Where ν is the kinematic viscosity, y is the distance from the wall of the first node, and u_* is the friction velocity defined by Equation (3.53).

$$u_* = \sqrt{\frac{\tau_w}{\rho}} \tag{3.53}$$

Where τ_w is the shear stress at the wall and ρ is the fluid density at the wall.

Figure 3.23 presents the results of the mesh study where it can be seen that grid independence was achieved. Figure 3.24 presents the final mesh used for all simulations.

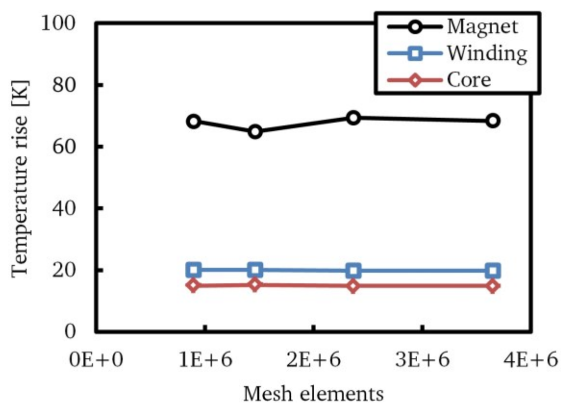

Figure 3.23 Results of the CHT mesh study, it can be seen that the solution is not sensitive to further refinement of the mesh

3.2.6 Computational Domain II

The objective of this numerical investigation was to provide the coefficient of heat transfer boundary condition in Computational Domain I which represented the interaction between the fluid in the coolant channels and the machine casing. While the results of the 'main' numerical model (the coupled EM FEA to CHT Computational Domain I) are presented in Chapter 6, the results of this analysis are presented here as it is considered part of the formulation of the 'main' model. The coolant channel geometry is shown in Figure 3.25.

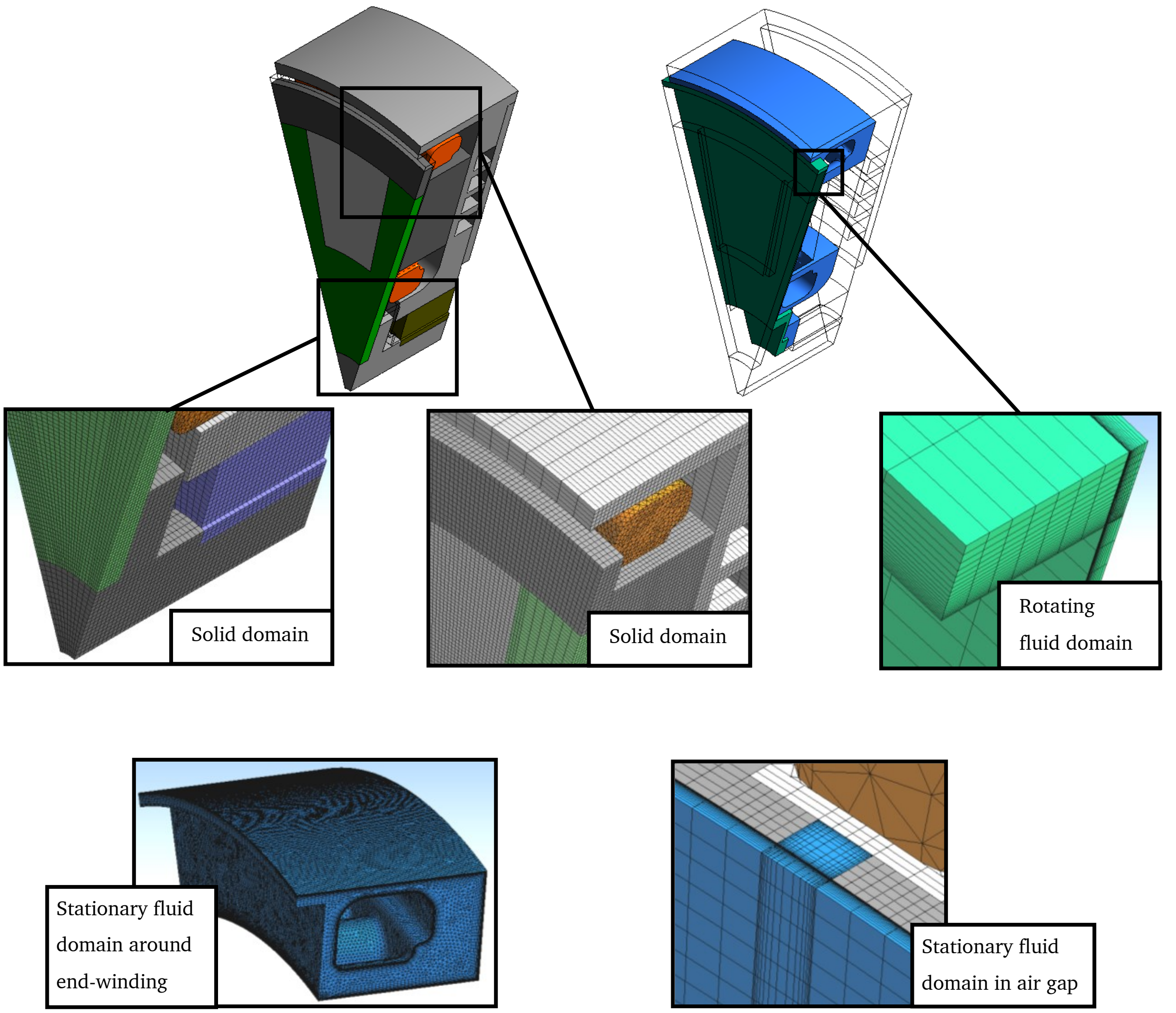

Figure 3.24 Final CHT computational mesh of the AF PMSM

The coolant jacket has two serpentine channels fed in parallel from a network of distribution channels which are located at the periphery of the machine. The serpentine channels have a corrugated cross section in order to increase the surface area of the coolant jacket and hence improve heat transfer. The channels are sealed via an aluminium plate which is fixed over their open boundary. The coolant medium is a 50/50 mix of water and glycol and the flow rate is

0.067 kg/s. Throughout this section the coefficient of convective heat transfer at the walls of the coolant channels will be defined as in (3.54).

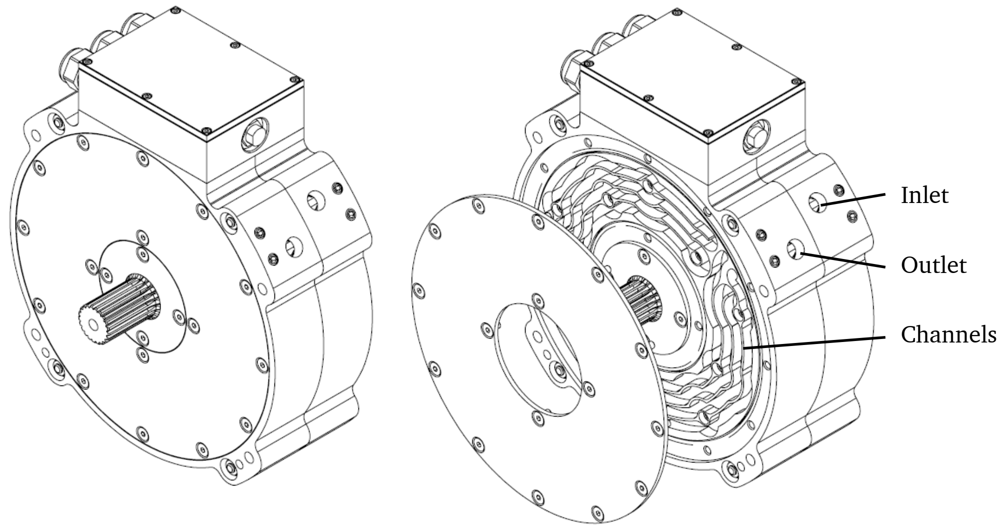

Figure 3.25 Coolant channel geometry

$$h = \frac{q''}{T_s - T_\infty} \tag{3.54}$$

Where q'' is the local heat flux at the surface, T_s is the local surface temperature, and T_∞ is average coolant temperature throughout the domain.

Material Properties

Table 3.10 gives the material properties of the coolant which were taken from the manufactures' data sheet [99]. The data sheet gives expressions which describe these properties as a function of temperature, and these were used during the conjugate heat transfer simulations to model the fluid. The material properties of the aluminium casing were identical to those of Computational Domain I.

Table 3.10 Properties of 50/50 water/glycol

Property	Value @ 323K	Value @ 342K
Density [kg/m^3]	1063	1052
Viscosity [Pa.s]	1.48e-3	8.32e-4
Specific Heat Capacity [J/kg.K]	3485	3547
Thermal Conductivity [W/m.K]	0.42	0.42

Flow Characteristics

In order to characterise the flow in the coolant channels, and hence select an approach for calculating the coefficient of convective heat transfer at the fluid-solid boundary, the Reynolds and Prandtl numbers were calculated as per:

$$Re_D = \frac{\rho \bar{V} D_h}{\mu} \tag{3.55}$$

$$Pr = \frac{\mu C_p}{k} \tag{3.56}$$

Where $\bar{V}$ and D_h were calculated from:

$$\bar{V} = \frac{\dot{m}}{\rho A} \tag{3.57}$$

$$D_h = \frac{4A}{P} \tag{3.58}$$

Where $\dot{m}$ is the mass flow rate, A is the cross sectional area of the channel, D_h is the hydraulic diameter, and P is the wetted perimeter of the channel cross section.

Values at two characteristic temperatures are shown in Table 3.11, the lower representing the conditions at the inlet of the coolant jacket and the higher representing conditions at the outlet. The outlet temperature was calculated using Equation (3.59) with a flow rate of 0.067kg/s and expected losses of 4368W estimated from the electrical machine manufacturer's efficiency map at a machine speed of 628rad/s and a machine torque of 100Nm:

$$q = \dot{m} C_p (T_o - T_i) \tag{3.59}$$

Table 3.11 Coolant channel flow characteristics

Property	Value at 323K	Value at 342K
Re_D	1937	3437
Pr	12.2	7.0

As can be seen from Table 3.11, although the Reynolds number at the inlet suggests that the flow is laminar ($Re_D < 2300$, [89] p.421), it will most likely move into a transitional flow regime at some point in the coolant jacket due to the temperature dependent material properties of the fluid. In addition to this, secondary flow structures induced by the turns in the channel geometry will modify the Reynolds number further. For these reasons calculation of the coefficient of convective heat transfer using analytical methods or empirical correlations seemed inappropriate and Ansys CFX was used to model the domain numerically. As the working fluid is a liquid compressibility effects were not modelled. Viscous dissipation was ignored in the thermal energy formulation of the fluid domain as it is usually negligible unless the flow is high sheer (lubrication applications) or compressible (high velocity gas flows).

Computational Domain and Boundary Conditions

Figure 3.26 shows the computational domain with labelled boundary conditions, which are identified in Table 3.12. As can be seen when compared with Figure 3.25 features such as screw threads and O-ring grooves have been removed in order to create a domain more suitable for the meshing procedure. The aluminium plate which seals the open boundary of the channel is connected to the heat sink via a thermal contact resistance. Explicitly modelling contact resistances is a complex task, as the resulting resistance is a function of surface finish, contact pressure, and surface hardness. Classically contact resistances are dealt with empirically, and this is the approach taken here with an equivalent air gap of 0.0023mm being used, the value of which was taken from [92].

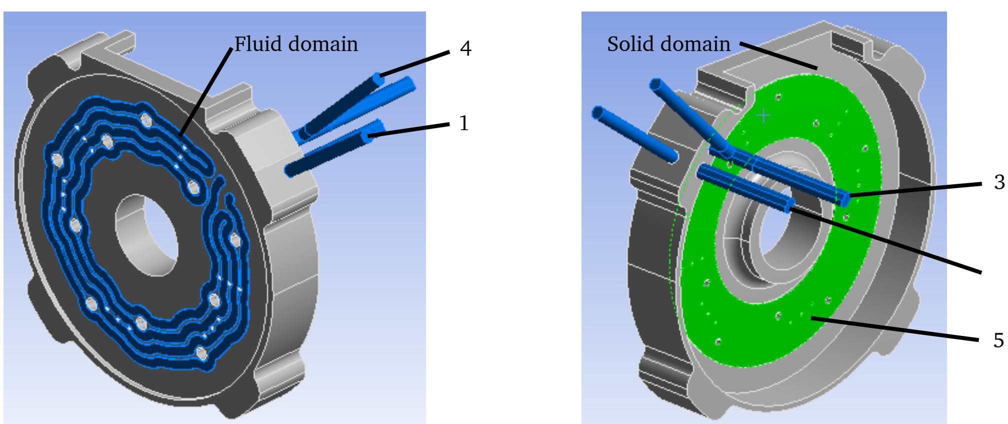

Figure 3.26 Coolant jacket computational domain

Table 3.12 Boundary conditions for computational domain II

Surface	Boundary Condition	Value
1	Mass flow in	0.067 kg/s@ 323 K
2	Mass flow out	0.034 kg/s
3	Mass flow in	0.034 kg/s@ 342 °C
4	Relative Static Pressure	0 Pa
5	Uniform heat flux	71140 W/m^2
The rest	Adiabatic	-

From the manufacturer's engineering drawings the surface roughness of the machined serpentine channel has been taken to be Ra 3.2μm, the hydraulic diameter D_h was 12.3mm. Using this to calculate the relative surface roughness, R, (Equation (3.60)), the Moody diagram in Figure 3.27 shows that the surface can be assumed to be hydrodynamically smooth, therefore no surface roughness affect has been modelled in the CHT analysis.

$$R = \frac{R_a}{D_h} \tag{3.60}$$

Mesh Study

In order to ensure the solution was independent of the numerical mesh a study was carried out on a straight piece of the corrugated channel which was modelled and solved, with appropriate boundary conditions. The mesh was successively refined until the heat transfer coefficient at the walls of the channel stopped changing according to a residual which was defined as per Equation (3.61). Figure 3.28 reports the results where number of elements in each mesh has been non-dimensionalised against the number of elements in the largest mesh.

For the final mesh, element densities were selected which corresponded to a 6% error in the heat transfer coefficient. Details of the final mesh can be seen in Table 3.13 and Figure 3.29, which shows the high level of discretisation required near the walls to resolve the flow and thermal fields.

Results

The solution predicted by the simulation is presented here briefly, with the focus being on how the results were post processed for use in Computational Domain I. Figure 3.30 shows the predicted heat transfer coefficient in a section of the domain. The values of heat transfer

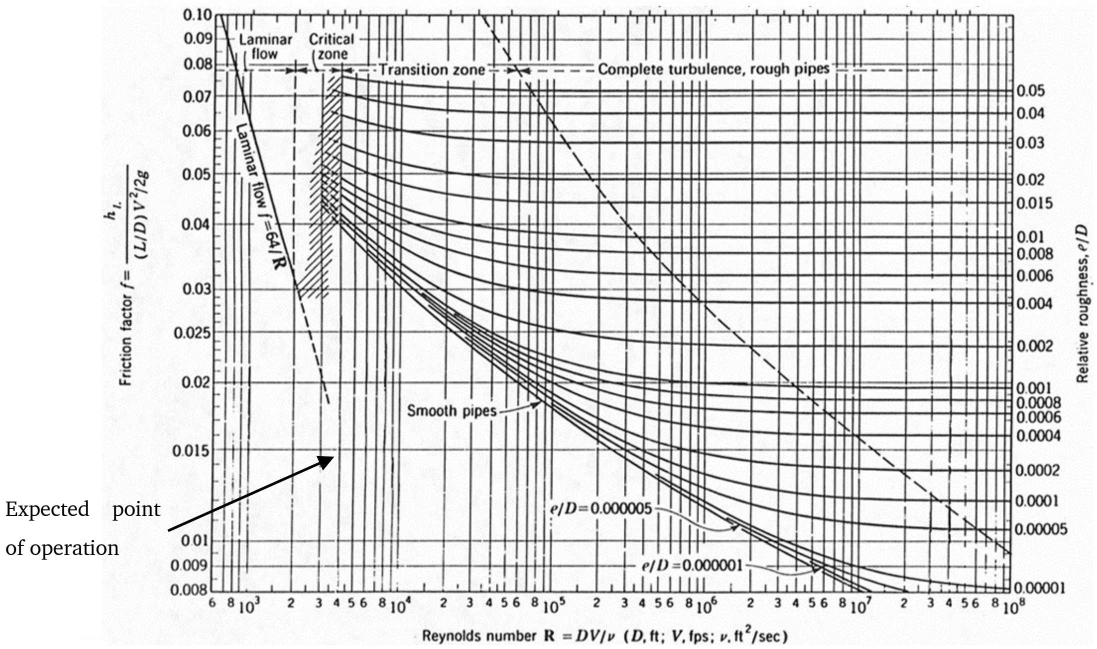

Figure 3.27 Moody diagram, from [89]

$$Residual = \sqrt{\left(\frac{\overline{h_\iota} - \overline{h_N}}{\overline{h_\iota}}\right)^2} \tag{3.61}$$

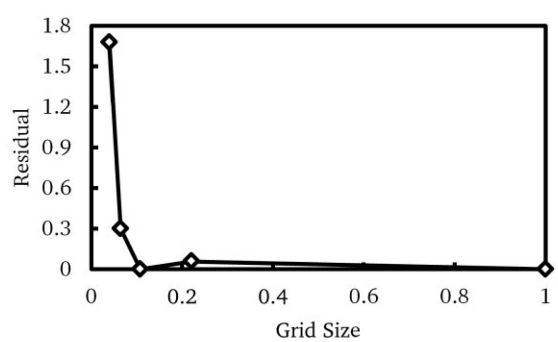

Figure 3.28 Results of the mesh study performed on the coolant channel geometry

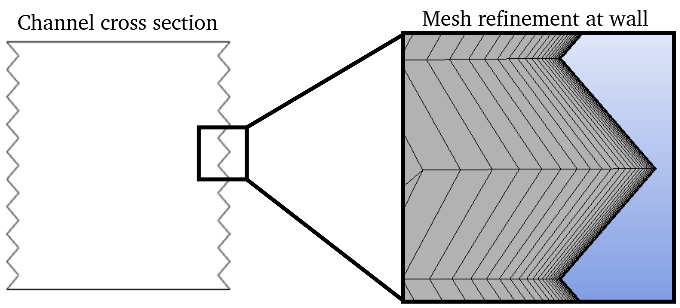

Figure 3.29 Final computational mesh for Computational Domain II

Table 3.13 Mesh details of Computational Domain II

Domain	Number of Mesh Elements
Channel	8,557,854
Inlet/Outlet	825,215
Solid	1,079,574

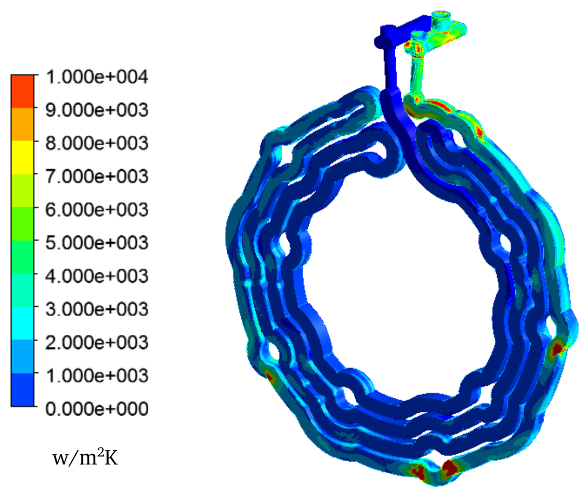

Figure 3.30 Predicted heat transfer coefficient at the fluid-solid boundary

coefficient can be seen to vary greatly. The highest values are found where the flow impinges on the wall as it is guided around a turn in the serpentine channel, and the lowest values are found in areas of separation where the boundary layer has detached from the wall.

It is instructive to look at the temperature rise in the casing, see Figure 3.31. It can be seen that the temperature rise is roughly axisymmetric, with a strong radial gradient.

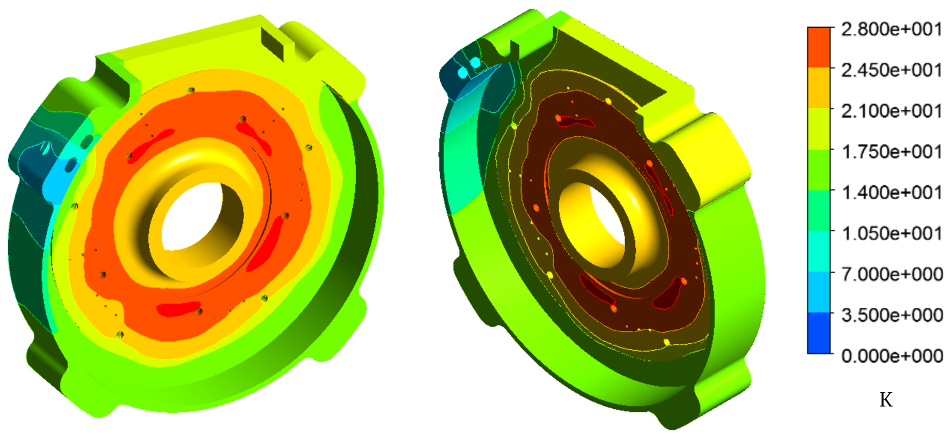

Figure 3.31 Predicted temperature rise in the casing

The effect of the coolant inlet and outlet stop the domain being truly axisymmetric, though neglecting this effect and developing an axisymmetric component appears to be a good approximation, with a huge computational saving possible for Computational Domain I.

In order to post process the CHT results the axisymmetric casing component seen in Computation Domain I is first developed from the actual geometry. The channel geometry was considered to be comprised of 4 concentric channels as shown in Figure 3.32.

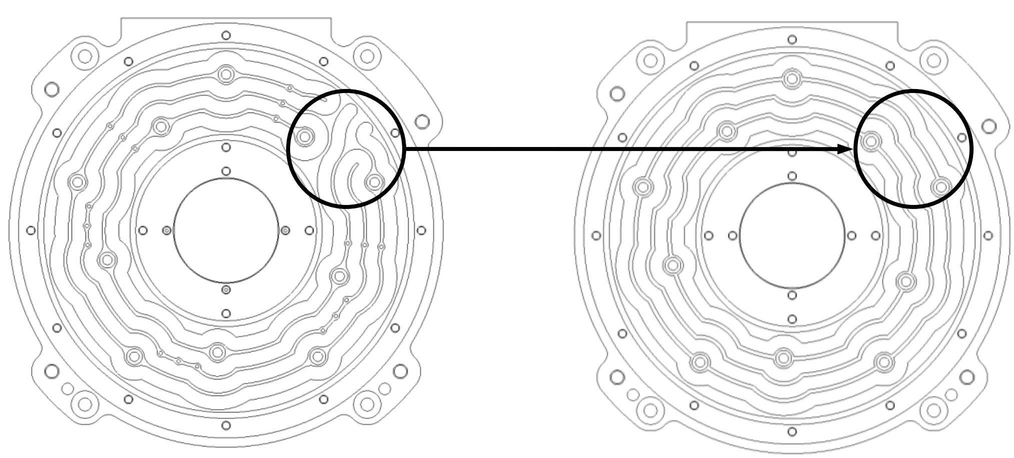

Figure 3.32 Approximation of the domain as concentric channels

The next step was to find the average radial position of each channel so that it could be represented by circular channels rather than the undulating/serpentine channel layout seen in

Figure 3.32. The average radial position of each channel was calculated using Equations (3.62) and (3.63), which refer to Figure 3.33.

$$r_3^2 = r_1^2 + r_2^2 - 2r_1r_2\cos\theta \tag{3.62}$$

$$r_{av}^2 = \frac{1}{\theta_2 - \theta_1}\int_{\theta_1}^{\theta_2} r_3^2\, d\theta \tag{3.63}$$

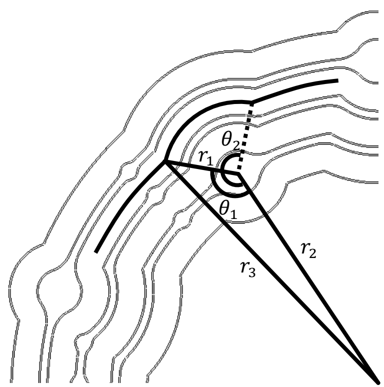

Figure 3.33 Radial position averaging of the coolant channels

The cross section of the channel was also simplified, the corrugations being removed as per Figure 3.34.

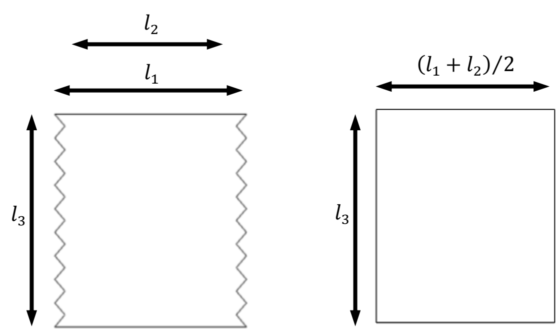

Figure 3.34 Channel cross section modification to remove corrugations

The predicted values of heat transfer coefficient were then exported from CFX. Based on their positional coordinates every element on the fluid-solid boundary was identified as belonging to one of the 4 channels, and within each channel as belonging to either the base, inner wall, outer wall, or sealing plate. See Figure 3.35.

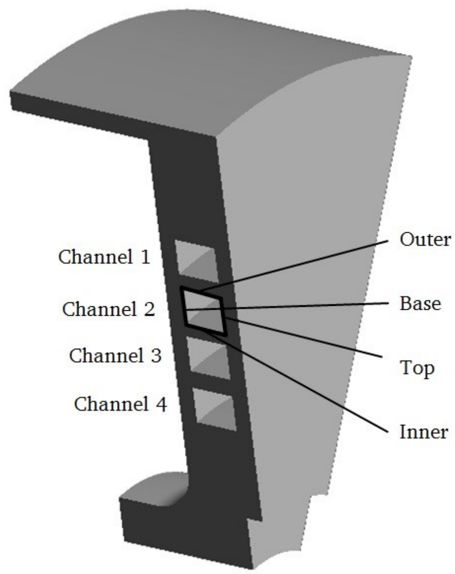

Figure 3.35 Final axisymmetric geometry of the casing

Figure 3.36 shows an example of a plot of coefficient of convective heat transfer against position at the boundaries of Channel 2. The variable z* is the non-dimensional axial position in the channel, where z*=0 is the base and z*=1 is the sealing plate. The variable r* is the non-dimensional radial position in the channel where r*=0.75 is the inner radius and r*=0.90 is the outer radius of the channel. As can be seen, no identifiable trend exists as a function of position so an average value of the coefficient of convective heat transfer was used for each wall.

As the wetted area of the axisymmetric casing is smaller per unit angle than the original geometry (due to the undulating twists and turns, as well as the corrugations, being removed) a correction factor was calculated to scale up the coefficient of convective heat transfer in order to keep the thermal conductance of each surface the same. Table 3.14 reports resulting coefficients of convective heat transfer applied to each surface of the casing component.

As a final validation of the process a steady state heat transfer analysis was carried out on the axisymmetric component in order to compare its thermal resistance with the original coolant jacket. The thermal resistance was defined as $R_{th} = (\overline{T_s} - T_\infty)/q$, where the heat q entering each domain was prescribed as a boundary condition (e.g. at surface 5 of Figure 3.26), $\overline{T_s}$ is the average temperature of surface 5 and T_∞ is the average fluid temperature. Table 3.15 compares the results and shows excellent agreement between the two models, validating the use of the axisymmetric component for use in Computational Domain I. The small discrepancy is most likely due to the inlet/outlet region of the coolant jacket being neglected during the averaging procedure; this makes sense as the axisymmetric component has a slightly higher thermal resistance.

An additional simulation was performed on the 'Full Coolant Jacket' model where the value of heat flux entering the domain (through surface 5 of Figure 3.26) was halved in order to gauge the sensitivity of the heat transfer coefficient at the walls to the temperature dependent fluid properties. The difference was seen to be small (0.5%), validating the use of the heat transfer coefficient values for differing levels of heat flux entering the domain.

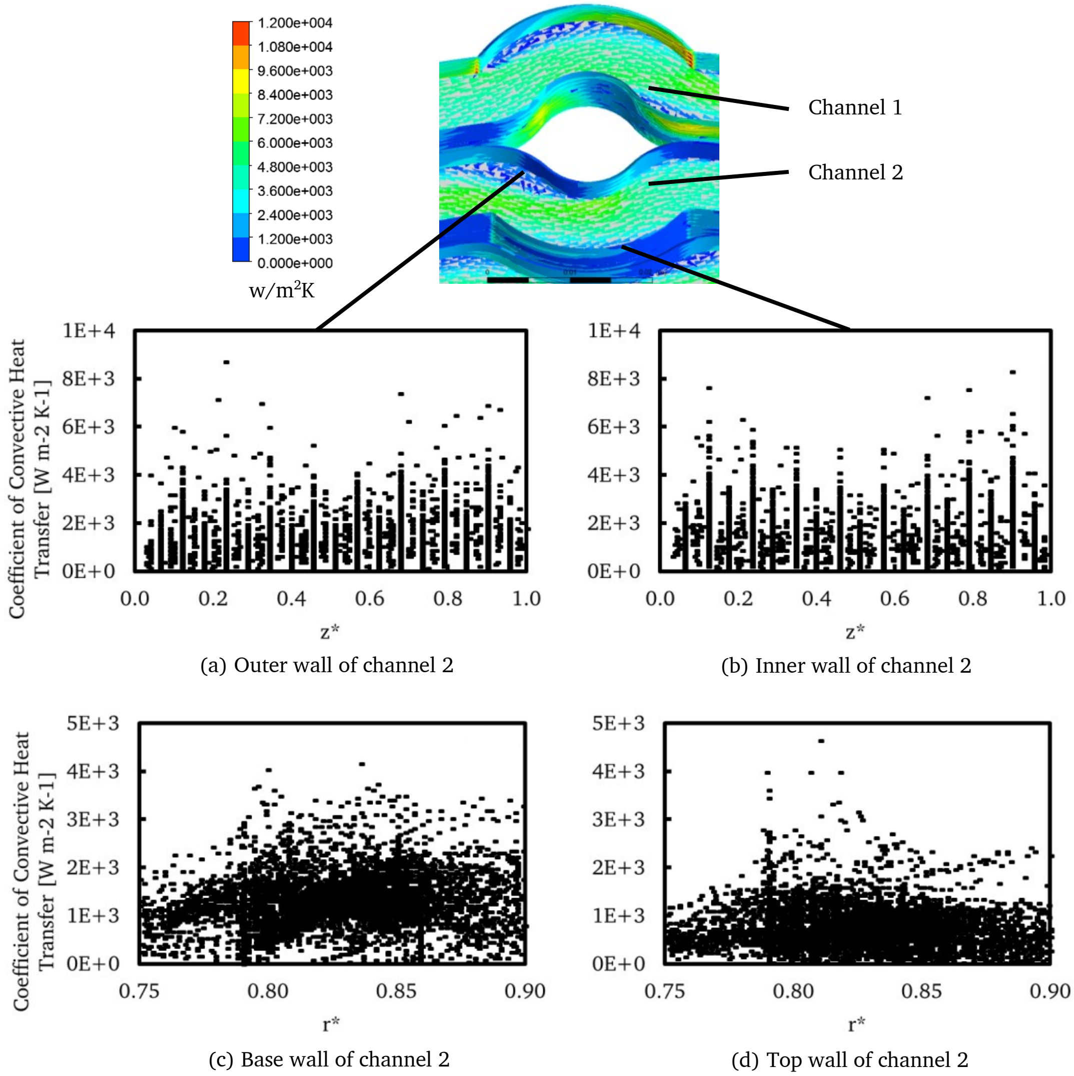

Figure 3.36 Coefficient of convective heat transfer as a function of position in Channel 2

Table 3.14 Averaged values of the coefficient of convective heat transfer in the coolant jacket

Channel	Outer [W/m^2.K]	Inner [W/m^2.K]	Base [W/m^2.K]	Top [W/m^2.K]
1	8030	6509	6248	6993
2	2787	3404	4293	2536
3	2146	3177	4254	1694
4	1468	1962	2584	1138

Table 3.15 Comparison of 'full' and axisymmetric coolant jacket thermal resistances

Model	Thermal Resistance [K W^{-1}]
Full Coolant Jacket	0.01053
Axisymmetric Coolant Jacket	0.01077

3.3 Summary

This chapter has presented the development of a numerical model which predicts the loss, flow, and temperature fields within an axial flux permanent magnet synchronous machine. The first component of the model is a transient three dimensional electromagnetic FEA which requires a phase current waveform as an input, and subsequently outputs the loss field within the magnets and stator core at every time step. The loss fields are then time averaged (the justification of this is presented in Chapter 4), while maintaining the spatial discretisation. The second component of the model takes the loss fields and uses them as source terms in a steady state CHT analysis. Additional source terms in the CHT analysis included experimental measurements of winding loss, and estimates of bearing loss. The output of the CHT analysis is a prediction of the flow and temperature fields within the electrical machine. See Figure 3.37 for an overview of the numerical model.

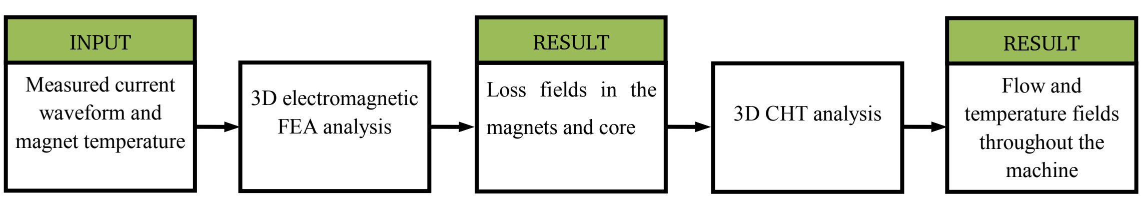

Figure 3.37 Overview of numerical multiphysics model

Chapter 4

Development of a Criterion for Assessing the Relative Importance of the Fluctuating Component of a Periodic Heat Source

This chapter proposes a criterion for assessing the relative importance of the fluctuating component of a periodic heat source on the temperature response of a device. In this work it is used to justify the method of defining the heat generation source terms in the CHT analysis from the loss profiles predicted by the electromagnetic FEA. As well as increasing the understanding of the thermal processes occurring within the PMSM, the main aim of the thesis, the criterion is a transferable contribution, applicable to any device or system with a periodic heat source.

To demonstrate the need for the justification of the procedure used to define the heat generation source terms used in the CHT analysis Figure 4.1 presents the magnet losses predicted at the

3000rpm 40A operating point (the electromagnetic FEA results are presented in full in Section 6.1.2).

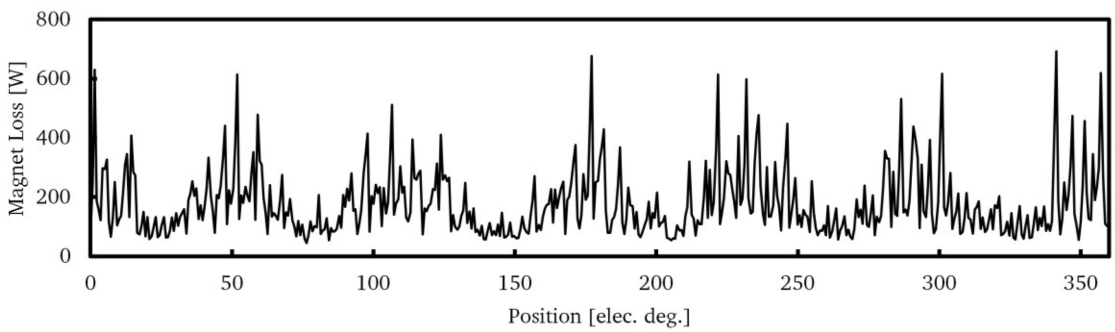

Figure 4.1 Predicted magnet losses at 3000rpm 40Arms

It can be seen that the value of loss varies greatly around its mean value. If the losses can be modelled using their time averaged values then a computational saving can be made, as the time step used to resolve the solid domain in the thermal model can be increased, reducing the number of steps necessary to reach steady state conditions. A criterion which can be used to estimate the relative importance of the fluctuating component of the heat sources is now presented. An additional use for the proposed criterion may be for the experimentalist to ascertain whether a measured temperature rise represents a mean or an instantaneous value of heat generation rate. It may also be used to justify the filter length applied to a transient temperature reading.

4.1 Criterion Derivation

To derive the criterion a typical thermal network element [89] (Figure 4.2) is considered:

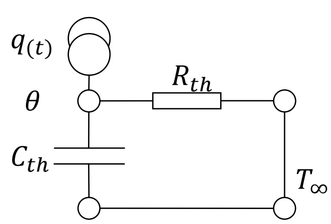

Figure 4.2 A thermal network element

The thermal network element consists of a thermal resistance R_{th}:

$$R_{th} = \frac{l}{kA} + \frac{1}{hA} \tag{4.1}$$

Where l is a length scale defined by $l = V/A$, k is the thermal conductivity of the material, A is the surface area, and h is the coefficient of heat transfer at the boundary of the element.

A thermal capacitance C_{th}:

$$C_{th} = \rho C_p V \tag{4.2}$$

Where ρ is the density of the material, C_p is the heat capacity of the material, and V is the volume of the element.

The temperature difference θ is defined as the difference between the point of interest and the outside temperature T_∞. A periodic heat source $q(t)$ acts as a forcing function on the element and is considered as being composed of mean and fluctuating components $\bar{q}$ and q' respectively, as shown in Equation (4.3):

$$q(t) = \bar{q} + q' \tag{4.3}$$

The temperature response of the thermal element to this heat source is shown in Figure 4.3.

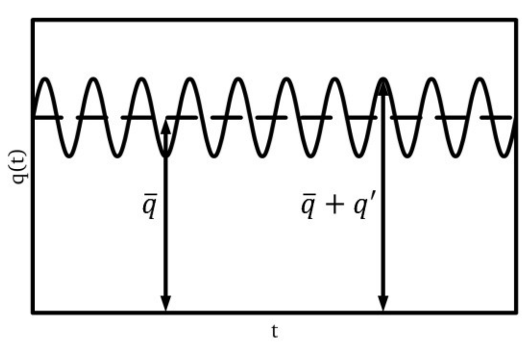

(a) Periodic heat source

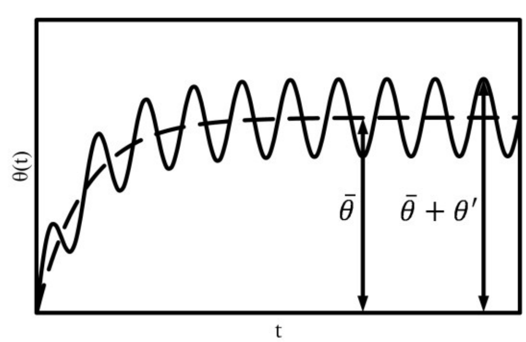

(b) Temperature response

Figure 4.3 Temperature response of a thermal element with a periodic heat source

By assuming temperature independent material properties the temperature response can also be decomposed into mean and fluctuating components $\bar{\theta}$ and θ' respectively. The steady state mean component is given by:

$$\bar{\theta} = \bar{q}R_{th} \tag{4.4}$$

While the steady state fluctuating component is given by:

$$C_{th}\frac{d\theta'}{dt} + \frac{1}{R_{th}}\theta' = q' \sin \omega t \tag{4.5}$$

Where ω is the angular frequency of the fluctuating component of the heat source and t is the time.

The solution of Equation (4.5) is given by:

$$\theta' = \frac{q'}{C_{th}\left(\frac{1}{\tau}^2 + \omega^2\right)}\left(\frac{1}{\tau}\sin \omega t - \omega \cos \omega t\right) \tag{4.6}$$

Where $\tau = R_{th}C_{th}$ is the thermal time constant.

Equation (4.6) is at a maximum when:

$$\frac{d}{dt}\left(\frac{1}{\tau}\sin \omega t - \omega \cos \omega t\right) = 0 \tag{4.7}$$

Solving Equation (4.7) for t and substituting back into Equation (4.6) yields:

$$\theta'_{MAX} = \frac{q'}{C_{th}\sqrt{\frac{1}{\tau}^2 + \omega^2}} \tag{4.8}$$

Where θ'_{MAX} is the maximum difference between the fluctuating and steady temperature components. The periodic heat source criterion υ is then defined by Equation (4.9) which can be seen to be the ratio between Equations (4.8) and (4.4).

$$\upsilon = \frac{q^*}{\sqrt{1 + \omega^{*2}}} \tag{4.9}$$

Where the non-dimensional heat source is defined as $q^* = q'/\bar{q}$, and the non-dimensional angular frequency as $\omega^* = \omega\tau$.

The criterion is simply the ratio between the maximum temperature rise above the mean, and the mean temperature rise above the outside temperature; for example $\upsilon = 0.1$ is interpreted as 'the fluctuating temperature component is 10% of the magnitude of the steady component' while $\upsilon = 1$ is interpreted as 'the fluctuating temperature component is the same magnitude as the steady component'.

The non-dimensional angular velocity ω^* is similar to the inverse of the Fourier number, Equation (4.10) [89], in fact if the variable h in R_{th} was neglected they would be identical. It has been included here in order to allow the criterion to account for problems with different Biot numbers, where the Biot number is defined by Equation (4.11) [89].

$$Fo = \frac{kt}{\rho C_p l^2} \tag{4.10}$$

$$Bi = \frac{hl}{k} \tag{4.11}$$

Figure 4.4 shows υ as a function of ω^*, where each plot line represents a different value of q^*. It can be seen that when $\omega^* < 1$ the criterion value tends to the same value as q^*, this indicates that the thermal capacitance of the element saturates within each heat source fluctuation and the temperature response will be 'as unsteady as the heat source'. When $\omega^* > 1$ the criterion value is attenuated rapidly, indicating that the thermal capacitance is smoothing the temperature response to the heat source fluctuation.

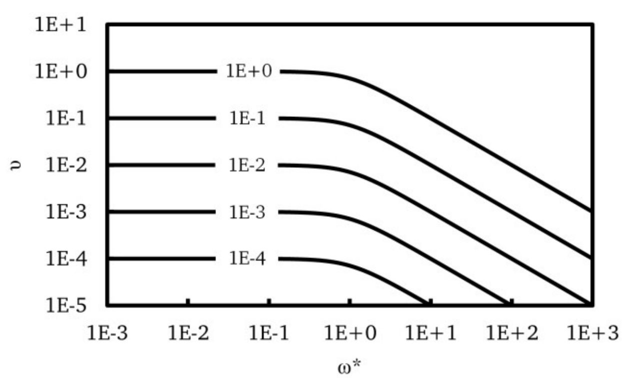

Figure 4.4 Periodic heat source criterion for different values of q^*

4.2 Non Sinusoidal Periodic Heat Sources

An attempt was made to extend the criterion to take into account heat sources of any periodic shape. A Fourier series expansion of the heat source was considered, as shown in Equation (4.12).

$$q_t = \bar{q} + \sum_{n=1}^{\infty} [q'_{an} \cos(n\omega t) + q'_{bn} \sin(n\omega t)] \tag{4.12}$$

Applying this heat source to the thermal element shown in Figure 4.2 and considering the mean and fluctuating components separately yields the generalised version of the criterion, shown in Equation (4.13). Again, this is the ratio between the maximum temperature rise above the mean, and the mean temperature rise above ambient.

$$\begin{aligned} \upsilon = max \Bigg\{ \sum_{n=1}^{\infty} \Bigg[& \left(\frac{q^*_{a_n}(1/\tau)}{((1/\tau)^2 + n\omega^2)} [(1/\tau)\cos(n\omega t) + n\omega \sin(n\omega t)] \right) \\ & + \left(\frac{q^*_{b_n}(1/\tau)}{((1/\tau)^2 + n\omega^2)} [(1/\tau)\sin(n\omega t) - n\omega \cos(n\omega t)] \right) \Bigg] \Bigg\} \end{aligned} \tag{4.13}$$

Where $q^*_{a_n} = \frac{q'_{a_n}}{\bar{q}}$, $q^*_{b_n} = \frac{q'_{b_n}}{\bar{q}}$ and q'_{a_n} and q'_{b_n} are the magnitudes of the Fourier components.

No analytical way of determining the maximum of this expression could be found, as there is no way of determining whether a root represents a global or local maxima or minima. Computationally efficient methods exist for determining global maxima/minima, as presented by Hauptman et al. [100]. However, in this author's opinion, within the context of this analysis anything other than an analytical solution renders the criterion less useful than determining the mean and fluctuating temperature components by time stepping the original differential equation to a steady periodic solution. It is therefore proposed that when heat sources are non-sinusoidal a characteristic fluctuating component and frequency are identified and input into Equation (4.9). This enables a quick assessment of the relative importance of the fluctuating component of a periodic heat source to be made, from which further analysis may be carried out if 'intermediate' values of the criterion are predicted. A method for determining the characteristic q' and ω parameters is presented within the validation case study in the following section.

4.3 Validation of Criterion

In order to validate the proposed criterion the EM FEA model described in Chapter 3 was used to predict the transient heat sources in the magnet, core, and winding. These predictions were made before the experimental measurements of current waveform were taken, therefore the windings of the EM FEA model were excited by a pulse width modulated (PWM) voltage waveform, generated by the intersective method. The FEA predictions of BEMF, synchronous inductance, and experimental measurements of resistance (see Chapter 6) were all used to solve the phasor diagram of the machine (see Figure 1.12) and hence predict the target voltage waveform to be approximated by the PWM waveform for 50Nm at 8000rpm. Figure 4.5 shows the results from the EM FEA, the loss profiles vary greatly around their mean values, though over very small time scales.

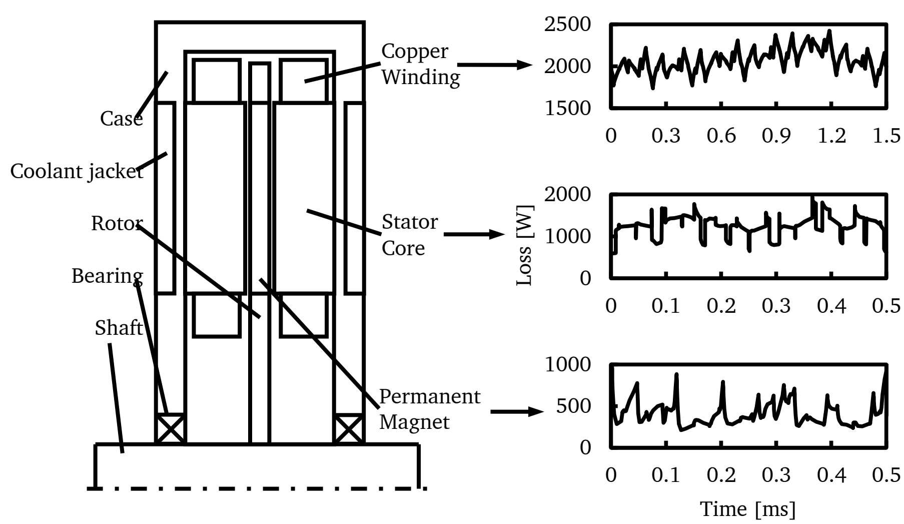

Figure 4.5 Prediction of losses generated in the AF PMSM at 8000rpm 50Nm

For clarity the calculation performed on the magnet component is now presented as a worked example. It is first assumed that the predominant heat flux path flows axially out of the domain into the air gap, the value of thermal conductivity is therefore taken as $k = k_z = 6.16\, Wm^{-1}K^{-1}$. The value of the convective heat transfer coefficient h was calculated to be $274\, Wm^{-2}K^{-1}$ from the correlation proposed by Boutarfa & Harmand [96] for turbulent flow in a stator-disc system:

$$Nu = 0.044Re^{0.75} \tag{4.14}$$

Where the Nusselt number Nu is defined as [89],

$$Nu = \frac{hr}{k_{air}} \tag{4.15}$$

While Equation (4.14) is only valid for a through flow topology machine it appears to be the best approximation available. The length scale of the magnet is calculated as the ratio between its total volume and the surface area of the convective heat transfer boundary. The characteristic R_{th}, C_{th}, and τ values are presented in Table 4.1.

Table 4.1 Characteristic R_{th}, C_{th}, and τ values for the permanent magnet

Parameter	Value
R_{th} [K/W]	0.0984
C_{th} [J/K]	710.0
τ [s]	69.86

The characteristic values of q' and ω were determined as shown in Figure 4.6. Applying the criterion (Equation (4.13)) to this parameter set gives a value for υ of 5.87e-7, indicating that the fluctuating temperature component is negligible when compared with the mean one.

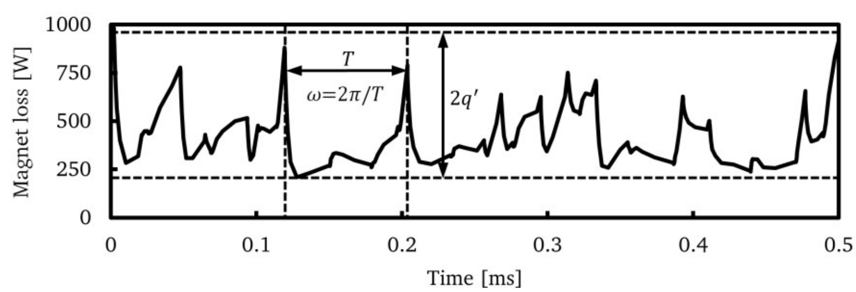

Figure 4.6 Characteristic values of q' and ω

For comparison the CHT model presented in Section 3.2 was modified and used to model the temperature response of the components to the heat sources explicitly, allowing numerical values of υ to be calculated from spatially averaged values of component temperatures. Modifications to the model included replacing the fluid domain with convective heat transfer values on solid surfaces taken from correlations proposed by Boutarfa et al. [96] and Howey et al. [61] and solving the problem transiently rather than in the steady state. It should be noted that it is a set of coupled partial differential equations which govern heat transfer in this system. This is a good test for the criterion as it is ignorant of the coupling effect, and treats each component as a single isolated lump. Another challenge for the criterion is that each of the heat generating components has an anisotropic thermal conductivity; as demonstrated in the worked example for the permanent magnet component the value taken was that in the predominant direction of the heat flux. Table 4.2 presents the results of both the criterion and the numerical study and it can be seen that the criterion has predicted the amount of unsteadiness in the temperature response of each component reasonably well, despite the complex nature of the thermal system. The accuracy is certainly fit for purpose, it allows the analyst to say with confidence that the temperature response of each heat generating component could, in this case, be accurately modelled using just the mean value of the heat source. It also allows the experimentalist to determine that the measured temperature rise in a heat generating component in this system represents the mean value of the heat source, rather than the instantaneous value.

Table 4.2 Comparison between criterion and numerical results

Component	Criterion υ	Numerical υ
Magnet	1.79e-7	5.09e-7
Stator Core	2.62e-7	1.02e-7
Copper Winding	2.05e-7	1.66e-7

To further validate the use of the criterion it has been used to investigate the thermal response of the electrical machine when operated on a duty cycle; Figure 4.7 presents the nomenclature used in this section when referring to duty cycles. The results of this analysis allow the analyst charged with modelling thermal performance over a range of duty cycles to identify which analyses must be transient, in order to determine peaks in temperature response, and which may be modelled accurately by a steady state analysis, as the peaks in temperature response are filtered out. An illustrative example is shown in Figure 4.8 and Figure 4.9 where the thermal response of two different devices (one with a ‘long’ time constant and one with a ‘short’ time constant) is shown. In Figure 4.8 it can be seen that a relatively accurate temperature response can be modelled while just considering the mean component of the transient heat source. Figure 4.9 shows the opposite where the ‘short’ time constant of the device means that the heat source must be modelled as a function of time.

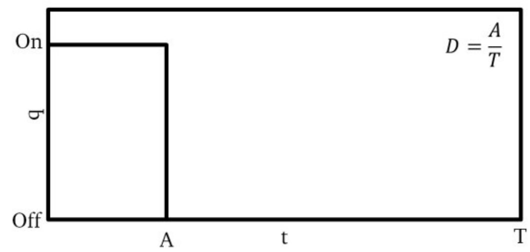

Figure 4.7 Nomenclature used to define a duty cycle

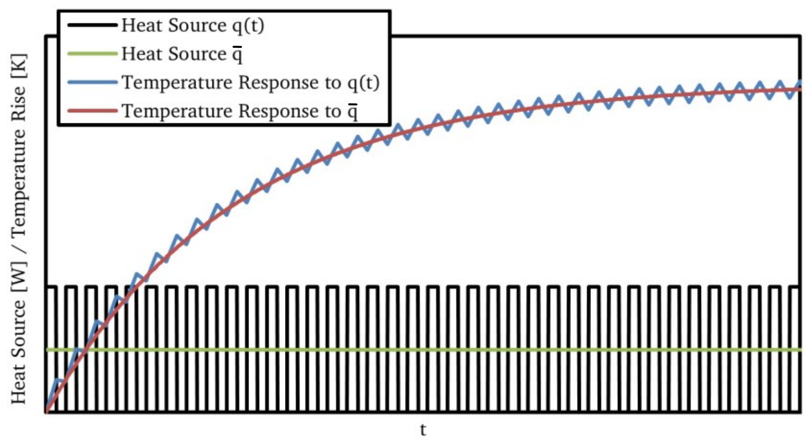

Figure 4.8 Transient temperature response to a duty cycle: Long time constant

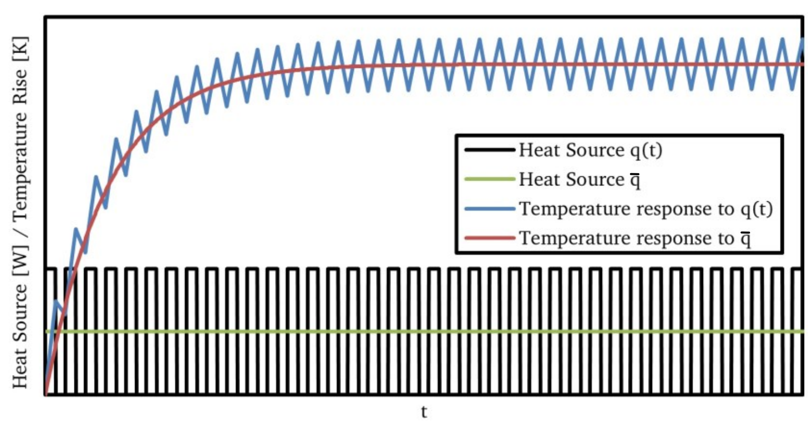

Figure 4.9 Transient temperature response to a duty cycle: Short time constant

In the 'on' state the machine is at the operating point previously investigated (50Nm, 8000rpm), and as shown the heat sources can be modelled by their mean values. In this case the selection of the fluctuating component of the heat source is made by considering the Fourier series representation of a duty cycle:

$$q_t = \frac{qA}{T} + \sum_{n=1}^{\infty} \frac{2q}{n\pi} \sin\left(\frac{\pi n A}{T}\right) \cos\left(\frac{2\pi n t}{T}\right) \tag{4.16}$$

The magnitude of each harmonic of the series is seen to be proportional to $1/n$, the most important component in the series is therefore the first one, which is seen to have the lowest frequency and greatest magnitude. It is the most likely to induce a transient temperature response. The magnitude and frequency of the first harmonic were therefore used to define q^*.

Using the same component values of τ as before and applying Equation (4.9), the criterion has been calculated over a range of frequencies for three duty cycles: $D = 0.25, 0.50, 0.75$. Figure 4.10 compares the criterion values with numerical results from the finite volume model.

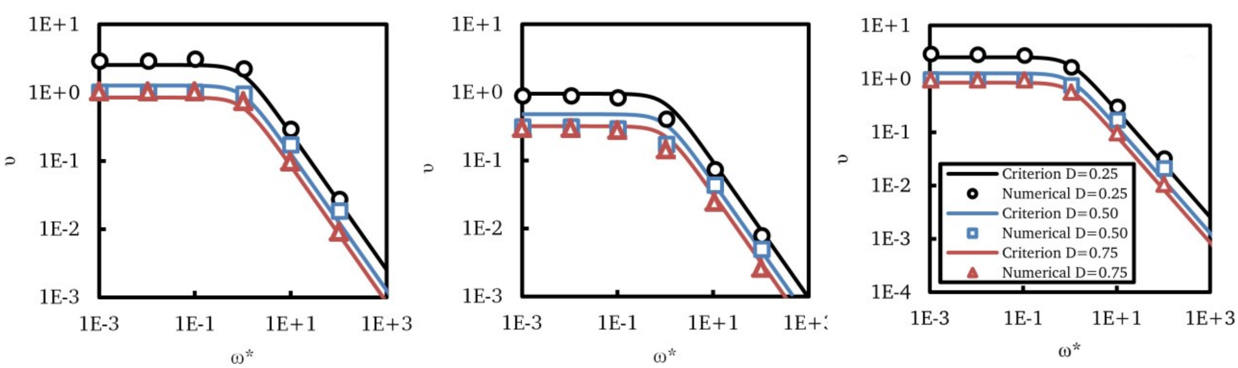

(a) Magnet (b) Core (c) Winding

Figure 4.10: Comparison between criterion and numerical values in the magnet, core, and winding over a range of duty cycles

Good agreement between the criterion and the numerical results can be seen for all components across the range investigated. The causes of the error in the criterion value can be identified by consideration of the assumptions made in the criterion's derivation, and in the definition of the fluctuating component of the heat source. As previously stated the criterion neglects anisotropic material properties, coupling effects due to neighbouring components and any 3D effects (the derivation assumed a lumped element). All of these effects were of course included in the numerical analysis, along with an accurate representation of the heat source (i.e. it was modelled as a pulse train rather than by the first harmonic only).

4.4 Summary

This chapter has presented the derivation and validation of a criterion which can be used to assess the relative importance of the fluctuating component of a periodic heat source. Validation of the proposed method included comparison of its predicted values to the results of a numerical thermal analysis which modelled the transient thermal response of all the heat generating components in the AF PMSM explicitly. The validation was performed across a wide range of time and magnitude scales. The criterion has been shown to be quick and easy to implement and give fit for purpose estimates of the magnitude of an unsteady temperature response: A valuable insight into the nature of any thermal system.

The criterion is used in this work to show that the predicted loss fields in the electrical machine can be accurately modelled using their time averaged values in the CHT analysis. This result is presented immediately after the predicted loss fields are presented in Section 6.2. However the contribution of this chapter is wider than the application within which it has been derived and validated. The criterion allows:

- The analyst to make a decision about whether to model a periodic heat source by its mean value or whether to model it as a function of time
- The experimentalist to determine whether a measured temperature response corresponds to a mean or an instantaneous heat generation rate
- The experimentalist to determine which frequencies can be filtered out of a transient temperature measurement without loss of fidelity

Chapter 5

Experimental Measurements in a Totally Enclosed Axial Flux Permanent Magnet Synchronous Machine

This chapter describes the experimental facility, prototype instrumentation, and experimental methods used to provide realistic boundary conditions for the numerical model, as well as providing empirical validation of its results. Included are many standard methods which will be familiar to the experienced reader along with a novel method used to measure magnet losses, which is one of a number of measures used to validate the EM FEA component of the numerical model. The experimental results are presented in Chapter 6 along with a discussion and comparison to the numerical results.

The magnet loss measurement technique is a key transferrable contribution of the thesis, the need for a quick practical method of measuring these losses was identified during the literature review of Chapter 2.

5.1 Experimental Facility

The experimental facility located at Evo Electric Ltd. was used to execute the methods presented in this section; details are shown in Figure 5.1 and Figure 5.2. Both inverters are connected to the same DC bus which is energised by an EA-PS 8500-90 switch mode DC power supply (voltage and current stability <0.05% and <0.15% respectively) configured to provide a constant voltage. On the motor side a KEB F26 (an IGBT based industrial sine wave drive which uses field oriented control), configured in current control takes power from the DC bus, converts it into 3-phase AC power and drives the motor. The mechanical power produced by the motor is converted back into electrical power by the generator which is controlled by another KEB F26 inverter configured in speed control. This inverter converts the AC power back into DC and feeds it into the DC bus, the DC power supply is therefore only required to produce enough power to make up for the losses in the system. Both inverters require rotor position feedback from the electrical machines which was provided by LTN RE-15 resolvers. N.B. The motor is the machine under test in the present work.

Measurements of voltage, current, frequency and power were taken using a Newton's 4th Ltd. PPA1530 power analyser on the DC bus while a Newton's 4th Ltd. PPA5530 was used to take measurements on each phase of the machine. Both power analysers used external shunts (HF500, also provided by Newton's 4th Ltd.) to measure current, while voltage was sensed internally. Voltage and current waveforms were measured using a LeCroy WaveRunner 64Xi equipped with PP008 and CP500 voltage and current probes respectively. Mechanical torque was measured using a Model 615 load cell from Tedea Huntleigh which reacted against the generator by means of a gimbal. The load cell signal was amplified and subsequently measured using a National Instruments Analogue Input module (NI9205). In order to filter out electrical noise, mechanical vibration, and ripple torque the reading was time averaged in Labview using Evo Electric Ltd.'s measurement studio.

5.2 Prototype Instrumentation

This section describes the instrumentation designed into the prototype and some of the techniques used to implement the manufacture of the design which the author feels are valuable and worthy of sharing.

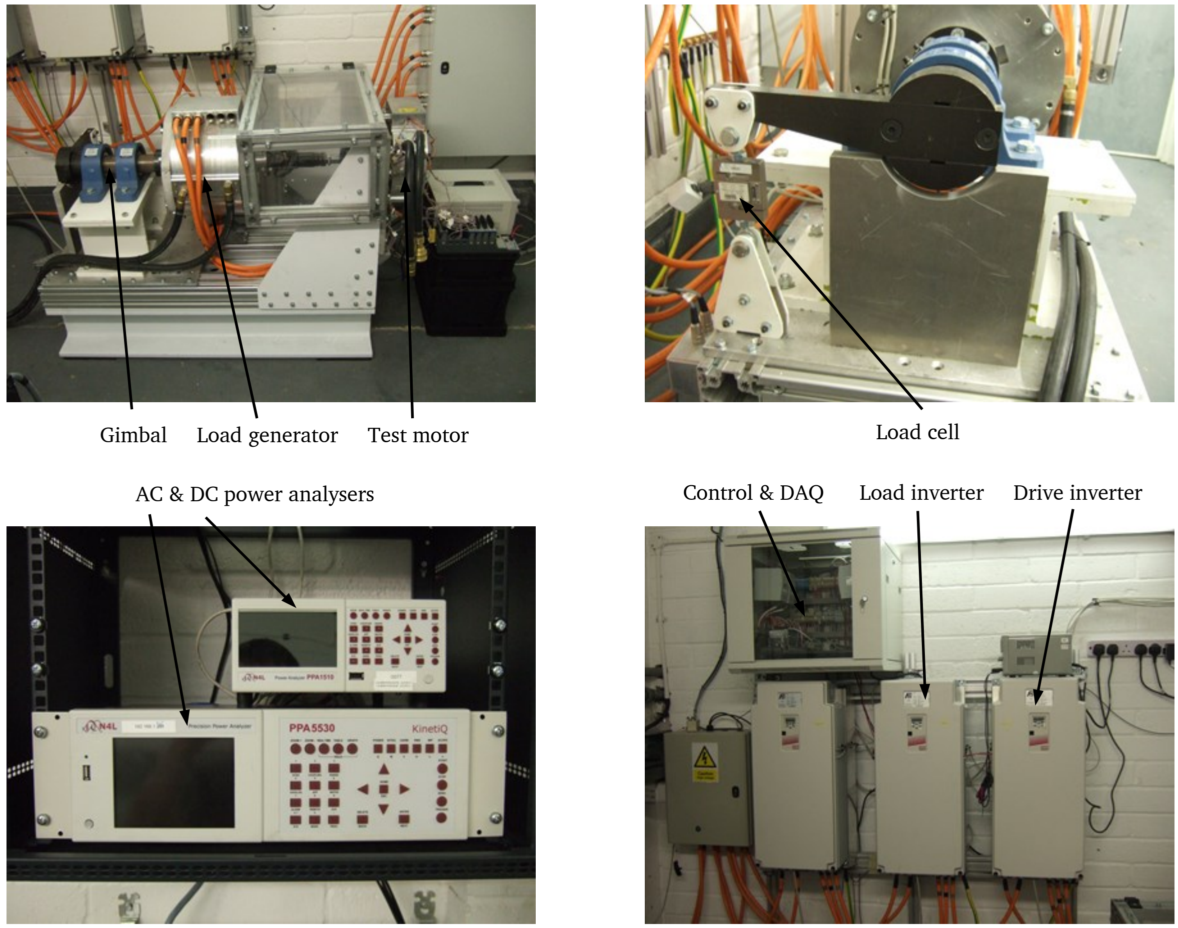

Figure 5.1 Major components of the experimental facility at Evo Electric Ltd.

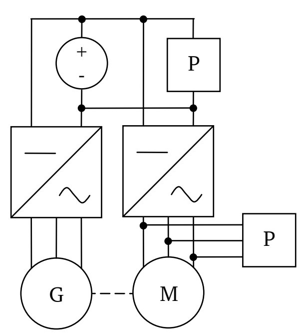

Figure 5.2 Schematic of the experimental facility at Evo Electric Ltd. P denotes a power analyser, G a generator, M a motor, and ---- a mechanical connection.

5.2.1 Winding, Core & Casing Temperature

During the manufacture of each stator T-type thermocouples were wound into the copper winding at the inner and outer end winding as well as the centre of the slot at the average stator core radius. These three sensor positions were repeated at two additional circumferential locations. Being a double layer winding, the thermocouples could be fixed into position by adhering them to the insulation sheet which separated the two winding layers.

Axial holes were drilled into both stator cores at the average radius to three different depths, these three sensor positions were repeated at two additional circumferential locations. T-type thermocouples were fixed to the bottom of each hole using a two part epoxy resin. Bosses were designed into the machine casing to allow the thermocouples to be routed out through the coolant jacket (see Figure 5.3).

Radial holes were drilled into the periphery of the machine casing at three circumferential locations and T-type thermocouples were fixed into these using a two part epoxy resin. Two additional thermocouples were fixed to the bottom of the threaded holes used to fix the cap which constrains the bearing. These were routed out using specially machined screws with axial holes drilled down their centre, see Figure 5.4. The thermocouples were read using a National Instruments CompactRio system equipped with NI9213 and NI9211 modules. Figure 5.5 summarises the location of each thermocouple.

5.2.2 Static Pressure in the Air Gap

Wall taps were used to measure the static pressure on the face of the stator in the air gap. The taps were fabricated in both stator cores using electrical discharge machining to the dimensions shown in Figure 5.6, these dimensions follow the guidelines given in [101] p.340. Traditional drilling techniques were trialled for this process; however it was found that because the operation had to be performed on the core before it was wound and impregnated the laminations flared open when the drill head broke through the surface of the core. The wall taps were positioned at three radial locations and repeated at three circumferential locations on both stators. Bosses were designed into the machine casing in order to route the tapings through the coolant jacket, see Figure 5.7. Static pressures were read using an FC016 Digital Manometer from Furness Controls.

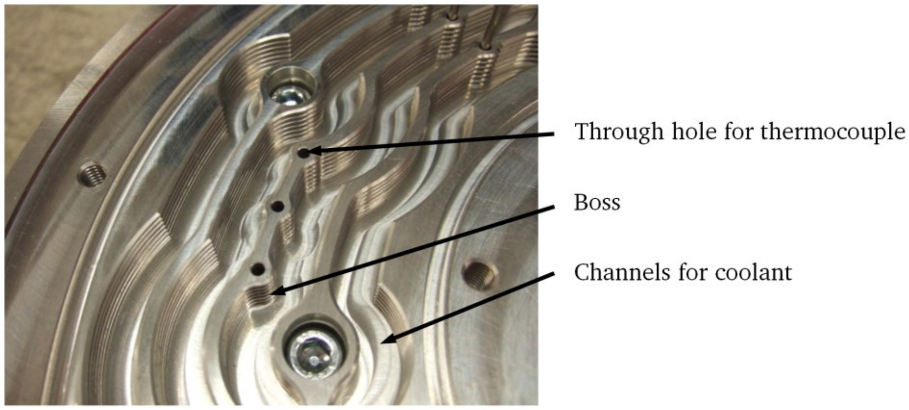

Figure 5.3 Bosses in casing to allow thermocouples to be routed through the coolant jacket

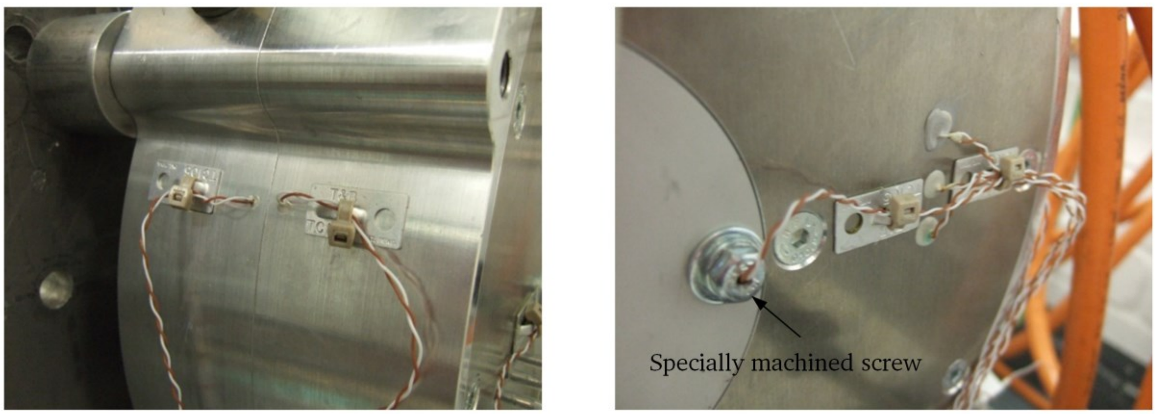

Figure 5.4 Thermocouples in the outer and inner casing

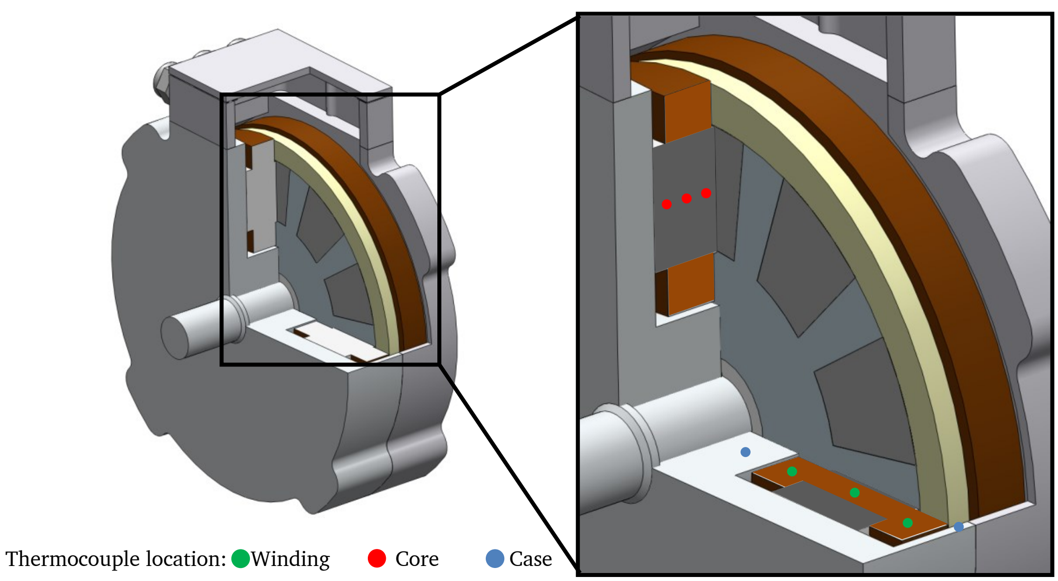

Figure 5.5 Summary of thermocouple locations in the prototype AF PMSM

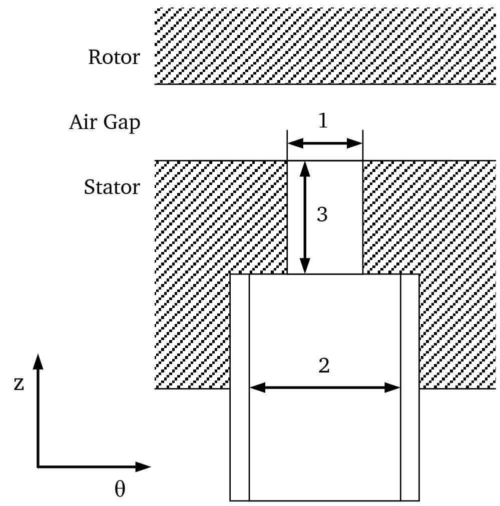

Figure 5.6 Static pressure wall tap geometry, dimensions in mm

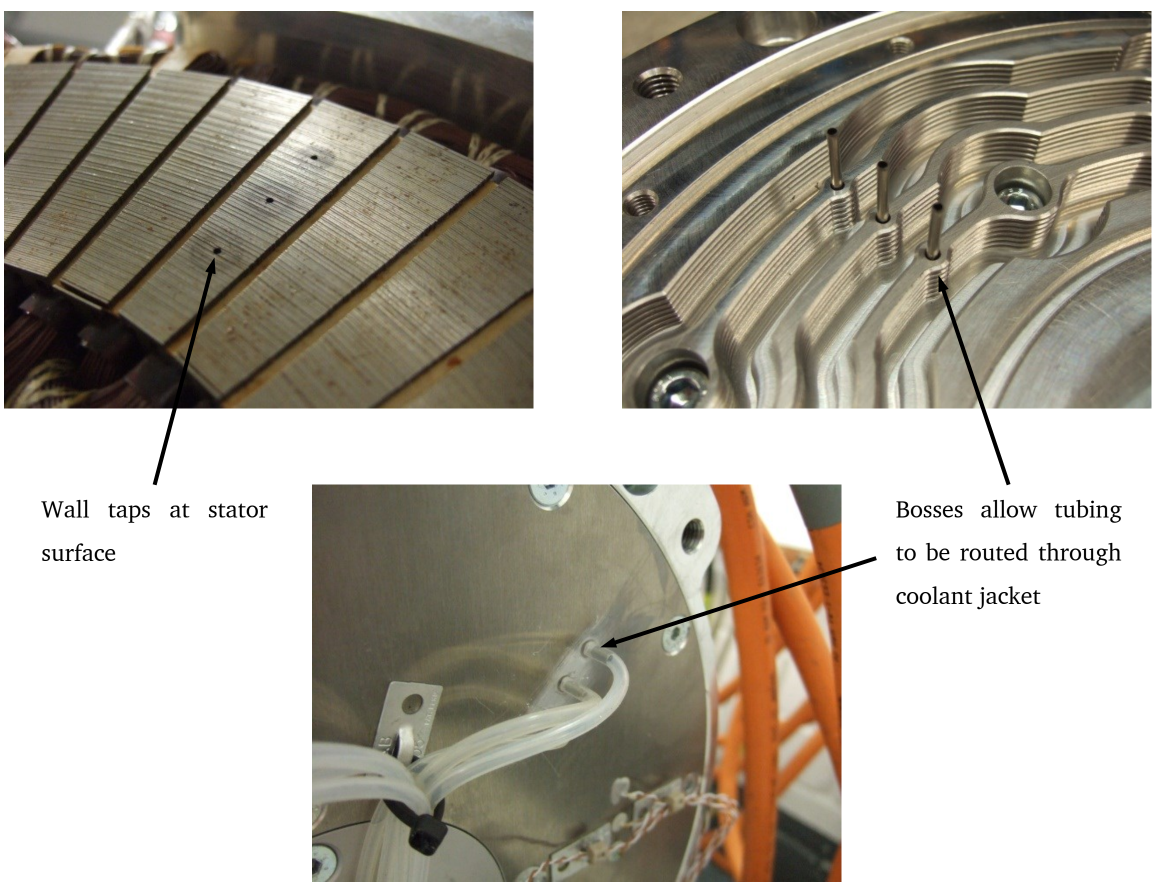

Figure 5.7 Static pressure tapings in the stator core

5.3 Experimental Methods

This section presents the experimental methods used to provide boundary conditions for, and validate, the numerical model.

5.3.1 Magnet Temperature

The measurement of magnet temperature is used in a variety of the following methods. The method is therefore presented here, while explanation of its importance is presented with the overriding method.

Magnet temperature was determined by measuring the voltage constant of the machine, see Equation (5.1). Due to the temperature dependent flux production of the permanent magnets, the flux linking the stator coils is temperature dependent. Therefore the voltage induced for any rotational speed is temperature dependent.

$$k_e(T_m) = \frac{e(T_m)}{\omega} \tag{5.1}$$

In order to determine the functional relationship between voltage constant and magnet temperature, an access window was drilled through the stator core so that a thermocouple probe could be used to take the surface temperature of the magnets. The thermocouple probe was read by a National Instruments thermocouple input module (NI 9213).

The machine was thermally soaked to a number of steady state temperatures in a laboratory oven; Figure 5.8 shows the uniformity of the temperature profile within the machine during calibration. Uniformity is good, with the only significant deviation seen at the outer periphery of the front casing, which is thought to be due to its proximity to the heater of the oven. The uniformity of the stator core temperatures, and their agreement with the rotor temperature reading, is good evidence that the rotor temperature was uniform, and the deviation at the case did not permeate into the internals of the machine.

At each discrete temperature point magnet temperature was measured along with voltage constant using a LeCroy WaveRunner 64-Xi Oscilloscope, while the machine was driven by a small induction motor, see Figure 5.9. Figure 5.10 shows the relationship established for magnet temperature rise as a function of change in voltage constant.

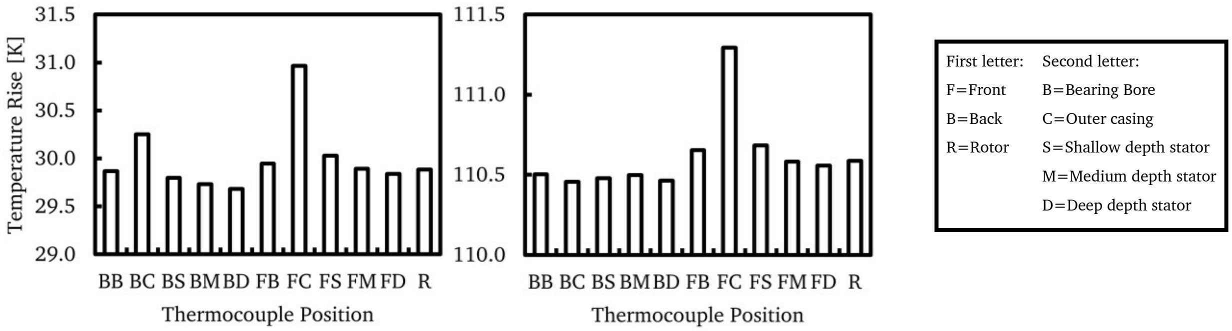

Figure 5.8 Uniformity of machine temperature at two different points during magnet temperature calibration

(a) Access window for surface temperature measurement of magnet

(b) Magnet temperature calibration rig in laboratory oven

Figure 5.9 Access window for magnet surface temperature measurement and calibration rig in laboratory oven

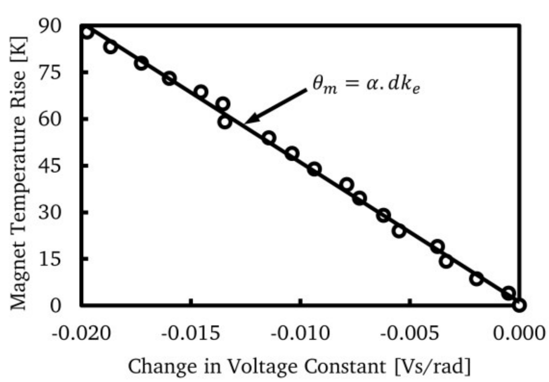

Figure 5.10 Relationship between voltage constant and magnet temperature, valid between 42 and 130^{o}C.

5.3.2 Open Circuit, Short Circuit, Resistance & Inductance

These machine parameters were measured using standard techniques described in the following sections, the values of which were used in a variety of the following methods. The method is therefore presented here, while explanation of its importance is presented with the overriding method.

Open and Short Circuit Tests

Open circuit voltage and short circuit current waveforms have been measured as part of the validation of the electromagnetic finite element model presented in section 3.1.3. Open circuit voltages were measured on each phase between the phase terminal and the star point at 1000rpm. Short circuit currents were measured by shorting each terminal to the next and measuring phase currents at 1000rpm. The measurements were taken as quickly as possible after the start of the test which began from a thermally steady state condition achieved by pumping 50deg coolant through the machine's coolant jacket.

Phase Resistance Measurement

The phase resistance was measured by linking the phases of each stator in series, applying a voltage across the terminals, and measuring the current. Resistance was then determined from Ohm's law where voltage was measured using a Fluke 87V multimeter and current was measured using a CP500 current probe linked to a LeCroy WaveRunner 64Xi. The measurement was taken at 20^{o}C achieved by pumping temperature controlled coolant through the coolant jacket of the machine. When phase resistance needed to be calculated at other temperatures (during the steady state and magnet loss tests described later) Equation (5.2) from [24] was used.

$$R_T = R_{20}[1 + \alpha_{20}(T_w - 20)] \tag{5.2}$$

The use of this method to measure resistance assumes that the AC and DC resistances of the winding are the same. The resistance of a winding can be dependent on the frequency of the current excitation due to the skin and proximity effects. The skin effect is the phenomenon seen in an AC conductor where the current tends to flow at the surface of the conductor, increasing its effective resistance [24]. The magnetising field caused by the AC current induces eddies which oppose the current flow in the centre of the conductor and add to it at the surface, effectively redistributing the current in the conductor. The proximity effect is similar to the skin effect, though the redistribution is caused by currents in neighbouring conductors. Both phenomena are characterised by the skin depth of the conductor; Equation (5.3) has been used to calculate the skin depth of the current flowing in the winding.

$$\delta = \sqrt{\frac{2}{\omega \sigma \mu_o \mu_r}} \tag{5.3}$$

The radius of the copper wires in the winding was 0.25mm, a skin depth below this would indicate a skin effect influence on resistance. At the 6th harmonic of the switching frequency the skin depth is 0.24mm, only the harmonic components of the current at this frequency and above are influenced by the skin effect. It is therefore assumed that the use of the DC resistance for this calculation incurs only a small error.

Synchronous Inductance Measurement

The synchronous inductance L_s was calculated from Equation (5.4), where every variable is measured. This method of calculating inductance assumes that $L_d = L_q$ and that saturation effects are negligible. This is a common assumption for a surface mounted permanent magnet machine as the air gap is relatively large and the permeability of the permanent magnets is similar to air [24].

$$L_s = \frac{\sqrt{\left(\frac{e}{i_{sc}}\right)^2 - R^2}}{\omega} \tag{5.4}$$

Where L_s is the synchronous inductance, and i_{sc} is the short circuit current at the angular frequency ω.

The value of L_s has been assumed to be temperature independent during this work, this assumes that the magnetic properties of the stator steel are temperature independent. Non-oriented electrical steels, such as the one used here, have been shown to be temperature independent up to 500°C by Takahashi et al. [102].

5.3.3 Steady State Tests

Steady state temperatures and static pressures were measured in order to validate the CHT model. Current waveforms were measured in order to provide realistic boundary conditions for the electromagnetic finite element model while mechanical torque was measured to validate the EM FEA predictions.

The speed and torque of the prototype were set using the previously described test set up. At each operating point temperatures and pressures were allowed to reach steady state conditions before being recorded along with current waveforms. Each operating point was repeated three times from a cold start. Coolant was pumped through the coolant jacket by a standalone cooler which kept the coolant inlet temperature at 50ºC; the flow rate was 4l/m. Once temperatures and pressures had stabilised magnet temperature was measured by removing the load from the machine and measuring the BEMF. The calibration curve in Figure 5.10 was then used to determine the temperature.

Due to the computational time required to solve the numerical model (2-3 weeks per operating point on a 6x3.33GHz core workstation with 16Gb of RAM) 3 operating points were selected for analysis. The thermal limits of the copper winding (Class H: 180deg) and the magnet material (N33EH) were used to select the operating points. For reference Figure B.4 in Appendix B shows the B-H characteristic of the magnet material as a function of temperature, a limit of 120deg was set for the magnets to ensure the knee point of the demagnetisation curve remained in the third quadrant. While this may appear conservative, only the average temperature of the magnets was being measured, hot spots may have exceeded this limit. It should also be noted that magnet temperature was only measured at the end of the test, so caution must be observed. It was found that the magnet temperature limit was reached at 4000rpm 40Arms, though mechanically the machine was rated to 8000rpm and thermally the winding had over 100deg of temperature rise capacity remaining. Based on this finding the other two operating points were set at 2000rpm 40Arms and 3000rpm 40Arms.

The 4000rpm operating point was conducted with temperatures and pressures being recorded from both halves of the machine. No significant circumferential temperature or pressure differences were seen therefore the repeated positions of each sensor have been averaged and are presented as one value. The lack of circumferential temperature and pressure gradients (between equivalent positions in one tooth/slot and the next) substantiates the periodic boundary conditions prescribed in the CHT model. Table 5.1 presents these results as % difference in temperature rise and static pressure between equivalent front and back sensors.

Agreement between the front and back pressure measurements is excellent, the small discrepancies may be due to:

- Uncertainty in sensor position
- Small burrs/blockages in tapping
- Rotor offset

At first the difference between the front and back casing temperatures appears alarming, however the absolute difference is 1K. Small offsets between front and back temperatures could have been caused by the test rig itself acting as a heat sink. Spacers were added in between the machine and test rig mounting plate to mitigate this effect as much as was practically possible, see Figure 5.11. Other reasons for discrepancies between front and back temperatures may include:

- Small differences in resistance between front and back stators causing imbalanced loss profiles
- Uncertainty in sensor position and contact with component
- Small differences between flow rates in front and back casings
- Natural convection from external casing surface
- Differences in thermal contact resistances

Overall Table 5.1 is good evidence that measurements need only be taken in one half of the machine.

Table 5.1 Difference in temperature rise between front and back halves of the AF PMSM

	Position	Difference between front and back [%]
Static Pressure Tap	Inner	4.1
	Middle	2.0
	Outer	1.5
Thermocouple	Winding Inner	0.6
	Winding Outer	5.0
	Core Deep	4.8
	Core Medium	5.7
	Core Shallow	11.9
	Case	23.7
	Bearing Housing	10.7

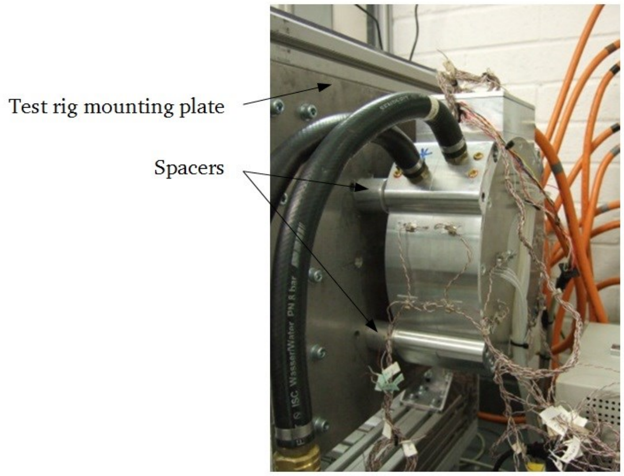

Figure 5.11 Prototype AF PMSM thermally spaced from test rig

5.3.4 Winding, Core and Friction Losses

Winding losses were calculated from the steady state test data using Equation (5.5) and were used as source terms in the CHT analysis.

$$q_{cu} = 3i^2R \tag{5.5}$$

The winding resistance was calculated from Equation (5.2) evaluated at the average temperature given by the thermocouples in the winding.

Core losses were estimated in order to validate the electromagnetic finite element model. They were calculated from,

$$q_{fe} = 3vi\cos\delta - T\omega - q_{cu} - q_m - q_w - q_{mech} \tag{5.6}$$

where the windage losses, q_w, were estimated from

$$q_w = C_m\rho\omega^3r^5 \tag{5.7}$$

which uses an empirical correlation for the drag torque coefficient C_m in a stator disc system from [95]:

$$C_m = 0.04G^{-0.167}Re^{-0.25} \tag{5.8}$$

The mechanical losses were estimated using the SKF bearing loss calculator [91]. Magnet losses and were measured as per Section 5.3.5.

5.3.5 Magnet Losses

Magnet losses have been measured as part of the validation of the electromagnetic finite element model. This author presented an alternative method to the below in [103]. The novel method presented here is an extension of this, though with reduced experimental effort and uncertainty.

If an element under thermally uniform, steady state, conditions is subjected to a unit step function of heat generation rate, the rate of temperature rise of the element is proportional to the heat generation rate, see Equation (5.9).

$$q = mC_p \left.\frac{dT}{dt}\right|_{t=0} \tag{5.9}$$

Where m is the mass.

This principle is applied in the proposed method. The magnets were weighed to determine their mass, and the heat capacity was taken from the manufacturer's data sheet [81]. The following method therefore aims to measure dT/dt at $t = 0$, and hence determine the magnet losses.

Measurement of magnet temperature

Magnet temperature was measured by measuring the voltage constant of the machine and using the calibration curve shown in Figure 5.10 to determine the temperature. During each test the voltage constant was calculated from measured variables using the voltage equation for the machine, derived from its equivalent circuit (Figure 1.10), see Equation (5.10).

$$k_e = \frac{\sqrt{v^2 - (\omega L_s i)^2} - iR}{\omega} \tag{5.10}$$

This form of the equation is suitable for electrical machines being operated outside of the field weakening range. The equation could be recast in terms of i_q and i_d in order to take measurements in the field weakening range; rotor position would have to be measured in order to decompose i into i_q and i_d.

The temperature rise in the magnets at any time during the test was then determined from Equation (5.11).

$$\theta_m = \alpha(k_{e1} - k_{e2}) \tag{5.11}$$

Where α is the calibration coefficient shown in Figure 5.10, k_{e1} is the voltage constant measured at the beginning of the test and k_{e2} is the voltage constant measured at any time after the start of the test.

This method of measuring magnet temperature was selected in preference to thermocouples or thermistors with slip rings, or infra-red imaging techniques, as it gives the average temperature of the magnets in the machine. When considering typical eddy current flows in the magnets of such devices (see Figure 5.12) it would take a large number of thermocouples embedded in the magnet to resolve the distribution of the loss field. Indeed, it could be argued that the presence of an embedded sensor would disrupt the eddy current flow and render the measurement meaningless, especially in small machines where the relative size of the sensor is large. Surface measurement techniques such as infra-red thermometry suffer from similar conceptual uncertainties.

After a review of the literature an additional on-line magnet temperature measurement technique was identified. Reigosa et al. [104] present a magnet temperature estimation technique where during machine operation a high frequency signal is superimposed onto the fundamental excitation in order to estimate the stator's transient impedance. They showed that the temperature of the magnets has a measurable impact on the stator impedance and therefore used the change in impedance to infer the magnet temperature. The advantage of their technique is that it can be implemented in a motor drive in real time. Their study included a sensitivity analysis which quantified the impact of using a motor drive's 'commanded' voltage rather than measured voltage as most drives do not include on-board voltage sensors. Estimates of magnet temperature had errors ranging from 1-3°C. This technique was not used in this thesis as modification to the inverter drive's PWM strategy is required, and this was not possible with the available resources. It also seems inappropriate to use such a technique to measure temperature in order to determine losses as the high frequency injection may have an impact on the generation of losses.

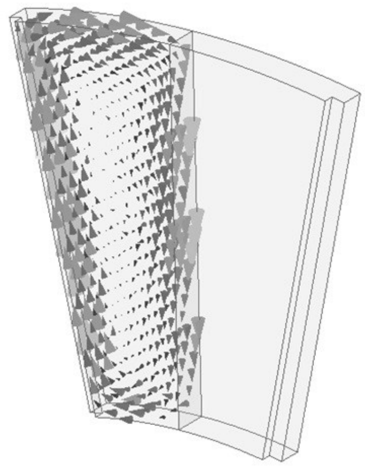

Figure 5.12 Eddy current visualization in a single magnet segment of the machine, taken from the finite element analysis results from section 6.1.2

Measurement of magnet losses

The PMSM machine parameters L_s and R are known from the previous tests presented in this chapter. The remaining variables which must be measured during the loss measurement in order to solve Equation (5.10) are therefore the fundamental components of voltage and current, along with the angular frequency. These were all measured using a Newtons4th PPA5530 power analyser as a unit step function of heat generation rate was applied to the magnets from a thermally uniform, steady state condition (as required for Equation (5.9) to hold). A thermally uniform, steady state condition was achieved in the machine by pumping temperature controlled coolant through its coolant jacket. The casing, core and winding thermocouples were all used to ensure the thermal condition had been reached. A unit step function of heat generation rate was approximated by first running the machine up to speed using the generator and then applying an AC current to the windings of the motor.

During the measurement the resistive losses meant that the winding temperature was increasing, therefore the phase resistance at each sample was calculated from Equation (5.2). The winding temperature was measured using two PT100 thermistors which were wound into the end winding and read by a National Instruments thermistor input module (NI 9217). These were used in preference to the thermocouples wound into the stator which were found to be adequate for steady state temperature measurement, but too noisy for transient measurements. A greater number of temperature sensors would provide a better average value for use in the resistance equation, however in the machine studied here the resistive voltage drop was small compared to the other components of Equation (5.10). The ratio of iR/e is considered as a measure of the sensitivity of to the overall experimental result and has been calculated to have ranged between 5.7e-3 and 2.3e-2 during the experimental work presented here. The sensitivity of the result to iR is therefore low, and the use of a small number of temperature sensors is justified.

Figure 5.13 shows measured data from a typical test, the reduction in phase voltage provided by the inverter to keep the current constant as the magnets and winding heat up can be seen. Figure 5.14 shows the magnet heating curves derived from this data using Equations (5.10) and (5.11) along with the regression used to determine dT/dt at $t = 0$, which was used in Equation (5.9) to determine the measured magnet losses.

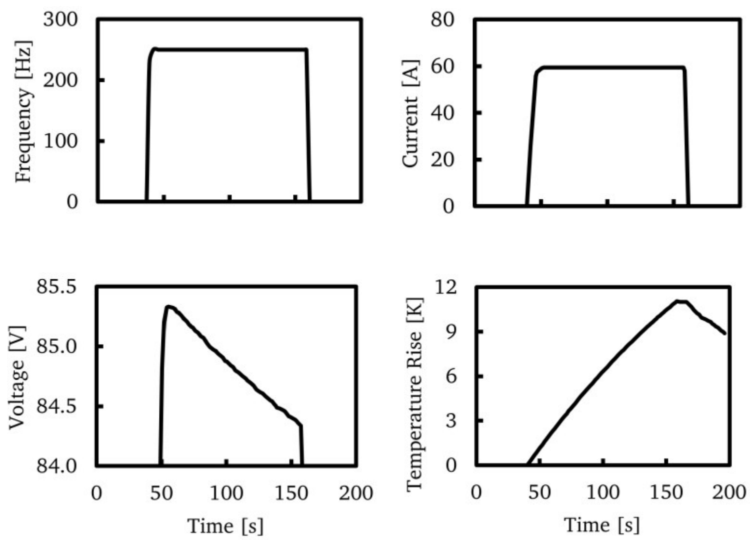

Figure 5.13 Measured data from a typical magnet loss test

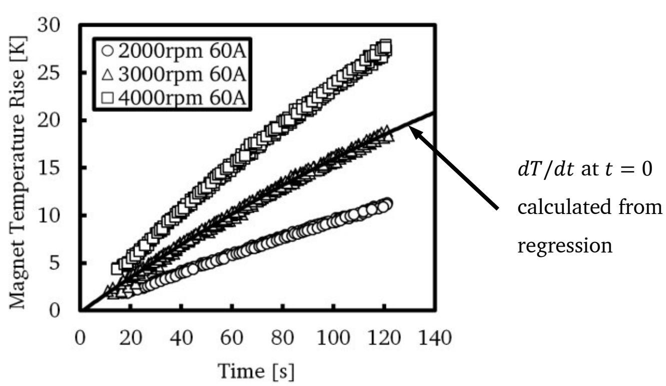

Figure 5.14 Heating curves derived from measured data

In Figure 5.13 it can be seen that there is some lag in the measurement system between the start of the test and the first 'good' measurement. This is reflected in Figure 5.14 which shows the rise in magnet temperature over time calculated from this data for a range of operating points. It can be seen that the first 15 seconds of temperature rise data were lost to this 'lag'. Calculation of the gradient at the start of the test therefore included backward extrapolation of a second order least squares regression. Although this is not ideal, its effect is included in the uncertainty analysis presented in Section 5.4, where the average uncertainty in a reading is found to be 9.7% with 95% confidence. Figure 5.14 is the amalgamation of five repeats of the experiment, it can be seen that the repeatability is good.

Temperature effects of magnet losses

The proposed method gives a value for magnet losses at the start of the experiment i.e. at the initial temperature. The resistivity of permanent magnet materials is temperature dependent, for the grade of material used here the relationship has been measured by [105] and is expressed as:

$$\rho = aT_m + b \tag{5.12}$$

Where a is a curve fitting coefficient with a value of 0.936e-3μΩm/°C and b is a curve fitting coefficient with a value of 1.24μΩm.

It may not always be practical to begin the experiment from the expected operating temperature of the magnets. If the driving EMF in the magnet domain is assumed to be constant with magnet or winding temperature then the magnet losses can be thought of as being inversely proportional to the material resistivity only. It is therefore proposed by that the results of the method could be adjusted to give an estimate of magnet losses at other temperatures by the following:

$$q_T = q_{Ti}\frac{\rho_{Ti}}{\rho_T} \tag{5.13}$$

Where q_T is the value of losses at the temperature of interest, q_{Ti} is the value of losses measured during the experiment, ρ_T is the resistivity at the temperature of interest, and ρ_{Ti} is the resistivity at the initial temperature of the experiment.

5.4 Uncertainty Analysis

An uncertainty analysis has been carried out following the methodologies described in [106]. Every uncertainty figure presented in this chapter is for 95% confidence. The general case for the uncertainty in an experimental result is now described and will be referred to throughout the following sections.

If an experimental result, r, is a function of J measured variables then its data reduction equation is:

$$r = r(X_1, X_2, \dots, X_J) \tag{5.14}$$

The uncertainty in r is then given by:

$$U_r^2 = B_r^2 + P_r^2 \tag{5.15}$$

Where

$$B_r^2 = \sum_{i=1}^{J} \theta_i^2 B_i^2 + 2 \sum_{i=1}^{J-1} \sum_{k=i+1}^{J} \theta_i \theta_k B_{ik} \tag{5.16}$$

$$P_r^2 = \sum_{i=1}^{J} \theta_i^2 P_i^2 \tag{5.17}$$

Where B_i is the systematic error and P_i is the random error in each of the variables X_i. The covariance estimator is denoted by B_{ik} and is described by

$$B_{ik} = \sum_{\alpha=1}^{L} B_{i_\alpha} B_{k_\alpha} \tag{5.18}$$

Where L is the number of elemental error sources shared by the measured variables. The term θ_i weights each error depending on its influence on the data reduction equation:

$$\theta_i = \frac{\partial r}{\partial X_i} \tag{5.19}$$

Random errors were calculated by repeating experiments a number of times and calculating the standard deviation of the mean from Equation (5.20) where S_r is the standard deviation of the sample and N is the number of measurements used to take the mean. The random error is then calculated from (5.21) where t is a value taken from the t-distribution (see [106] p237).

$$S_{\bar{r}} = \frac{S_r}{\sqrt{N}} \tag{5.20}$$

$$P_r^2 = tS_{\bar{r}} \tag{5.21}$$

Steady State Temperature Rise

As the steady state temperature rise was calculated as the difference in a thermocouple's reading between the beginning and end of the test the systematic error is taken as 0 (as the systematic error in each reading effects both measurements by the same amount). Each thermocouple position was repeated 3 times around the machine, and each test was repeated 3 times giving a total of 9 measurements. In this way the uncertainty in the position of each thermocouple is taken into account as a random, rather than a systematic, error.

Static Pressure

The digital manometer used to measure static pressure was calibrated by Trescal Ltd. The applied pressure during the calibration had an uncertainty of 3.50Pa and the random uncertainty in the regression was 2.16Pa (calculated as twice the standard error of the regression). This gives a total systematic error of 4.11Pa. Each wall tap position was repeated 3 times around the machine, and each test was repeated 3 times giving a total of 9 measurements. In this way the uncertainty in the position of each wall tap is taken into account as a random, rather than a systematic, error.

Torque

The load cell and torque arm assembly was calibrated by fixing a specially machined bar to the front face of the load machine and hanging calibrated masses from the bar at a known distance from the axis. The systematic uncertainty in the calibrated masses and machined bar was 0.01% and 0.02% respectively. The random uncertainty in the calibration regression shown in Figure 5.15 was 0.52Nm (calculated as twice the standard error of the regression) giving a total systematic error in the torque reading of 0.52Nm.

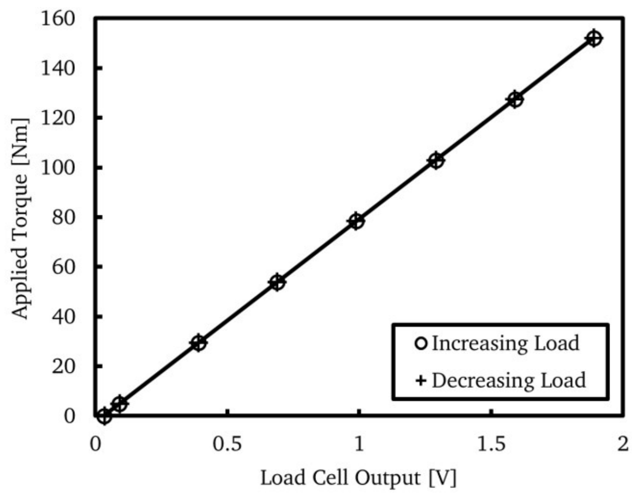

Figure 5.15 Torque measurement calibration curve

Phase Resistance

The systematic uncertainty in the voltage and current measurements was 0.05% and 1%±500mA respectively; this gave a total systematic uncertainty of 0.288mΩ. Random uncertainty in the measurement was calculated to be 0.020mΩ, giving a total uncertainty of 0.289mΩ.

When resistance was calculated from Equation (5.2), the total uncertainty quoted above became a fossilised systematic uncertainty in the R_{20} value. Systematic uncertainties for the value of α_{20} could not be found, and the systematic uncertainty in the temperature rise was again taken as 0. Conceptual uncertainties regarding using point measurements of temperature to calculate average resistances have not been taken into account.

Synchronous Inductance

The systematic uncertainty in the voltage and current measurements was 1% and 1%±500mA respectively. Uncertainty in the resistance measurement is described above. Uncertainty in the angular frequency is neglected as the uncertainty in the time interval of the oscilloscope was 5.025e-6%. The total systematic uncertainty in the inductance measurement was found to be 2.1μH (1.56%).

Winding Losses

The systematic uncertainty in the current measurement taken with the power analyser and shunt was 0.11A. Together with the uncertainty in the resistance measurement the systematic uncertainty in the winding loss measurement was 3.44W (~4.3%).

Core and Friction Losses

No uncertainty analysis has been performed on the core and friction loss values as these are estimates, rather than measured values.

Magnet Losses

The total uncertainty in the experimental result is given by Equation (5.22).

$$U_q^2 = U_m^2 + U_{C_p}^2 + U_{dT/dt}^2 \tag{5.22}$$

Where U_q is the uncertainty in the magnet loss, U_{C_p} is the uncertainty in the heat capacity, and $U_{dT/dt}$ is the uncertainty in the initial temperature rise of the magnets.

The mass of the magnets was measured using Kern EMB 500-1 scales with an uncertainty of 0.02%. The heat capacity of the magnet material was taken from the manufacturer's data sheet with an estimated uncertainty of 5%. The uncertainty in the initial temperature rise of the magnets was determined from Equation (5.23).

$$U_{dT/dt}^2 = \left(2S_{dT/dt}\right)^2 + \sum_{i=0}^{N} \left\{\frac{\partial(dT/dt)}{\partial T_i}\right\}^2 B_{T_i}^2 \tag{5.23}$$

Where $S_{dT/dt}$ is the standard error in the regression coefficient dT/dt representing the random error in the result, and B_{T_i} is the systematic uncertainty in each temperature rise measurement. The partial derivatives $\partial(dT/dt)/\partial T_i$ were calculated numerically from each data set using a forward differencing scheme.

The systematic uncertainty in each temperature rise measurement is described by Equation (5.24).

$$B_{T_i}^2 = U_\alpha^2 + B_{dke}^2 \tag{5.24}$$

Where U_α is the uncertainty in α (the relationship between the change in voltage constant and the magnet temperature rise determined during calibration), and B_{dke} is the systematic uncertainty in the change in voltage constant during the experiment.

During the voltage constant calibration procedure all of the systematic uncertainties in the measured change in voltage constant were correlated, this is also true of the temperature rise measurement. The remaining uncertainty (U_α) in the correlation is then the random error which is estimated as twice the standard error in the gradient of the regression, this was found to be 2.9%.

It is now shown that B_{dke} can be considered negligible when compared with U_α. During the experiment the voltage constant is determined from Equation (5.10), the uncertainty in the change in voltage constant is then given by Equation (5.25). The uncertainty in any individual voltage constant measurement is given by Equation (5.26).

$$B_{dke}^2 = B_{dke_1}^2 + B_{dke_2}^2 - 2B_{ke_1ke_2} \tag{5.25}$$

Where $B_{dke_1}$and B_{dke_2} are the systematic uncertainties in individual voltage constant measurements and $B_{ke_1ke_2}$ is the correlated systematic uncertainty between the two measurements, given by Equation (5.27).

$$B_{ke_i}^2 = \left(\frac{\partial ke_i}{\partial V}\right)^2 U_V^2 + \left(\frac{\partial ke_i}{\partial XI}\right)^2 U_{XI}^2 + \left(\frac{\partial ke_i}{\partial IR}\right)^2 U_{IR}^2 + \left(\frac{\partial ke_i}{\partial \omega}\right)^2 U_\omega^2 \tag{5.26}$$

$$B_{ke_1ke_2} = \sum_{\alpha=1}^{L} B_{ke_{1\alpha}} B_{ke_{2\alpha}} \tag{5.27}$$

Where L is the total number of elemental error sources shared between the measured variables. If B_{ke_1} and B_{ke_2} were equal the systematic error would be zero. However as most instrument errors are given as % of reading rather than % of full scale the values differ slightly. The value of B_{dke} has been calculated for the data set which showed the largest temperature rise (4000rpm 80A), and is shown in Figure 5.16. As can be seen its value is negligible when compared with U_α. The small deviations from a smooth curve in Figure 5.16 are due to random fluctuations in the measured data. When considering Equation (5.28) is can be seen that different values of B_{dke} can be calculated for identical values of ∂ke.

The resulting values of uncertainty in magnet loss range from 9.2-10.5% for 95% confidence, where the average value of 9.7% has been plotted on all graphs in Chapter 6. It is useful to examine the breakdown of uncertainty from Equation (5.22) to see where the method could be improved. This breakdown is shown in Table 5.2 where it can be seen that the systematic error in determining dT/dt dominates the total uncertainty. Part of this uncertainty comes from the regression performed to determine the relationship between the change in voltage constant and the magnet temperature rise. Assuming that the random error in the calibration data remains constant as more data points are taken it can be seen from the classical expression for the standard error in the slope of a regression that $S_m \propto 1/\sqrt{N}$ [106]. It has been calculated that increasing the number of points on the calibration curve from 19 to 76 would decrease the overall uncertainty to 7%. For reference each point on the curve took approximately 1 hour to take (time taken for uniform steady state temperature to develop in machine) and time constraints made it impractical to increase the number of calibration points in the present work. The delay of the measurement system at the beginning of the test also contributed to the systematic error in determining dT/dt. It is difficult to quantify the potential benefit of reducing the delay as the partial derivatives $\partial(dT/dt)/\partial T_i$ were calculated numerically from the actual data. Any study which attempted to do this would need to create data at the beginning of the test to assess its impact on the overall uncertainty.

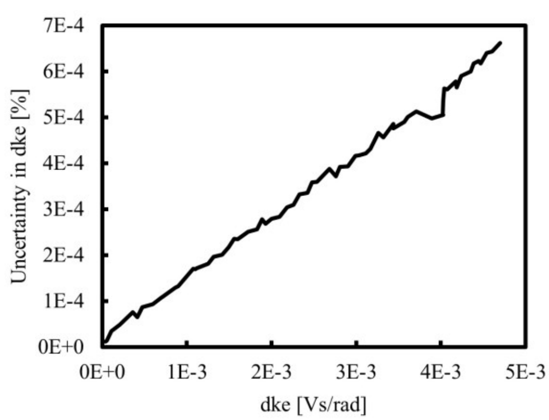

Figure 5.16 Uncertainty in dk_e during 4000rpm 80Arms experiment

Table 5.2 Sources of uncertainty in the magnet loss measurement

Uncertainty Source	Contribution [%]
Mass	4.4e-4
Heat Capacity	27.7
Systematic Error in dT/dt	68.9
Random Error in dT/dt	3.4

5.5 Summary

This chapter has presented a number of experimental methods used to provide boundary conditions for the numerical model, as well as to provide data to validate the model against. The instrumentation of the prototype machine was presented along with a description of the experimental facility used to take the measurements. The method used to calculate the uncertainty in each measurement has been presented; the results of this are presented alongside the experimental results in Chapter 6. A summary of the measurements described in this section is presented in Table 5.3.

The range of techniques presented in this Chapter forms a methodology which can be applied to other electrical machines. The novel method presented for measuring magnet losses is a particularly strong contribution. Together these techniques improve the understanding of the loss, flow and temperature fields within an electrical machine, which is the aim of the thesis.

Table 5.3 Overview of measurements taken on prototype

Measurement	Method	Purpose
Winding Temperature	Thermocouple	DC test to tune CHT, steady state test to validate CHT
Stator Core Temperature	Thermocouple	DC test to tune CHT, steady state test to validate CHT
Casing Temperature	Thermocouple	DC test to tune CHT, steady state test to validate CHT
Static pressure on stator face	Wall taps	Validate CHT
Magnet Temperature	Voltage Constant Calibration	Validate CHT and Material Condition in EM FEA
Open Circuit Voltage	Oscilloscope	Validate EM FEA and part of synchronous inductance measurement
Short Circuit Current	Oscilloscope	Validate EM FEA and part of synchronous inductance measurement
Resistance	Ohm's Law	Part of synchronous inductance and magnet loss measurement
Inductance	Impedance	Magnet loss measurement
Copper Losses	Ohm's Law	Source term in CHT
Magnet Losses	Novel technique	Validate EM FEA
Current Waveform	Oscilloscope	Boundary condition in EM FEA

Chapter 6

Results and Discussion

In this chapter the numerical predictions of loss, flow, and temperature field are presented and discussed, followed by a similar treatment of the experimental results. Characteristic features of the loss and flow fields are identified, explaining the position and magnitude of magnet hot spots. The factors affecting magnet heating and cooling are identified and discussed leading to a greater understanding of the physical system. The numerical predictions are then compared with the experimental measurements in order to validate the analyses.

6.1 Prediction of the Loss Field in an Axial Flux Permanent Magnet Synchronous Machine

This section builds up to a presentation of the predicted loss field in the magnets and core of the electrical machine. However, as additional validation points for the EM FEA model, open circuit voltage, short circuit current, and electromagnetic torque were all predicted, and these are presented first.

6.1.1 Prediction of Open Circuit Voltage and Short Circuit Current

Simulations were performed with the current in each phase set to 0 (open circuit) and all phases shorted together. An FFT was performed on each waveform in order to identify its fundamental component. The fundamental components of open circuit voltage, e_f, and short circuit current, i_f, were then used to calculate the impedance, Z, of the phase from:

$$Z = \frac{e_f}{i_f} \tag{6.1}$$

The synchronous inductance was then calculated from:

$$L_s = \frac{\sqrt{Z^2 - R^2}}{\omega} \tag{6.2}$$

Figure 6.1 presents the open circuit voltage waveform of the machine at 1000rpm, 50deg magnet temperature. The result of the FFT is also shown where the magnitude of the fundamental component is 40.18V.

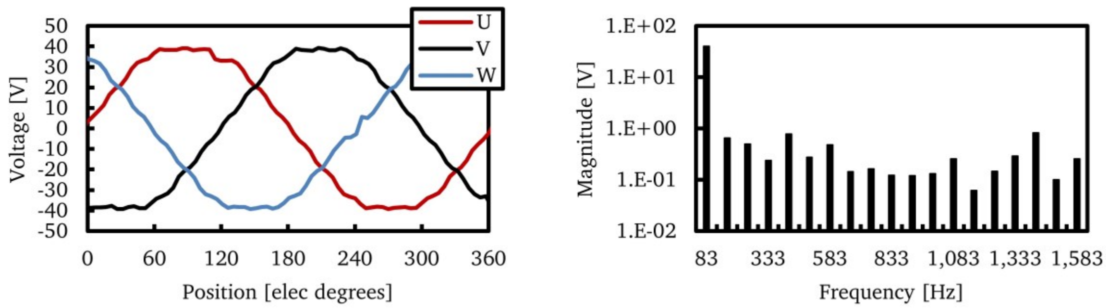

(a) Open circuit voltage: time domain

(b) Open circuit voltage: frequency domain

Figure 6.1 Predicted open circuit voltage waveform at 1000rpm

Figure 6.2 shows the short circuit current waveform of the machine at 1000rpm, 50deg magnet temperature. The result of the FFT is also shown where the fundamental component of the phase current is seen to be 612.85A. Equation (6.2) was then used to calculate the predicted synchronous inductance of the winding which was found to be 122.0μH.

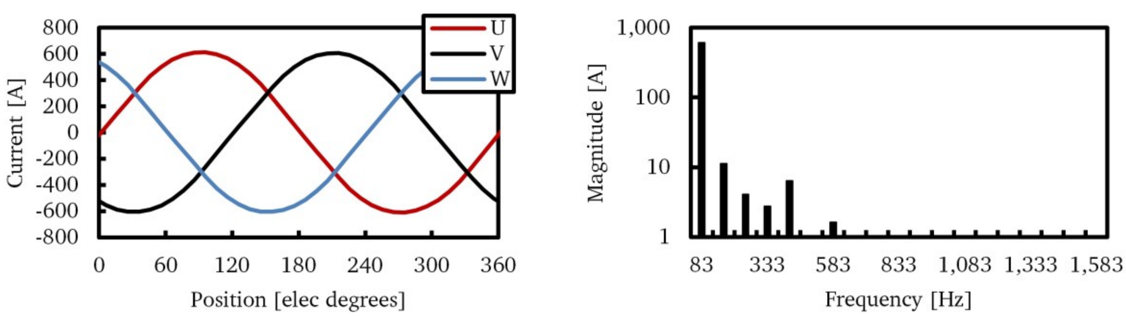

(a) Short circuit current: time domain

(b) Short circuit current: frequency domain

Figure 6.2 Predicted short circuit current waveform at 1000rpm

6.1.2 Predicted Torque, Magnet Loss Field and Core Loss Field

In the following simulations measured current waveforms were used to excite the windings of the electromagnetic model in order to predict values of torque, magnet loss and core loss. The measured waveforms can be seen in Figure 6.3.

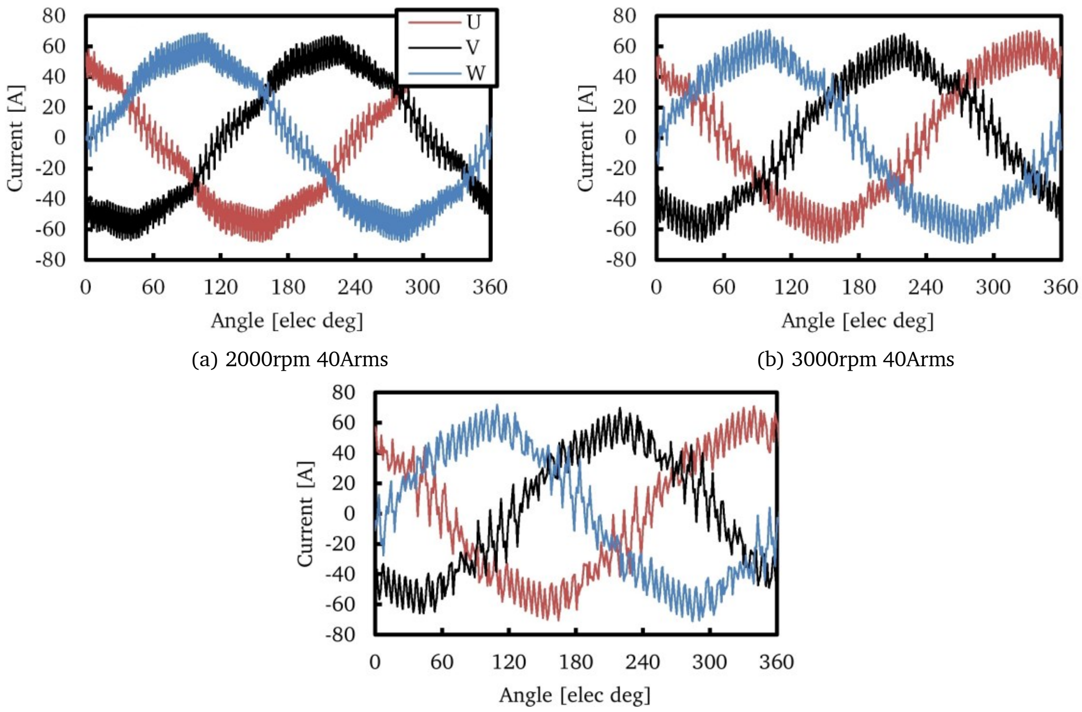

(a) 2000rpm 40Arms

(b) 3000rpm 40Arms

(a) 4000rpm 40Arms

Figure 6.3 Measured current waveforms prescribed in the windings of the EM FEA model, space vector modulated waveform with a carrier frequency of 12kHz

Predicted Torque

Electromagnetic torque was predicted in order to provide an additional value which the EM FEA model could be validated against. Predictions of electromagnetic torque are presented in Figure 6.4. It is not appropriate to present a full investigation into the shape of the predicted torque waveform, as this is not the focus of the thesis. However, in order to check that the solution makes physical sense, an FFT of each waveform is presented. Below the switching frequency (12kHz) the torque ripple is due to reluctance changes, interactions between the rotor and stator field harmonics. Above the switching frequency additional high frequency components of the ripple torque can be seen at 24kHz and 36kHz, these are most likely due to current ripple caused by the carrier.

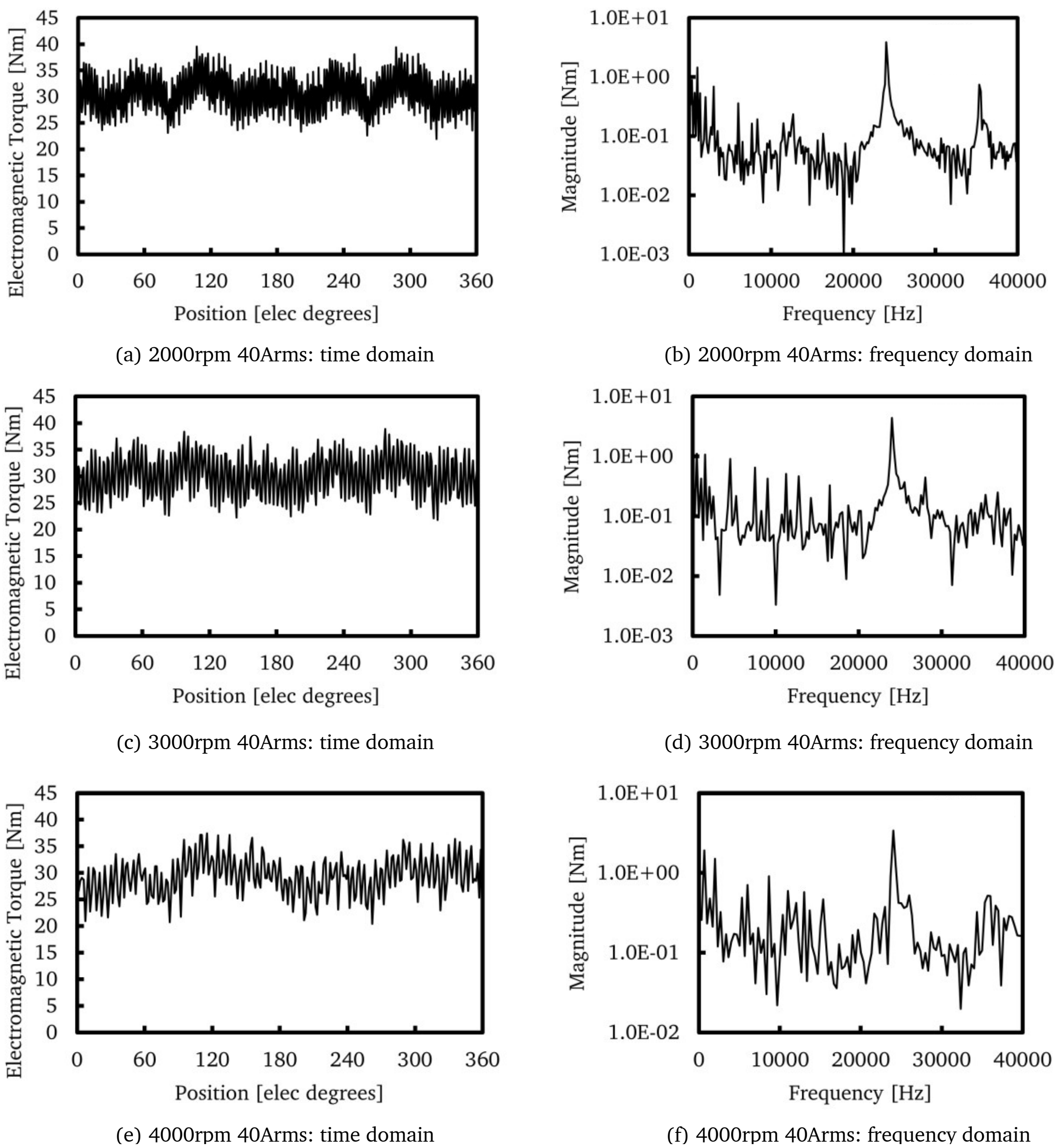

(a) 2000rpm 40Arms: time domain

(b) 2000rpm 40Arms: frequency domain

(c) 3000rpm 40Arms: time domain

(d) 3000rpm 40Arms: frequency domain

(e) 4000rpm 40Arms: time domain

(f) 4000rpm 40Arms: frequency domain

Figure 6.4 Predicted electromagnetic torque in the time and frequency domain

Predicted Magnet Loss Field

A visualisation of the predicted eddy current flow in the permanent magnets at various angular positions is shown in Figure 6.5. The current density was sampled at a point within the magnet domain and its components are plotted in Figure 6.6. The solution is as expected, with eddy currents flowing in the r-θ plane, causing a reaction field in the z direction. The EM FEA simulations were repeated without calculating eddy currents in the magnets in order to examine the changing magnetic fields that caused them. Figure 6.7 shows the results which show a large variation in flux density in the z direction, corroborating the current density plots.

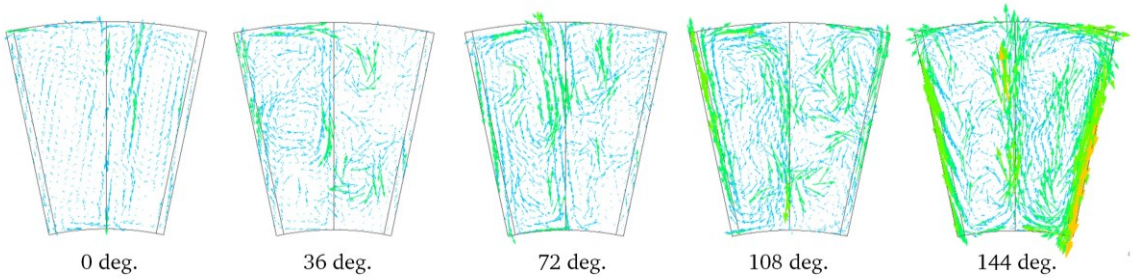

(a) 2000rpm 40Arms

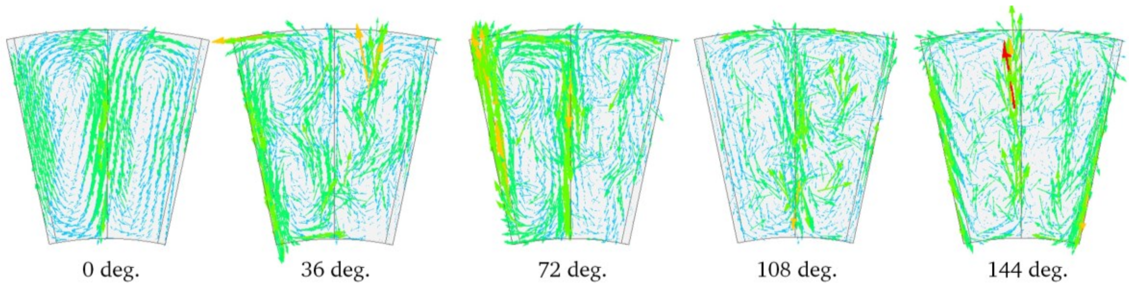

(b) 3000rpm 40Arms

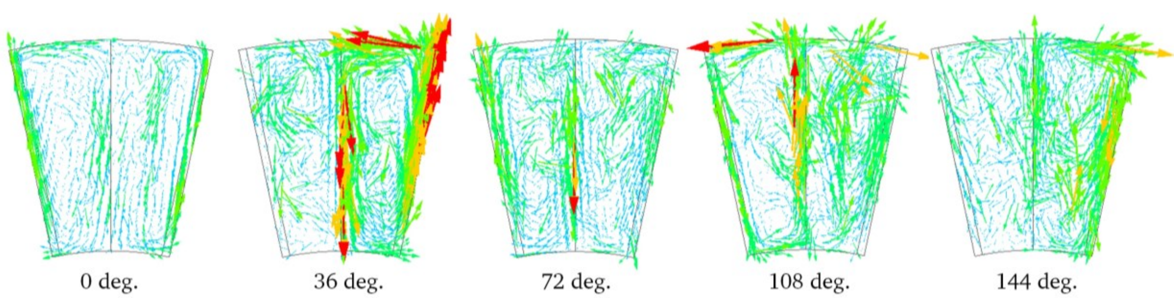

(c) 4000rpm 40Arms

Figure 6.5 Eddy current visualisation in the permanent magnets at various angular positions

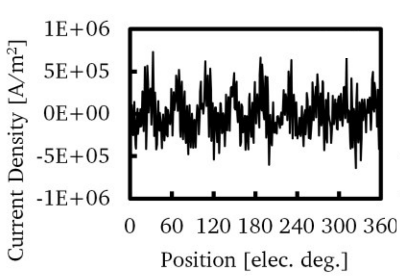

(a) Radial

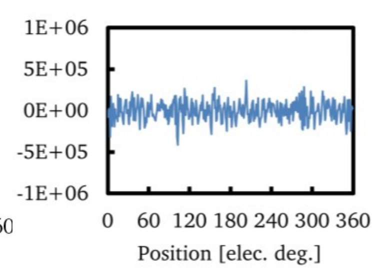

(b) Theta

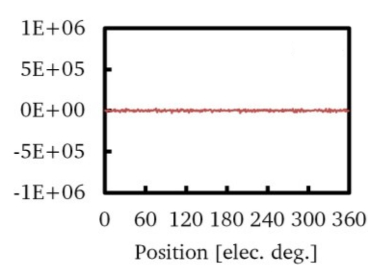

(c) Axial

Figure 6.6 Radial, theta, and axial current density components in magnet at 3000rpm 40Arms

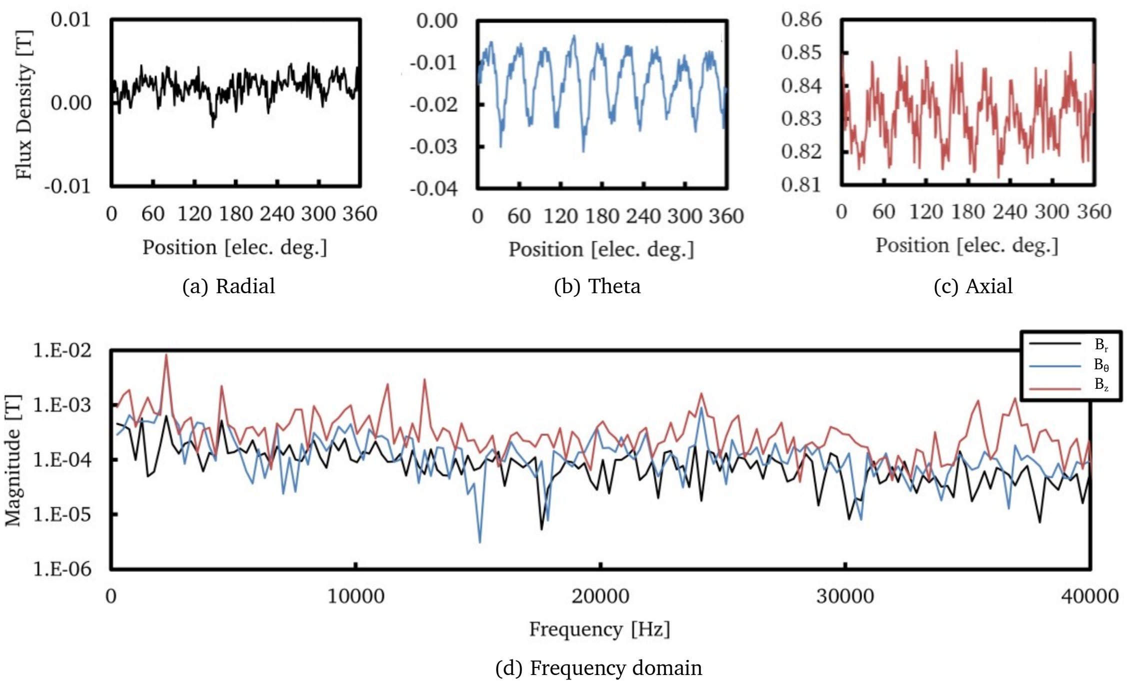

Figure 6.7 Radial, theta, and axial components of flux density in a magnet without eddy currents at 3000rpm 40Arms, time and frequency domain

A relatively large variation can also be seen in the tangential component of the flux density though only a small reaction is seen in the r-z plane. There are two reasons for this: firstly, when examining the harmonic content of the flux density waveforms the tangential variation is relatively low frequency; secondly, the aspect ratio of the magnets influences the effective resistance. In the r-θ plane the eddies have a large area to flow in compared with the r-z plane. The effective resistance to eddy current flow is larger in the r-z plane.

Figure 6.8 shows the results of applying Equation (3.9) to the current density predictions in each magnet segment to calculate the instantaneous loss at each angular position. For reference Equation (3.9) multiplies the volume integral of the current density in each mesh element and divides it by the conductivity of the material to give a value of loss. An interesting effect is seen if the losses in each segment of the magnet are time averaged and compared, the results of this are shown in Table 6.1, see Figure 6.9 for the location of each segment within the rotor. It can be seen that within one magnet, the losses in the two segments are not equal, though the difference in losses between equivalent segments in different magnets is small. The difference in losses between segments for the 2000rpm and 3000rpm operating points can be explained by considering the resultant flux density in the stator beneath the magnet. As, in this case, the stator flux is in quadrature with the rotor flux, the peak in resultant flux density is not directly underneath the magnet pole, see Figure 6.10. This means the level of saturation underneath each segment of a magnet is different, introducing a spatial variation in the inductance of the winding. Current variations in a conductor within a heavily saturated piece of the stator will produce smaller flux variations, and therefore magnet losses, than current variations within an unsaturated part of the stator. Figure 6.9 shows the position of the magnet segments at two different rotor positions, 50 and 110 electrical degrees. At 50 electrical degrees segment N2 is directly over a stator tooth. At 110 electrical degrees segment N1 is directly over the same stator tooth. Figure 6.11 shows the spatially averaged axial component of flux density on the 'tooth plane' as a function of rotor position.

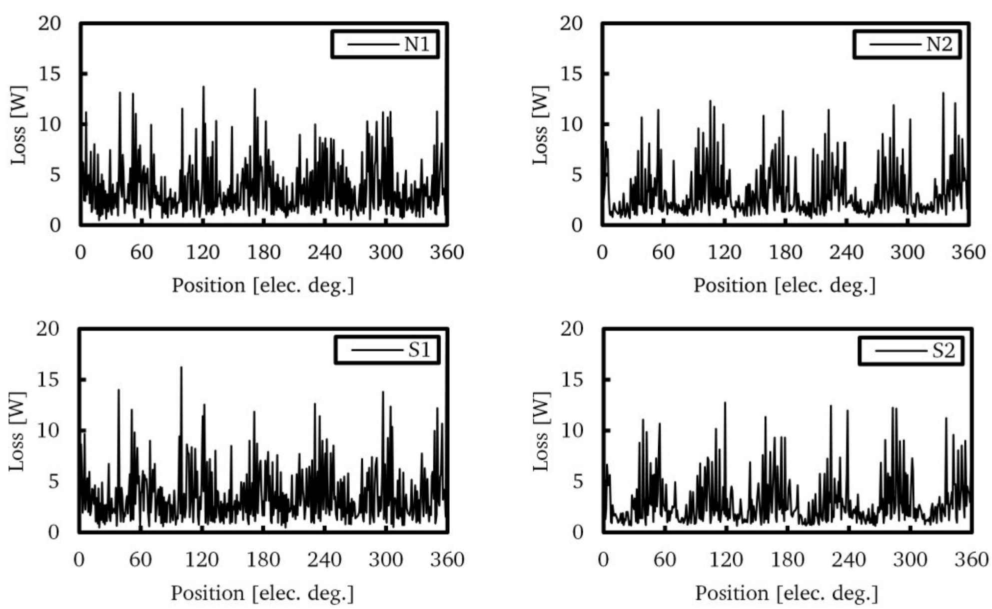

Figure 6.8 Magnet losses in each segment at 3000rpm 40Arms

Table 6.1 Time averaged magnet losses in each segment

Operating point	Losses N1 [W]	Losses N2 [W]	Losses S1 [W]	Losses S2 [W]
2000rpm 40Arms	2.08	1.58	2.03	1.50
3000rpm 40Arms	3.79	3.15	3.75	2.97
4000rpm 40Arms	4.14	4.60	4.42	4.46

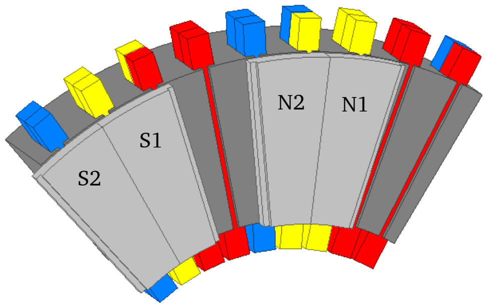

(a) 50 electrical degrees

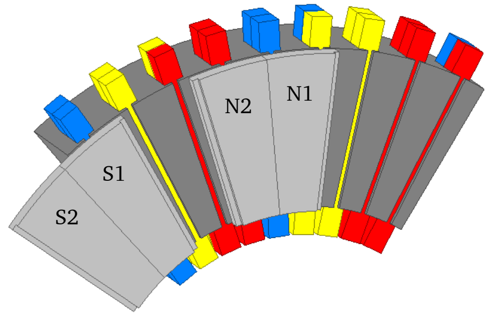

(b) 110 electrical degrees

Figure 6.9 Position of magnet segments at 50 and 110 electrical degrees

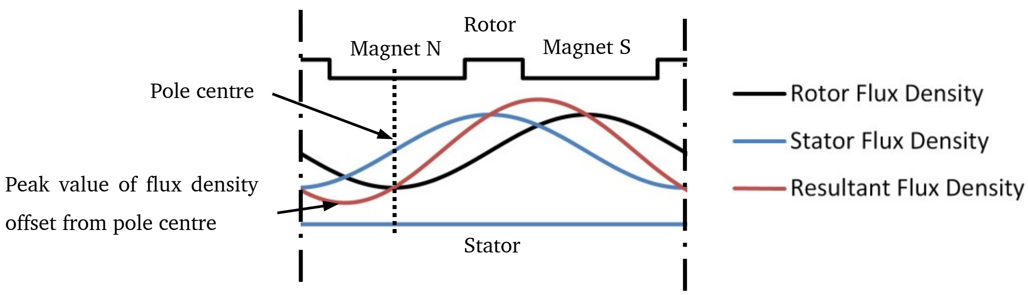

Figure 6.10 Superposition of rotor and stator flux densities

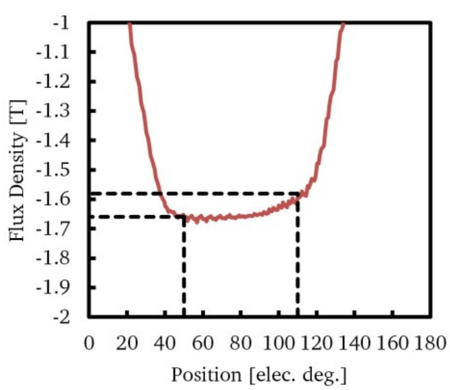

(a) Axial component of flux density in tooth plane

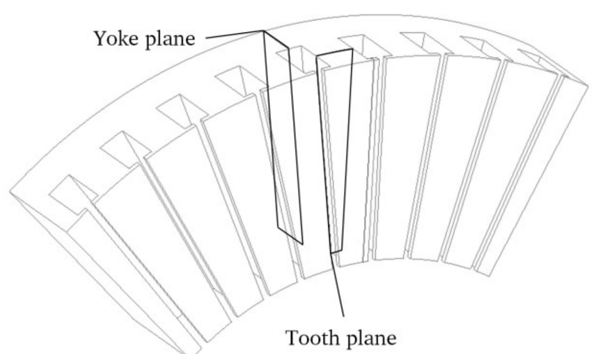

(b) Plane designation

Figure 6.11 Average axial component of flux density in the tooth plane vs. rotor position

It can be seen that as the magnet moves over the tooth it is in a higher state of saturation when segment N2 is over it than when segment N1 is. The change in flux density seems relatively small, however when referring back to the manufacturers data sheet for the stator steel [107] the relative permeability changes from 132 at 1.5T to 28 at 1.7T, a relatively large change. This result is important, as it has an influence on the predicted temperature profile in the magnet. This will be discussed further in Section 6.3.3.1.

The difference in losses between each segment is not as pronounced in the 4000rpm operating point. Figure 6.12 presents the power spectrum of the average flux density vector in the z direction in each segment at each operating point. As would be expected from the previous discussion the peak at 24kHz (second harmonic of the switching frequency) is lower in segment N2 than it is in N1 due to the level of saturation in the tooth underneath the segment at this position. The 4000rpm operating point seems to differ from the other two however in that is has a much larger flux density variation at 12kHz (first harmonic of the switching frequency), which seems not to be attenuated by the increase in saturation. Further analysis of this phenomenon has not been carried out here, though it seems to be a promising avenue for further research.

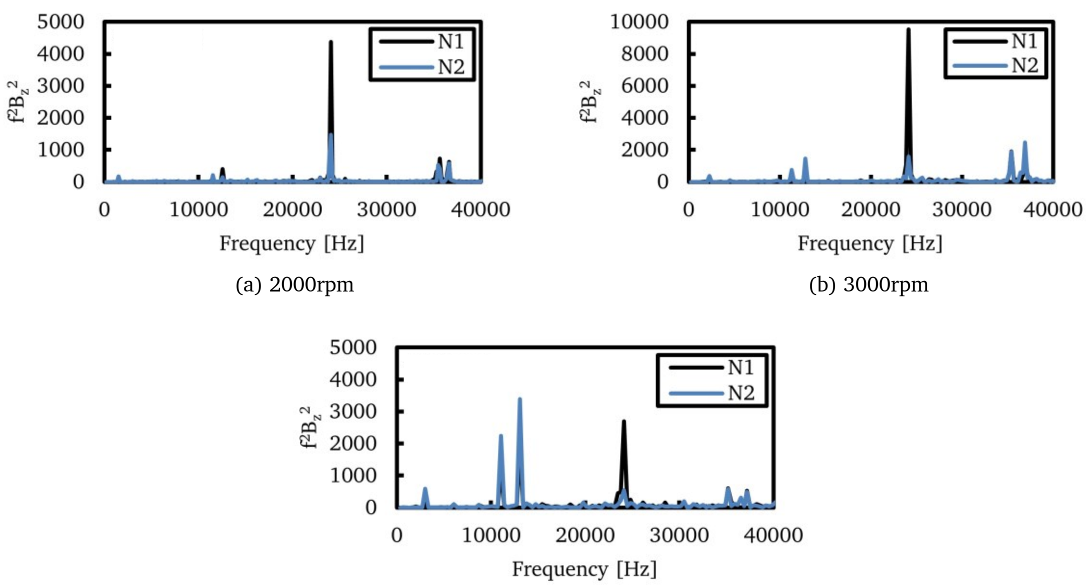

(a) 2000rpm

(b) 3000rpm

(c) 4000rpm

Figure 6.12 Power spectrum of flux density variations in magnet segments

The predicted magnet losses have been decomposed into components based on the source of the flux variation in the magnets. In order to do this, an additional two EM FEA simulations were run per operating point. To remove the losses caused by the current harmonics an analysis was performed where the current waveform was represented by its fundamental component only. In order to predict the losses induced by reluctance variations an additional analysis was performed with the phase currents set to zero. The differences in loss prediction between these two analyses and the original analysis were then attributed to the various phenomena included or excluded from each analysis. This superposition method assumes that the system is linear. This has been shown to be a good approximation for eddy current prediction in surface mounted PMSMs by Deng [108] and Sergeant et al. [33]. The results are presented in Figure 6.13 as ratios of the total magnet loss. As can be seen, across all of the operating points the vast majority (71-79%) of magnet loss was due to harmonics in the current waveform, while 15-20% was due to winding MMF harmonics and only 6-9% was due to reluctance changes.

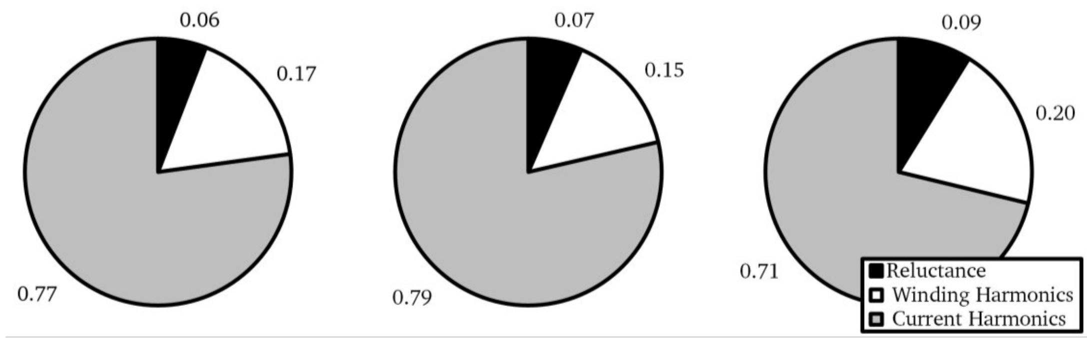

(a) 2000rpm (b) 3000rpm (c) 4000rpm

Figure 6.13 Magnet losses attributed to sources

Predicted Core Loss Field

As described in Chapter 3 core losses were calculated from Ansoft's transient core loss model, these values were used to define the source terms in the core during the CHT analysis. However, in order to gain an insight into the sources of the core losses the familiar Steinmetz equation [24] was used to estimate the relative amounts of loss caused by the different harmonics contained within the flux density distributions. Values of flux density were spatially averaged at the planar locations shown in Figure 6.11, the resulting temporal flux densities in the tooth and yoke can be seen in Figure 6.14 and Figure 6.15.

An FFT was performed on the flux density waveforms and the subsequent frequency spectrum was analysed using the Steinmetz equation to estimate the loss at each frequency, the results of this are shown in Figure 6.16 for the 3000rpm 40Arms operating point. The loss is dominated by flux density variations at the fundamental electrical frequency. In order to interpret this data in a quantifiable way the individual loss-frequency pairs have been grouped according to their source.

The sources have been defined as:

- Fundamental: Fundamental frequency only
- Winding MMF harmonic/Magnet harmonic: Frequencies above the fundamental but below the switching frequency
- Current harmonic: all frequencies including and above the switching frequency

The integral of the frequency spectrum has been taken over these bandwidths to determine a total loss density value for a particular source, the results are shown as proportions of the total loss density at their planar location in Figure 6.17

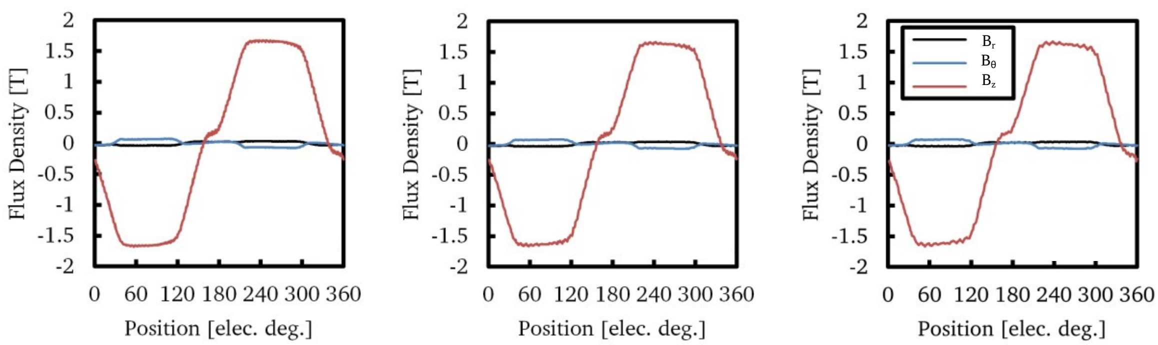

(a) 2000rpm (b) 3000rpm (c) 4000rpm

Figure 6.14 Flux density components in the stator tooth at 2000, 3000, and 4000rpm

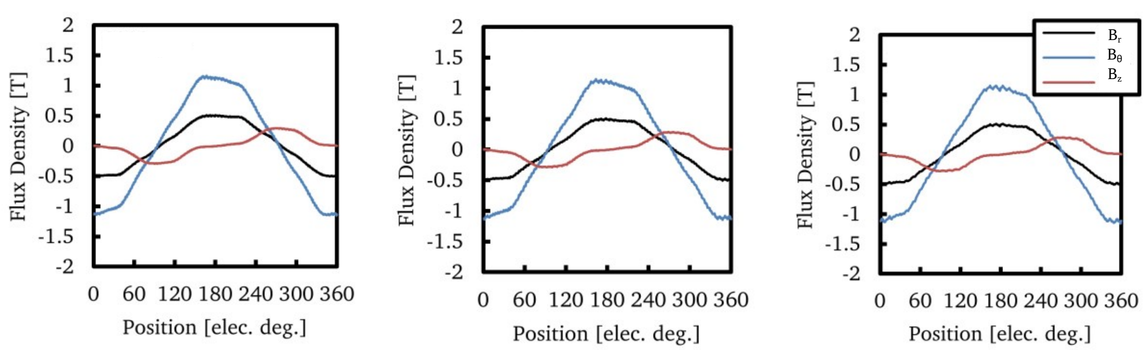

(a) 2000rpm (b) 3000rpm (c) 4000rpm

Figure 6.15 Flux density components in the stator yoke at 2000, 3000, and 4000rpm

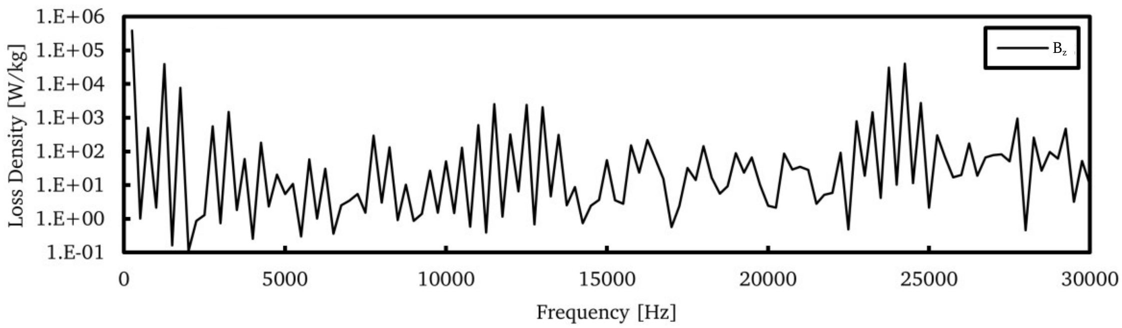

(a) Tooth plane

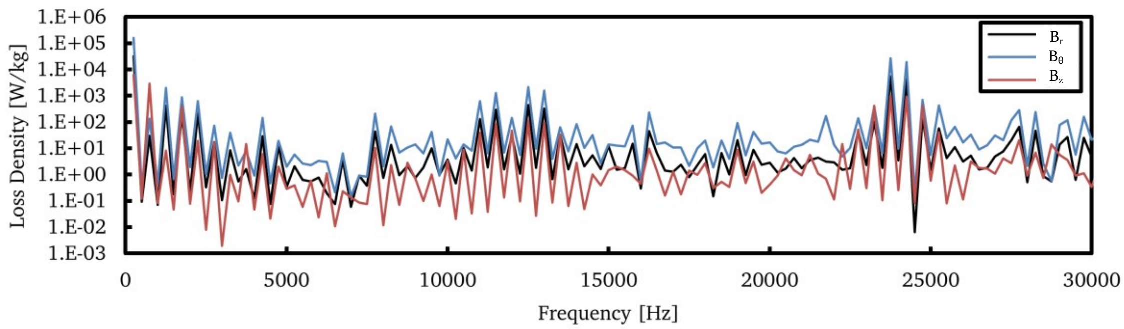

(b) Yoke plane

Figure 6.16 Loss density in the frequency domain at 3000rpm 40Arms

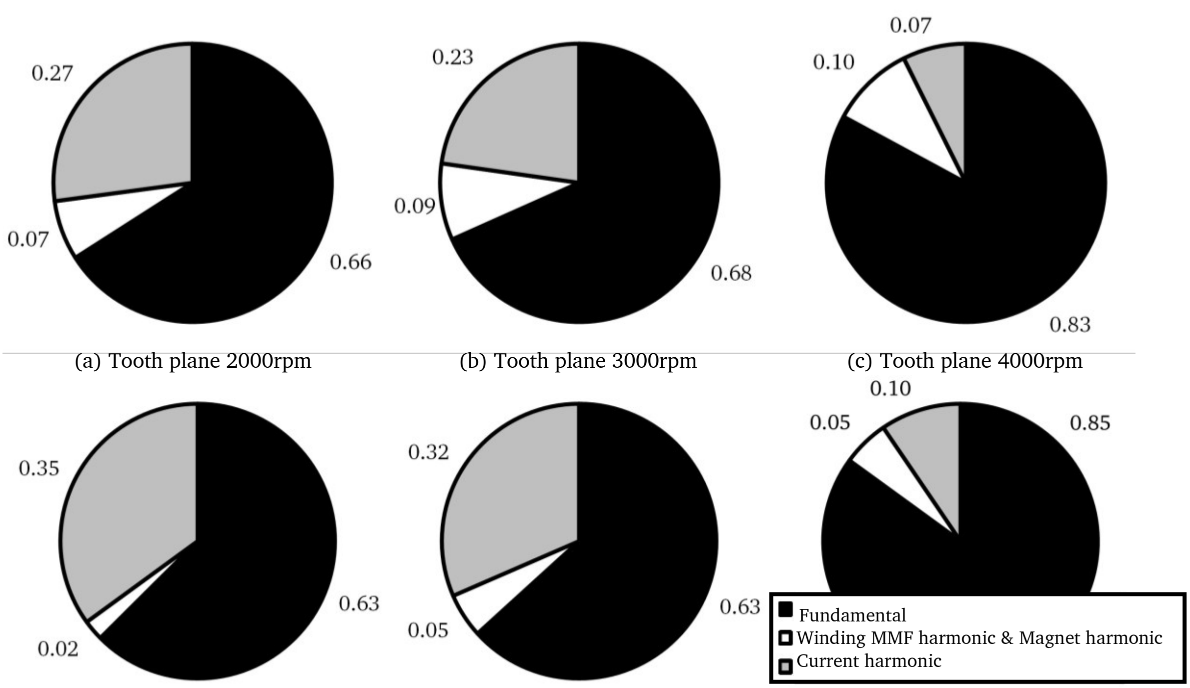

(a) Tooth plane 2000rpm (b) Tooth plane 3000rpm (c) Tooth plane 4000rpm

(d) Yoke plane 2000rpm (d) Yoke plane 3000rpm (e) Yoke plane 4000rpm

Figure 6.17 Core losses attributed to sources

Losses at the fundamental frequency dominate the core loss at all operating points and core locations accounting for 63-85% of the total core loss. Across the operating range the magnet and winding harmonics caused 2-10% of the total losses. The proportion of loss caused by the magnet and winding harmonics is smaller in the yoke than in the tooth, this makes sense since these spatial harmonics diffuse with increasing distance from the source. At the 2000rpm and 3000rpm operating points losses at the switching frequency are relatively high, ranging from 23-35% of the whole. They are much lower at the 4000rpm operating point, accounting for only 7-10% of the whole.

6.2 Assessment of the Relative Importance of the Fluctuating Components of the Loss Fields in an Axial Flux Permanent Magnet Synchronous Machine

This section presents the results of applying the criterion proposed in Chapter 4 to the loss fields predicted by the EM FEA. The resultant time averaged loss fields used in the CHT analysis are shown and discussed.

6.2.1 Application of the Periodic Heat Source Criterion

The resultant current densities in the magnet domains have been processed as described by Equation (3.9) to calculate the spatially averaged magnet and core loss as a function of time. See Figure 6.18 for the resultant transient magnet loss. The value of losses can be seen to vary greatly around their mean values.

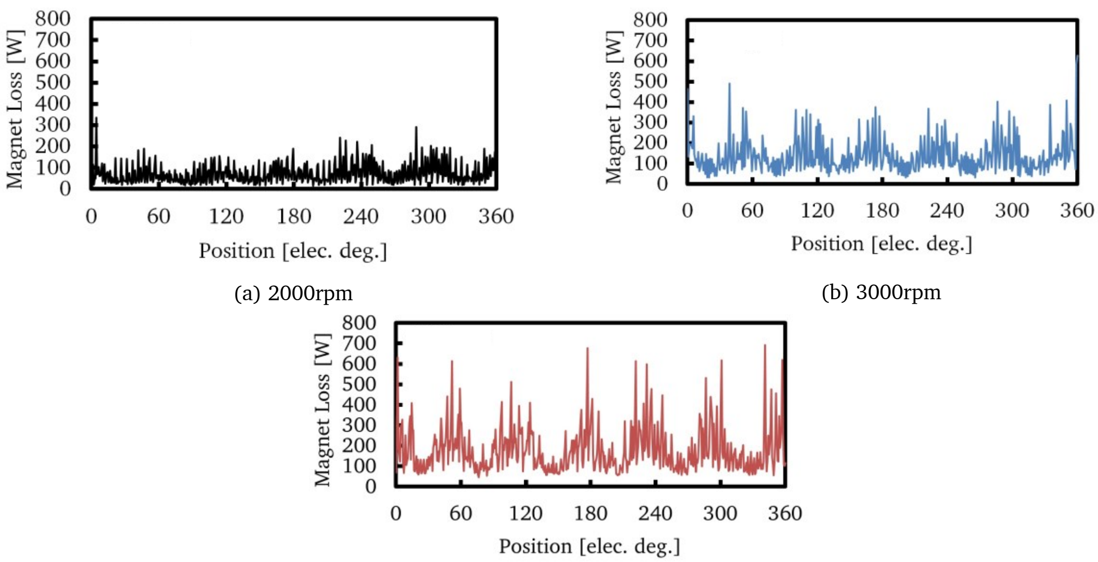

(a) 2000rpm (b) 3000rpm

(c) 4000rpm

Figure 6.18 Time variant magnet losses, the variation is large over a cycle

Characteristic values of fluctuating loss and frequency were defined as shown in Figure 4.6, and the criterion was applied in the same way as the case study presented in Section 4.3. The values calculated for the criterion are shown in Table 6.2. It can be seen that the values are small, and therefore only a small error is incurred by time averaging the loss profiles for use in the CHT analysis. For reference this allowed a steady state analysis with a pseudo-time step of 10s to be used in the solid domain. If the loss profiles had been modelled explicitly then modelling loss variation at the switching frequency would have required a time step of 4.16e-5s, and a computationally expensive transient analysis to be conducted.

Table 6.2 Results of applying the criterion to the fluctuating loss components

Operating point	Magnet Criterion Value	Core Criterion Value	Winding Criterion Value
2000rpm 40Arms	4.17e-7	9.15e-7	6.16e-8
3000rpm 40Arms	3.15e-7	6.45e-7	7.16e-8
4000rpm 40Arms	3.35e-7	6.72e-7	6.64e-8

6.2.2 Processing of the Predicted Loss Profiles

Ansys CFX uses the 'average value theorem' to interpolate between values of loss density specified at points within a domain. In order to minimised the loss in fidelity when transposing the predicted loss profiles from the EM FEA solution to the CHT source term a study was conducted to ensure that a sufficient sample resolution was used. The losses predicted by the EM FEA were sampled over the first 10 time steps using three grids of differing densities, see Figure 6.19.

The results obtained from the sampling procedure are shown in Figure 6.20 where the volume averaged value for magnet losses obtained from each sample grid are compared against the EM FEA solution. As the EM FEA solution only gives values for core loss in the whole domain (rather than the four teeth sampled for the CHT analysis) the volume averaged core losses were compared against the solution obtained by using the finest sample grid. A 1% error between the EM FEA solution and the sampled solution was deemed acceptable and therefore grids 1 and 2 were used to sample the stator core and magnet domain solutions at every time step. The resultant time-averaged, spatially-discretised, loss profiles are presented in non-dimensional format. See Figure 6.21 and Equations (6.3)-(6.8) for a summary of the non-dimensional nomenclature used to define the non-dimensional quantities.

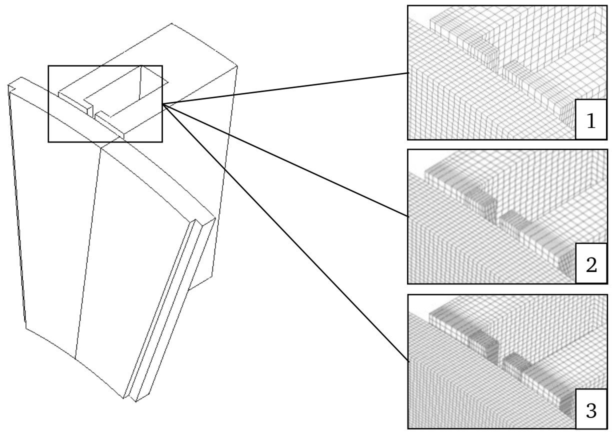

Figure 6.19 Grids used to sample the EM FEA solution

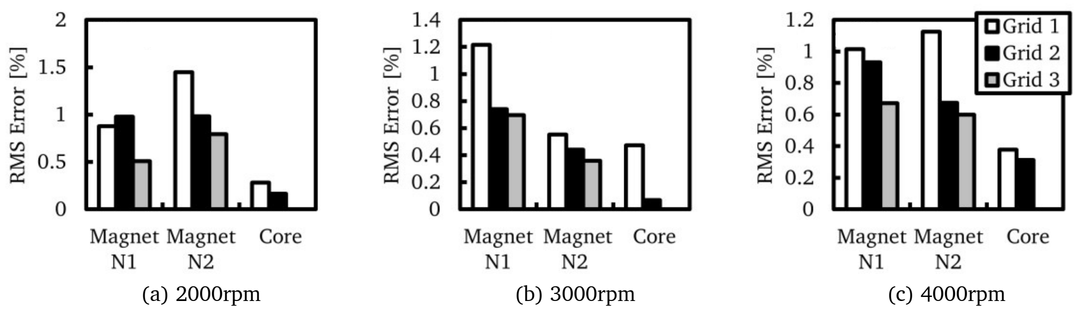

Figure 6.20 Error between sampled loss values and EM FEA predictions at 2000, 3000, and 4000rpm 40Arms

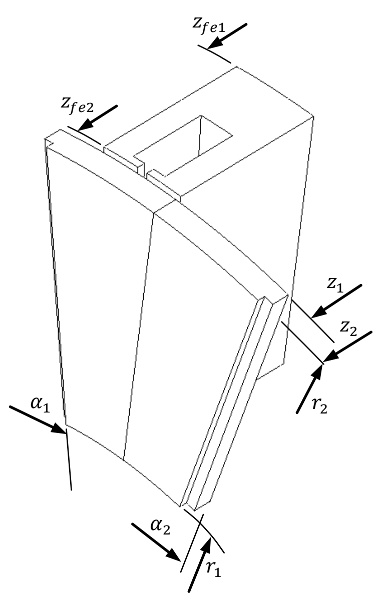

Figure 6.21 Non-dimensional nomenclature used to describe the EM FEA domain

The non-dimensional radial position is defined as:

$$r^* = \frac{r - r_1}{r_2 - r_1} \tag{6.3}$$

A value of $r^* = 0$ therefore represents r_1 while $r^* = 1$ represents r_2.

The non-dimensional axial position in the magnet is defined as:

$$z^* = \frac{z - z_1}{z_2 - z_1} \tag{6.4}$$

A value of $z^* = 0$ therefore represents z_1 while a value of $z^* = 1$ represents z_2.

The non-dimensional angular position in the magnet is defined as:

$$\alpha^* = \frac{\alpha - \alpha_1}{\alpha_1 - \alpha_2} \tag{6.5}$$

A value of $\alpha^* = 0$ therefore represents α_1 while a value of $\alpha^* = 1$ represents α_2.

The non-dimensional magnet loss density is defined as:

$$\dot{q}_m^* = \frac{\dot{q}}{\overline{\dot{q_m}}} \tag{6.6}$$

Where $\dot{q}$ is the local loss density and $\overline{\dot{q_m}}$ is the average loss density in the magnet.

The non-dimensional axial position in the core is defined as:

$$z_{fe}^* = \frac{z - z_{fe1}}{z_{fe2} - z_{fe1}} \tag{6.7}$$

A value of $z_{fe}^* = 0$ therefore represents z_{fe1} while a value of $z_{fe}^* = 1$ represents z_{fe2}.

The non-dimensional core loss density is defined as:

$$\dot{q}_{fe}^* = \frac{\dot{q}}{\overline{\dot{q_{fe}}}} \tag{6.8}$$

Where $\dot{q}$ is the local loss density and $\overline{\dot{q_{fe}}}$ is the average loss density in the core.

The resultant time-averaged, spatially-discretised, loss profiles are presented in non-dimensional form in Figure 6.22 to Figure 6.25.

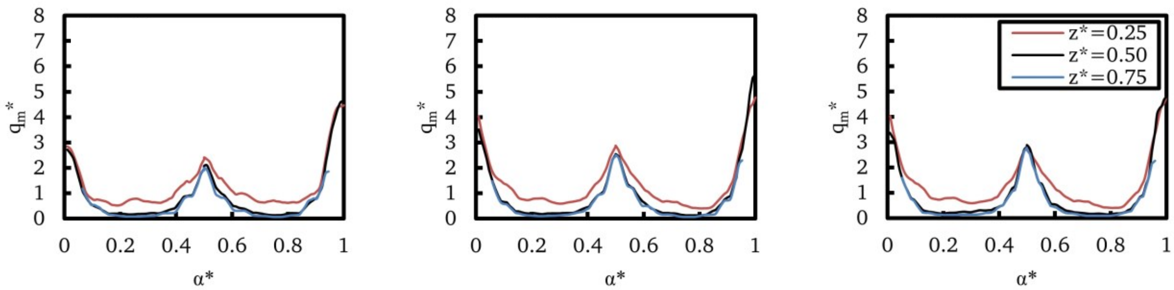

(a) r*=0.25 (b) r*=0.50 (c) r*=0.75

Figure 6.22 Time averaged magnet loss density, 2000rpm 40Arms

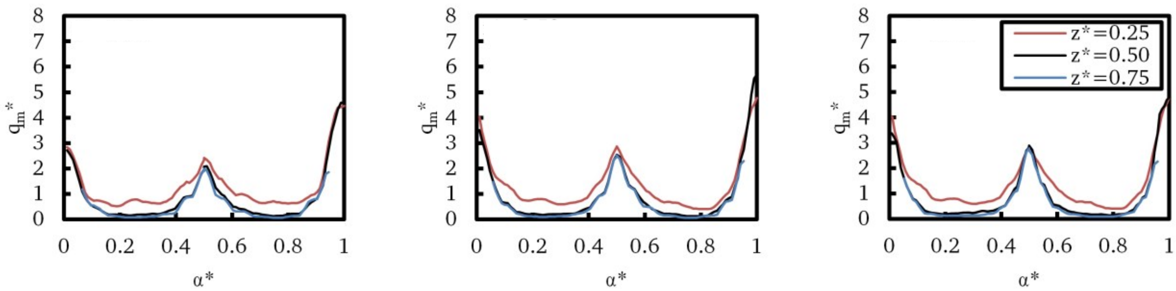

(a) r*=0.25 (b) r*=0.50 (c) r*=0.75

Figure 6.23 Time averaged magnet loss density, 3000rpm 40Arms

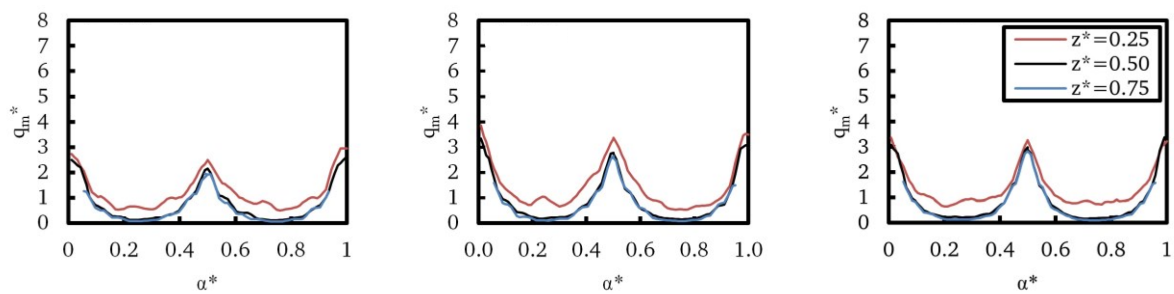

(a) r*=0.25 (b) r*=0.50 (c) r*=0.75

Figure 6.24 Time averaged magnet loss density, 4000rpm 40Arms

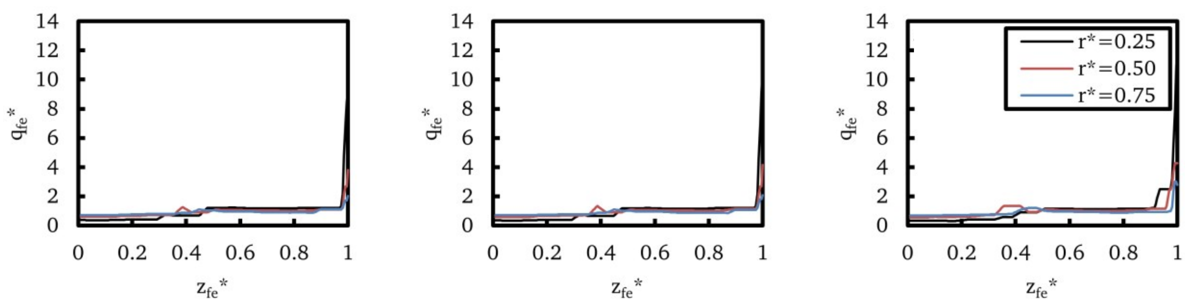

(a) 2000rpm (b) 3000rpm (c) 4000rpm

Figure 6.25 Time averaged stator core loss density at the centre of the tooth

The distribution of losses in the magnet domain is concentrated at the edges of the magnet segments (note that $\alpha^* = 0.5$ is the boundary between the two segments), a result pre-empted by the skin depth calculations in Section 3.1.4. The previous finding that the losses in segment N1 are higher than in segment N2 for the 2000rpm and 3000rpm operating points is again seen here where the loss density is seen to peak at $\alpha^* = 1$. It should be noted that even though a fine mesh was used to generate and sample the solution the predicted loss profile is not smooth. This may suggest that an even finer mesh is required in the electromagnetic FEA. A further investigation was not possible within the time scale of this project, as the computational time required for each loss field prediction was 2 weeks. The 'ripples' in the loss field are also small when compared with the peak values seen at the edges of the domain, thus the major features of the loss profile were incorporated in the CHT analysis.

The distribution of losses in the stator core domain follows from the flux density loadings shown in Figure 6.14 and Figure 6.15. Values of loss density between $0.45<z_{fe}<1$ are in the tooth of the core, and can be seen to be higher than in the yoke ($z_{fe}<0.45$), a direct consequence of the higher flux loading in the tooth compared with the yoke. Small differences in loss density as a function of r* can be seen. These are due to the three dimensional nature of the axial flux machine, where the ratio of magnet area to tooth area increases with increasing radius, leading to higher flux loading at the inner radius. The opposite is the case in the yoke where the ratio of magnet area to yoke area decreases with increasing radius, leading to higher magnetic loading and losses at the outer radii.

6.3 Prediction of the Flow and Temperature Fields in an Axial Flux Permanent Magnet Synchronous Machine

The section presents the results of the CHT analysis. It is shown in this section that to understand the shape of the temperature field within the electrical machine (especially the magnets) a thorough understanding of the flow in the internal cavity is required. Hence this section starts with an analysis of the predicted flow and temperature fields within the internal cavity. This is followed by a presentation of the predicted temperature fields within the key electromagnetic components (the magnets, stator core, and winding).

6.3.1 Predicted Velocity Field in the Fluid Domain

Figure 6.26 reviews the shape of the internal cavity of the machine for the reader, and introduces the terminology used in this section to describe the domain. A one quarter periodic slice of the domain is shown here for clarity, for a full description of the domain please refer back to Figure 3.13 in Section 3.2.5.

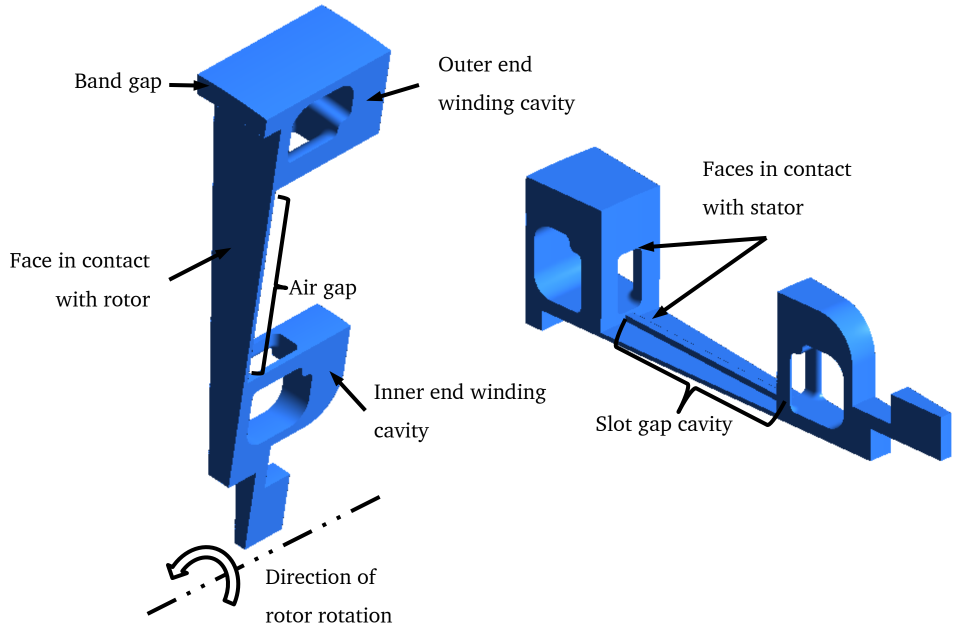

Figure 6.26 Terminology used to describe areas of the inner cavity

Throughout this section vector and contour plots will be presented. These have been plotted on the planes labelled in Figure 6.27.

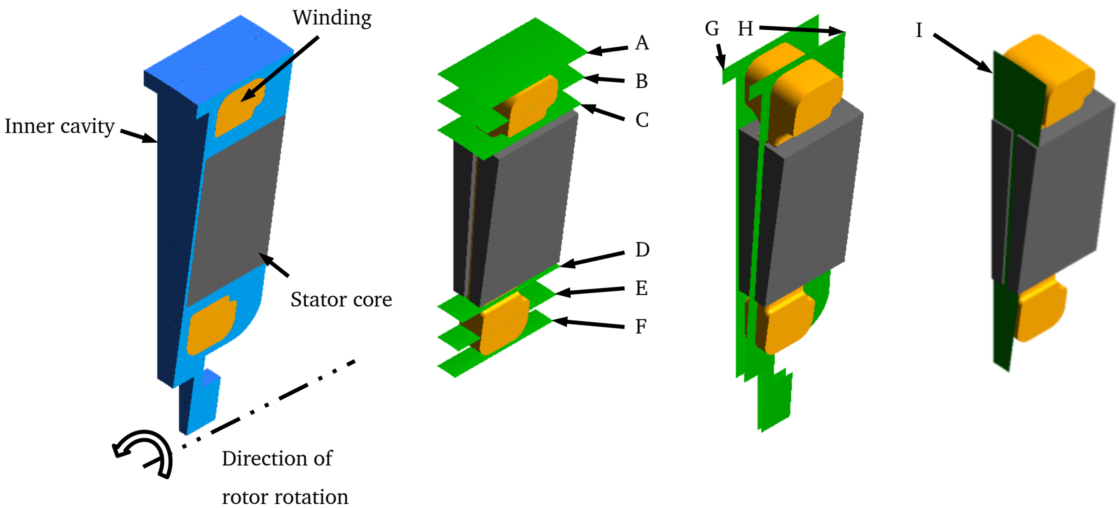

Figure 6.27 Planes used to plot quantities in the inner cavity

Air Gap

Figure 6.28 shows velocity streamlines throughout the fluid domain. It can be seen that the predominant flow direction is circumferential. This motion is induced by the rotation of the rotor, and is described in Figure 6.29 which presents the circumferential velocity profiles in the air gap against axial position within the air gap. In this figure the velocities have been non-dimensionalised against the tip speed of the rotor, and the axial position has been non-dimensionalised such that 0 is the stator face and 1 is the rotor face. The plot shows velocity profiles at three non-dimensional radial locations where r*=0 is the stator core inner diameter and r*=1 is the stator core outer diameter. The rotation of the fluid induces a centrifugal force on the fluid elements which in turn induces a radial out flow of fluid in the air gap, this can be seen in the radial velocity profiles presented in Figure 6.29. Conservation of mass means that the fluid flowing radially out through the air gap must be replaced. As the system is enclosed it follows that the fluid must 'replace itself'. In a traditional annular cavity fluid would be seen flowing radially down the stator face in order to replace the fluid flowing radially out at the rotor face. This is also the case here, though the slot gap acts as additional 'return path' for the flow. This can be seen in Figure 6.30 which plots the radial component of velocity along an axial line between the base of the slot gap and the rotor. In this figure the axial position, z*, is defined the same way as in Figure 6.29, a negative value therefore indicates a position within the slot gap.

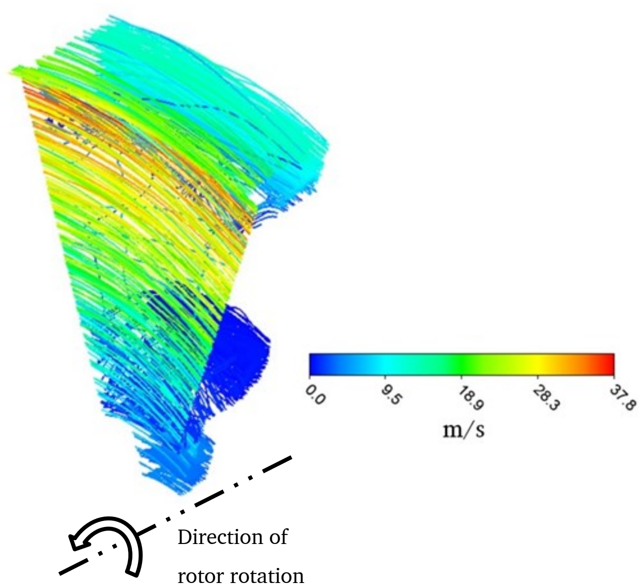

Figure 6.28 Velocity streamlines in the fluid domain, 3000rpm 40Arms

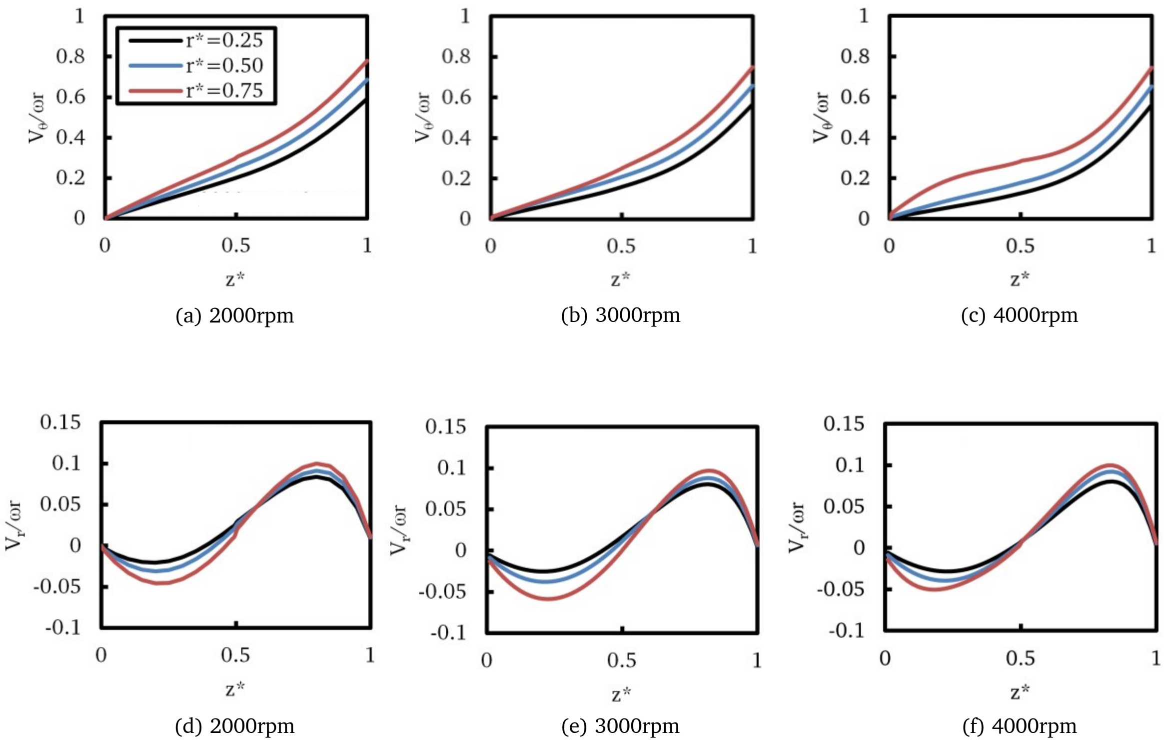

Figure 6.29 Velocity profiles in the air gap, z*=0 is the stator face, z*=1 is the rotor face

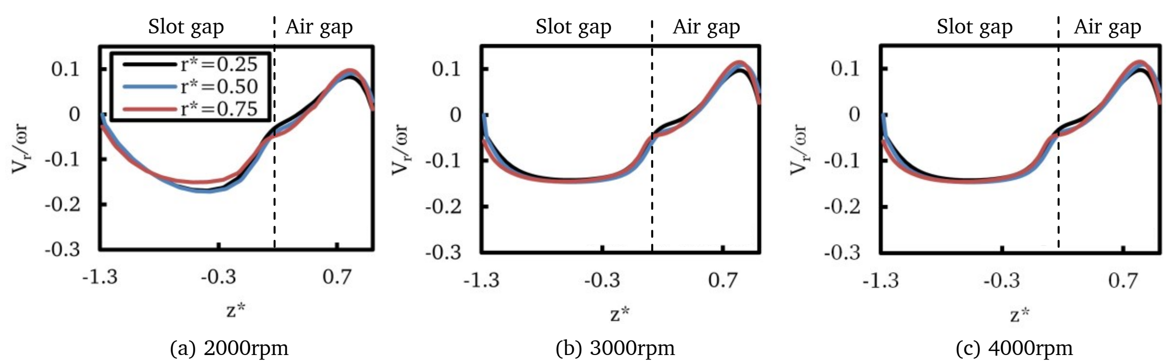

Figure 6.30 Radial velocity in the slot gap

There is almost dimensional similarity between all the predicted air gap flow regimes. In general they are similar to the standard laminar flow seen in a rotor-stator system, however the effects of transition can be seen at r*=0.75 in the 4000rpm operating point, where this tangential velocity profile begins to resemble the standard turbulent flow velocity profile shown in Figure 6.31.

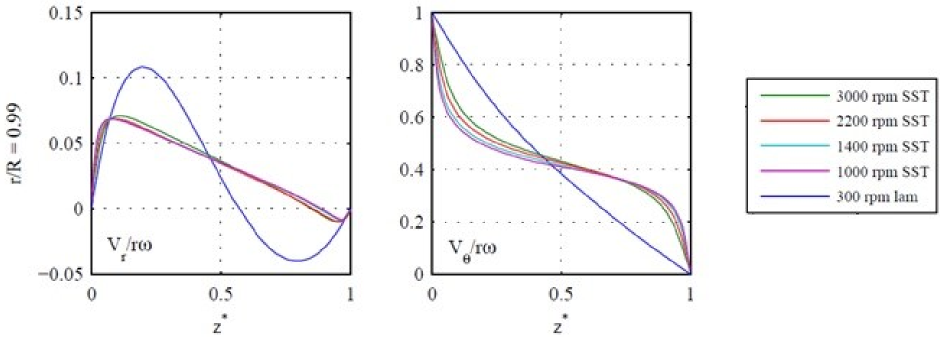

Figure 6.31 Laminar and turbulent velocity profiles in a rotor-stator system G=0.0106, [109]

Outer End Winding Cavity

When the fluid is pumped radially out of the air gap the path it follows to return to the slot gap is via the outer end winding cavity. Together Figure 6.32 to Figure 6.33 describe the flow around the outer end winding for the 2000rpm and 3000rpm operating points. The flow is still predominantly circumferential, with a secondary flow structure recirculating fluid around the end winding: The tangential projection of the velocity vector onto Plane G in Figure 6.32 shows the flow being pumped radially out at the air gap and interacting with a recirculating region of the flow flowing around the end winding. The vector projection onto Plane H shows the same phenomenon; on careful examination of the figure around the slot gap area it appears that the mass flow has 'appeared' from nowhere, before returning down the slot gap. This is simply the three dimensional nature of the flow, the fluid is being entrained orthogonally from the projected plane. This can be seen in the streamlines plotted around the end winding in Figure 6.33, and the vector plot in Figure 6.34.

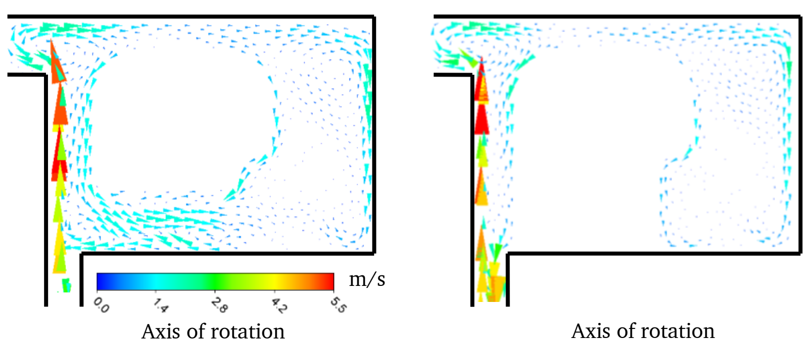

(a) Plane G (b) Plane H

Figure 6.32 Radial-axial velocity vectors of flow around the outer end winding 3000rpm

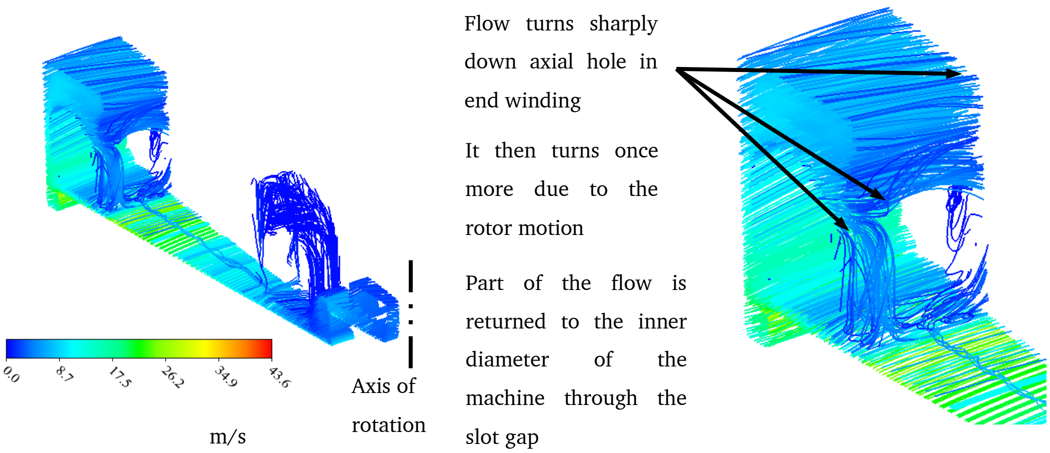

Figure 6.33 Streamlines of flow around the outer end winding

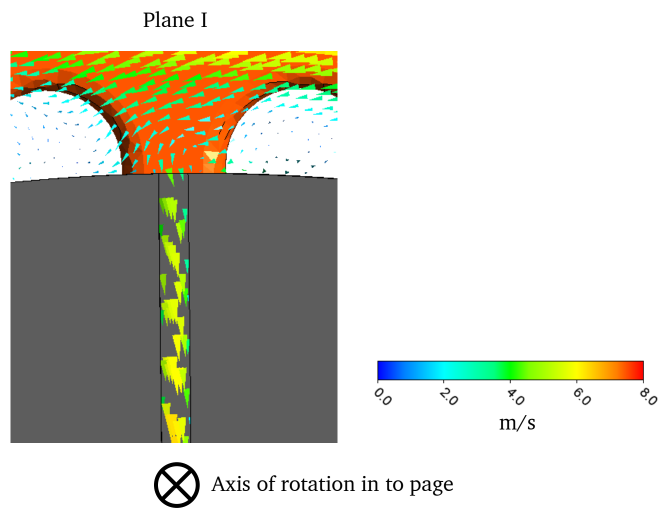

Figure 6.34 Tangential-radial velocity vectors of flow returning down the slot gap

It is instructive to view the recirculating region as it is presented in Figure 6.35. In plane A, as the flow moves away from the rotor the axial component of the velocity vector grows until it begins to be suppressed by the casing. As the fluid moves down from Plane A through Plane B to Plane C near the casing the axial component changes direction and begins to point back towards the rotor. As the flow must return through the axial holes in the winding it is forced to turn sharply and becomes almost completely axial. As the flow turns it separates from the downstream wall of the winding and is pushed against the upstream wall. After flowing through the axial holes it is then forced to turn again due to the rotation of the rotor where it then splits, some of the flow returns to the inner diameter of the machine through the slot gap while the rest is centrifuged back out and around the end winding by the rotor.

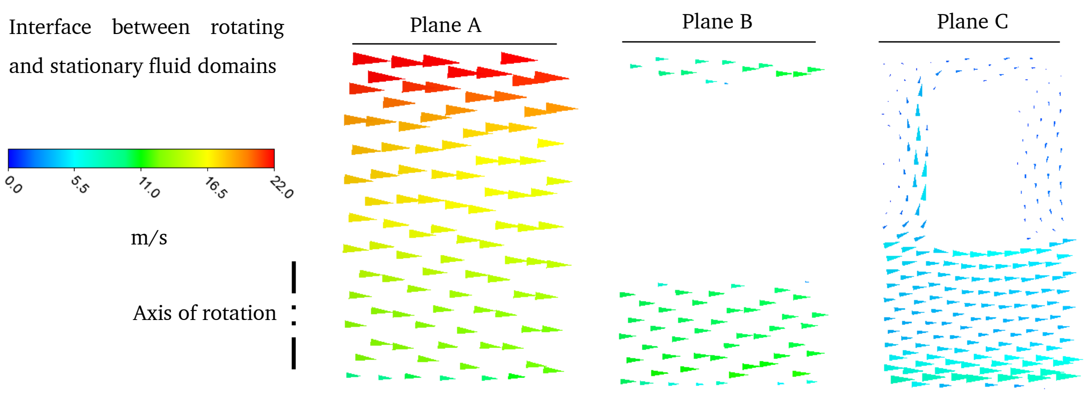

Figure 6.35 Tangential-axial velocity vectors of flow around the outer end winding

At the 4000rpm operating point the flow structure around the end winding is slightly different. Figure 6.36 compares the flow around the outer end winding for the 3000 and 4000rpm operating points. Whereas at 3000rpm the flow appeared to return to the air gap via two mechanisms (recirculating regions *in front* of the end winding and *around* the end winding) at the 4000rpm operating point the flow appears to mainly return to the air gap via the path *around* the end winding. This is because the flow has begun to transition to turbulence between the two operating points. Figure 6.37 plots the ratio between the eddy viscosity and the molecular viscosity, μ_t/μ. It can be seen that the effective viscosity at 4000rpm is much higher than at 3000rpm, forcing more recirculation flow around the outer end winding.

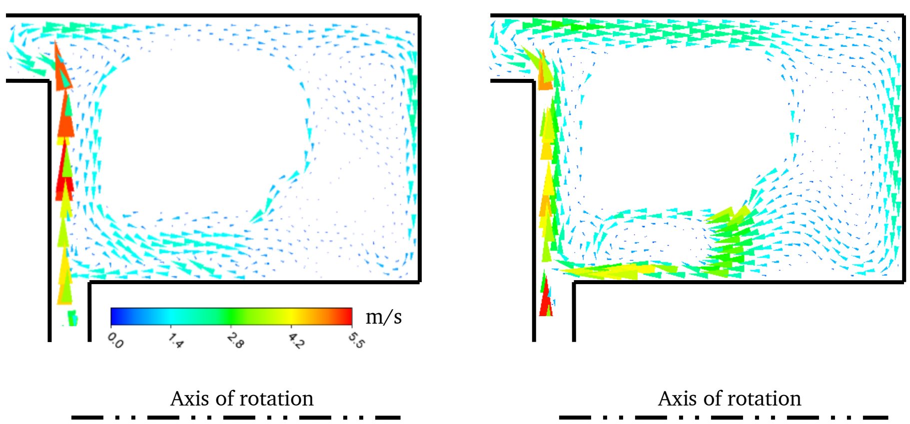

(a) 3000rpm, Plane G

(b) 4000rpm, Plane G

Figure 6.36 Radial-axial velocity vectors of flow around the outer end winding at 3000 and 4000rpm

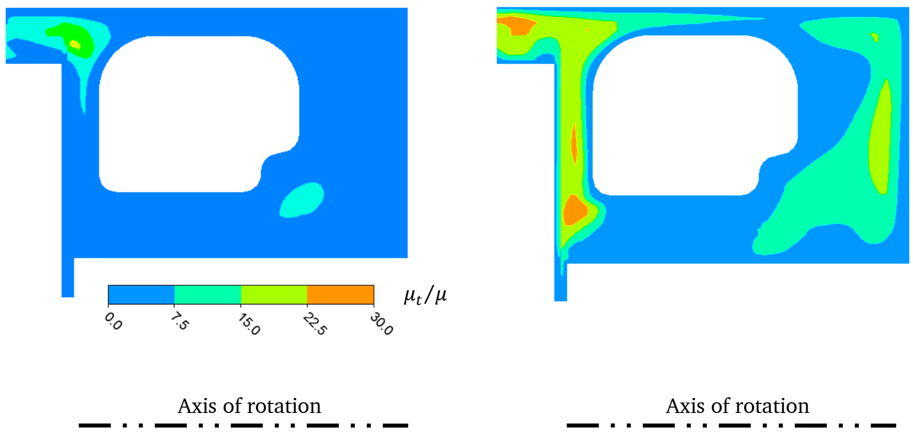

(a) 3000rpm (b) 4000rpm

Figure 6.37 Viscosity ratio at the outer end winding region

Inner End Winding Cavity

Turning now to the flow structure around the inner end winding, the flow can be seen to exit the slot gap and turn (due to the motion of the rotor) into the inner end winding domain, see Figure 6.38. The flow then moves down the front face of the inner end winding where it is then entrained by the rotor, this can be seen in Figure 6.39. The remaining flow in the domain is mainly circumferential, with little interaction with the main flow paths seen in the air gap.

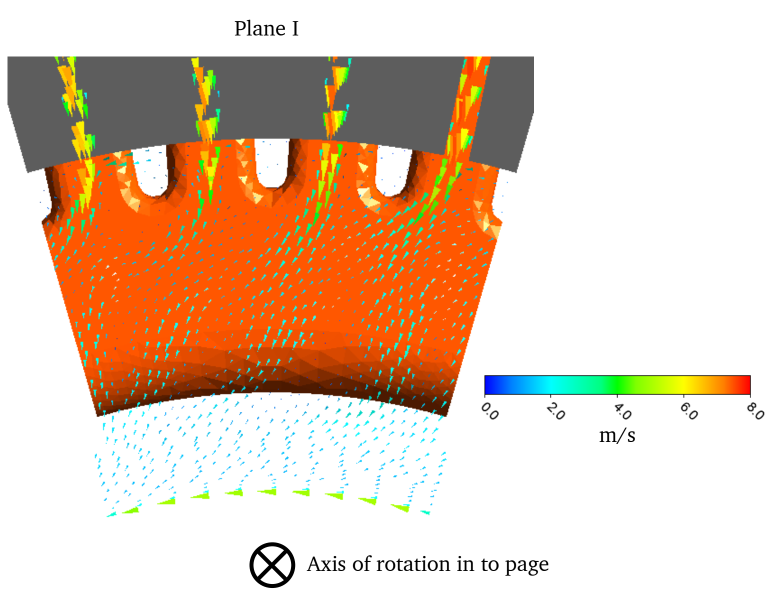

Figure 6.38 Circumferential-radial velocity vectors of flow entering the inner end winding region

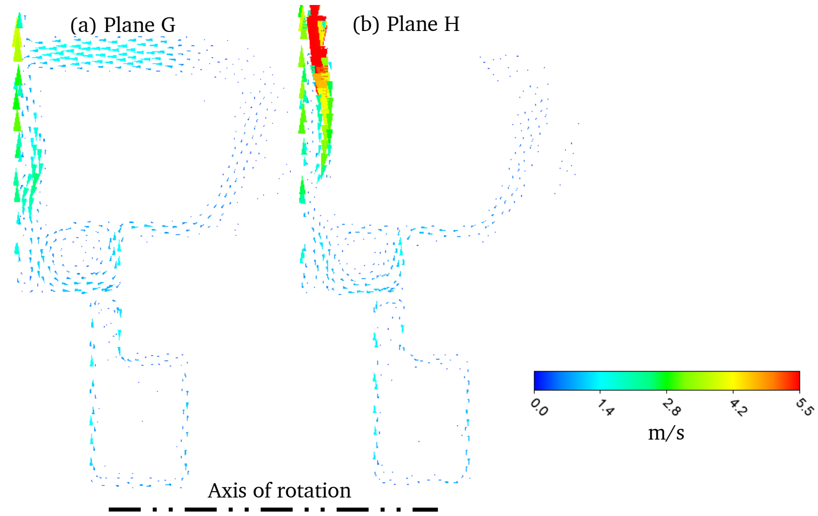

Figure 6.39 Radial-axial velocity components of flow around the inner end winding

6.3.2 Predicted Temperature Field and Heat Flux through the Fluid Domain

The Air Gap

Now that the velocity field is well understood, the temperature field can be interpreted. Figure 6.40 presents the predicted temperature field on plane G and H in the fluid domain for the 3000rpm 40Arms operating point (N.B. the aspect ratio of the air gap has been exaggerated for clarity). As can be seen in the figure, cool air is entrained by the rotor from the inner end winding cavity where it then flows over the rotor face and heats up as it convects heat away from the rotor. The plot on Plane H in the figure shows the fluid temperature in the slot gap. Air temperature is relatively low here as the air has been cooled by the outer casing as it flowed around the outer end winding. Figure 6.41 present plots of temperature profile across the air gap at different radial positions (where $r^*=0$ is the inner diameter and $r^*=1$ is the outer diameter of the stator core respectively). As was the case with the velocity profiles, a value of $z^*<0$ indicates a value in the slot gap.

Figure 6.42 shows the temperature rise in the air gap as a function of radius at five axial locations. Note that $z^*=0$ is the stator core face and $z^*=1$ is the magnet face. The 2000rpm and 3000rpm operating points are seen to be dimensionally similar, with a smooth increase in temperature through the air gap at $z^*=0.75$, which is in the rotor boundary layer. At $z^*=0.25$, in the stator boundary layer, where fluid is flowing back down the stator face, cold fluid is seen to enter the domain at $r^*=1$. This fluid quickly heats up between $0.9<r^*<1$ as is comes into contact with the warm air in the rotor boundary layer. When $r^*<0.9$ the fluid in the stator boundary layer is being cooled by the stator face, and a decrease in temperature is seen as r* decreases.

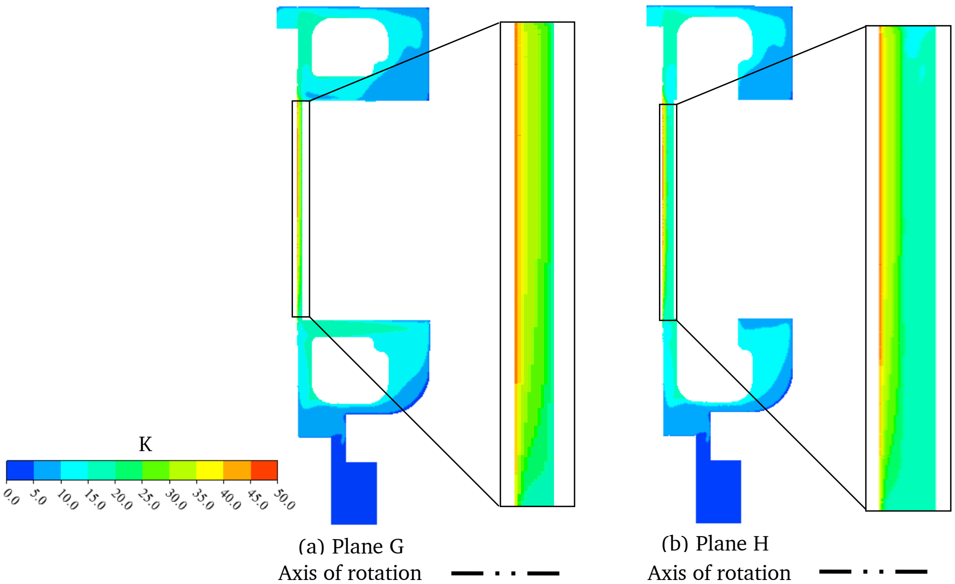

Figure 6.40 Temperature contours in the air gap, 3000rpm 40Arms

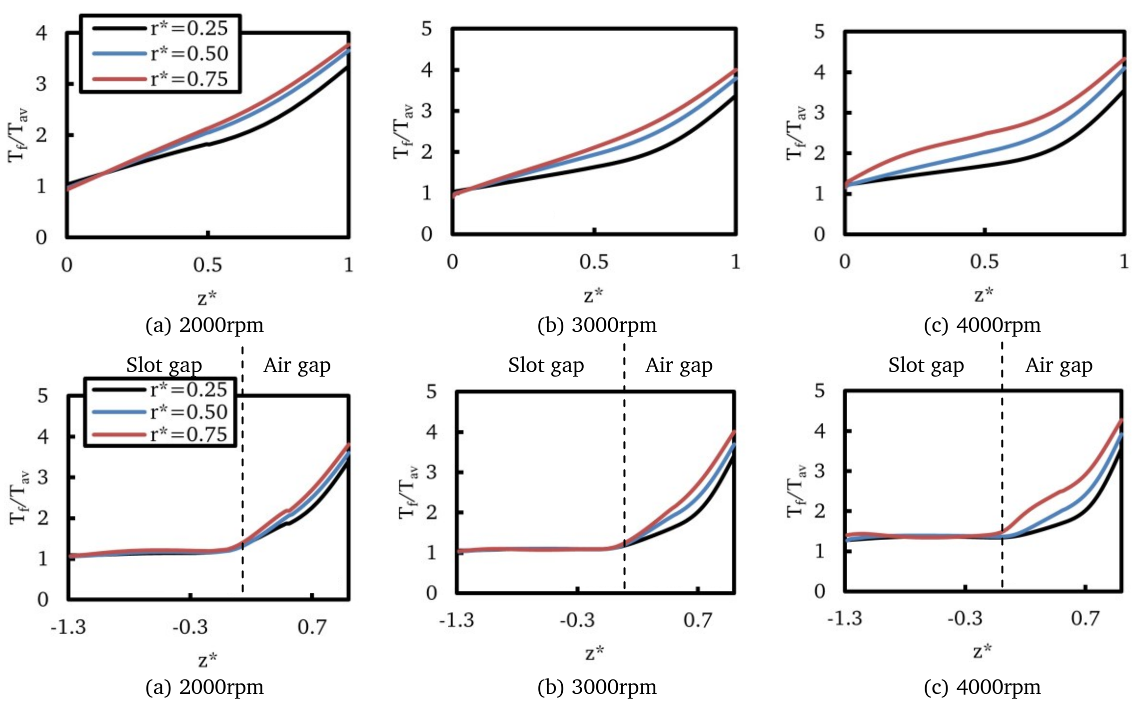

Figure 6.41 Temperature profile across the air gap including the slot gap, z*=0 is the stator face, z*=1 is the rotor face

The temperature rise through the air gap for the 4000rpm operating point shares the same basic features as the 2000rpm and 3000rpm operating points, though a distinct difference can be seen when r*>0.7. In this region there is a sudden increase in temperature throughout both rotor and stator boundary layers. This is due to the model predicting the onset of transition to turbulence in this area, with a corresponding increase in mixing and therefore heat flux across the air gap. This can be seen in Figure 6.43, which plots the ratio of turbulent to conductive heat flux in the axial direction in the air gap.

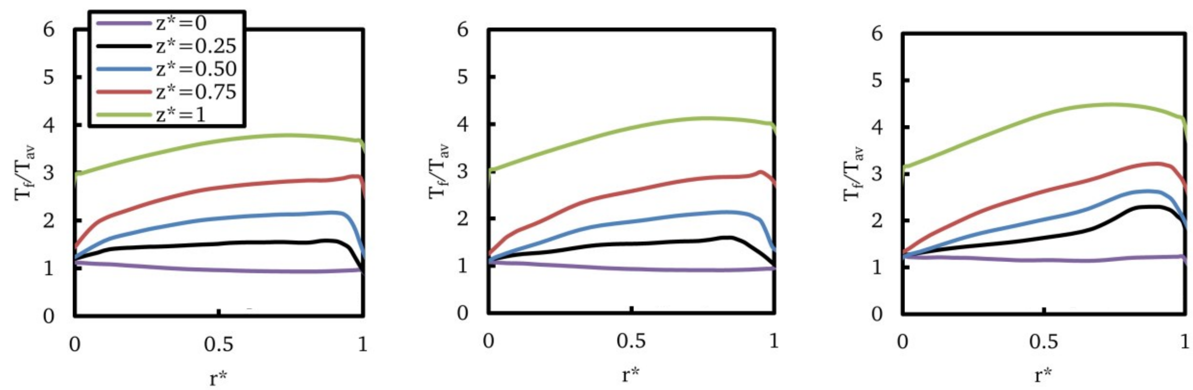

(a) 2000rpm (b) 3000rpm (c) 4000rpm

Figure 6.42 Temperature rise through the air gap, 2000 and 3000rpm 40Arms, z*=0 is the stator face, z*=1 is the rotor face

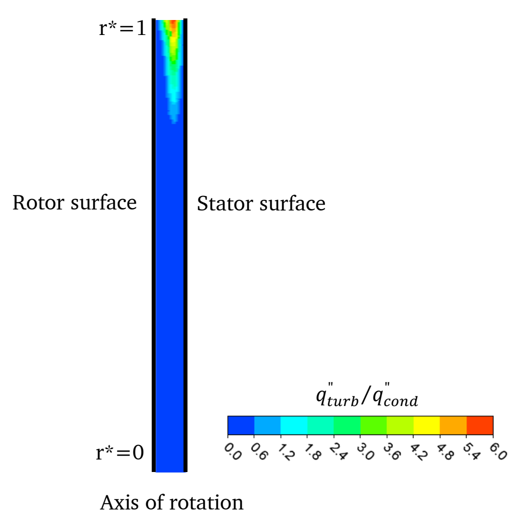

Figure 6.43 Ratio of turbulent to conductive heat flux across the air gap at 4000rpm 40Arms, r*=0 is the inner magnet radius, r*=1 is the outer magnet radius

Outer end winding region

Figure 6.44 shows temperature contours in the outer end winding region. As fluid exits the air gap it immediately mixes with the cooler fluid recirculating around the end winding. As the fluid leaves the outer tip of the rotor and flows between the outer casing and the end winding it is cooled by the casing.

Inner end winding region

Figure 6.45 shows temperature contours in the inner end winding cavity. As stated during the review of the flow field, the fluid is quickly entrained by the rotor and re-enters the air gap. There is therefore little interaction here in terms of heat transfer, as the fluid leaves the air gap it has already been cooled significantly by the outer casing and stator face.

Overview of Heat Transfer through the Fluid Domain

Table 6.3 gives an overview of the heat being transferred into, and out of, the fluid domain. In these figures the non-dimensional value of heat q_f^* moving into, or out of, the domain is described by Equation (6.9).

$$q_f^* = \frac{q}{q_f} \tag{6.9}$$

The variable q_f is the total amount of heat entering the fluid domain. Note that the fluid is also generating its own internal heat through viscous heating. A positive value of q_f^* indicates heat moving into the fluid domain. With the results non-dimensionalised like this a similar pattern is seen across all of the operating points investigated. Between 86.8-93.3% of the heat passing through the fluid domain comes from the magnets, banding, and rotor, with the rest coming from the end windings. The main contributors to the cooling of the fluid domain are the stator core (28.1-41.4%) and the casing (56.2-61.6%). Viscous heating in the domain is small, ranging from 2.4-3.6% of the whole.

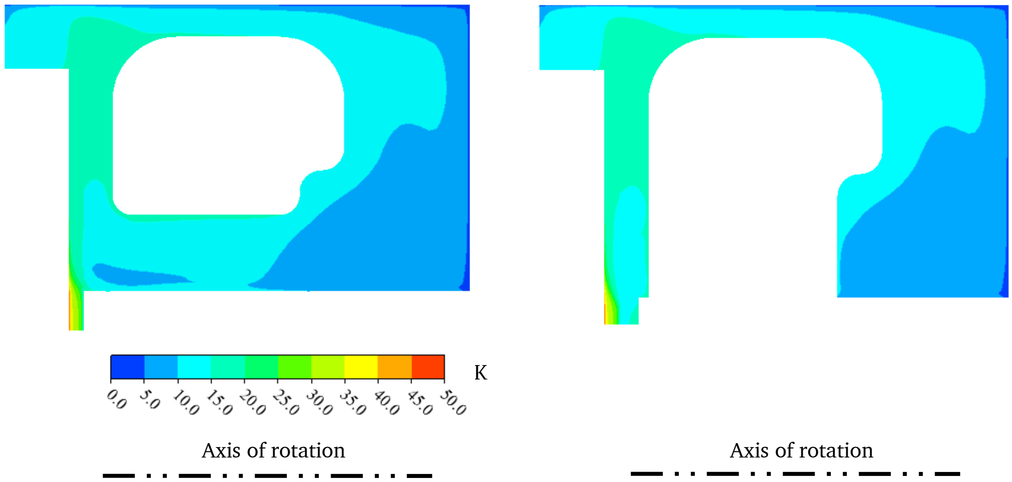

(a) Plane G

(b) Plane H

Figure 6.44 Fluid temperature contours in the outer end winding cavity, 3000rpm 40Arms

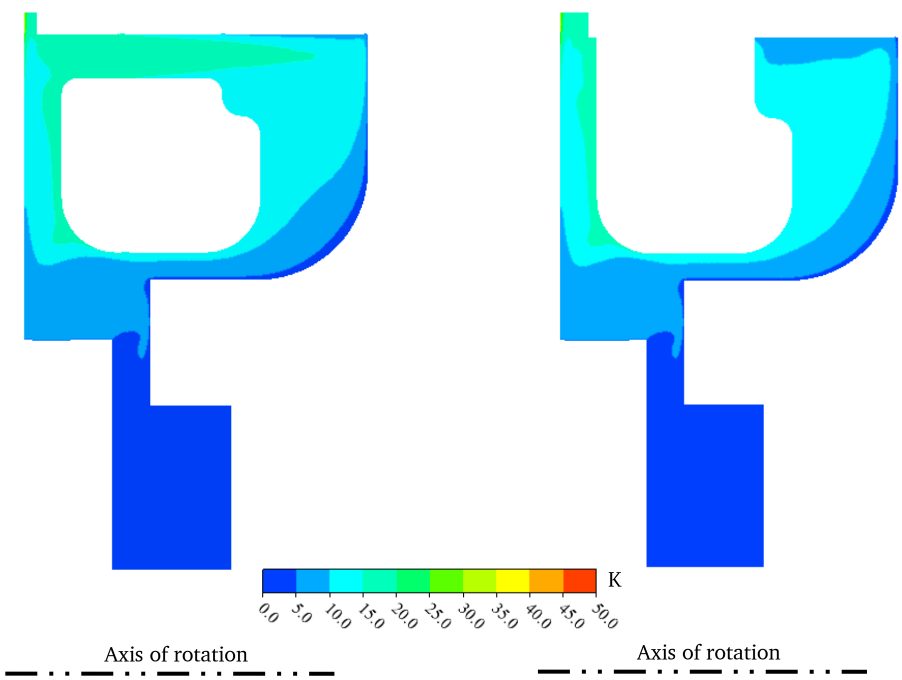

(a) Plane G

(b) Plane H

Figure 6.45 Fluid temperature contours in the inner end winding cavity, 3000rpm 40Arms

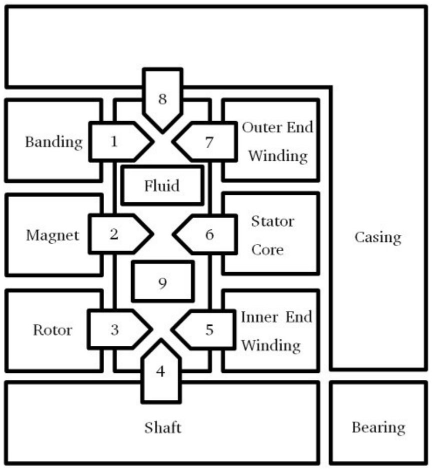

Table 6.3 Heat transfer in the fluid domain

Domain Interaction	Description	q_f^* 2000rpm 40Arms	3000rpm 40Arms	4000rpm 40Arms
1	Banding -Fluid	0.098	0.076	0.115
2	Magnet-Fluid	0.699	0.741	0.666
3	Rotor-Fluid	0.131	0.116	0.087
4	Shaft-Fluid	-0.008	-0.014	-0.014
5	Inner Winding-Fluid	0.029	0.026	0.019
6	Core-Fluid	-0.414	-0.281	-0.327
7	Outer Winding-Fluid	0.102	-0.079	0.032
8	Case-Fluid	-0.562	-0.616	-0.610
9	Viscous heating	0.024	0.031	0.036

6.3.3 Predicted Temperature Field in the Solid Domain

6.3.3.1 Predicted Temperature Field in the Magnets

In order to provide an overview of the solution Figure 6.46 shows contour plots of temperature rise at each operating point. When looking at the data in this 'global' way it can be seen that at all operating points the magnets incur the largest temperature rise, with steep temperature gradient throughout the rotor domain (due to the low thermal conductivity of the rotor material). The hot spots in the magnet domain can be seen to be at the locations where the loss densities presented in Figure 6.24 were largest, i.e. at the edges of each segment.

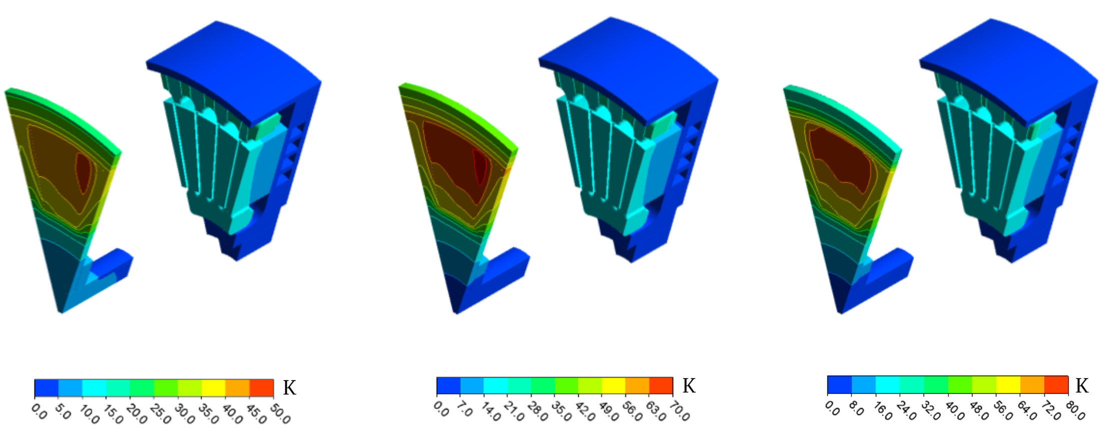

(a) 2000rpm 40Arms (b) 3000rpm 40Arms (c) 4000rpm 40Arms

Figure 6.46 Contour plots of temperature rise at each operating point

Magnet hot spot magnitude and location can be seen more clearly in Figure 6.47 which shows the non-dimensional temperature rise throughout the magnet domain at all operating points. The non-dimensional temperature rise is defined as

$$\theta_m^* = \frac{T - T_\infty}{\bar{T}_m - T_\infty} \tag{6.10}$$

Where T_∞ is the coolant temperature in the coolant jacket.

The choice of the average temperature rise above the reference temperature, $\bar{T}_m - T_\infty$, has been made as it useful build up a picture of how large the hot spots are in comparison to the average temperature. Across the operating points investigated here hot spots exceeded the average temperature by up to 13%. This kind of information would be especially useful during experimental work where (in this work at least) the *average* magnet temperature is measured via the BEMF.

Figure 6.47 shows an increase in magnet temperature with radius. This can be explained by the increase in fluid temperature in the air gap with radius seen in Figure 6.42. Figure 6.47 also shows that the leading edge of the magnet is consistently cooler than the trailing edge. The reason for this can be seen in Figure 6.48, which shows non-dimensional temperature rise plotted on streamlines in the air gap (the image on the far left of the figure serves to orient the reader). The streamlines are plotted in the rotating frame of reference, and it can be seen that the fluid heats up as it flows over the face of the magnets, leading to higher temperatures at the trailing edge of the magnet. The non-dimensional temperature rise θ_a^* has been defined as $\theta_a/\overline{\theta_a}$, where $\theta_a = T_a - T_\infty$.

The relative contribution of convection and conduction to the cooling of the magnets (radiation was neglected by the model, see Section 3.2.5.3) has been determined and is shown in Table 6.4. In these figures the non-dimensional value of heat q_{rot}^* moving into, or out of, the rotating domain is defined by Equations (6.11).

$$q_{rot}^* = \frac{q}{q_m} \tag{6.11}$$

Where q_m is the total magnet loss. A positive value denotes heat moving into the first domain listed in the relationship. For example, Magnet-Fluid q_{rot}^*=-0.752 indicates that 75.2% of the heat being generated in the magnets is being transferred into the fluid domain.

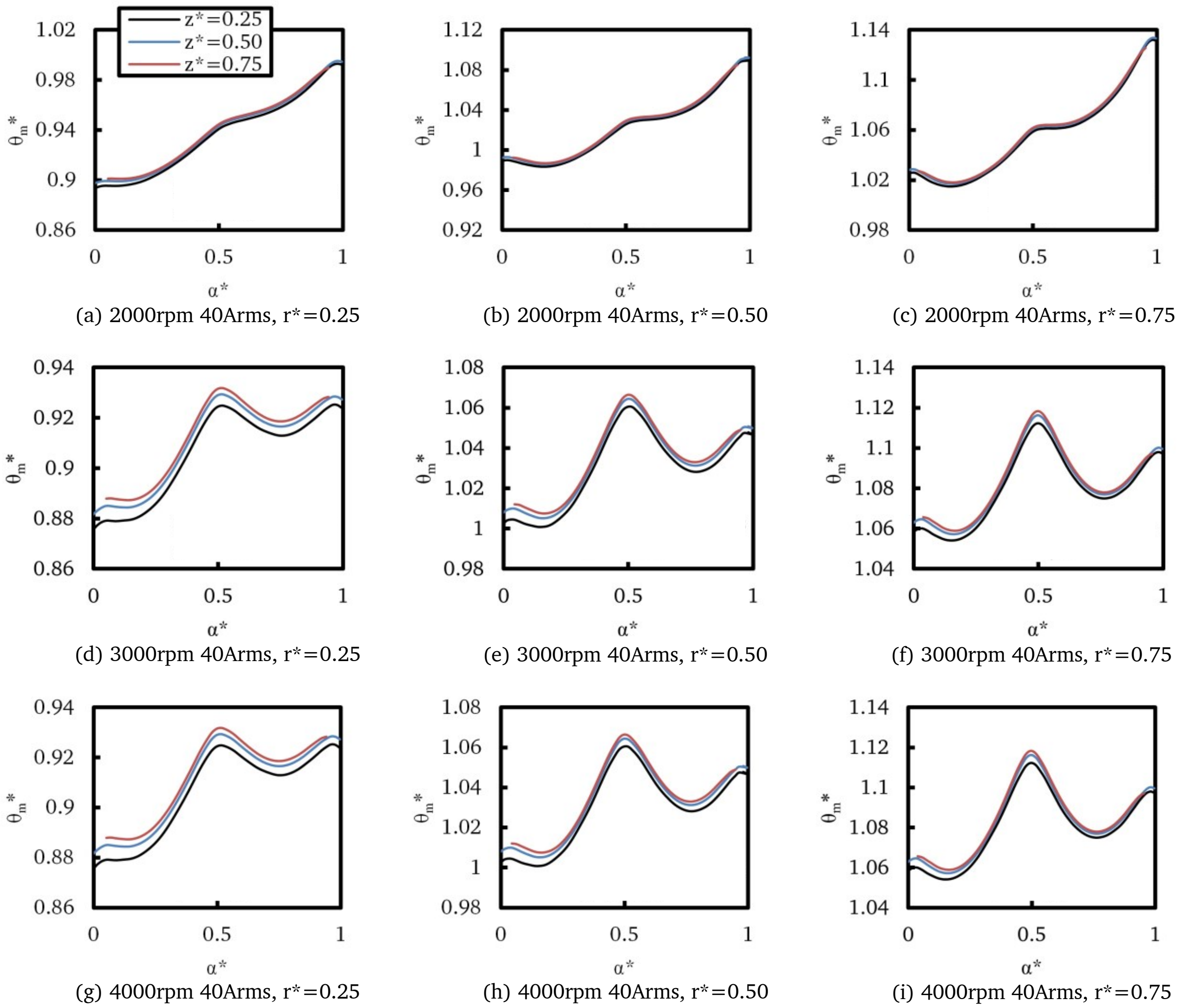

Figure 6.47 Non dimensional temperature rise in the magnet domain

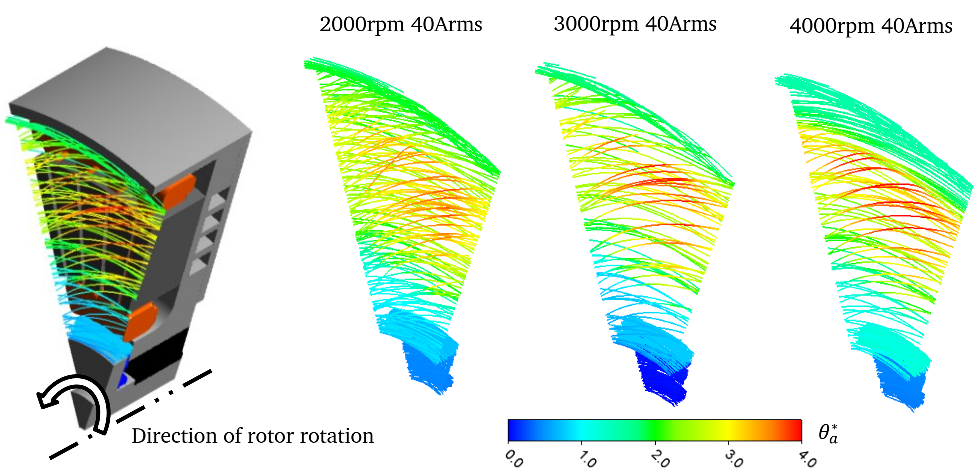

Figure 6.48 Non-dimensional temperature rise along streamlines in the fluid domain, rotating frame of reference

For every operating point the table shows that the majority (75.2-79.2%) of the heat generated in the magnet is transferred into the fluid in the air gap. Almost all of the rest of the heat generated by the magnets is first conducted into the banding (8.3-10.5%) and rotor (11.2-14.6%) domains before also being transferred into the fluid in the air gap. Only 0.5% of the heat generated is conducted to the shaft, this heat is joined by another 0.8-1.6% being transferred from the fluid to the shaft (which could be from any of the heat generating domains). This heat is conducted through the bearing and dissipated by the casing to the coolant.

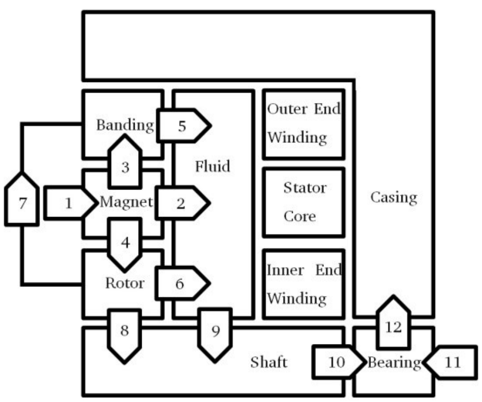

Table 6.4 Heat transfer in the rotating domain

Domain Interaction	Description	q^*_{rot} 2000rpm 40Arms	3000rpm 40Arms	4000rpm 40Arms
1	Magnet Loss	1	1	1
2	Magnet-Fluid	-0.752	-0.792	-0.766
3	Magnet-Banding	-0.105	-0.083	-0.126
4	Magnet-Rotor	-0.146	-0.129	-0.112
5	Banding-Fluid	-0.105	-0.082	-0.132
6	Rotor-Fluid	-0.141	-0.124	-0.100
7	Rotor-Banding	0.000	0.001	-0.006
8	Rotor-Shaft	-0.005	-0.005	-0.005
9	Shaft-Fluid	0.008	0.015	0.016
10	Shaft-Bearing	-0.014	-0.020	-0.020
11	Bearing Loss	0.142	0.076	0.060
12	Bearing-Casing	-0.156	-0.096	0.080

In terms of thermal management of the permanent magnets it has been shown in this section that the net heat flux is out of the magnet domain, with the magnet temperature 'sitting above' the air gap and rotor temperatures. This means that the magnet temperature rise above the surrounding components is due to the losses generated within them (rather than heat being transferred to them from other components). The magnets are not in the thermal path of any other heat generating component. A reduction in magnet losses would therefore lead to a direct reduction in magnet temperature. A reduction in magnet losses may be achieved by any of the methods previously discussed in the literature review of Chapter 2, these included: Segmentation, eddy current shields, rotor and stator shapes, and winding layout. With regards to this machine, as the largest contributor to losses are the current harmonics an additional possibility may be to investigate alternative inverter switching strategies.

6.3.3.2 Predicted Temperature Field in the Stator

Turning now to the stator core temperature field, it can be seen in Figure 6.49 that for all operating points there is a strong temperature gradient between the stator air gap face and the face in contact with the casing. Here $z^* = 0$ is the face in contact with the casing and $z^* = 1$ is the face in contact with the air gap. A value of $r^* = 0$ represents the inner diameter of the stator core, while $r^* = 1$ represents the outer diameter.

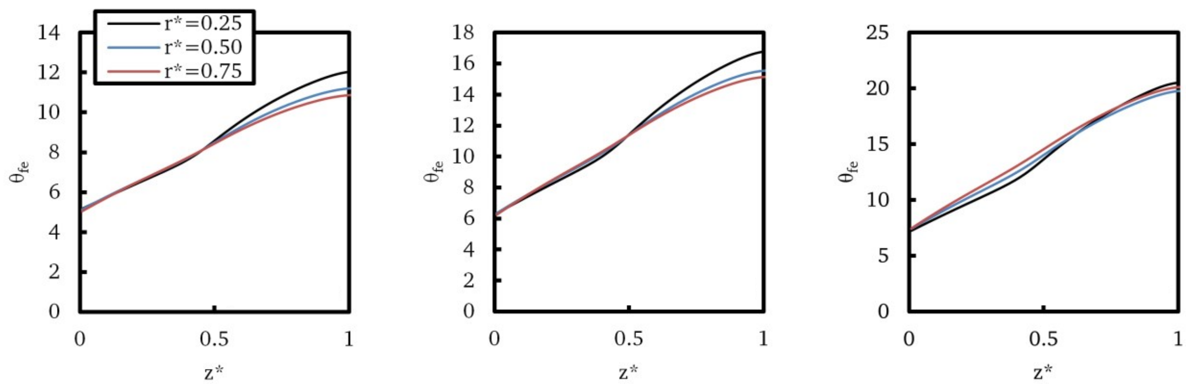

(a) 2000rpm 40Arms (b) 3000rpm 40Arms (c) 4000rpm 40Arms

Figure 6.49 Stator core temperature profiles, z*=0 is the face in contact with the casing and z*=1 is the face in contact with the air gap

The shape of the profile can be understood by first examining the domain interactions between the stator and the surrounding components, shown in and Table 6.5, where all values of heat transfer rate have been non-dimensionalised against the total loss generated in the stator, see Equation (6.12).

$$q^*_{stat} = \frac{q}{q_{cu} + q_{fe}} \tag{6.12}$$

Where q_{cu} is the winding loss and q_{fe} is the stator core loss. A positive value denotes heat moving into the first domain listed in the relationship. For example, Winding-Core q^*_{stat}=-0.157 indicates that 15.7% of the heat being generated in the stator is being transferred from the winding into the core.

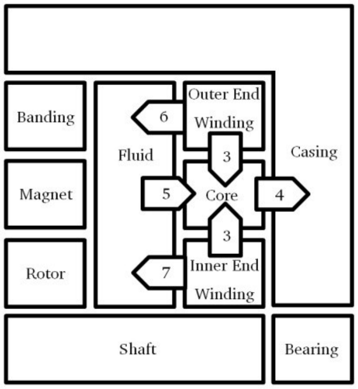

Table 6.5 Heat transfer in the stator domain

Domain Interaction	Description	q^*_{stat} 2000rpm 40Arms	3000rpm 40Arms	4000rpm 40Arms
1	Core Loss	0.836	0.893	0.918
2	Winding Loss	0.164	0.107	0.082
3	Winding-Core	-0.157	-0.114	-0.071
4	Core-Case	-1.063	-1.064	-1.056
5	Fluid-Core	-0.065	-0.530	-0.064
6	Outer Winding-Fluid	0.000	-0.015	-0.006
7	Inner Winding-Fluid	-0.005	-0.005	-0.004

It can be seen that all of the heat generated in the stator core is dissipated by conduction to the casing, with additional heat transferred from the winding and fluid domain. In addition to this the loss density profile in the core was found to be relatively uniform, though higher in the tooth area than the yoke. The quadratic temperature profile is then due to accumulation of thermal energy in the axial direction, as the major component of heat flux is in the axial direction. This can be seen when considering the solution to the heat equation applied along a line element, where heat is being generated uniformly along the line, one end of the line is adiabatic while the other is at a fixed temperature. In this case the heat equation reads:

$$q'' = k\frac{dT}{dz} \tag{6.13}$$

Where, because the heat being generated along the line is uniform the heat flux q'' can be thought of as being proportional to position:

$$q'' = az \tag{6.14}$$

Where a is a constant of proportionality. Substituting this into Equation (6.13) yields:

$$az = k\frac{dT}{dz} \tag{6.15}$$

The solution of which is seen to be:

$$T = \frac{az^2}{2k} + C \tag{6.16}$$

Where C is an integration constant.

The difference in temperature profile in the core at different radii is relatively small, though across the three operating points a similar trend is seen. When z*<0.5 temperature increases with radius, whereas when z*>0.5 the relationship is reversed. This is could be due to the predicted loss profiles in the core which showed larger loss densities in the tooth at lower radii due to the changing ratio of areas between the magnet and tooth, and smaller loss densities in the yoke at lower radii due to the increasing ratio of magnet arc length to yoke depth with radius.

The winding temperature profiles are shown in Figure 6.50 where $r^* = 0$ represents the inner diameter of the stator core and $r^* = 1$ represents the outer diameter. A value of r^* greater than 1 or less than 0 therefore indicated a position within the end winding. A value of z^*=0 represents the base of the stator slot, while a value of 1 indicates the top of the slot. It can be seen that there is little variation in winding temperature with radius, this is due to the large thermal conductivity prescribed in the radial direction, previously discussed in Section 3.2.5. The axial gradient is seen to be much larger, with higher temperatures seen at axial positions furthest from the casing, this again follows from the small value of thermal conductivity prescribed in the axial and circumferential directions as discussed in Section 3.2.5.

Contours of temperature rise in the stator are plotted in Figure 6.51. As can be seen, the hot spot in the winding occurs at the centre-top of the slot. This makes sense since the vast majority of the heat generated in the stator leaves the domain via conduction to the casing. The centre-top of the slot is physically furthest away from the casing, and therefore incurs the largest temperature rise.

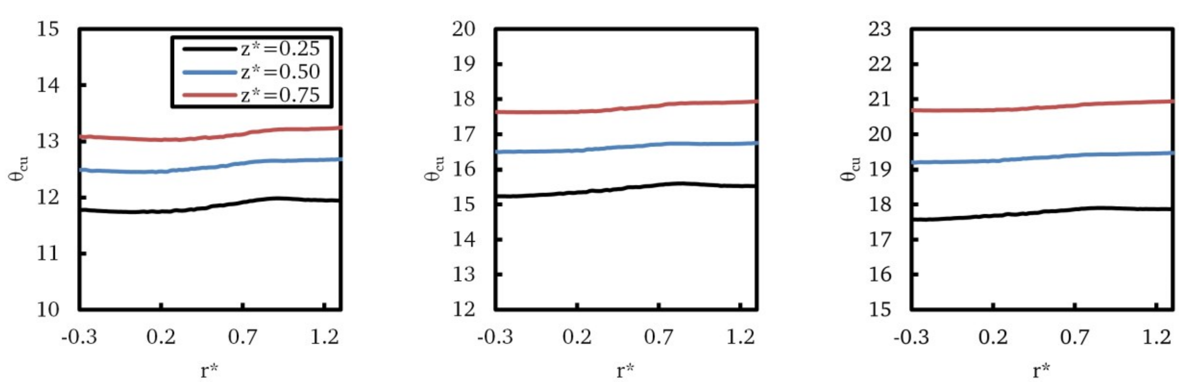

(a) 2000rpm 40Arms (b) 3000rpm 40Arms (c) 4000rpm 40Arms

Figure 6.50 Winding temperature rise profiles, r*=-0.3 is the inner diameter of the end winding and r*=1.3 is the outer diameter of the end winding

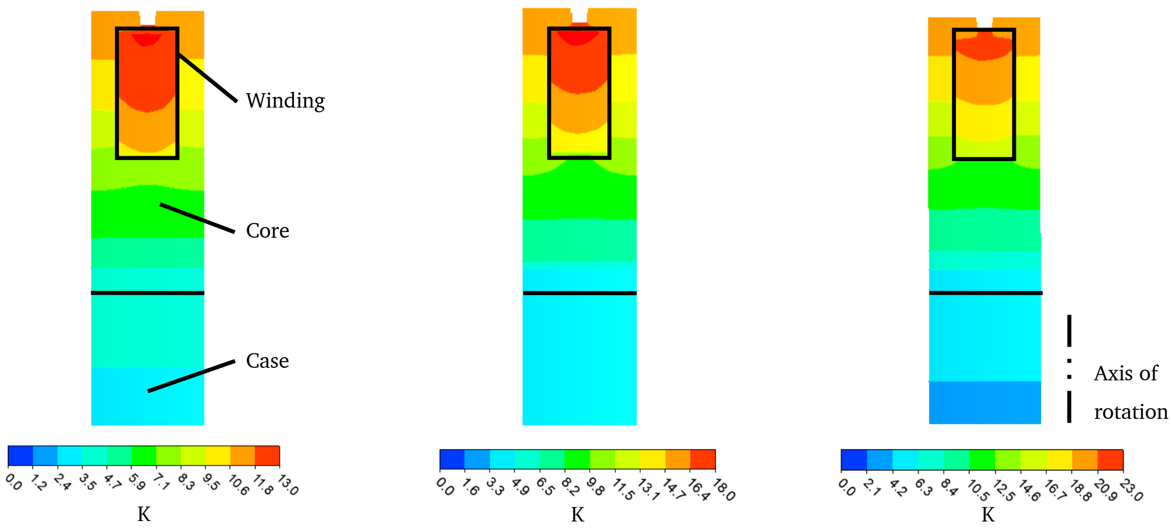

(a) 2000rpm 40Arms (b) 3000rpm 40Arms (c) 4000rpm 40Arms

Figure 6.51 Stator temperature rise contours at r*=0.50

It has been found in this section that a large contributor to magnet cooling is heat transfer from the air gap to the core. With this knowledge the core loss results presented in Section 6.1.2 become important when considering the thermal management of the magnets. A reduction in core losses and therefore core temperature would lead to a reduction in magnet temperature. Existing schemes such as pole shaping could be employed to reduce the losses induced by magnet harmonics, which contributed 2-10% of the whole. Perhaps other winding schemes would induce lower harmonics losses in the core. A large proportion (23-35%) of the core loss comes from the switching of the current waveform – alternative switching schemes, or a higher inductance winding could be investigated to reduce these losses.

6.4 Experimental Results and Comparison to Predicted Values

6.4.1 Open & Short Circuit, Resistance & Inductance Tests

The results of the open and short circuit tests are shown in Figure 6.52, where they are compared against the predicted values. Table 6.6 presents the results of the resistance and inductance measurements, and compares the inductance measurement with the predicted value. Agreement between the waveforms and inductance values is excellent, and is good evidence that the EM FEA model is predicting the distribution of flux throughout the machine correctly.

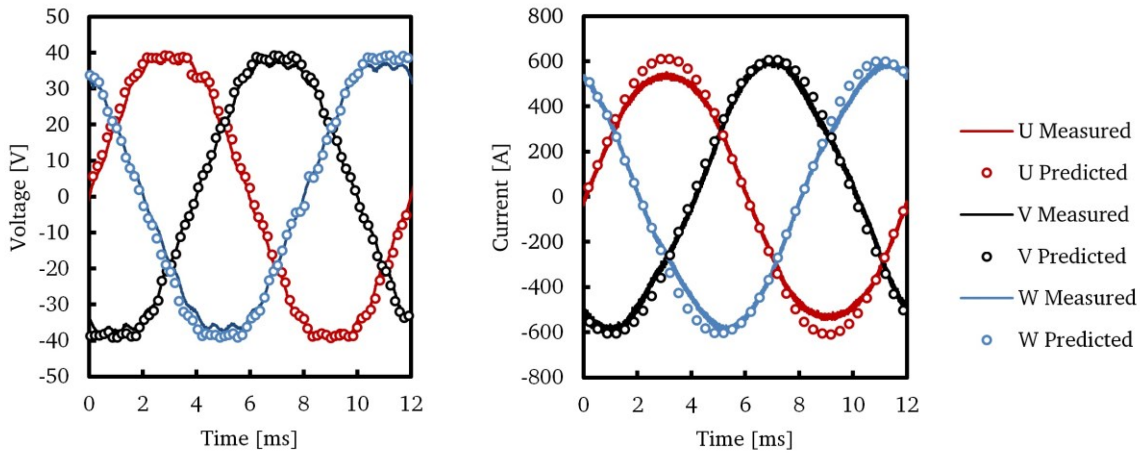

(a) Open circuit voltage (b) Short circuit current

Figure 6.52 Predicted and measured open circuit phase-neutral voltage and short circuit current waveforms at 1000rpm, 50deg coolant

Table 6.6 Measured phase resistance and inductance

Parameter	Measured	±	Predicted	Error [%]
Phase resistance at 20°C [mΩ]	14.4	0.289	N/A	N/A
U Phase inductance [μH]	133	2.1	122	8.3

6.4.2 Winding, Core and Friction Losses

Values of measured/estimated losses are presented in Table 6.7. The small increase in winding loss over the speed range is seen to come from the increase in winding temperature as the core temperature increases with speed (due to the increase in core losses). Figure 6.53 compares the measured and predicted core loss values. Good agreement can be seen at the 2000 and 3000rpm operating points, though relatively poor agreement is seen at the 4000rpm point. As the phase current was fixed the increase in core loss with speed must be solely due to the increase in excitation frequency and total harmonic distortion of the waveform. The relationship is roughly quadratic (though relatively few points have been measured), as predicted by the Steinmetz formula, Equation (3.16).

Based on the agreement seen between the rest of the measured and predicted electromagnetic values it can be argued that the predicted distribution of flux within the machine is relatively accurate, the most likely cause for the discrepancy in the core loss prediction are the material loss coefficients k_h, k_c, and k_e. These values were derived from the manufactures' loss data [107] which was most likely determined for a sample of the core material in an Epstein frame test. Stress and strain within the material, introduced during component manufacture, are likely to change the loss coefficients of the material [24].

Table 6.7 Overview of measured and estimated losses

Losses [W]	2000rpm 40A	±	3000rpm 40A	±	4000rpm 40A	±
Copper	83.0	3.4	83.7	3.4	84.5	3.5
Core	328.3	N/A	638.0	N/A	1097.4	N/A
Magnet	76.6	7.4	125.5	12.2	190.0	18.4
Windage	2.0	N/A	6.2	N/A	13.6	N/A
Bearing	2.7	N/A	5.8	N/A	10.4	N/A

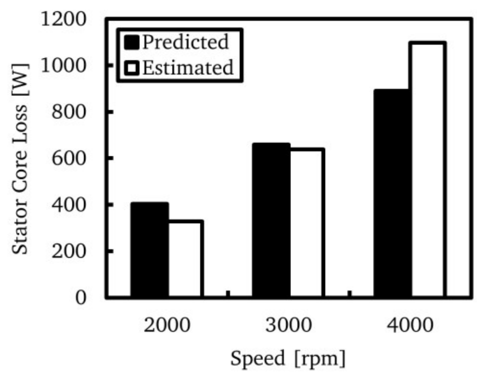

Figure 6.53 Predicted and measured stator core losses

6.4.3 Magnet Losses

Comparison between the predicted and measured magnet loss values is shown in Figure 6.54. Good agreement can be seen at 2000 and 4000rpm, with reasonable agreement seen at 3000rpm. All predicted values are within the error bars of the experimental values, so it is unclear as to where the discrepancies come from. The uncertainty in the experimental measurement has already been discussed in Section 5.4. Errors in the predicted values may come from:

- Uncertainties in the value of resistivity provided by the magnet material manufacturer

- Differences between the 'real' and given stator steel properties (though the given properties proved good enough for use during the open and short circuit simulations)
- Experimental uncertainty in the measured current waveforms (used as boundary conditions for the EM FEA analyses)
- The magnet segments in the analysis were assumed to be perfectly electrically insulated from each other, in reality a finite resistance must exist between the segments
- The effect of core loss on the field solution is not taken into account by the EM FEA simulation

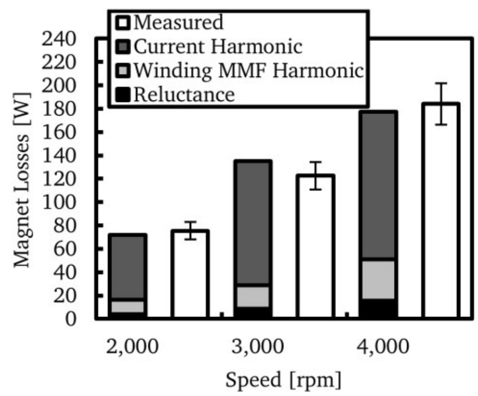

Figure 6.54 Predicted and measured magnet losses

Figure 6.55 presents the measured magnet losses over a range of speed and current loadings. The relationship of each component of loss to speed is clear and expected; in terms of reluctance and MMF induced losses these increase with the square of the speed because the frequency of excitation increases, this is described by Faraday's law, Equation (3.2). The current harmonic induced losses increase with speed as the switching frequency of the inverter is fixed, therefore at higher speeds fewer switching events represent the waveform every period. This increases the distortion of the waveform and therefore the $\partial\vec{B}$ component of Faraday's law.

The relationship of the total magnet loss to current loading in Figure 6.55 is less clear, especially when the uncertainty in each measurement is considered. To further understand the relationship an additional EM FEA simulation has been used to interpret the experimental result. Figure 6.56 compares the predicted losses at 3000rpm 40Arms and 80Arms with the measured values. Agreement with the experimental data is within the uncertainty band of the measurement giving confidence in the values predicted for the decomposed losses. The FEA result reveals that while losses associated with winding MMFs increased with current by 25% (because the $\partial\vec{B}$ component in Faraday's law had increased), the losses caused by harmonic variations in the current waveform decreased by 11% equating to only a very small change in total losses. The harmonic content of the current waveform decreases with increasing current as the shape of the current trace during a switching event more closely matches the ideal sinusoidal current. In terms of the thermal management of the permanent magnets this is an interesting result. It indicates that over this current range (40-80Arms) the total losses in the magnets will stay relatively constant, though considering the CHT analysis the increase in winding temperature due to the increase in winding losses will cause the air cavity temperature to increase and therefore the magnet temperature also to increase. If the phase current was increased further the balance between the sources of magnet loss may change. Consequently the distribution of loss would change within the magnet as higher frequency carrier induced losses are substituted for lower frequency MMF induced losses. This would have an effect on the magnitude and position of hot spots within the magnet and maybe an interesting avenue for further research.

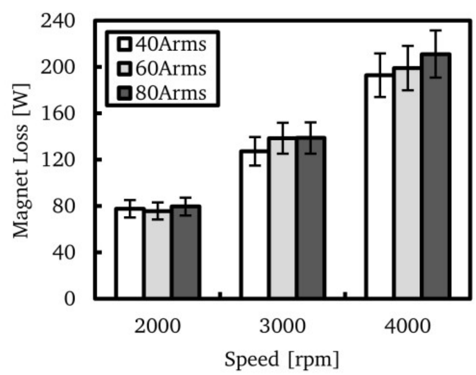

Figure 6.55 Measured magnet losses over a variety of speeds and current loadings

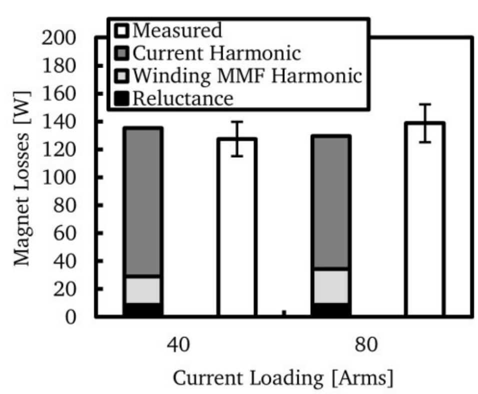

Figure 6.56 Measured and predicted magnet losses at 3000rpm, from 40A to 80A the MMF losses are seen to increase, while the current harmonic induced losses decrease

An additional investigation was carried out in order to investigate the effect on magnet losses of varying the DC bus voltage of the system. Figure 6.57 presents the measured magnet losses for a 3000rpm, 40Arms loading over a range of DC bus voltages. In this work the measured losses are plotted against the non-dimensional ratio of the fundamental phase-neutral voltage and the DC bus voltage:

$$v^* = \frac{2v}{V_{DC}} \tag{6.17}$$

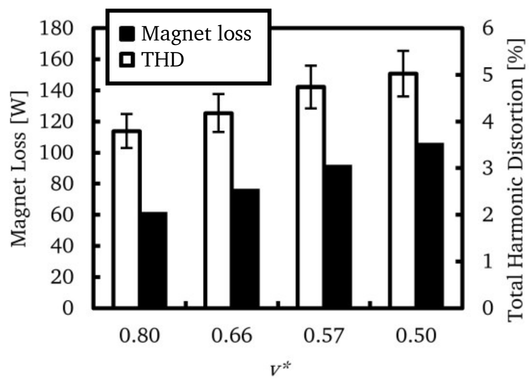

Figure 6.57 Measured magnet losses and THD of the current waveform at 3000rpm 40Arms over a range of DC bus voltages

As would be expected, as v^* decreases, magnet losses increase because the total harmonic distortion (THD) of the current waveform increases. The increase in losses from $v^* = 0.80$ to $v^* = 0.50$ to is 32%. Apart from the loss in efficiency this is an important characterisation for an electrical machine of this type, as was shown in the CHT study the temperature of the magnets is heavily dependent on the losses generated within them. If a linear thermal system is assumed, the 32% increase in losses would lead to a steady state temperature rise increase of 32% in the magnets. This may be exacerbated further when considering the core loss breakdown previously presented in Figure 6.17, where ~25% of core loss was attributed to harmonic distortion of the current waveform. The CHT analysis showed that the cooling of the magnets depended heavily on heat transfer from the air gap to the stator core. An increase in core losses and therefore core temperature would reduce the effectiveness of this heat transfer path, leading to further increases in magnet temperature.

6.4.4 Steady State Tests

Torque

Figure 6.58 presents the measured and predicted torques during the steady state tests. In order to compare the predicted and measured torques the effect of core loss on the predicted torque must be taken into account. This has been done using the following,

$$T_{mech} = T_{EM} - \frac{q_{fe}}{\omega} \tag{6.18}$$

which simply considers the predicted core loss as a drag torque, and subtracts it from the predicted electromagnetic torque. Figure 6.58 presents the comparison where excellent agreement can be seen. As was the case with the open circuit, short circuit, and inductance predictions the good agreement is evidence that the predicted distribution of flux throughout the machine is correct.

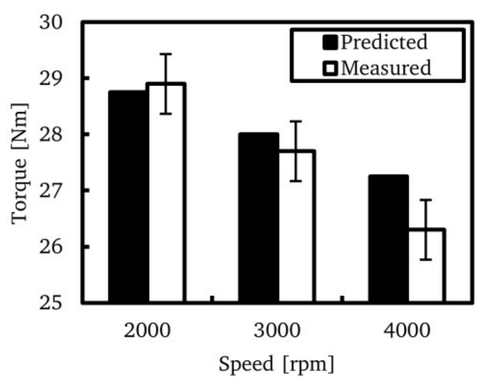

Figure 6.58 Predicted and measured torque

Static Pressure

Predicted and measured static pressures in the air gap are presented in Figure 6.59. In general agreement is good, though there is a slight discrepancy seen at the 3000rpm operating point. The agreement is good evidence that the predicted flow field within the electrical machine is accurate. Further validation may be obtained by taking measurements of velocity using a hot wire probe or similar. In order to do this it would be necessary to build a scaled up model of the electrical machine to increase the space available for sensors in the internal cavity.

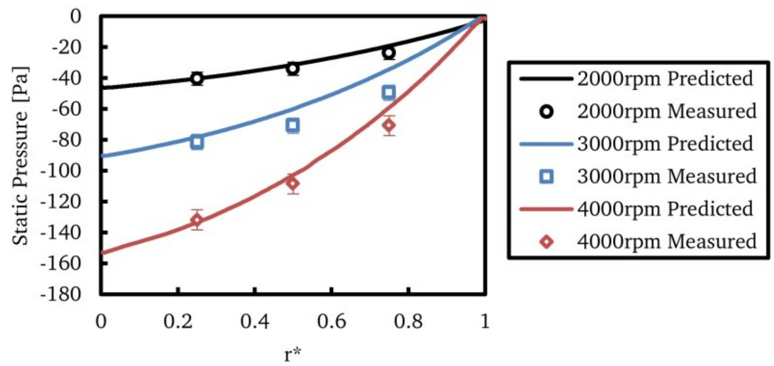

Figure 6.59 Predicted and measured static pressure in the air gap

The negative gradient measured from outer to inner radius is evidence of radial flow along the stator face. This is expected when considering typical flow regimes in enclosed stator-disc systems where the fluid is often seen flowing radially out along the rotor and back in along the stator. The quadratic relationship with radius can be explained by considering the radial equilibrium equation from [110] where the pressure force balances the centrifugal force for a small rotating fluid element:

$$\frac{1}{\rho}\frac{dP}{dr} = \frac{V_\theta^2}{r} \tag{6.19}$$

If V_θ is proportional to r then

$$\frac{dP}{dr} = kr \tag{6.20}$$

Integrating this with respect to r gives

$$P = \frac{kr^2}{2} + C \tag{6.21}$$

Component Temperatures

The predicted and measured stator core and winding temperature rise is presented in Figure 6.60. No significant radial temperature gradient was seen in the winding temperature, while a strong axial temperature gradient was seen in the stator core. Good agreement between measured and predicted values is seen across the operating range for the stator core.

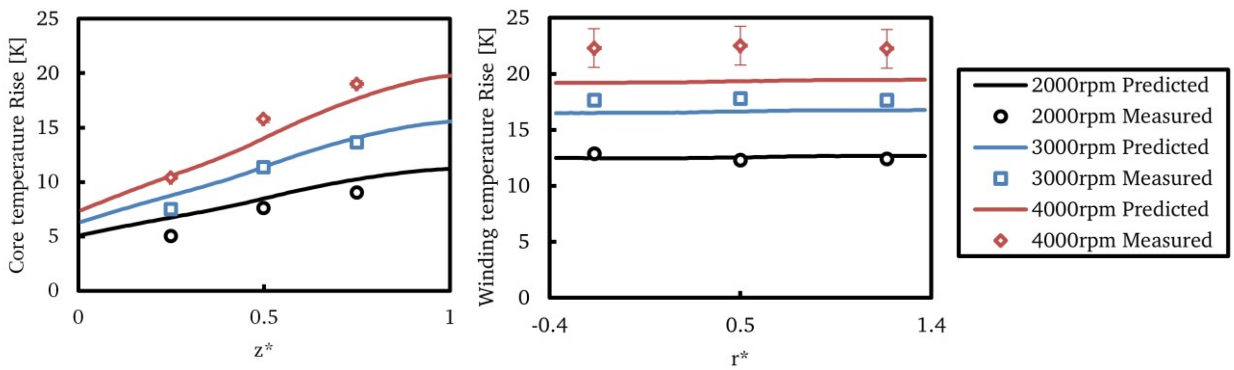

(a) Core temperature rise

(b) Winding temperature rise

Figure 6.60 Predicted and measured core and winding temperature rise

With regards to the winding temperature, good agreement can be seen for the 2000rpm and 3000rpm operating points, while there has been an under prediction of temperature rise at 4000rpm. As the DC heating test tuning procedure produced such good agreement between predicted and measured temperature rises (refer to Appendix C) it is postulated that the error in prediction here is due to an over prediction of convective heat transfer from the end windings. There could be many reasons for this, including:

- Differences in geometry between the model and the real component (the real winding does not have a smooth surface for example)
- As the agreement at 2000rpm (laminar) was good the over prediction in heat transfer at 3000 and 4000rpm could be due to the choice of turbulence model

Figure 6.61 presents the measured temperature rise in the winding and stator core components over the speed range. An important relationship to note is the fairly uniform temperature difference between the winding and stator core over the speed range. As the current in the winding was kept constant copper losses were only a function of temperature change within the winding, these values are presented formally later but ranged from 83-84.5W across the speed range. As the losses and temperature difference were both fairly constant it could be that the convective 'link' between the winding and casing is either a weak function of speed, or negligible when compared with the conductive 'link' to the heat sink. Another possibility here is that the assumption that proximity losses were negligible was incorrect and that the convective exchange with the casing masks the increase in losses with speed.

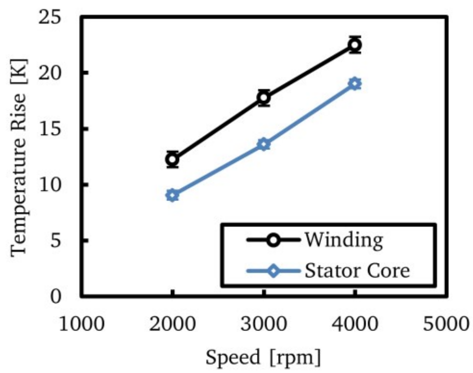

Figure 6.61 Measured temperature rise in the winding and stator core over the speed range

Figure 6.62 presents the predicted and measured magnet temperature rise. Excellent agreement is seen for the 2000 and 4000rpm operating points, while there has been an over prediction in temperature for the 3000rpm operating point. This is most likely due to the over prediction in losses seen in Figure 6.54. The agreement seen here is good evidence that the predicted temperature distribution in the magnets is accurate. Further validation may be obtained by measuring temperatures at discrete locations using thermocouples/thermistors, routed out through the machine using slip rings. This has the disadvantage of potentially disrupting the eddy current flow in the magnets. It may be possible to take surface temperature measurements using a thermal imaging camera, though a viewing window would have to be cut through the stator to do this, potentially increasing the magnet losses.

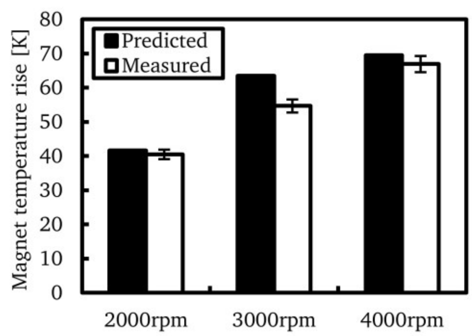

Figure 6.62 Predicted and measured magnet temperature rise

The measured magnet temperature and mechanical torque are presented in Figure 6.63. As the current was kept constant across the speed range the reduction in torque can be attributed to the increase in magnet temperature and core losses. The effect of the core losses has been removed using (6.22).

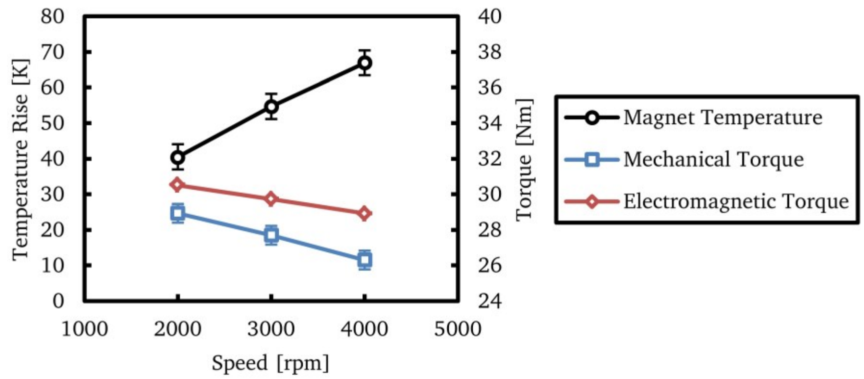

Figure 6.63 Magnet temperature and mechanical torque across the speed range

$$T_{EM} = T_{mech} + \frac{q_{fe}}{\omega} \tag{6.22}$$

The remaining reduction in torque (5.2%) can therefore be attributed to the increase in magnet temperature (26.4K). Note that this only accounts for the increase in temperature from 2000-4000rpm (not the temperature rise from ambient). As the coercivity and remanence of the magnet material reduce linearly with temperature [81] it can be said that the torque production of the prototype axial flux machine changes by 0.2%/K of magnet temperature rise. This emphasises the sensitivity of torque production to magnet temperature, and quantifies the potential performance improvement if methods of keeping the magnets cool can be implemented: At the 4000rpm operating point if the magnets could be kept at the coolant temperature the electromagnetic torque would have been 14% higher.

Figure 6.64 presents the predicted and measured outer casing and bearing bore temperature rises. Relatively poor agreement can be seen between the predicted and measured outer casing temperature, though absolute errors are small. Reasonable agreement is seen at the bearing bore.

The bearing bore temperature measurement increased linearly with speed. This may have been due to increased bearing losses with speed, increased convection from the inner cavity to the casing, or due to a general increase in casing temperature due to the increase in losses being dissipated by the heat sink.

The outer casing temperature also increased with speed. Again this may have been due to a general increase in casing temperature due to the increase in total losses being dissipated by the heat sink. It may also indicate an increase in convective heat transfer from the inner cavity to the outer casing with speed.

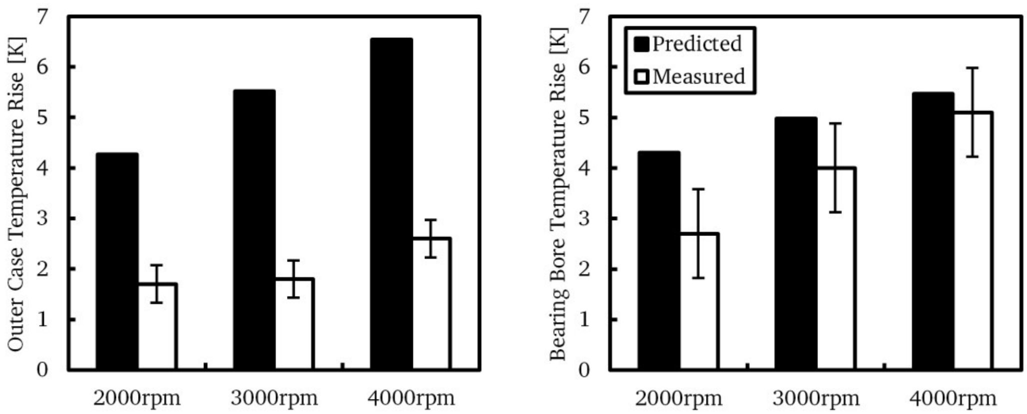

(a) Outer casing

(b) Bearing bore

Figure 6.64 Predicted and measured casing temperature rise

For reference Table C.2 in Appendix C presents the complete results from the steady state tests with uncertainties.

6.5 Summary

This chapter has presented and discussed the numerical predictions of loss, flow and temperature field within the electrical machine, as well as comparing them with the measured values. The detailed information provided by the numerical model has enabled an understanding of the thermal processes affecting the magnet temperature to be developed. The experimental work has also provided insights into the thermal management of the magnets as well as providing data to compare the numerical model too, increasing the confidence in the numerical predictions.

It was found that losses in the magnets were concentrated at the edges of the segments, as the majority (71-79%) of the loss was caused by high frequency current harmonics. The magnets depend almost exclusively on the internal cavity for cooling, which in turn is cooled by interaction with the core and casing components. The shape of the temperature field in the air gap, as well as the fact that the trailing segment has a higher loss generated in it, leads the trailing edge of the magnet to be up to 13% warmer than the average magnet temperature rise.

The interaction of the air in the internal cavity with the core allows other areas for further research to be identified. It can be postulated that magnet temperature will decrease as core losses (and therefore temperature) decrease. This may be achieved by a number of existing techniques: Pole shaping, alternate materials, switching schemes etc.

The interaction of the air in the internal cavity with the case also allows other areas for further research to be identified. The numerical model, now shown to produce accurate results, could be used to investigate alternate casing geometries which may enhance heat transfer in this area.

The novel magnet loss measurement technique combined with the FEA simulations showed that over the current loading range investigated losses remained relatively constant. This was because as the current loading was increased the increase in MMF induced losses balanced the reduction in current harmonic induced losses. It was noted that this may impact the size and position of hot spots at other operating points, and this has been identified as an avenue for further research.

Magnet losses were found to be sensitive to v^*, with a change from 0.8 to 0.5 increasing losses by 32%. It was noted that this is an important characterisation for this electrical machine, because the CHT analysis showed that the resulting magnet temperature was sensitive to the losses induced in the magnets.

Chapter 7

Conclusions and Future Work

Elevated permanent magnet temperature in PMSMs reduces torque production and efficiency while increasing the risk of demagnetisation. Costly thermal stabilisers are used to increase the temperature rating of magnet materials. It was found that axial flux PMSMs are promising in applications requiring high torque and power density, though little is known of the factors which affect permanent magnet temperature, especially in the totally enclosed topology. This thesis aimed to increase the knowledge available in this area by presenting a detailed analysis of the loss, flow, and temperature fields within a totally enclosed axial flux PMSM. Key contributions of the thesis include:

- A detailed description and analysis of the loss, flow, and temperature fields within a totally enclosed axial flux PMSM **(Objective 1)**
- A novel criterion for assessing the relative importance of the fluctuating component of a periodic heat source on the temperature rise of a device **(Objective 1)**
- The provision of a link between existing design methods and how these would affect magnet temperature. For example reducing the temperature in the stator core was identified as a possible method for reducing magnet temperature **(Objective 1&2)**
- The advantages of a multiphysics field solution in magnetic devices are made clear. Hot spot magnitude in the magnets was found to be significant. This is a critical piece of information when assessing the risk of demagnetisation in such devices **(Objective 2)**
- A novel experimental method for measuring magnet losses in PMSMs **(Objective 3)**

7.1 Objective 1

The first objective was to:

Describe and understand the thermal processes occurring within an enclosed AF PMSM by developing and analysing the results of a numerical model which predicts the loss, temperature, and flow fields within the device.

A numerical model was developed and presented in Chapter 3 which had the capability to predict the loss, flow and temperature fields within an axial flux PMSM. The numerical model had two coupled components, the first was a three dimensional transient EM FEA which predicted the loss fields within the magnets and core of the PMSM using measured current waveforms as an input. The predicted loss densities varied greatly about their mean values. A novel criterion was developed in Chapter 4 which assessed the relative importance of the fluctuating component of the loss field on the temperature response of the PMSM. In the operating points studied here it was found that the fluctuating components had little impact on the thermal system. This meant that they could be time-averaged, allowing the second component of the numerical model to be a steady state (rather than transient) CHT analysis. The criterion was found to be a useful tool for building an understanding of the thermal processes occurring in devices with periodic heat sources. It was validated by comparing its estimates of temperature response to numerical simulations of the electrical machine. The agreement was found to be fit for purpose.

Results from the numerical model allowed an analysis of the loss, flow, and temperature fields to be made. Magnet losses were found to be dominated by current harmonic induced losses which comprised 71-79% of the whole. Winding MMF harmonics contributed 15-20% while reluctance variations contributed 6-9%. The magnets incurred the largest temperature rise of any component in the machine and relied on convection to the inner cavity for cooling; over 99% of the heat generated in the magnets was convected to the inner cavity.

Core losses were found to be dominated by flux density variations occurring at the fundamental frequency, these comprised 63-85% of the whole. Magnet and winding MMF harmonics contributed 2-10% while current harmonic induced losses contributed 23-35%. All of the heat generated in the core was found to be conducted to the casing before being dissipated by the coolant jacket. Between 87-96% of the winding losses were conducted to the casing via the core before being dissipated by the coolant jacket. The remaining winding losses were convected to the inner cavity.

The flow structure in the inner cavity was found to be key to understanding the thermal processes occurring within the PMSM. The flow structure in the air gap of the inner cavity was found to be similar to that found in the much studied rotor-stator system. The flow was found to be mainly circumferential, with a radial component flowing out in the rotor boundary layer and returning in the stator boundary layer. The main difference between the flow studied here and the classic rotor-stator system was that a significant proportion of the flow was seen to return to the inner diameter of the machine via the slot gap. In the outer end winding region the flow was seen to exit the air gap and join one of two recirculating regions; the first was a large eddy seen to recirculate between the rotor banding and the end winding; the second was a large eddy seen to flow over and around the outer end winding. Both of these eddies fed the stator boundary layer and slot gap return paths. In the inner end winding region the flow was seen to exit the air gap, join an eddy recirculating between the rotor and inner end winding, before being entrained again by the rotor.

A result of the inner cavity's recirculating flow structure (described in 6.3.1 and 6.3.2) was that it convects heat away from the magnets and dissipates it to the outer casing and core. As a proportion of all heat moving through the inner cavity 56-62% left via convection to the outer casing while 28-41% left via convection to the core.

The wider implications of this work are promising: Modern numerical analysis techniques have been used successfully to predict the thermal performance of a totally enclosed AF PMSM. This increases confidence in relying on these techniques more heavily during the design stage of a machine development program.

7.2 Objective 2

The second objective was to:

Describe and understand the thermal processes affecting permanent magnet temperature and discuss methods which may reduce it.

The dominant cause of loss in the magnets was found to be due to current harmonics caused by the PWM waveform of the inverter. Due to the skin depth of the magnet material at the inverter switching frequency the predicted loss profile showed large concentrations of loss at the edges of the magnet segments. It was found that it was necessary to resolve these profiles in the CHT analysis as hot spots within the magnet occurred at the locations where the greatest loss occurred. Hot spots were found to be up to 13% greater than the mean temperature rise in the domain. The resultant temperature profile in the magnets was also affected by the direction of rotation. The predicted flow and temperature fields showed that in the rotor frame of reference the air is seen to flow from the leading to the trailing edge of the magnet as it is centrifuged radially outwards. The air heats up as it flows over the magnets leading to the trailing edge of the magnet seeing warmer air than the leading edge. This was seen to greatly affect the temperature profile within the magnets, with the leading edge incurring up to a 10% lower temperature rise than the trailing edge. This finding emphasises the value of a field solution in devices such as this where local demagnetisation may be of concern.

Magnet losses were measured at different DC bus voltages and it was shown that as the voltage increased by 60% losses increased by 32% at the operating point investigated. This finding is important as in a linear thermal system this would lead to a 32% increase in magnet temperature rise, resulting in a reduction in torque production and an increase in risk of demagnetisation.

With regards to reducing magnet temperature many potential methods of achieving this, which have been validated independently by other investigators (often for other purposes), have been identified. The contribution of the thesis here is to provide the link between existing known design methods and how these would affect magnet temperature. It was shown that the magnets are not in the heat path of any other heat generating components. This means that any reduction in magnet losses will result in a reduction in magnet temperature. Methods of reducing magnet losses were reviewed in Chapter 2 and included segmentation, rotor/stator pole shaping, and eddy current shields.

The core was shown to be a major contributor to cooling the inner cavity, which in turn was shown to be a major contributor to cooling the magnets. A reduction in core losses would lead to a reduction in core temperature and ultimately a reduction in magnet temperature. This can be achieved by using alternative core materials, winding layouts, and pole shaping.

7.3 Objective 3

The third objective was to:

Develop an experimental procedure whose results improve the understanding of the numerical model's assumptions, and validate the numerical predictions.

An experimental procedure was developed and presented in Chapter 5. A number of standard experimental techniques were used, including measurements of winding, core, and case temperatures under steady state conditions to validate the CHT model. Measurements of static pressure in the air gap were used to validate the flow predictions of CHT model. Open circuit voltage, short circuit current, and torque were all measured to validate the electromagnetic FEA model.

The temperature and static pressure measurements were taken in both halves of the machine, and in different circumferential positions. It was found that there were no significant differences in measured quantities in either half of the machine, or at different circumferential locations. This finding was used to justify the use of symmetry and periodic boundary conditions in the numerical model, saving days of computational time.

The thesis contributes a novel method of measuring magnet losses and magnet temperature, which provided a strong validation of the loss and temperature predictions. The method has several advantages when compared with the existing method proposed by Alberti et al. [30]. It is relatively quick to implement, using standard laboratory equipment to take a direct measurement from a machine operating under realistic conditions. An analysis showed that the uncertainty in the loss measurements was 9.7% for 95% confidence.

7.4 Future Work

A number of areas worthy of further investigation have been identified throughout this work. During the analysis of the magnet loss field in Section 6.1.2 it was noted that geometrically identical magnet segments incurred different amounts of loss. It was proposed that this was due to saturation effects in the core adding a spatial variation to the winding inductance, and therefore subjecting different magnet segments to different flux density variations. This hypothesis requires further investigation to be proven. A useful outcome from this future work may be an optimised segmentation scheme, i.e. to maximise the reduction in magnet losses with the fewest number of segments.

The numerical model presented in this work, now validated, can be used to assess alternative magnet cooling schemes. Alternative schemes may include improving the conductive heat path between the magnets and the coolant jacket, as this was found to be a bottle neck during the analysis. Numerous improvements to the internal air flow heat transfer mechanism could be proposed and numerically tested. These may include adding fan blades to rotating components, or increasing the surface area of regions like the outer casing which were found to contribute significantly to the cooling of the domain.

Both magnet and core losses were shown to have large components attributed to inverter switching. The effect of alternative inverter switching schemes on magnet temperature could be investigated. These results would be valuable during a combined motor/inverter development program.

To complete the understanding and validation of magnet losses in surface mounted PMSMs the novel magnet loss measurement method proposed and implemented in this work could be extended to take measurements in the field weakening region of a machine's operation. In order to do this Equation (5.10) would be recast in terms of i_q and i_d where $i^2 = i_q^2 + i_d^2$. During the measurement, rotor position would be measured in order to decompose the apparent current into q and d components. The resulting formulation used to determine the voltage constant during the magnet loss tests is derived from Figure 1.14, and replaces Equation (5.10) in the method:

$$k_e = \frac{\sqrt{v^2 - \left(i_q \omega L_q + i_d R\right)^2} - i_q R - i_d \omega L_d}{\omega} \tag{7.1}$$

Publications

1. Adam C Malloy, Ricardo F Martinez-Botas, Malte Jaensch, and Michael Lamperth, "Measurement of heat generation rate in the permanent magnets of rotating electrical machines," in *Power Electronics Machines and Drives*, Bristol, 2012.
2. Adam C Malloy, Ricardo F Martinez-Botas, and Michael Lamperth,"Measurement of Magnet Losses in a Surface Mounted Permanent Magnet Synchronous Machine," *IEEE Transactions on Energy Conversion*, In press 2014.

Bibliography

[1] J Gieras and M Wing, *Permanent Magnet Motor Technology*. New York: Marcel Dekker, 2002.

[2] International Energy Agency, "World Energy Outlook 2012," 2012.

[3] K Ribeiro et al., "2007: Transport and its infrastructure. ," in *Climate Change 2007: Mitigation. Contribution of Working Group III to the Fourth Assessment Report of the Intergovernmental Panel on Climate Change*. Cambridge: Cambridge University Press, 2007, pp. 325-380.

[4] Hong Huo, Michael Wang, Larry Johnson, and Dongquan He, "Projection of Chinese Motor Vehicle Growth, Oil Demand, and CO2 Emissions Through 2050," *Transportation Research Record: Journal of the Transportation Research Board*, vol. 2038, pp. 69-77, 2008.

[5] International Energy Agency, "Trnasport, Energy and CO2," 2009.

[6] David Howey, Robin North, and Ricardo Martinez-Botas, "Road transport technology and climate change mitigation," London, 2010.

[7] H Toda, J Xia, J Wang, K Atallah, and D Howe, "Rotor Eddy-Current Loss in Permanent Magnet Brushless Macines," *IEEE Transactions on Magnetics*, vol. 40, no. 4, pp. 2104-2106, 2004.

[8] H Polinder and M J Hoeijmakers, "Eddy-current losses in the permanent magnets of a PM machine," in *IEEE International Conference on Electrical Machines and Drives*, Cambridge, 1997, pp. 138-142.

[9] J F Gieras, R J Wang, and M J Kamper, *Axial flux permanent magnet brushless machines.*: Springer Verlag, 2008.

[10] M U Lamperth, A Beaudet, and M Jaensch, "Disc Motors for Automotive Applications," in *IET Hybrid and Eco-Friendly Vehicle Conference*, 2008.

[11] Andrea Cavagnino, Mario Lazzari, Francesco Profumo, and Alberto Tenconi, "A Comparison Between the Axial Flux and the Radial Flux Structures for PM Synchronous Motors," *IEEE Transactions on Inductry Applications*, vol. 38, no. 6, pp. 1517-1524, 2002.

[12] J R Bumby and R Martin, "Axial-flux permanent-magnet air-cored generator for small-scale wind turbines," *IEE Proceedings Electrical Power Applications*, vol. 152, no. 5, pp. 1065-1075, 2005.

[13] Yu-Seop Park, Seok-Myeong Jang, Ji-Hwan Choi, Jang-Young Choi, and Dae-Joon You, "Characteristic Analysis on Axial Flux Permanent Magnet Synchronous Generator Considering Wind Turbine Characteristics According to Wind Speed for Small-Scale Power Application," *IEEE Transactions on Magnetics*, vol. 48, no. 11, pp. 2937-2940, 2012.

[14] P Wannakarn, T Tanmaneeprasert, N Rugthaicharoencheep, and S Nedphograw, "Design and Construction of Axial Flux Permanent Magnet Generator for Wind Turbine Generated DC Voltage at Rated Power 1500W," in *4th International Conference on Electric Utility Deredulation and Restructuring and Power Technologies*, 2011.

[15] Don-Ha Hwang et al., "An Modular-type Axial-flux Permanent Magnet Synchronous Generator for Gearless Wind Power Systems," in *The 30th Annual Conference of the IEEE Industrial Electronics Society*, Busan, 2004.

[16] J D Patterson, "High efficiency permanent magnet drive systems for electric vehicles," in *23rd International Conference on Industrial Electronics, Control and Instrumentation*, 1997.

[17] P Anpalahan and M Lamperth, "Design of multi-stack axial flux permanent magnet

generator for a hybrid electric vehicle," in *IEEE Power and Propulsion Conference*, 2006.

[18] T J Woolmer and M D McCulloch, "Analysis of the Yokeless And Segmented Armature Machine," in *IEEE International Elecreic Machines & Drives Conference*, 2007.

[19] N Takorabet, J P Martin, F Meibody-Tabar, F Sharif, and P Fontaine, "Design and Optimization of a Permanent Magnet Axial Flux Wheel Motors for Electric Vehicle," in *20th International Conference on Electrical Machines*, 2012.

[20] Sukumar De, Milan Rajne, Srikant Poosapati, and Chintan Patel, "Low Inductance Axial Flux BLDC Motor Drive for More Electric Aircraft," in *IEEE Aerospace Conference*, 2011.

[21] R J Hill-Cottingham et al., "Multi-disc axial flux Stratospheric Aircraft Propeller Drive," in *IEEE Industrial Applications Conference*, 2001.

[22] H Jussila, J Nerg, J Pyrhonen, and A Parviainen, "Concentrated Winding Axial Flux Permanent Magnet Motor for Industrial Use," in *19th International Conference on Electrical Machines*, Rome, 2010.

[23] Jungfeng Wu, "Design of a Miniature Axial Flux Flywheel Motor with PCB Winding for Nanosatellites," in *International Conference on Optoelectronics and Microelectronics*, 2012.

[24] J R Hendershot and T J E Miller, *Design of brushless permanent magnet machines*. Venice: Motor Design Books LCC, 2010.

[25] Sadarangani Chandur, *Electrical Machines*. Stockholm: Royal Institute of Technology, 2006.

[26] P Campbell, *Permanent Magnet Materials and their Application*. Cambridge: Cambridge University Press, 1994.

[27] Chandur Sadarangani, *Electrical Machines*. Stockholm: KTH Royal Institute of Technology, 2006.

[28] Arnold Magnetics Ltd. Arnold Magnetic Technologies. [Online]. http://www.arnoldmagnetics.com/

[29] Metal-Pages Ltd. (2014, April) Metal-pages.com. [Online]. http://www.metal-pages.com/metalprices/

[30] Luigi Alberti, Emanuele Fornasiero, Nicola Bianchi, and Silverio Bolognani, "Rotor losses measurements in an axial flux permanent magnet machine," *IEEE Transactions on Energy Conversion*, vol. 26, no. 2, pp. 639-645, 2011.

[31] Y Kawase, T Ota, and H Fukunaga, "3-D Eddy Current Analysis in Permanent Magnet of Interior Permanent Magnet Motors," *IEEE Transactions on Magnetics*, vol. 36, no. 4, pp. 1863-1866, 2000.

[32] K Atallah, D Howe, P H Mellor, and D A Stone, "Rotor Loss in Permanent Magnet Brushless AC Machines," *IEEE Transactions on Industry Applications*, vol. 36, no. 6, pp. 1612-1618, 2000.

[33] P Sergeant and A Van den Bossche, "Segmentation of Magnets to Reduce Losses in Permanent-Magnet Synchronous Machines," *IEEE Transactions on Magnetics*, vol. 44, no. 11, pp. 4409-4412, 2008.

[34] Katsumi Yamazaki and Atsushi Abe, "Loss Investigation of Interior Permanent-Magnet Motors Considering Carrier Harmonics and Magnet Eddy Currents," *IEEE Transactions on Industry Applications*, vol. 45, no. 2, pp. 659-665, 2009.

[35] H Wan-Ying, R Bettayeb, R Kaczmarek, and J C Vannier, "Optimization of Magnet Segmentation for Reduction of Eddy-Current Losses in Permanent Magnet Synchronous Machine," *IEEE Transactions on Energy Conversion*, vol. 25, no. 2, pp. 381-387, 2010.

[36] K Yamazaki, Y Fukushima, and M Sato, "Loss Analysis of Permanent-Magnet Motors With Concentrated Windings - Variation of Magnet Eddy-Current Loss Due to Stator and Rotor Shapes," *IEEE Transactions on Industry Applications*, vol. 45, no. 4, pp. 1334-1342, 2009.

[37] P Madina, J Poza, G Ugalde, and G Almandoz, "Magnet eddy current loss calculation

methos for segmentation analysis on Permanent Magnet Machines," in *Proceedings of the 14th European Conference on Power Electronics and Applications*, 2011.

[38] T Woolmer and M McCulloch, "Analysis of the Yokeless And Segmented Armature Machine," in *IEEE International Electric Machines & Drives Conference*, 2007.

[39] H Vansompel, P Sergeant, and L Dupré, "Effect of Segmentation on Eddy-Current Loss in Permanent-Magnets of Axial-Flux PM Machines using a Multilayer-2D - 2D Coupled Model," in *XXth International Conference on Electrical machines*, 2012.

[40] W Fu and Z Liu, "Estimation of Eddy-Current Loss in Permanent Magnets of Electric Motors Using Network-Field Coupled Multislice Time-Stepping Finite-Element Method," *IEEE Transactions on Magnetics*, vol. 38, no. 2, pp. 1225-1228, 2002.

[41] H Jussila, P Salminen, A Parviainen, J Nerg, and J Pyrhonen, "Concentrated Winding Axial Flux Permanent Magnet Motor with Plastic Bonded MAgnets and Sintered Segmented Magnets," in *18th International Conference on Electrical Machines*, 2008.

[42] T Nguyen, K Tseng, C Zhang, and S Zhang, "Loss Study of a Novel Axial Flux Permanent Magnet Machine," in *IEEE International Electric Machines and Drives Conference*, 2011.

[43] F Zhou, J Shen, W Fei, and R Lin, "Study of Retaining Sleeve and Conductive Shield and Their Influence on Rotor Loss in High-Speed PM BLDC Motors," *IEEE Transactions on Magnetics*, vol. 42, no. 10, pp. 3398-3400, 2006.

[44] F Al-Naemi and A Moses, "FEM modeling of rotor losses in PM motors," *Journal of Magnetism and Magnetic Materials*, vol. 304, no. 2, pp. e794-e797, 2006.

[45] H Cho, S Jang, and S Choi, "A Design Approach to Reduce Rotor Losses in High-Speed Permanent Magnet Machine for Turbo-Compressor," *IEEE Transactions on Magnetics*, vol. 42, no. 10, pp. 3521-3523, 2006.

[46] Z Kolondzovski, A Belahcen, and A Arkkio, "Comparative thermal analysis of different rotor types for a high-speed permanent-magnet electrical machine," *IET Electrical Power Applications*, vol. 3, no. 4, pp. 279-288, 2009.

[47] D Ishak, Z Zhu, and D Howe, "Eddy-Current Loss in the Rotor Magnets of Permanent-Magnet Brushless Machines Having a Fractional Number of Slots Per Pole," *IEEE Transactions on Magnetics*, vol. 41, no. 9, pp. 2462-2469, 2005.

[48] M Nakano, H Kometani, and M Kawamura, "A Study on Eddy-Current Losses in Rotors of Surface Permanent-Magnet Synchronous Machines," *IEEE Transactions on Industry Applications*, vol. 42, no. 2, pp. 429-435, 2006.

[49] N Bianchi and E Fornasiero, "Index of rotor losses in three-phase fractional-slot permanent magnet machines," *IET Electric Power Applications*, vol. 3, no. 5, pp. 381-388, 2009.

[50] J Li, D Choi, D Son, and Y Cho, "Effects of MMF Harmonics on Rotor Eddy-Current Losses for Inner-Rotor Fractional Slot Axial Flux Permanent Magnet Synchronous Machines," *IEEE Transactions on Magnetics*, vol. 48, no. 2, pp. 839-842, 2012.

[51] K Yamazaki et al., "Reduction of Magnet Eddy-Current Loss in Interior Permanent-Magnet Motors With Concentrated Windings," *IEEE Transactions on Industry Applications*, vol. 46, no. 6, pp. 2434-2441, 2010.

[52] K Yamazaki and K Kitayuguchi, "Teeth Shape Optimization of Surface and Interior Permanent-Magnet Motors with Concentrated Windings to Reduce Magnet Eddy Current Losses," in *International Conference on Electrical Machines and Systems*, 2010.

[53] Y Aoyma, K Miyata, and K Ohashi, "Simulations and experiments on eddy current in Nd-Fe-B," *IEEE Transactions on Magnetics*, vol. 41, no. 10, pp. 3790-3792, 2005.

[54] P Mellor, D Roberts, and D Turner, "Lumped parameter thermal model for electrical machines of TEFC design," *Electric Power Applications, IEE Proceedings B*, vol. 138, no. 5, pp. 205-218, 1991.

[55] J Nerg, M Rilla, and J Pyrhonen, "Thermal Analysis of Radial-Flux Electrical Machines With a High Power Density," *IEEE Transactions on Industrial Electronics*, vol. 55, no. 10, pp. 3543-3554, 2008.

[56] S Scowby, M Dobson, and M Kamper, "Thermal modelling of an axial flux permanent magnet machine," *Applied Thermal Energy*, vol. 24, pp. 193-207, 2004.

[57] E Belicov and V Hrabovcova, "Analysis of an Axial Flux Permanent Magnet Machine (AFPM) Based on Coupling of Two Seperated Simulation Models (Electrical and Thermal Ones)," *Journal of Electrical Engineering*, vol. 58, no. 1, pp. 3-9, 2007.

[58] R Wang, M Kamper, and R Dobson, "Development of a Thermofluid Model of Axial Field Permanent-Magnet Machines," *IEEE Transactions on Energy Conversion*, vol. 20, no. 1, pp. 80-87, 2005.

[59] C Lim et al., "2-D Lumped-Parameter Thermal Modelling of Axial Flux Permanent Magnet Generators," in *International Conference on Electrical Machines*, 2008.

[60] F Sahin, A Tuckey, and A Vandenput, "Design, development and testing of a high-speed axial-flux permanent-magnet machine," in *IEEE Indusrial Applications Conference*, 2001.

[61] D Howey, P Childs, and A Holmes, "Air-gap convection in rotating electrical machines," *IEEE Transactions on Industrial Electronics*, vol. 59, no. 3, pp. 1367-1375, 2012.

[62] S Borges, C Cezario, and T Kunz, "Design of Water Cooled Electric Motors Using CFD and Thermography Techniques," in *The 18th International Conference on Electrical Machines*, 2008.

[63] C Micallef, S Pickering, K Simmons, and K Bradley, "Improved Cooling in the End Region of a Strip-Wound Totally Enclosed Fan-Cooled Induction Electrical Machine," *IEEE Transactions on Industrial Electronics*, vol. 55, no. 10, pp. 3517-3524, 2008.

[64] M Hetteger, B Streibl, O Biro, and H Neudorfer, "Identifying the heat transfer coefficients on end-windings of an electrical machine by measurements and simulations," in *The XIX International Conference on Electrical Machines*, Rome, 2010.

[65] D Lampard, S Pickering, and J Mugglestone, "The use of Computational Fluid Dynamics to Model the Air Flow in the End Region of a TEFC Induction Motor," in *The IEE Colloquium on Modeling Performance of Electrical Machines*, 1997.

[66] M Kuosa, P Sallinen, and J Larjola, "Numerical and Experimental Modelling of Gas Flow and Heat Transfer in the Air Gap of an Electric Machine," *Journal of Thermal Science*, vol. 13, no. 3, pp. 264-278, 2004.

[67] M Kuosa et al., "Numerical and Experimental Modelling of Gas Flow and Heat Transfer in the Air Gap of an Electric Machine. Part II: Grooved Surfaces," *Journal of Thermal Science*, vol. 14, no. 1, pp. 48-55, 2005.

[68] H Li, "Cooling of a permanent magnet electric motor with a centrifugal impeller," *International Journal of Heat and Mass Transfer*, vol. 53, no. 4, pp. 797-810, 2010.

[69] B Maynes, R Kee, C Tindall, and R Kenny, "Simulation of airflow and heat transfer in small alternators using CFD," *IEE Proceedings B Electric Power Applications*, vol. 150, no. 2, pp. 146-152, 2003.

[70] S Pickering, M Lampard, and M Shanel, "Modelling Ventilation and Cooling of the Rotors of Salient Pole Machines," in *IEEE International Electric Machines and Drives Conference*, 2001.

[71] M Shanel, S Pickering, and D Lampard, "Conjugate Heat Transfer Analysis of a Salient Pole Rotor in an Air Cooled Synchronous Generatoe," in *IEEE International Electric Machines and Drives Conference*, 2003.

[72] J Trigeol, Y Bertin, and P Lagonotte, "Thermal Modeling of an Induction Machine Through the Association of Two Numerical Approaches," *IEEE Transactions on Energy Conversion*, vol. 21, no. 2, pp. 314-323, 2006.

[73] P Connor, S Pickering, C Gerada, C Eastwick, and C Micallef, "CFD Modelling of an Entire Synchronous Generator for Improved Thermal Management," in *The 6th IET international conference on power electronics, machines and drives*, Bristol, 2012.

[74] G Airoldi et al., "Computations in Heat Transfer in Axial Flux Permanent Magnet Machines," in *Proceedings of the 2008 International Conference on Electrical Machines*, 2008.

[75] G Airoldi et al., "Air flow and heat transfer modeling of an Axial Flux Permanent Magnet Generator," *World Academy of Science, Engineering and Technology*, vol. 34, pp. 809-813, 2009.

[76] D Howey, A Holmes, and K Pullen, "Measurement and CFD Prediction of Heat Transfer in Air-Cooled Disc-Type Electrical Machines," *IEEE Transactions on Industrial Applications*, vol. 47, no. 4, pp. 1716-1723, 2011.

[77] F Marignetti, V Colli, and Y Coia, "Design of Axial Flux PM Synchronous Machines Through 3-D Coupled Electromagnetic Thermal and Fluid-Dynamical Finite Element Analysis," *IEEE Transactions on Industrial Electronics*, vol. 55, no. 10, pp. 3591-3601, 2008.

[78] F Marignetti and V Colli, "Thermal Analysis of and Axial Flux Permanent-Magnet Machine," *IEEE Transactions on Magnetics*, vol. 45, no. 7, pp. 2970-2975, 2009.

[79] P Silvester and R Ferrari, *Finite Elements for Electrical Engineers*. Cambridge: Cambridge University Press, 1990.

[80] M Perry, *Low frequency electromagnetic design.*: Marcel Dekker INC., 1985.

[81] Arnold Magnetic Technologies Corp. (2014, May) arnoldmagnetics. [Online]. http://www.arnoldmagnetics.com/Neodymium_Literature.aspx

[82] D Lin et al., "A New Nonlinear Anisotropic Model for Soft Magnetic Materials," *IEEE Transactions on Magnetics*, vol. 42, no. 4, pp. 963-966, 2006.

[83] D Lin, P Zhou, W Fu, Z Badics, and Z Cendes, "A Dynamic Core Loss Model for Soft Ferromagnetic and Power Ferrite Materials in Transient Finite Element Analysis," *IEEE Transactions on Magnetics*, vol. 40, no. 2, pp. 1318-1321, 2004.

[84] F White, *Fluid Mechanics.*: McGraw-Hill, 2008.

[85] H Versteeg and W Malalasekera, *An Introduction to Computational Fluid Dynamics*. Harlow: Pearson Education Limited, 2007.

[86] D C Wilcox, *Turbulence modeling for CFD.*: La Canada, CA: DCW Industries, 1993.

[87] Motoyuki Itoh, Yutaka Yamada, Shigeki Imao, and Masahiro Gonda, "Experiments on Turbulent Flow due to an Enclosed Rotating Disk," *Experimental Thermal and Fluid Science*, vol. 5, pp. 359-368, 1992.

[88] R B Langtry and F R Menter, "Correlation-Based Transition Modeling for Unstructured Parallelized Computational Fluid Dynamics Codes," *AIAA*, vol. 47, no. 12, pp. 2894-2906, 2009.

[89] F Incropera and D DeWitt, *Fundamentals of Heat and Mass Transfer.*, 1996.

[90] Dave Staton, Aldo Boglietti, and Andrea Cavagnino, "Solving the More Difficult Aspects of Electric Motor Thermal Analysis inSmall and Medium Size Industrial Induction Motors," *IEEE Transactions on Energy Conversion*, vol. 20, no. 3, pp. 620-628, 2005.

[91] SKF Limited. SKF Bearing Caculator. [Online]. http://www.skf.com/uk/knowledge-centre/engineering-tools/skfbearingcalculator.html

[92] J P Holman, *Heat Transfer*. New York: McGraw-Hill, 1997.

[93] Brian Launder, Sebastien Poncet, and Eric Serre, "Laminar, Transitional, and Turbulent Flows in Rotor-Stator Cavities," *Annual Review of Fluid Mechanics*, vol. 42, pp. 229-248, 2010.

[94] S L Soo, "Laminar flow over an enclosed rotating disk," *Transactions of the ASME*, vol. 80, no. 2, pp. 287-296, 1958.

[95] J W Daily and R E Nece, "Chamber dimension effects on induced flow and frictional resistance of enclosed rotating disks," *Journal of Basic Engineering*, vol. 82, pp. 217-232, 1960.

[96] Rachid Boutarfa and Souad Harmand, "Local convective heat transfer for laminar and turbulent flow in a rotor-stator system," *Experiments in Fluids*, vol. 38, pp. 209-221, 2005.

[97] F White, *Heat and Mass Transfer*. Reading: Addison-Wesley, 1988.

[98] Michael F Modest, *Radiative Heat Transfer*. San Diego: Elsevier Science, 2003.

[99] ME Global. (2014, May) ME Global. [Online]. http://www.meglobal.biz/media/product_guides/MEGlobal_MEG.pdf

[100] H Hauptman and J Karle, "Locating the Principal Maxima of a Fourier Series," *Acta Cryst.*, vol. 6, pp. 469-473, 1953.

[101] Robert P Benedict, *Fundamentals of Temperature, Pressure, and Flow Measurements*. New York: John Wiley & Sons, 1984.

[102] N Takahashi, M Morishita, D Miyagi, and M Nakano, "Examination of magnetic properties of magnetic materials at high temperatures using a rind specimen," *IEEE Transactions on Magnetics*, vol. 46, no. 2, pp. 548-551, February 2010.

[103] Adam Christopher Malloy, Ricardo F Martinez-Botas, Malte Jaensch, and Michael Lamperth, "Measurement of heat generation rate in the permanent magnets of rotating electrical machines," in *Power Electronics Machines and Drives*, Bristol, 2012.

[104] David Reigosa, Briz Fernando, Pablo Garcia, Juan Manuel Guerrero, and Michael W Degner, "Magnet Temperature Estimation in Surface PM Machines Using High Frequency Signal Injection," *IEEE Transactions on Industry Applications*, vol. 46, no. 4, pp. 1468-1475, July-Aug 2010.

[105] Sami Ruoho, Minna Haavisto, Eelis Takala, Timo Santa-Nokki, and Martti Paju, "Temperature Dependance of Resistivity of Sintered Rare-Earth Permanent-Magnet Materials," *IEEE Transactions on Magnetics*, vol. 46, no. 1, pp. 15-20, 2010.

[106] Hugh W Coleman and W Glenn Steele, *Experimentation and Uncertainty Analysis for Engineers*. New York: John Wiley & Sons, 1999.

[107] Sura. (2014, May) Sura. [Online]. http://www.sura.se/Sura/hp_products.nsf/vOpendocument/03A8B2433FAE16C4C1256

AA8002280E6/$FILE/330-35.pdf?OpenElement

[108] F Deng, "Commutation-Caused Eddy-Current Losses in Permanent-Magnet Brushless DC Motors," *IEEE Transactions on Magnetics*, vol. 33, no. 5, pp. 4310-4318, September 1997.

[109] D A Howey, "Thermal design of air-cooled axial flux permanent magnet machines," London, 2010.

[110] S L Dixon, *Fluid Mechanics and Thermodynamics of Turbomachinery.*: Butterworth Heinemann, 2005.

[111] P Zhou, W Fu, D Lin, S Stanton, and Z Cendes, "Numerical Modeling of Magnetic Devices," *IEEE Transactions on Magnetics*, vol. 40, no. 4, pp. 1803-1809, 2004.

[112] Torayca. (2014, May) Tarayca. [Online]. http://www.toraycfa.com/pdfs/t800hdatasheet.pdf

[113] M Spittel and T Spittel, "Advanced Material and Technologies," in *Metal Forming Data of Ferrous Alloys - deformation behaviour*, H Warlimont, Ed. Berlin, Germany: Springer Berlin Heidelberg, 2009, pp. 948-953.

[114] Aalco Ltd. (2014, May) Aalco. [Online]. http://www.aalco.co.uk/datasheets/Aluminium-Alloy-6082-T6T651-Plate_148.ashx

[115] Superior Essex. (2014, May) Superior Essex. [Online]. http://www.superioressex.com/uploadedFiles/Magnet_Wire_and_Distribution/North_America/Magnet_Wire_-_Winding_Wire/US_b.pdf

[116] Dolph's, "Dolphon CC-1105-HTC," Dolph's, Technical Data Sheet.

[117] Dupont. (2014, May) Dupont. [Online]. http://www2.dupont.com/Energy_Solutions/en_US/assets/downloads/Nomex%20Paper%20410/DPP_Nomex410_K20612-1.pdf

Appendices

Appendix A Numerical Formulation

A.1 Finite Element Formulation

Ansoft uses the $\vec{T} - \Omega$ finite element formulation to solve 3D transient electromagnetic problems; a summary of the formulation is given here for reference with details presented in the work of Zhou et al [111]. In order to reduce the number of degrees of freedom in the system, field quantities are represented as potentials as shown in Equations (A.1) and (A.2), where $\vec{T}$ is the current vector potential, Ω is the magnetic scalar potential, $\vec{H}_c$ is the source field due to permanent magnets and $\vec{H}_s$ is the source field due to known currents. When these potentials are inserted into Faraday's law and Gauss's law (Equations (3.2) and (3.4) respectively) Equations (A.3) and (A.4) result for conducting regions while Equation (A.5) results for non-conducting regions.

$$\vec{J} = \nabla \times \vec{T} \tag{A.1}$$

$$\vec{H} = \vec{H}_c + \vec{H}_s + \vec{T} + \nabla\Omega \tag{A.2}$$

$$\nabla \times \left(\frac{1}{\sigma}\nabla \times \vec{T}\right) + \frac{d}{dt}\left(\mu\vec{T} + \mu\nabla\Omega\right) = -\frac{d}{dt}\left(\mu\vec{H}_c + \mu\vec{H}_s\right) \tag{A.3}$$

$$\nabla \cdot \left(\mu\vec{T} + \mu\nabla\Omega\right) = -\nabla \cdot \left(\mu\vec{H}_c + \mu\vec{H}_s\right) \tag{A.4}$$

$$\nabla \cdot (\mu\nabla\Omega) = -\nabla \cdot \left(\mu\vec{H}_c + \mu\vec{H}_s\right) \tag{A.5}$$

The FEM is based on minimising the energy stored in the solution domain and therefore an expression for the energy stored needs to be derived. Details of the derivation of such functionals can be found in Silvester and Ferrari [79] or in a more succinct form in the book by Gieras and Wing [1] which is specific to electrical machines.

Spatial Discretisation

Ansoft breaks the computational domain up into a number of discrete second order tetrahedral elements as shown in Figure A.1 where the energy stored in each element is assumed to be a quadratic function of position, see Equation (A.6). Information about the shape of each element and therefore how the solution of $\vec{T}$ and Ω vary within them are assembled into coefficient matrices $[S]$, $[Q]$ and $[B]$ which are inverted to solve for $\vec{T}$ and Ω at each node, see Equation (A.7), $\{g\}$ is a column vector of source terms (winding currents and permanent magnet coercivities).

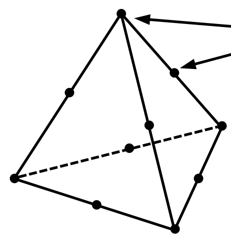

Figure A.1 Second order tetrahedral element

$$W(x,y,z) = a_0 + a_1x + a_2y + a_3z + a_4xy + a_5yz + a_6xz + a_7x^2 + a_8y^2 + a_9z^2 \qquad \text{(A.6)}$$

$$\left([S] + \frac{d}{dt}[Q]\right)\{\vec{T}\} + \frac{d}{dt}[B]\{\Omega\} = \{g\} \qquad \text{(A.7)}$$

Non-Linear Material Properties

The permeability of electrical steel is a non-linear function of the flux density it is carrying. Ansoft uses the Newton-Raphson method to account for this with Equation (A.7) being solved repeatedly until the change in material permeability with each iteration has dropped below a prescribed threshold.

Temporal Discretisation

A backwards time stepping scheme is used to approximate the time derivative of any variable x at any time step t_n as shown in Equation (A.8).

$$\frac{dx^{t_n}}{dt} = \frac{x^{t_n} - x^{t_{n-1}}}{t_n - t_{n-1}} \qquad \text{(A.8)}$$

A.2 Core Loss Prediction

This summary is provided for reference, full details are given by Lin et al [83].

In order to calculate hysteresis loss in the time domain the magnetic field H of the hysteresis loop shown in Figure A.2 is decomposed into reversible and irreversible components, where $H_{rev}dB$ equals reactive power and $H_{irr}dB$ equals hysteresis loss. Instantaneous hysteresis loss is then given by Equation (A.9), where H_{irr} is evaluated by considering the elliptical loop in Figure A.2 whose area is the same as the original hysteresis loop and is given by Equation (A.10).

$$q_h(t) = H_{irr}\frac{dB}{dt} \tag{A.9}$$

$$\begin{cases} B = B_m \sin\theta \\ H_{irr} = H_m \cos\theta \end{cases} \tag{A.10}$$

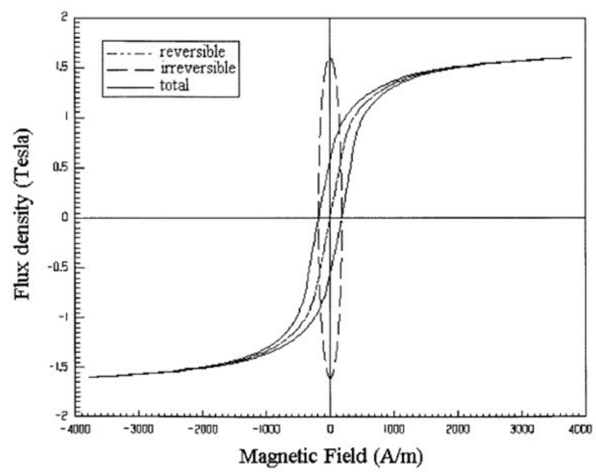

Figure A.2 Equivalent elliptical loop, from [83]

The value of B_m is obtained directly from the history of the transient solution whereas H_m is determined by requiring that the core loss calculated in the time domain must be the same as is calculated in the frequency domain under the same sinusoidal excitation. This is achieved by applying a sinusoidal excitation of B to (A.9), time averaging, and setting this equal to the hysteresis component of the Steinmetz equation. This results in Equation (A.11) which gives a value for H_{irr} based only on the standard empirical coefficient and B_m.

$$H_{irr} = \frac{1}{\pi}k_h B_m \cos\theta \tag{A.11}$$

The authors derive expressions for eddy current and excess losses in a similar way; the whole formulation is given in Equations (A.12), (A.13), and (A.14).

$$q_h(t) = \left|\vec{H}_{\boldsymbol{irr}} \frac{d\vec{B}}{dt}\right|^2 \tag{A.12}$$

$$q_c(t) = \frac{1}{2\pi^2} k_c \left(\frac{d\vec{B}}{dt}\right)^2 \tag{A.13}$$

$$q_e(t) = \frac{1}{C_e} k_e \left\{\left(\frac{d\vec{B}}{dt}\right)^2\right\}^{0.75} \tag{A.14}$$

A.3 Finite Volume Formulation

Ansys CFX breaks the computational domain up into a number of elements as shown in Figure A.3. Finite volumes are then constructed around each node, using edge and element centres to define the boundaries.

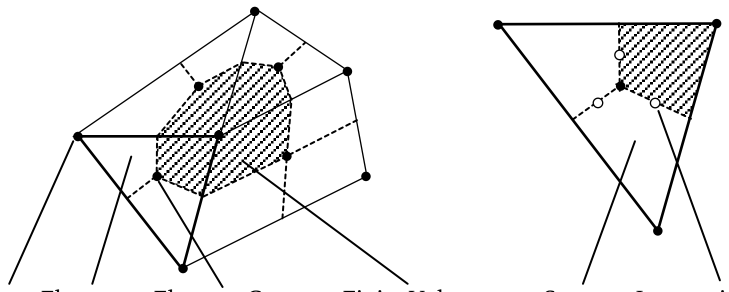

Figure A.3 Finite volume discretisation

The governing equations, (3.20) and (3.21), are integrated over the volumes and converted into discrete form before being solved. Equations (A.15)-(A.18) describe this process for the transport of a scalar quantity, φ, where Gauss' divergence theorem is used to convert some of the volume integrals into surface integrals, allowing them to be evaluated over finite volume boundaries. The resulting volume integrals are evaluated for each element sector and then added to the control volume to which the sector belongs. The surface integrals are evaluated at the integration points on each surface segment, and then attributed to the finite volume on each side of the segment.

$$\frac{\partial(\rho\varphi)}{\partial t} + \nabla \cdot \left(\rho\vec{V}\varphi\right) = \nabla \cdot (\Gamma\nabla\varphi) + S_\varphi \tag{A.15}$$

$$\frac{d}{dt}\int_V \rho\varphi\, dV + \int_V \nabla \cdot \left(\rho\vec{V}\varphi\right) dV = \int_V \nabla \cdot (\Gamma\nabla\varphi) dV + \int_V S_\varphi\, dV \tag{A.16}$$

$$\frac{d}{dt}\int_V \rho\varphi\, dV + \int_S \rho\vec{V}\varphi d\vec{n} = \int_S \Gamma\nabla\varphi d\vec{n} + \int_V S_\varphi\, dV \tag{A.17}$$

$$V\left(\frac{\rho\varphi_{t_n} - \rho\varphi_{t_{n-1}}}{t_n - t_{n-1}}\right) + \sum_{ip}(\dot{m}\varphi)_{ip} = \sum_{ip}(\Gamma\nabla\varphi\Delta n)_{ip} + \bar{S}_\varphi V \tag{A.18}$$

The analyses presented in this thesis are all steady state, however in order to solve the discretised equations the solver time steps the solution until the time derivative components of each equation are relatively small. For brevity the above set of equations was shown with a first order backwards Euler time discretisation scheme, Ansys CFX actually uses a second order backward Euler scheme where the start and end time step values are given by Equations (A.19) and (A.20). When these values are substituted back into Equation (A.18) the resulting discretisation is as in Equation (A.21).

$$(\rho\varphi)^{n-\frac{1}{2}} = (\rho\varphi)^{n-1} + \frac{1}{2}((\rho\varphi)^{n-1} - (\rho\varphi)^{n-2}) \tag{A.19}$$

$$(\rho\varphi)^{n+\frac{1}{2}} = (\rho\varphi)^{n} + \frac{1}{2}((\rho\varphi)^{n} - (\rho\varphi)^{n-1}) \tag{A.20}$$

$$\frac{d}{dt}\int_V \rho\varphi \, dV \approx \frac{1}{\Delta t}\left(\frac{3}{2}(\rho\varphi) - 2(\rho\varphi)^{n-1} + \frac{1}{2}(\rho\varphi)^{n-2}\right) \tag{A.21}$$

The linearized equations are assembled into a matrix equation shown in Equation (A.22) where $[A]$ is a coefficient matrix, $\{\varphi\}$ is the field solution and $\{b\}$ contains any source terms. CFX solves this equation iteratively, beginning with an initial guess for $\{\varphi\}$ then calculating the error in the solution from Equation (A.23) and finally generating the next guess from Equations (A.24) and (A.25). The process is repeated until the error r^n is acceptable small. As was the case with the FEM presented earlier in this section the solution, or its normal derivative, must be prescribed at the boundaries of the problem.

$$[A]\{\varphi\} = \{b\} \tag{A.22}$$

$$r^n = \{b\} - [A]\{\varphi^n\} \tag{A.23}$$

$$\varphi^{n+1} = \varphi^n + \varphi' \tag{A.24}$$

$$\varphi' = [A]^{-1} r^n \tag{A.25}$$

Appendix B Material Properties

B.1 Material Properties

Table B.1 summarises the thermal properties of each material used in the CHT analysis. Figure B.4 shows the demagnetisation characteristic of N33 EH at a range of temperatures.

Table B.1 Summary of material properties used in CHT simulations

Component	Material	Density [kg/m^3]	Heat Capacity [J/kgK]	Thermal Conductivity [W/mK]	Source
Magnet	N33 EH	7500	460	r=6.75 θ=6.75 z=6.16	[81]
Rotor	Glass Fibre	2500	800	0.25	
Banding	Carbon Fibre	1810	753	35.1	[112]
	Resin	1190	1175	0.175	[112]
Shaft	Steel 13NiCr15	7862	476	35.5	[113]
Casing &	Aluminium	2700	875	180	[114]
Winding	Copper	8960	385	400	[115]
	Resin	1190	1175	0.325	[116]
Stator Core	Steel M330-35A	7650	476	36	[107]
	Resin	1190	1175	0.325	[116]
Slot Closer	Nomex 410	1080	1050	0.175	[117]

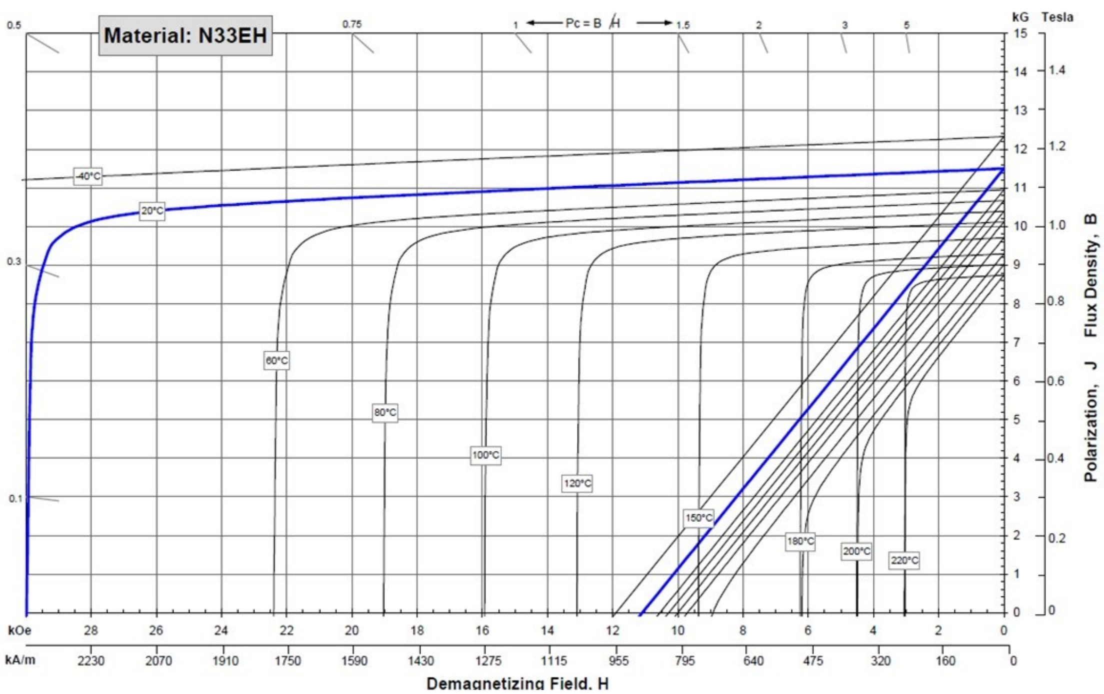

Figure B.4 Demagnetisation characteristic of N33EH taken from [81], the blue lines plot the characteristic at 20°C

Appendix C Experimental Results

C.1 Steady State Test Results

For reference, the experimental results from the steady state tests presented in Section 6.4.2 are given in Table C.2. These results are the average of 3 repeats of the experiment.

Table C.2 Steady state results

	Variable	2000rpm 40A	±	3000rpm 40A	±	4000rpm 40A	±
DC	Voltage [V]	359.18	2.03	358.76	2.16	358.31	1.13
	Current [A]	20.62	0.13	29.06	0.19	36.97	0.23
	Power [kW]	7.41	0.01	10.42	0.02	13.25	0.04
AC	Frequency [Hz]	166.65	0.02	249.97	0.05	333.36	0.00
	Voltage [Vrms]	135.66	2.98	142.20	1.43	145.89	2.24
	Current [Arms]	40.63	0.50	40.45	0.50	40.28	0.50
	Power Factor	0.40	0.01	0.55	0.01	0.70	0.01
	Power [kW]	6.61	0.02	9.56	0.03	12.41	0.01
Mechanical	Torque [Nm]	28.9	0.53	27.7	0.52	26.3	0.52
	Power [kW]	6.06	0.11	8.70	0.16	11.01	0.11
Coolant	Flow Rate [l/m]	4.0	0.20	4.0	0.20	4.0	0.20
	Inlet Temperature [ºC]	50.0	0.28	50.0	0.28	50.0	0.28
Static Pressure [Pa]	Inner	-40.4	4.15	-81.3	4.56	-131.8	5.37
	Middle	-34.1	4.30	-71.0	4.45	-108.7	6.25
	Outer	-25.0	4.39	-53.1	5.60	-76.8	7.82
Temperature Rise [K]	Winding Inner	12.8	1.31	17.7	0.45	22.3	0.64
	Winding Middle	12.3	1.16	17.8	0.39	22.5	0.56
	Winding Outer	12.4	0.44	17.6	0.48	22.2	0.48
	Core Deep	9.1	0.26	13.6	0.38	19.0	0.51
	Core Medium	7.6	0.07	11.4	0.07	15.7	0.14
	Core Shallow	5.0	0.05	7.5	0.09	10.4	0.15
	Case	1.7	0.20	1.8	0.32	2.6	0.59
	Bearing Housing	2.7	1.55	4.0	0.20	5.1	0.88
	Magnets	40.5	3.70	54.7	3.54	66.9	3.39

C.2 DC Heating Tests

Method

Certain thermal properties in electrical machines are difficult to determine analytically or numerically [90]. These include the thermal conductivity of copper windings and thermal contact resistances, which tend to vary from machine to machine (even within one manufactured batch). One accepted approach is to conduct a DC heating test where all phases of the machine are connected in series and a DC current is passed through them. In this way, the losses in the machine are only the i^2R losses and the internal convective coefficients are assumed small as the rotor is stationary. The remaining degrees of freedom are the unknown material properties and contact resistances. This test was conducted on the machine in the present work, coolant was pumped through the coolant jacket by a standalone cooler which kept the coolant inlet temperature at 50deg, the flow rate was 4l/m. The test was repeated with three different power dissipations (300W, 600W, and 1200W) in the windings with steady state temperatures in the winding, core and casing being recorded.

Results

Table C.3 presents the experimental results in tabular form for reference. The results of the DC Heating experiments were used to determine the values of the winding equivalent thermal conductivity and the case to core thermal interface. The computational domain presented in Section 3.2.5 was modified to replicate the boundary conditions assumed to be present during the experiment i.e. the fluid domain was removed and adiabatic boundaries were applied to all solid surfaces which were once joined to the fluid domain. Losses in the core and magnets were set to 0 and losses in the winding were set to the value recorded during the experiment. The simulation was solved iteratively with the winding thermal conductivity and core-case interface being adjusted to best match the experimental results of the 600W experiment. The winding equivalent thermal conductivity was found to be 0.75 W/mK in the axial and circumferential directions; the core-case interface resistance was found to be 0.00011 W/m^{2}K. As a check the 300W and 1200W experiments were simulated with the same thermal properties as determined by the 600W study. Figure C.5 shows the measured and predicted temperature profiles in the winding and stator core, where the tuning process has been deemed to be successful.

Table C.3 DC heating test results

		300W	±	600W	±	1200W	±
Temperature Rise [K]	Winding Inner	14.0	0.98	28.7	2.40	53.1	4.23
	Winding Middle	13.5		27.8		51.4	
	Winding Outer	13.6		27.8		51.6	
	Core Deep	5.6	0.36	11.0	0.43	20.8	0.67
	Core Medium	4.5		8.7		16.3	
	Core Shallow	3.0		5.7		10.9	
	Case	2.0	0.32	2.2	0.46	3.6	0.81
	Bearing Housing	1.6		2.8		5.5	

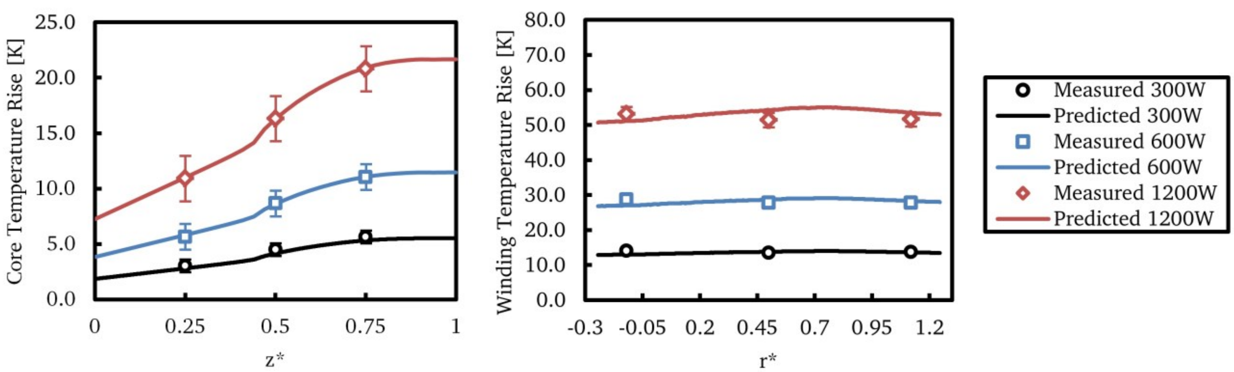

(a) Core temperature rise

(b) Winding temperature rise

Figure C.5 Comparison between measured and predicted temperature profile during DC heating experiment